

**Dissertation**  
**submitted to the**  
**Combined Faculties for the Natural Sciences and for Mathematics**  
**of the Ruperto-Carola University of Heidelberg, Germany**  
**for the degree of**  
**Doctor of Natural Sciences**

**Put forward by**  
**Diplom-Physikerin Franziska Ruth Winter**  
**Born in: Berlin**  
**Oral examination: 13 January 2016**



# Multicolour STED nanoscopy with hyperspectral detection

Referees:

Prof. Dr. Stefan W. Hell  
Prof. Dr. Ulrich Schwarz



# Abstract

## **Multicolour STED nanoscopy with hyperspectral detection**

Within the scope of this thesis, a new multicolour STED microscope with a hyperspectral detection was designed and built. The challenges regarding the limitation of usable fluorophores as well as the stability of the optical set-up were overcome. Different existing spectral unmixing methods were compared to a self-implemented algorithm, both in simulations and using experimental data. A detailed study of the best separation conditions for several dye combinations was carried out for each of the methods. During the experiments, a spectral blue shift of several dyes was observed and its mechanisms were investigated. The optical resolution of the set-up was dye dependent and better than 80 nm for all dyes. Moreover, an excellent separation for three fluorescent bead species and good a separation for a four-colour fixed-cell sample was achieved. This was done for the first time by purely distinguishing the different emission spectra using only one wavelength for excitation and a single STED beam for depletion.

## **Mehrfarben-STED Nanoskopie mit hyperspektraler Detektion**

In der vorliegenden Arbeit wurde ein neuartiges Mehrfarben-STED Mikroskop mit hyperspektraler Detektion konzipiert und aufgebaut. Die Herausforderungen sowohl der Einschränkung an verwendbaren Fluorophoren sowie auch der Stabilität des optischen Aufbaus wurden bewältigt. Verschiedene bereits existierende Methoden zum spektralen Entmischen wurden mit einem selbst programmierten Algorithmus in Simulationen und mit Hilfe experimenteller Daten verglichen. Eine Studie zu den besten Trennungsbedingungen für verschiedene Farbstoffkombinationen für die einzelnen Methoden wurde durchgeführt. Experimentell wurde eine spektrale Blauverschiebung einiger Farbstoffe beobachtet und ihre Mechanismen untersucht. Die optische Auflösung war farbstoffabhängig aber stets besser als 80 nm. Ferner wurde eine exzellente Trennung für drei verschieden farbige, fluoreszente Kügelchen und eine gute Trennung in einer vierfach gefärbten, fixierten Zellprobe erzielt. Die Unterscheidung basierte dabei erstmals lediglich auf den Emissionsspektren und wurde mit nur einer Anregungswellenlänge und einem einzigen STED Strahl erreicht.



# Glossary of symbols and acronyms

<b>A</b>	transfer matrix; percentage dye distribution per channel
<b>C</b>	cost function
<b>d</b>	minimal distance/feature size
<b><math>\delta</math></b>	difference of the percentage distribution $r_i$ between the confocal images before and after a blueing condition
<b><math>\kappa</math></b>	segregation bias parameter
<b><math>\lambda</math></b>	wavelength
<b>P<sub>sat</sub></b>	saturation intensity
<b>P<sub>STED</sub></b>	STED power in the back aperture of the objective
<b>T</b>	percentage dye distribution per time gate
<b><math>\tau</math></b>	fluorescence lifetime
<b><math>\tau_D</math></b>	diffusion time through the focal spot
<b><math>r_i</math></b>	percentage distribution in channel $i$
<b>Q</b>	strength of excitation per dye
<b>X</b>	dye distribution per pixel
<b><math>\xi</math></b>	measure for the goodness of the unmixing result
<b>Y</b>	measured data
<b>APD</b>	avalanche photo diode
<b>AOTF</b>	acousto-optical tunable filter
<b>AOBS</b>	acousto-optical beam splitter
<b>FCS</b>	fluorescence correlation spectroscopy
<b>FPGA</b>	field-programmable gate array
<b>FSK</b>	frequency shift keying
<b>FWHM</b>	full width at half maximum
<b>GSD</b>	ground state depletion microscopy
<b>GSDIM</b>	GSD followed by individual molecule return
<b>HyperSTED</b>	multicolour STED set-up with a hyperspectral detection
<b>ImageJ</b>	PoissonNMF plugin for ImageJ
<b>LinUnmix</b>	linear unmixing
<b>MCR</b>	multivariate curve resolution
<b>NA</b>	numerical aperture
<b>NNMF</b>	non-negative matrix factorization
<b>PAINT</b>	point accumulation for imaging in nanoscale topography

PALM	photoactivated localization microscopy
PALMIRA	PALM with independently running acquisition
PMT	photo multiplier tube
PSF	point spread function
QS	quadscanner
RESOLFT	reversible saturable optical (fluorescent) transitions
RF	radio frequency
SEM	scanning electron microscopy
SNR	signal-to-noise ratio
SPA	spectral phasor analysis
SPDM	spectral precision distance microscopy
STED	stimulated emission depletion
STORM	stochastic optical reconstruction microscopy

# Contents

<b>1</b>	<b>Introduction</b>	<b>1</b>
<b>2</b>	<b>Theoretical background</b>	<b>5</b>
2.1	Light microscopy . . . . .	5
2.2	Stimulated emission depletion . . . . .	6
2.3	Acousto-optical tunable filters . . . . .	8
2.4	Data analysis algorithms . . . . .	10
2.4.1	Linear unmixing . . . . .	10
2.4.2	Non-negative matrix factorization . . . . .	11
2.4.3	PoissonNMF plugin for ImageJ . . . . .	13
2.4.4	Estimating $\mathbf{A}$ with a probability approach . . . . .	13
<b>3</b>	<b>Experimental set-up</b>	<b>17</b>
3.1	Overview and beam paths . . . . .	17
3.2	Acousto-optical beam splitter . . . . .	20
3.3	Beam scanning with the quadscanner . . . . .	22
3.4	Detection unit . . . . .	23
3.5	Experimental control and electronic pathways . . . . .	27
3.6	Set-up characterization . . . . .	28
3.6.1	Choosing the excitation wavelength . . . . .	28
3.6.2	PSF measurements and beam alignment . . . . .	30
3.6.3	Run time and timing issues of excitation and STED . . . . .	33
3.6.4	Setting the time gating parameters . . . . .	34
3.6.5	Available STED power and resolution . . . . .	34
<b>4</b>	<b>Simulations</b>	<b>35</b>
4.1	Input parameters . . . . .	35
4.2	Introduction of the measure $\xi$ . . . . .	38
4.3	Number of iterations needed for NNMF . . . . .	38
4.4	Excitation with one wavelength . . . . .	39
4.4.1	Separation and crosstalk of two dyes . . . . .	40
4.4.2	Separation and crosstalk of three dyes . . . . .	43
4.4.3	Separation and crosstalk of four dyes . . . . .	46

4.4.4	Summary of the simulations with one wavelength . . . . .	50
4.5	Excitation with two wavelengths . . . . .	51
4.6	Lifetime and one excitation wavelength . . . . .	52
4.6.1	Lifetime separation via two time gates . . . . .	52
4.6.2	Separation and Crosstalk of two, three and four dyes . . . . .	53
4.7	Conclusion of the simulations . . . . .	56
<b>5</b>	<b>Experimental results</b>	<b>57</b>
5.1	Fluorescent beads . . . . .	58
5.1.1	Optical resolution on 24 nm crimson beads . . . . .	59
5.1.2	Data analysis and crosstalk of three bead species . . . . .	59
5.2	Dependence of the resolution on the dye . . . . .	64
5.2.1	Estimating $P_{\text{sat}}$ via pump probe measurements . . . . .	64
5.2.2	Estimating $P_{\text{sat}}$ via FCS measurements . . . . .	66
5.3	Organic dyes feasible for HyperSTED . . . . .	69
5.4	STED imaging with one excitation wavelength . . . . .	71
5.4.1	Minimal distance of emission maxima . . . . .	71
5.4.2	Four-colour separation in a fixed-cell sample . . . . .	74
5.5	STED imaging with two excitation wavelengths . . . . .	81
5.5.1	Multiplexing a two-colour sample . . . . .	81
5.5.2	Different emission spectra when multiplexing . . . . .	86
5.6	Spectral blueing during STED imaging . . . . .	90
5.6.1	Examined dyes and detection configurations . . . . .	90
5.6.2	Measuring scheme, blueing conditions and analysis . . . . .	92
5.6.3	Results for the two sets of dyes . . . . .	94
5.6.4	Hypothesis of the origin of the blue population . . . . .	101
5.7	Conclusion of the results . . . . .	102
<b>6</b>	<b>Discussion and outlook</b>	<b>105</b>
	<b>Appendix A Antibodies</b>	<b>111</b>
	<b>Appendix B Sample Preparation</b>	<b>113</b>
	<b>Appendix C Algorithms</b>	<b>115</b>
	<b>Appendix D Further organic dyes</b>	<b>119</b>
	<b>Appendix E Supplementary images</b>	<b>121</b>
	<b>Bibliography</b>	<b>137</b>

# Chapter 1

## Introduction

*„Der, die, das,  
wer, wie, was,  
wieso, weshalb, warum,  
wer nicht fragt bleibt dumm!“*

Titellied der Sesamstraße

Curiosity is at the core of all understanding. And the first reaction when encountering something unknown is to take a closer look and observe. For it is the visual stimulus that convinces us most easily that something either is or is not. Therefore, it is not surprising that the examination by sight is one of the most used investigation methods by man. With the invention of the compound light microscope in the 17<sup>th</sup> century [38], the possibility of observing smaller objects took a drastic leap forward. Limited at first by the quality of the optics and then by the diffraction of light, the resolution of these microscopes was confined roughly to half the wavelength of the probing light [2]. This insight, discovered by Ernst Abbe in the 19<sup>th</sup> century, heralded the beginning of modern light microscopy. Even the fluorescence microscopy introduced in the early 1900s [1] and the confocal microscopy in the middle of the 20<sup>th</sup> century [73] are bound by this fundamental law. With these light microscopes observations of features smaller than roughly 200 nm are impossible. Finer details down to a size of several nm can be studied with electron microscopy introduced at the beginning of the 20<sup>th</sup> century [30]. However, the requirements imposed on the samples for scanning electron microscopy (SEM) are enormous. Biological specimens need to be fixated, dehydrated and made electronically conductive to be observed in the vacuum chamber of a SEM [30]. These constraints on the samples do not exist in light microscopy. With the upcoming of super resolution techniques in fluorescence microscopy at the end of the 20<sup>th</sup> century, even the diffraction limit of light could be broken. This opened up the possibility of studying structures down to a size of several tens of nm with light microscopy. It took another two decades before "the development of super-resolved fluorescence microscopy" by Stefan W. Hell,

Eric Betzig and William E. Moerner was awarded the Nobel Prize in Chemistry in 2014 [72].

Since the first proposal of a super resolution technique by Hell and Wichmann in 1994 [45] called stimulated emission depletion (STED) which is part of the more general concept of reversible saturable optical (fluorescent) transitions (RESOLFT) [44], several other super resolution methods have emerged. Amongst others, there are stochastic optical reconstruction microscopy (STORM) [79, 80], photoactivated localization microscopy (PALM) [8], PALM with independently running acquisition (PALMIRA) [28], point accumulation for imaging in nanoscale topography (PAINT) [83], ground state depletion microscopy (GSD) [39], GSD followed by individual molecule return (GSDIM) [26] and spectral precision distance microscopy (SPDM) [56]. Whereas STED, RESOLFT and GSD rely on a saturation effect and a targeted readout mode to confine the fluorescence to a diffraction unlimited spot, PALM, STORM, GSDIM, SPDM and PAINT use a stochastic readout approach in which the molecules blink randomly and only a few of them emit fluorescence at any one time. The centre position of these isolated molecules is then localized. Because only very few molecules fluoresce simultaneously, all stochastic approaches require the evaluation of many frames which results in rather long image acquisition times of several minutes to hours. Further, the need for image reconstruction is prone to analyzing artifacts. But stochastic methods often provide higher resolution since the latter is mainly subjected to the localization precision of individual molecules which can be very good. In contrast, with the targeted readout mode of STED the images can be obtained in several seconds or even at video rate [94]. Here, the superposition of a Gaussian excitation beam and a doughnut shaped STED beam keeps all molecules in the periphery of the excitation beam in a dark state. This stimulated deexcitation is the key for breaking the diffraction limit [43]. Note that other STED beam modes are also possible [48, 51]. Drawbacks of this method are the need of matching the excitation and STED wavelengths, the high intensity of the STED beam, as well as a fluorescence detection that also needs to be adapted to the lasers and the used fluorescent markers. All these methods have been shown to achieve resolutions below 30 nm.

The aforementioned fluorescent super resolution techniques are well suited to study biological processes and complexes that are often the interplay of various proteins, structures and compounds (e.g. cells during apoptosis [33] or the nuclear pore complex [89]). To unravel their details, it is inevitable to observe and distinguish the individual participants simultaneously and at nanoscale resolution. Discrimination of the fluorescent markers can thereby take place by excitation, emission, lifetime, photostability or any combination thereof. However, the need for separation of more markers is accompanied by a rise in complexity of the optical set-up, often at the expense of usability and stability.

So far, several attempts of two-colour imaging using various super resolution tech-

---

niques were reported, often combining two separation methods and involving up to four different laser beams and up to two spectral or temporal detection channels. For PALM there are, for example, the works of Shroff et al. in 2007 [84] and Subach et al. in 2009 [88]. For RESOLFT, there are the works of Lavoie-Cardinal et al. in 2014 [54] and Testa et al. in 2015 [90]. For PALMIRA, there is Bock et al. in 2007 [12]. For STORM, there is Bates et al. in 2007 [5], where three-colour discrimination was demonstrated as well. There are also the works of Schmidt et al. in 2008 [81] and Aquino et al. in 2011 [3] that showed two-colour separation in 3D with 4pi STED and STORM respectively. Then, there are several reports employing various two-colour STED set-ups. The first was performed by Donnert et al. in 2007 [22], followed by Meyer et al. in 2008 [64] and Neumann et al. in 2010 [71]. In 2011, we have of Tønnesen et al [92] and Pellet et al. [74] followed by Berning et al. in 2012 [7] and Kempf et al. [49], Göttfert et al. [32] in 2013. Finally, there are the works of D’Este et al. [20] using conventional STED and Bergermann et al. [6] using parallelized STED in 2015. Surely, there are more reports on dual-colour imaging than listed above and there are still many more to come, but the ones referenced here give a good overview on what has been done so far.

When it comes to three-colour imaging, the successful reports become scarcer. In the stochastic readout approach, there are Bates et al. in 2007 [5] and Bossi et al. in 2008 [13]. For STED, we have Bückers et al. in 2011 [15] and Görlitz et al. in 2014 [29].

Four-colour discrimination was so far mainly reported for the stochastic readout methods. It was shown by Testa et al. in 2010 for GSDIM [91], by Dempsey et al. in 2011 for STORM [19], by Jungmann et al. in 2014 for PAINT [47] and by Zhang et al. in 2015 for spectrally resolved STORM [95]. For STED, it was demonstrated by Rönnlund et al. [77] in 2014.

Whereas the number of observable markers in confocal microscopy surpassed the number of five in 2004 [58, 85, 86] and reached the number of 8 in 2013 [18], the super resolution techniques continue to struggle to distinguish more than a few labels. An exception is the work of Jungmann et al. [47] in which 10 colours were separated by Exchange-PAINT. Although this greatly increased the number of separable labels, it came at the cost of repeated imaging-washing steps which tremendously increased the image acquisition times. Nevertheless, the lack of any targeted super resolution method capable of discriminating more than two colours purely based on their different emission properties, marks the starting point of this thesis.

The aim of this work was to design and build a versatile yet simple and stable STED set-up suitable for the separation of as many colours as possible. To ensure a good stability of the optical set-up, only two lasers were implemented: a supercontinuum source and a single STED beam at 775 nm. The versatility was granted by the combination of the supercontinuum source with an AOTF to allow an arbitrary choice

of up to 8 different excitation wavelengths. Since with the supercontinuum source and the single STED laser, only two beams needed to be superimposed, the stability of the optical set-up was greatly improved without sacrificing the flexibility of choosing any desired excitation wavelength. Another benefit of employing a single STED beam, which albeit put a constraint on the spectrum of the usable dyes, was the advantage of delivering less energy to the sample and thus rendering the imaging process less phototoxic to the cell under observation.

Following the concept of hyperspectral detection demonstrated in multicolour confocal methods [18, 58, 85, 86], a highly sensitive detection unit was designed that spanned a total range of 270 nm (480 nm–750 nm) divided into 8 spectral channels. This enabled the use of any fluorophore with an emission spectrum in this range. Hence most of the former limitation regarding the choice of the fluorophores was removed. The only remaining one for imaging one colour, was that the fluorophore needed to be depletable with 775 nm. In multicolour experiments there was an additional constraint, namely the separability. The chosen fluorophores had to be spectrally distinct enough so they could be separated, making their choice a crucial element. Whether or not two fluorophores were distinguishable depended on their actual emission spectra, the precise edges of the detection windows and the spectral unmixing algorithm. There are currently several algorithms available: spectral phasor analysis (SPA) [25], multivariate curve resolution (MCR) [34, 35], non-negative matrix factorization (NNMF) [68, 69, 70] and linear unmixing (LinUnmix) [96]. Here, NNMF and LinUnmix were extensively used for separation, but MCR and SPA should also be applicable.

This thesis is divided into 6 chapters. Chapter 1 gives an introduction to multicolour super resolution imaging. Chapter 2 explains the theoretical background needed to understand the contents of this work, while chapter 3 describes the new design of an experimental STED set-up with hyperspectral detection (HyperSTED). Chapters 4 and 5 show the results of the separation capability of the here presented set-up obtained by simulations and performed experiments. Finally, chapter 6 concludes this thesis and gives an outlook on future work.

# Chapter 2

## Theoretical background

In this chapter a short summary of the theoretical background of light microscopy and stimulated emission depletion (STED) microscopy will be given (see sections 2.1 and 2.2). The functional principle of an acousto-optical tunable filter (AOTF) will be explained in section 2.3. Further, the mathematical foundations of the different analysis methods for hyperspectral images will be described in section 2.4.

### 2.1 Light microscopy

Light microscopy is one of the most used investigation methods of modern science. The foundations of modern light microscopy date back to the 19<sup>th</sup> century and the research of Ernst Abbe [2]. He showed that the image of a point source in the focal plane of an ideal objective with a circular aperture is not infinitely small. Because it is subjected to diffraction, its image results in a circular Airy pattern with radius

$$r_{\text{Airy}} = \frac{1.22 \cdot \lambda}{2 \cdot \text{NA}}, \quad (2.1)$$

where  $\lambda$  is the wavelength and  $\text{NA} = n \cdot \sin \alpha$  the numerical aperture of the objective with  $n$  denoting the refractive index and  $\alpha$  the half cone angle. The factor of 1.22 stems from the corresponding Bessel functions (see [38] or [73] for details).

The Airy pattern must not be confused with the point spread function (PSF) of an optical system. The PSF describes the system's image of a point source. In it, all aberrations introduced by the optical components are included. So, for an ideal system with no aberrations, the resulting PSF is a perfect Airy pattern [38, 73].

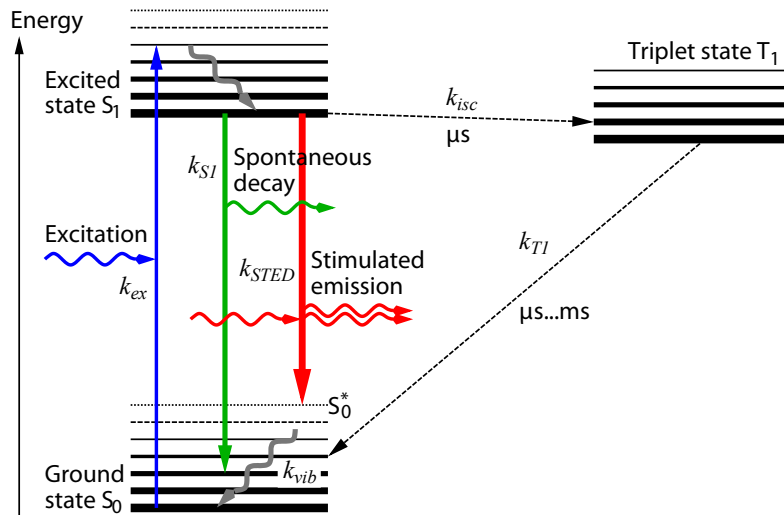
According to the Rayleigh criterion, two small objects that are separated by the distance  $d$  in the specimen plane are said to be resolvable in the image plane if  $d$  is larger or equal to the radius of the Airy disc [38, 73].

$$d = r_{\text{Airy}} = \frac{0.61 \cdot \lambda}{\text{NA}} \quad (2.2)$$

The distance  $d$  in equation (2.2) is in general called the diffraction limited resolution or resolving power of a microscope. Note that equations (2.1) and (2.2) are the same due to the definition of the Rayleigh criterion. Choosing a different criterion leads to different coefficients in equation (2.2) but the proportionality between  $d$  and  $\lambda/\text{NA}$  remains.

## 2.2 Stimulated emission depletion

Stimulated emission depletion (STED) microscopy is an advancement of confocal fluorescence microscopy. In confocal microscopy, a pinhole is used in front of the detector to suppress the scattered light from those parts of the sample other than the focal spot (see [73] or [53] for details). To visualize the processes occurring in a chromophore during fluorescence microscopy, Jablonski diagrams are used. Such a diagram is depicted in figure 2.1.



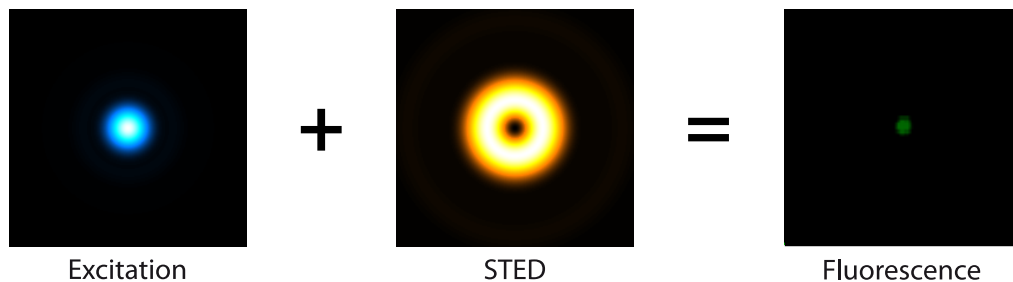
**Figure 2.1:** Typical Jablonski diagram of a fluorophore illustrating the different basic states (ground state  $S_0$ , excited state  $S_1$  and triplet state  $T_1$ ) as well as the rates for absorption  $k_{ex}$ , spontaneous decay  $k_{S1}$ , stimulated emission  $k_{STED}$ , vibrational relaxation  $k_{vib}$  and inter system crossing from  $S_1$  to  $T_1$   $k_{isc}$  and from  $T_1$  to  $S_0$   $k_{T1}$ . Image modified from [57].

Figure 2.1 shows that in fluorescence, a fluorophore absorbs the energy of a photon with rate  $k_{ex}$ , which brings it into the excited  $S_1$  state. A fluorescence photon is generated when the fluorophore spontaneously falls back with rate  $k_{S1}$  into its ground state  $S_0$ . Usually the energy of the fluorescence photon is less than the energy of the absorbed photon, manifesting itself in longer emission wavelengths. This phenomenon is known as Stokes shift [53, 73].

In STED microscopy, there is an additional process competing with the spontaneous

decay  $k_{S1}$ : the stimulated emission  $k_{STED}$ . It brings the fluorophore back into a vibrationally excited ground state  $S_0^*$  from which it radiationless relaxes into the ground state  $S_0$  with rate  $k_{vib}$ . During stimulated emission a second photon of the same wavelength as the one used for stimulation is emitted [57].

To benefit from the stimulated emission in terms of resolution, the STED beam must have a special shape featuring a minimum, at best a zero, in its PSF. Typically, this is accomplished with a doughnut shape (see fig. 2.2).



**Figure 2.2:** Typical beam configurations in STED microscopy. A Gaussian excitation beam (left) is superimposed with a doughnut shaped STED beam (middle) resulting in a no longer diffraction limited focal spot from which fluorescence is emitted (right).

Figure 2.2 shows the overlay of a Gaussian excitation beam with a doughnut shaped STED beam. This configuration keeps all excited fluorophores in the periphery of the Gaussian excitation in a dark state ( $S_0$ ) due to stimulated emission. Fluorescence photons are only emitted from the focal spot in the centre of the STED beam. Further descriptions can be found in [40, 41, 42, 46].

The size of the focal spot is now controlled by the intensity of the STED beam and no longer subjected to Abbe's diffraction limit. The resolution which in conventional light microscopy is diffraction limited and given by equation (2.2), now needs to be modified to include the STED intensity and the fluorophore specific saturation intensity in the formula.

$$d = \frac{\lambda}{2 \cdot NA \sqrt{1 + \frac{P_{STED}}{P_{sat}}}} \quad (2.3)$$

where  $\lambda$  is the excitation wavelength, NA the numerical aperture,  $P_{STED}$  the intensity of the STED beam and  $P_{sat}$  the saturation intensity. The latter depends on the lifetime of the  $S_1$  state, the STED wavelength and is dye specific.

Equation (2.3) gives the achievable resolution that is now primarily subjected to the ratio of the STED intensity  $P_{STED}$  and the saturation intensity  $P_{sat}$ . Theoretically, this means unlimited resolution. Further details and derivations of equation (2.3) are given in [21, 37, 57].

### 2.3 Acousto-optical tunable filters

An acousto-optical tunable filter (AOTF) is a device that exploits the acousto-optic diffraction in an anisotropic medium (i.e. a birefringent uniaxial crystal) [16, 17]. By means of an applied radio frequency (RF) the index of refraction is periodically modulated, which diffracts those portions of the incident light satisfying the phase matching condition

$$\vec{k}_i = \vec{k}_d \pm \vec{k}_a, \quad (2.4)$$

where  $\vec{k}_i$ ,  $\vec{k}_d$  and  $\vec{k}_a$  are the wave vectors of the incident, diffracted and acoustic waves respectively [17].

In the case of a non-collinear AOTF in an anisotropic medium the phase matching condition (eq. 2.4) can be maintained for a range of incident angles by coupling the incident polarized light into the orthogonal polarization via the acoustic wave (see fig. 2.3). This is achieved by choosing the acoustic wave vector such that the tangents of the incident and diffracted light are parallel (see fig. 2.3). In an isotropic medium the phase matching condition (eq. 2.4) is extremely sensitive to the angle of incidence [17].

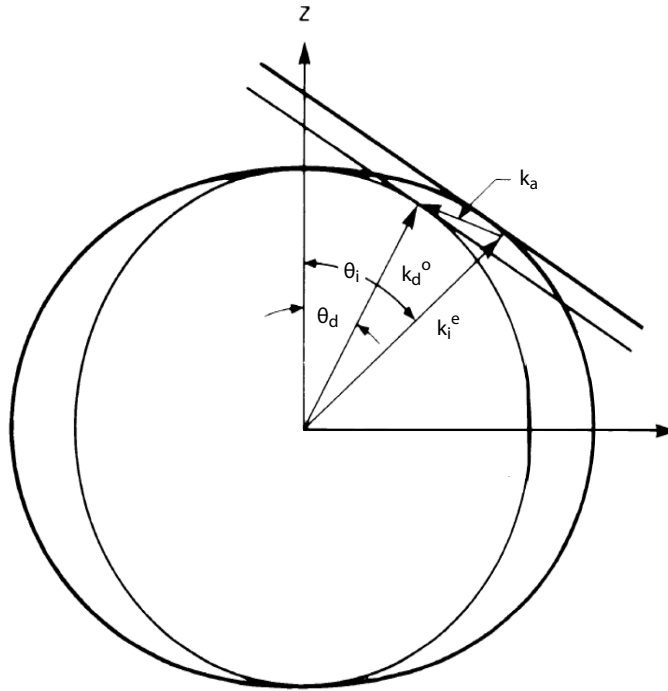


**Figure 2.3:** Wave vector diagram of a non-collinear AOTF;  $\theta_i$ : angle of incidence,  $\theta_d$ : angle of diffraction,  $k_i^o$ ,  $k_i^e$ : wave vectors of the ordinary and extraordinary incident waves,  $k_d^o$ ,  $k_d^e$ : wave vectors of the ordinary and extraordinary diffracted waves,  $k_a$ : wave vector of the acoustic wave. Image taken from [16].

Figure 2.3 shows the interplay of the different wave vectors in a non-collinear AOTF. The subscripts  $i$ ,  $d$  and  $a$  stand for the incident, diffracted and acoustic waves whereas the superscripts  $o$  and  $e$  refer to the ordinary and extraordinary beams, respectively.

An outline of the beam paths of a commercial AOTF is depicted in figure 2.4.

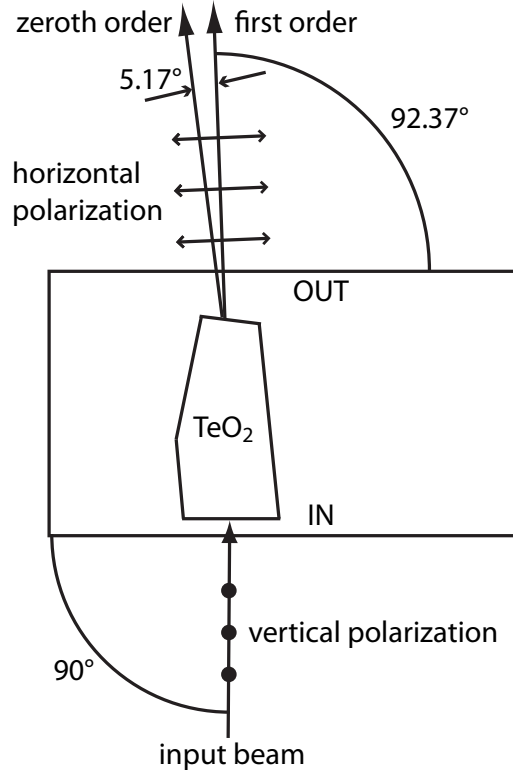


**Figure 2.4:** Outline of the beam paths and polarizations of an AOTF from Crystal Technology, now Gooch & Housego, Ilminster, GB.

Figure 2.4 shows the beam paths and polarizations of an AOTF from Crystal Technology, now Gooch & Housego, Ilminster, GB. The input polarization is vertical and the output polarization horizontal, hence it is a non-collinear AOTF where the phase condition in equation (2.4) is met for a range of incident angles. If the acoustic wave is chosen appropriately, the diffracted light emerges with a 5.17° difference in the first order with respect to the zeroth order.

The intensity of the light diffracted into the first order ( $I_d$ ) is proportional to

$$I_d \propto \sin^2 \left( \frac{\pi^2}{2} \frac{M_2}{\lambda_0^2} P_d L^2 \right)^{\frac{1}{2}}, \quad (2.5)$$

where  $P_d$  is the acoustic power density,  $M_2$  the acousto-optic figure of merit,  $L$  the

interaction length and  $\lambda_0$  the optical wavelength in vacuum. The ratio of the first sidelobe to the main peak is  $\sim -13\text{dB}$  [16, 17].

The full width at half maximum (FWHM) of the spectral passband is

$$\Delta\lambda = \frac{1.8\pi\lambda_0}{bL \sin^2 \theta_i}, \quad (2.6)$$

where  $b$  is a dispersive constant and  $\theta_i$  the angle of incidence [16, 17].

## 2.4 Data analysis algorithms

Hyperspectral data require some post-processing. The highly overlapping emission spectra of the various dyes generate a large crosstalk in the different detection channels. In order to correctly extract the distribution of the individual dyes per pixel from the measured counts, one needs to perform spectral unmixing. Here, three methods were investigated: linear unmixing (see section 2.4.1), non-negative matrix factorization (see section 2.4.2) and PoissonNMF which is a plugin for ImageJ (see section 2.4.3). Further, an alternative approach was taken to obtain the entries of the transfer matrix  $\mathbf{A}$  (see section 2.4.4). The mathematical models will be explained and later, in chapter 4, their results will be discussed.

### 2.4.1 Linear unmixing

The method of linear unmixing (LinUnmix) is based on minimizing the sum of the squared errors for every pixel. The underlying model states that each pixel consists of a linear combination of the true spectra of the different markers present in the sample [96].

$$\mathbf{Y} = \mathbf{A} \cdot \mathbf{X} \quad \text{or} \quad y_{ij} = \sum_k a_{ik} x_{kj}, \quad (2.7)$$

where  $i$ ,  $j$  and  $k$  are the indices for the detection channel, pixel and dye respectively.  $N_i$ ,  $N_j$  and  $N_k$  are the number of channels, pixels and dyes respectively.  $\mathbf{Y}$  is the measured data and has dimensions  $N_i \times N_j$ .  $\mathbf{A}$  is the transfer matrix and contains the distribution of the dyes in the different channels. Note that the sum over all channels for one dye is equal to one. Therefore, its dimensions are  $N_i \times N_k$ . The matrix  $\mathbf{X}$  represents the true dye distribution per pixel and is the wanted quantity. Its dimensions are  $N_k \times N_j$ .

If  $\mathbf{A}$  is known and  $\mathbf{Y}$  is measured,  $\mathbf{X}$  is obtained by minimizing the cost function  $C_j$  for each pixel  $j$  which is the sum of squared errors. This is equivalent to a least square fit.

$$C_j = \sum_i \left( y_{ij} - \sum_k a_{ik} x_{kj} \right)^2 \quad (2.8)$$

$$\frac{\partial C_j}{\partial x_{rj}} = 0, \quad x_{rj} \geq 0 \quad (2.9)$$

The least square fit of equation (2.9) is done pixelwise under the condition that the solution for  $\mathbf{X}$  only contains positive values. This is appropriate since  $\mathbf{X}$  represents dye concentrations and any value below zero would not be physically reasonable [96].

If multiple excitation wavelengths or lifetime windows should be included in the analysis of linear unmixing, it could be done by creating a combined transfer matrix  $\mathbf{A}$  where the index  $i$  for the channel is replaced by a combined index  $il$  for the channel and excitation wavelengths or lifetime windows. In this approach it is no longer possible to explicitly track the contributions from the individual parameters.

The exact code for the LinUnmix algorithm as used within this thesis can be found in appendix C.

## 2.4.2 Non-negative matrix factorization

Non-negative matrix factorization (NNMF) [68, 70] is a generalization of Linear Unmixing explained in section 2.4.1. Like the latter, NNMF is based on the assumption that the signal in each pixel is a linear combination of all the dyes present in the sample at this pixel. Additionally, it takes explicitly into account that the various dyes are excited at different strength at different wavelengths. This is done by adding the matrix  $\mathbf{Q}$  to the model of equation (2.7).

$$y_{ijl} = \sum_k a_{ik} x_{kj} q_{kl}, \quad (2.10)$$

where  $i, j, l$  and  $k$  are the indices for the channel, pixel, excitation and dye respectively.  $N_i, N_j, N_l$  and  $N_k$  are the number of channels, pixels, dyes and excitations respectively.  $\mathbf{Y}$  is the measured data having dimensions  $N_i \times N_j \times N_l$ .  $\mathbf{A}$  is the transfer matrix displaying the dye distributions across the detection channels. Note that the sum over all channels for one dye is equal to one. Its dimensions are  $N_i \times N_k$ .  $\mathbf{X}$  is the representation of the true dye concentrations in every pixel. Its dimensions are  $N_k \times N_j$ . The matrix  $\mathbf{Q}$  with elements  $q_{kl}$  consists of entries between zero and one stating how well a dye is excited by a specific wavelength. Therefore, its dimensions are  $N_k \times N_l$ .

The cost function  $C$  that is optimized is the sum over all channels, pixels and excitations and is the negative log-likelihood function of a Poissonian noise distribution,

where the mean is replaced by the model in equation (2.10) [55].

$$C = \sum_{ijl} \left( \sum_k a_{ik} x_{kj} q_{kl} - y_{ijl} \cdot \ln \left( \sum_k a_{ik} x_{kj} q_{kl} \right) \right) \quad (2.11)$$

In order to guarantee only positive entries in the matrices  $\mathbf{A}$ ,  $\mathbf{X}$  and  $\mathbf{Q}$  multiplicative update rules are used. This is done by choosing the parameters  $\eta_{rs}^{a,x,q}$  such that multiplicative update rules are obtained [70].

$$a_{rs} \Rightarrow a_{rs} - \eta_{rs}^a \cdot \frac{\partial C}{\partial a_{rs}} = \frac{a_{rs}}{\sum_{jl} x_{sj} q_{sl}} \sum_{jl} \frac{y_{rjl} x_{sj} q_{sl}}{\sum_k a_{rk} x_{kj} q_{kl}} \quad (2.12)$$

$$x_{rs} \Rightarrow x_{rs} - \eta_{rs}^x \cdot \frac{\partial C}{\partial x_{rs}} = \frac{x_{rs}}{\sum_{il} a_{ir} q_{rl}} \sum_{il} \frac{y_{isl} a_{ir} q_{rl}}{\sum_k a_{ik} x_{ks} q_{kl}} \quad (2.13)$$

$$q_{rs} \Rightarrow q_{rs} - \eta_{rs}^q \cdot \frac{\partial C}{\partial q_{rs}} = \frac{q_{rs}}{\sum_{ij} a_{ir} x_{rj}} \sum_{ij} \frac{y_{ijs} a_{ir} x_{rj}}{\sum_k a_{ik} x_{kj} q_{ks}} \quad (2.14)$$

The purpose of the multiple excitations described by the matrix  $\mathbf{Q}$  is to eliminate ambiguities that can arise from the estimation of the matrices  $\mathbf{A}$  and  $\mathbf{X}$  simultaneously [70]. With this approach it might not only be possible to estimate the true dye distribution per pixel  $\mathbf{X}$  but also the transfer matrix  $\mathbf{A}$ . Furthermore, using multiple excitation wavelengths in the experiments is intrinsically included in the analysis. For further details see [68, 70].

Within this thesis, a NNMF algorithm was programmed based on the cost function in equation (2.11) and the resulting update rules of equations (2.12), (2.13) and (2.14). A more detailed description and the code can be found in appendix C.

Moreover, the NNMF algorithm can include the lifetime information. In the case where instead of different excitation wavelengths, distinct time windows are used to record the fluorescence, one can simply use the matrix  $\mathbf{Q}$  in equation (2.10) with lifetime windows instead of excitation wavelengths.

In the case of multiple excitation wavelengths as well as several time windows the model, cost function and update rules are as follows, where  $i$  is the index for the channels,  $j$  for the pixels,  $l$  for the excitation wavelengths,  $m$  for the time windows and  $k$  for the dyes.

$$y_{ijlm} = \sum_k a_{ik} x_{kj} q_{kl} t_{km}, \quad (2.15)$$

$$C = \sum_{ijlm} \left( \sum_k a_{ik} x_{kj} q_{kl} t_{km} - y_{ijlm} \cdot \ln \left( \sum_k a_{ik} x_{kj} q_{kl} t_{km} \right) \right) \quad (2.16)$$

$$a_{rs} \Rightarrow a_{rs} - \eta_{rs}^a \cdot \frac{\partial C}{\partial a_{rs}} = \frac{a_{rs}}{\sum_{jlm} x_{sj} q_{sl} t_{sm}} \sum_{jlm} \frac{y_{rjlm} x_{sj} q_{sl} t_{sm}}{\sum_k a_{rk} x_{kj} q_{kl} t_{km}} \quad (2.17)$$

$$x_{rs} \Rightarrow x_{rs} - \eta_{rs}^x \cdot \frac{\partial C}{\partial x_{rs}} = \frac{x_{rs}}{\sum_{ilm} a_{ir} q_{rl} t_{rm}} \sum_{ilm} \frac{y_{islm} a_{ir} q_{rl} t_{rm}}{\sum_k a_{ik} x_{ks} q_{kl} t_{km}} \quad (2.18)$$

$$q_{rs} \Rightarrow q_{rs} - \eta_{rs}^q \cdot \frac{\partial C}{\partial q_{rs}} = \frac{q_{rs}}{\sum_{ijm} a_{ir} x_{rj} t_{rm}} \sum_{ijm} \frac{y_{ijsm} a_{ir} x_{rj} t_{rm}}{\sum_k a_{ik} x_{kj} q_{ks} t_{km}} \quad (2.19)$$

$$t_{rs} \Rightarrow t_{rs} - \eta_{rs}^t \cdot \frac{\partial C}{\partial t_{rs}} = \frac{t_{rs}}{\sum_{ijl} a_{ir} x_{rj} q_{rl}} \sum_{ijl} \frac{y_{ijls} a_{ir} x_{rj} q_{rl}}{\sum_k a_{ik} x_{kj} q_{kl} t_{ks}} \quad (2.20)$$

### 2.4.3 PoissonNMF plugin for ImageJ

The PoissonNMF plugin for ImageJ (ImageJ) [69] is based, like NMF (see section 2.4.2), on the algorithm of non-negative matrix factorization published in [70]. The difference is that ImageJ, like linear unmixing (see section 2.4.1) does not have and explicit matrix  $\mathbf{Q}$ . Instead it introduces a so called segregation bias term in the cost function to eliminate ambiguities in the estimation of  $\mathbf{A}$  and  $\mathbf{X}$ . This term pushes the NMF algorithm to maximally overlapping spectra [70]. The additional term reads

$$E = -\kappa \cdot \sum_j \frac{\sum_k |x_{kj}|}{\sqrt{\sum_k x_{kj}^2}}, \quad (2.21)$$

where  $j$  and  $k$  are the indices for the number of pixels and dyes respectively.  $\kappa$  is the weight of the term and is in the order of one [69].

The segregation bias term in equation (2.21) effects only the update rule for the true dye concentration matrix  $\mathbf{X}$  (see section 2.4.2) and changes it to

$$x_{rs} = \frac{x_{rs}}{\sum_i a_{ir}} \left[ \sum_i \frac{y_{is} a_{ir}}{\sum_k a_{ik} x_{ks}} - \kappa \left( \frac{1}{(\sum_k x_{ks}^2)^{0.5}} - \frac{x_{rs} \sum_k x_{ks}}{(\sum_k x_{ks}^2)^{1.5}} \right) \right]. \quad (2.22)$$

In the input parameter dialog, there are several options and input parameters to be specified (see [69] for further details). The values of the specific parameters can be found in appendix C.

### 2.4.4 Estimating $\mathbf{A}$ with a probability approach

As will be shown in chapter 4 the estimate of  $\mathbf{A}$  in equation (2.12) does not always yield reasonable results. Hence, a different approach was used to estimate the entries of  $\mathbf{A}$ . It was a probability approach that led to a new transfer matrix  $\mathbf{A}_{\text{mac}}$  and is described in more detail in [63].

The algorithm for  $\mathbf{A}_{\text{mac}}$  is based on the assumption that each pixel contains exactly

one colour. Thus, it is a pixel based algorithm. In a first step, it calculates the probability that a certain pixel  $j$  contains a specific colour  $k$  given a measured transfer matrix  $A_k^i$  as a reference multiplied by a brightness value  $b$ .

$$(y_i = b \cdot A_k^i)_j, \quad (2.23)$$

where  $i, j$  are the indices for the different channels or pixels,  $y_i$  is the data in channel  $i$ ,  $A_k^i$  are the ratios of dye  $k$  in channel  $i$  and  $b$  is the brightness.

The wanted quantity is the probability  $P(y_i|A_k^i)$  which gives the probability that  $y_i$  is produced by  $A_k^i$ . It is obtained by using Bayes' theorem [11, 14]

$$P(b|y_i, A_k^i) = \frac{P(y_i|b, A_k^i) \cdot P(b)}{P(y_i|A_k^i)} \quad (2.24)$$

and the fact that every  $b$  has the same probability, meaning that  $P(b) = 1$ . Integrating equation 2.24 over  $b$ , one obtains

$$P(y_i|A_k^i) = \int P(y_i|b, A_k^i) db. \quad (2.25)$$

The probability  $P(y_i|b, A_k^i)$  is calculated by assuming a Poissonian noise distribution [14] as a model

$$P(d|\mu) = \frac{\mu^d}{d!} \cdot e^{-\mu}, \quad (2.26)$$

where  $d$  is the data and  $\mu$  the mean of the distribution.

Substituting  $d$  with  $y_i$  and  $\mu$  with  $b \cdot A_k^i$  in equation (2.26), the integral over  $b$  in equation (2.25) becomes analytically solvable, leading to

$$P(y_i|A_k^i) = \left( \sum_i y_i \right)! \cdot \prod_i \frac{(A_k^i)^{y_i}}{y_i!}, \quad (2.27)$$

where  $i$  is the index for the different channels,  $y_i$  is the data in channel  $i$  and  $A_k^i$  are the ratios of dye  $k$  in channel  $i$ .

Note that equation (2.27) is independent of channel  $i$ . For every pixel and each dye, the probability  $P(y_i|A_k^i)$  is calculated that this dye is present in this specific pixel. Afterwards, the probability in equation (2.27) is weighted by the sum of all probabilities for all dyes, giving a weighted probability  $P_w^k$ .

$$P_w^k = \frac{P(y_i|A_k^i)}{\sum_k P(y_i|A_k^i)}, \quad (2.28)$$

where the nomenclature is identical to equation (2.27) with the addition of  $k$  being the index for the number of dyes.

Now, the new transfer matrix  $\mathbf{A}_{\text{mac}}$  is obtained by weighting the data  $y_i$  with  $P_w^k$  and calculating the new ratios for the sum of all pixels.

$$\mathbf{A}_{\text{mac}}^{in} = \frac{\sum_j P_w^k(j) \cdot y_i(j)}{\sum_{ij} P_w^k(j) \cdot y_i(j)}, \quad (2.29)$$

where  $i, j, k$  are the indices for the different channels, pixels and dyes respectively.  $N_i$  and  $N_k$  are the number of channels and dyes respectively.  $\mathbf{A}_{\text{mac}}$  has dimensions  $N_i \times N_k$  (see [63] for further details).

The algorithm may be run for several iterations. But changes became very quickly non-noticeable. Usually three iterations were performed.



# Chapter 3

## Experimental set-up

Within the scope of this thesis a versatile and simple multicolour STED set-up was designed and built (see section 3.1). It allowed the selection of 8 different excitation wavelengths via the combination of a supercontinuum source with an acousto-optical beam splitter (see section 3.2). The choice of the wavelengths was arbitrary as long as they were within the spectral range of the supercontinuum source. Additionally, they could be used simultaneously or sequentially. Furthermore, the set-up provided a single STED beam at 775 nm. Both lasers, the supercontinuum source and the STED laser, were synchronized and operated at a repetition rate of 38.956 MHz. The set-up allowed a hyperspectral detection of four channels that spanned a total range of 150 nm for the 775 nm STED beam. Their number could be increased to 8 when a second, bluer STED wavelength would be needed (see section 3.4). Scanning was achieved with the quadscanner which was a beam scanning device that combined easy alignment with reasonable scanning speed (see section 3.3). The central control component of the set-up was a field-programmable gate array. It was responsible for data acquisition and laser control as well as the setting of the scan area and the time gates (see section 3.5). The characteristic properties of the here presented set-up will be described in section 3.6.

### 3.1 Overview and beam paths

A general overview of the experimental set-up is depicted in figure 3.1.

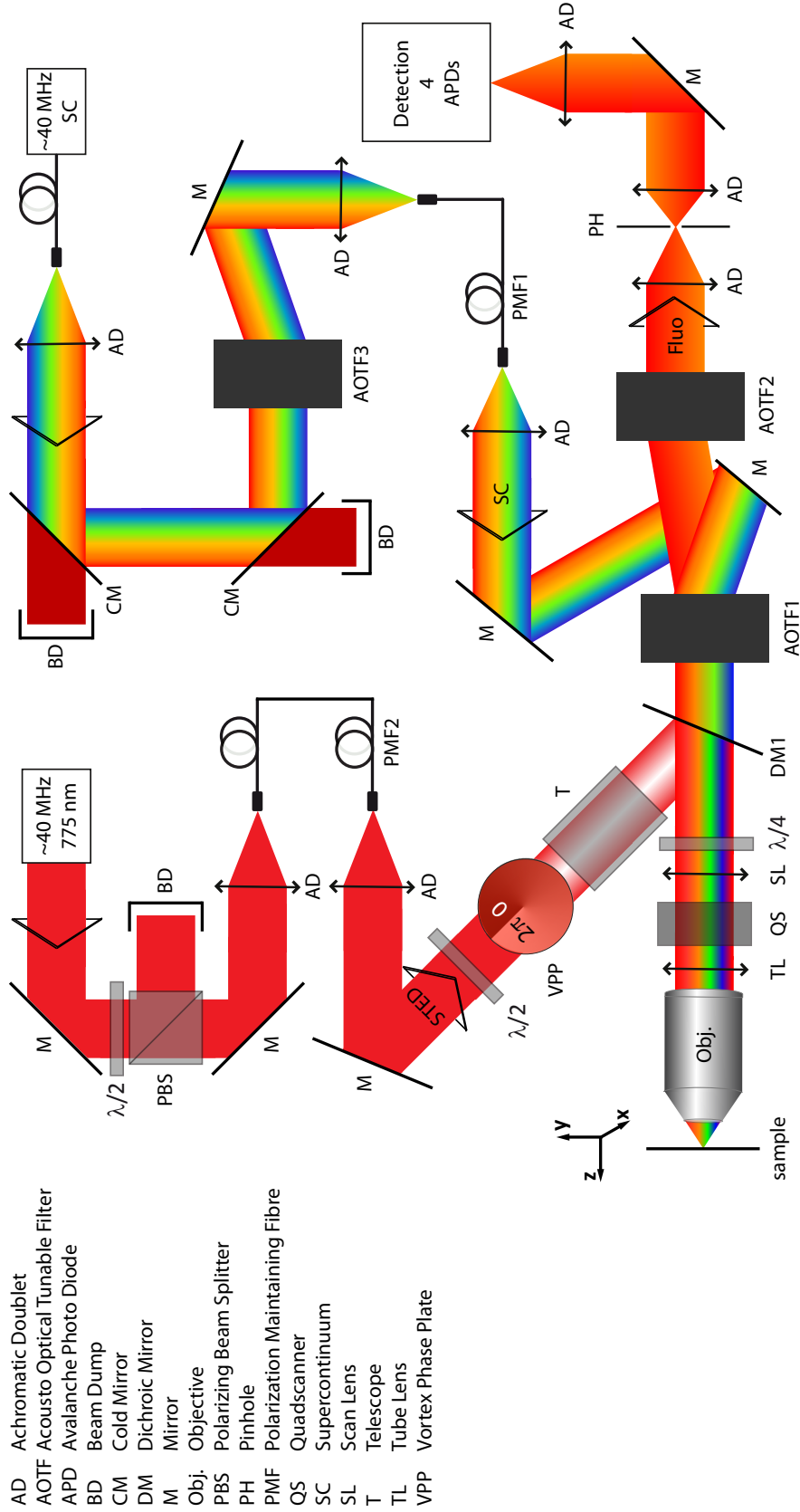


**Figure 3.1:** Overview of the experimental set-up. The excitation light was provided by a supercontinuum source and the STED wavelength was 775 nm. Both were operated at a repetition rate of 38.956 MHz. Selection of the excitation wavelength was done by AOTF1 and AOTF3. Beam scanning was achieved by the quadscanner (QS). The fluorescence light was collected by four APDs after passing through a 100  $\mu\text{m}$  pinhole (PH).

The excitation wavelengths were provided by a supercontinuum source (model EXWB-6, NKT Photonics, Birkerød, DK). It generated coherent light ranging from 450–1500 nm and ran at a repetition rate of 38.956 MHz. The infrared part of the spectrum was removed by two cold mirrors (CM) (M254C45, Thorlabs, Newton, US). After that the beam went through AOTF3 (PCAOM 97-02838-01, Crystal Technology, now Gooch & Housego, Ilminster, GB) which preselected the desired excitation wavelength. The beam was then coupled into a 2 m long polarization maintaining single mode fibre (PMF1) (PM488, Thorlabs, Newton, US) which acted as a spatial filter. This was necessary to remove unwanted wavelengths that emerged from the AOTF under different angles. The light coming out at the exit end of the fibre then passed through AOTF1 in backwards direction where the final excitation wavelength was determined. Note that similar radio frequencies (RF) had to be applied to both, AOTF1 and AOTF3, otherwise no excitation light would reach the objective. The selected excitation wavelength left AOTF1 in first order direction, was reflected by several dielectric mirrors before it was combined with the STED beam at the dichroic mirror DM1 (KP750, MSO Jena now Optics Balzers, Balzers, LI).

The STED beam was provided by a fibre laser (model Katana08-HP, Onewave, Zürich, CH) that was externally triggered by pulses from the supercontinuum source. The light traveled through a combination of a halfwave plate and a polarizing beam splitter (PBS) (B. Halle Nachfl. GmbH, Berlin, DE), both optimized for 600–900 nm to enable arbitrary tuning of the STED power. After that the linearly polarized light was coupled into a 5 m polarization maintaining single mode fibre (PMF2) (780PM, Thorlabs, Newton, US). The light coming out of the fibre passed through another halfwave plate optimized for 600–900 nm (B. Halle Nachfl. GmbH, Berlin, DE) before it reached the vortex phase plate (VPP) (RPC Photonics, Rochester, US). The latter imprinted a continuous circular phase change in space ranging from 0 to  $2\pi$  radians on the beam. This phase and the circular polarization of the beam led to a doughnut shaped PSF in the focus. After the VPP the beam traveled through a telescope (T) with a magnification of 0.75 which enabled the overlay of the excitation and STED beams along the optical axis. The beam was then reflected by the dichroic mirror (DM1) (KP750, MSO Jena now Optics Balzers, Balzers, LI) which was optimized for an angle of incidence (AOI) of  $22.5^\circ$  and which combined the excitation and the STED beams. Both beams then traveled through a quarter wave plate optimized for 600–900 nm (B. Halle Nachfl. GmbH, Berlin, DE), the achromatic scan lens (SL) ( $f=50$  mm, ARB2 coating, Qioptiq, Göttingen, DE), the quadscanner (QS) (see section 3.3) and were finally injected into the microscope stand (model DMI6000CS, Leica Microsystems, Wetzlar, DE). The latter housed the tube lens (TL) of focal length  $f=200$  mm. After having traveled through the tube lens, both beams were being focused by a 100x oil objective (Obj.) with a NA of 1.4–0.7 (model HCX APO CL 100x, Leica Microsystems, Wetzlar, DE).

The fluorescence light from the sample traveled backwards through the objective

(Obj.), the tube lens (TL), the quadscanner (QS), the scan lens (SL), the dichroic mirror (DM1) and the acousto-optical beam splitter comprising AOTF1 and AOTF2 (see section 3.2). The fluorescent light was then focused by an achromatic lens of 140 mm focal length (ARB2 coating from Qioptiq, Göttingen, DE) onto a 100  $\mu\text{m}$  pinhole (PH) before it was distributed into four detection channels. Each channel had an avalanche photo diode (APD) (model SPCM-ARQH-13, Excelitas Technologies Corp., Waltham, US) as detector (see section 3.4).

Scanning of the sample was done by the quadscanner (QS). This was a beam scanning device where two galvanometer driven silver coated mirrors (model 6215HSB, Cambridge Technology, Bedford, US) were responsible for scanning one direction, meaning that for x and y directions a total number of four mirrors was needed (see section 3.3).

Fine tuning of the z position was achieved with a one axis piezo stage with a travel range of 200  $\mu\text{m}$  in closed feedback loop control (Mipos250 CAP, Piezosystem Jena, Jena, DE). The latter ensured good z stability during an xy-scan.

## 3.2 Acousto-optical beam splitter

An acousto-optical beam splitter (AOBS) consists of two acousto-optical tunable filters (AOTF) (see fig. 3.2). All AOTFs used in this set-up were from Crystal Technology, now Gooch & Housego, Ilminster, GB, model 97-02838-01. They selected a very narrow band of about 2 nm bandwidth from the input beam by means of the applied radio frequency (RF). Further they allowed tuning of the power of the chosen wavelength by varying the amplitude of the acousto-optic wave. The shape of the  $\text{TeO}_2$  crystal was such that all selected wavelengths emerged from the AOTF at the same angle (see section 2.3).

As can be seen from figure 3.2 AOTF1 was operated in the backwards direction, meaning that the excitation light was coupled in by a D-shaped mirror to the output aperture under the angle of the first order diffraction. This resulted in a beam emerging from the input aperture perpendicular to the housing of the AOTF when the applied RF was chosen appropriately for the desired wavelength.

The fluorescence light passed AOTF1 in the forward direction, where the portion of the fluorescence corresponding to the excitation wavelength was deflected in the first order. All other wavelengths traveled through AOTF1 in the 0<sup>th</sup> order beam acquiring some dispersion due to the crystal itself. Therefore the fluorescence needed to pass through AOTF2 in backwards direction. This enabled compensation of the dispersion resulting in a parallel yet slightly bigger beam after AOTF2. Furthermore, the RF applied to AOTF2 increased the suppression of the excitation wavelength in the detection channels (see fig. 3.3).

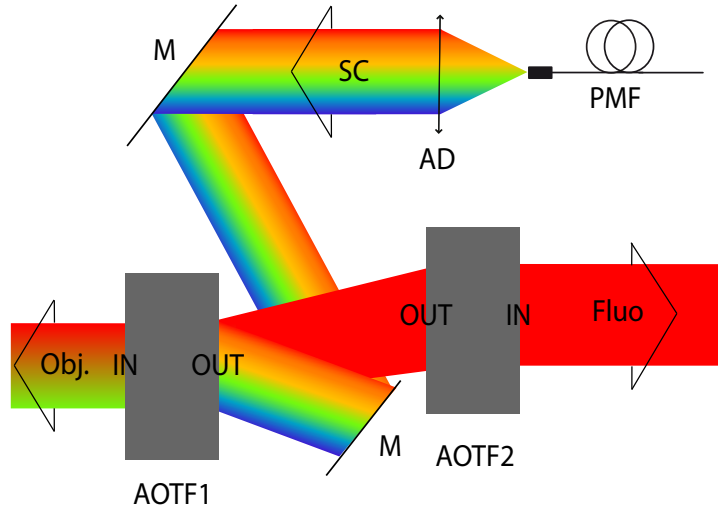


**Figure 3.2:** Beam paths of the acousto-optical beam splitter (AOBS). Light was coupled into the output aperture of AOTF1 under the angle of the first order beam. AOTF1 selected the excitation wavelength which traveled to the objective. Fluorescence from the sample passed AOTF1 in the zeroth order beam thereby acquiring a slight dispersion from the crystal. AOTF2 corrected for this dispersion resulting in a parallel beam leaving AOTF2. To do so the output apertures of AOTF1 and AOTF2 had to face each other. M: mirror, AD: achromatic doublet, SC: supercontinuum.

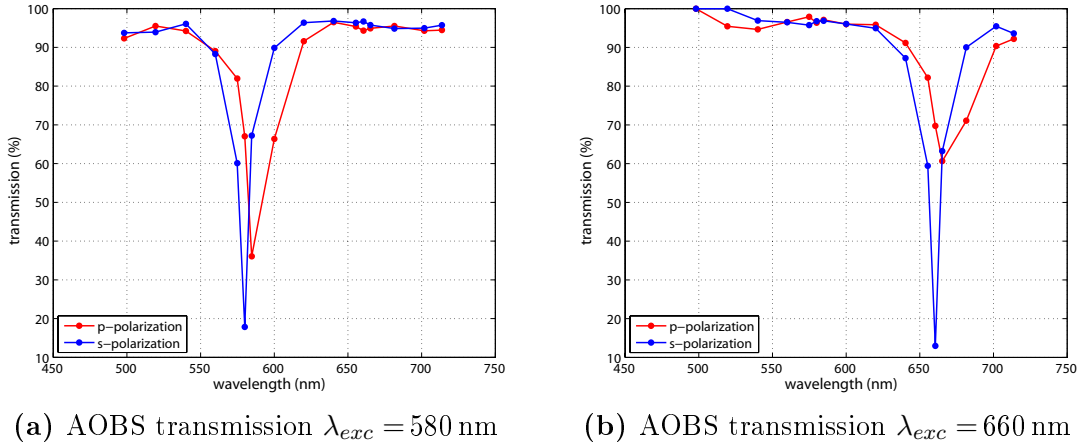


**Figure 3.3:** Transmission efficiency of the AOBS for 580 nm (left) and 660 nm (right) when the same radio frequency was applied to AOTF1 and AOTF2. blue: s-polarized light, red: p-polarized light.

Figure 3.3 shows the transmission efficiency of the AOBS when either 102.9 MHz = 580 nm (see fig. 3.3a) or 87.6 MHz = 660 nm (see fig. 3.3b) were applied to AOTF1 and AOTF2. One can clearly see that the transmission of the AOBS was well above 90% and only dropped at the wavelength corresponding to the applied RF. However, the residual transmission at the wavelength of the applied RF was still in the

range of 10 %. This was insufficient for a fluorescence microscopy STED set-up and implied the requirement of an additional filter in the detection path.

Further, figure 3.3 shows a difference for the s- and p-polarized components. For the p-polarized light the point of maximum suppression was shifted to the red compared to the s-polarized light. Moreover, it seemed that for the p-polarized component the suppression was not as efficient as for s-polarized component. But this conclusion could not be drawn from figure 3.3 because the sample rate of ca. 20 nm was too coarse to detect a shift of  $\approx 5$  nm as it appeared to be the case. Measurements were not taken with a finer sampling rate because the transmission efficiency for the not chosen wavelengths was more important. This information can be extracted from figure 3.3.

### 3.3 Beam scanning with the quadscanner

The quadscanner (QS) was a device that enabled scanning of the beam across the sample [23]. It consisted of four galvanometer driven silver coated mirrors (model 6215HSB, Cambridge Technology, Bedford, US). Thereby always two opposite mirrors were responsible for the beam deflection in one direction (see fig. 3.4 and [29] for further details).

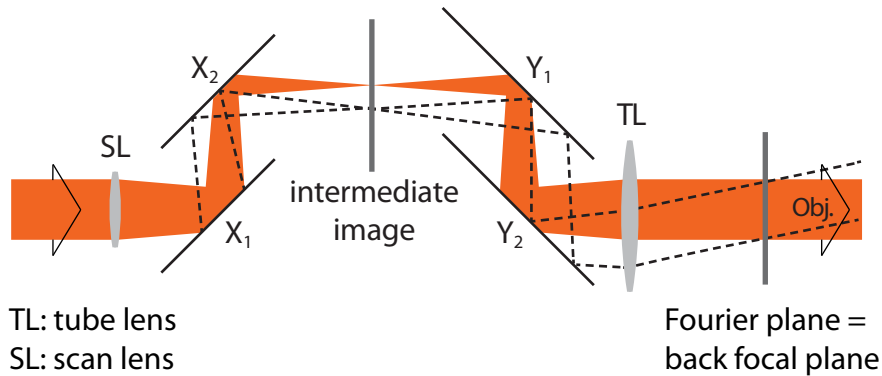


**Figure 3.4:** Beam path of the quadscanner. Galvanometer driven mirrors that altered x and y positions are denoted X<sub>1</sub>, X<sub>2</sub> and Y<sub>1</sub>, Y<sub>2</sub> respectively. This configuration ensured a stable beam position in the Fourier plane. Only the angle varied. Image modified from [31].

From figure 3.4 it can be seen that the QS was situated between two lenses; the tube lens (TL) which was inside the microscope stand and the scan lens (SL) which was a conventional achromatic doublet of focal length  $f = 50$  mm (model G052012000, Qioptiq, Göttingen, DE). The position of the QS was adjusted in such a way that the focus of either of these lenses lay between mirrors X<sub>2</sub> and Y<sub>1</sub> of the configuration. This ensured the best scanning conditions [9, 10, 29, 31]. Further, figure 3.4 shows that while scanning, the position of the beam in the Fourier plane, which

corresponded to the back focal plane of the objective, did not change. Only the angle varied which then transformed into a change in the focus position after the objective.

The galvanometer controllers needed a DC voltage of  $\pm 18\text{--}24\text{ V}$  which was provided by a dual power supply (model 3032B, Protek, Malé, MDV).

The field of view ranged from several hundred nanometers up to  $65\ \mu\text{m}$ . The minimal dwell time per pixel was  $5\ \mu\text{s}$ . This enabled a scanning speed of 1 frame every 53 s at full range with a pixel size of 20 nm. If one limited the field of view to  $10\ \mu\text{m} \times 10\ \mu\text{m}$  with  $5\ \mu\text{s}$  dwell time and a pixel size of 20 nm, one could scan 1 frame in 1.25 s.

### 3.4 Detection unit

The set-up was designed to accommodate 8 detection channels covering a range from 480–750 nm (see fig. 3.5). However, in this thesis, solely APDs 3 through 8 were mounted and only four of them could be used simultaneously for measurements.

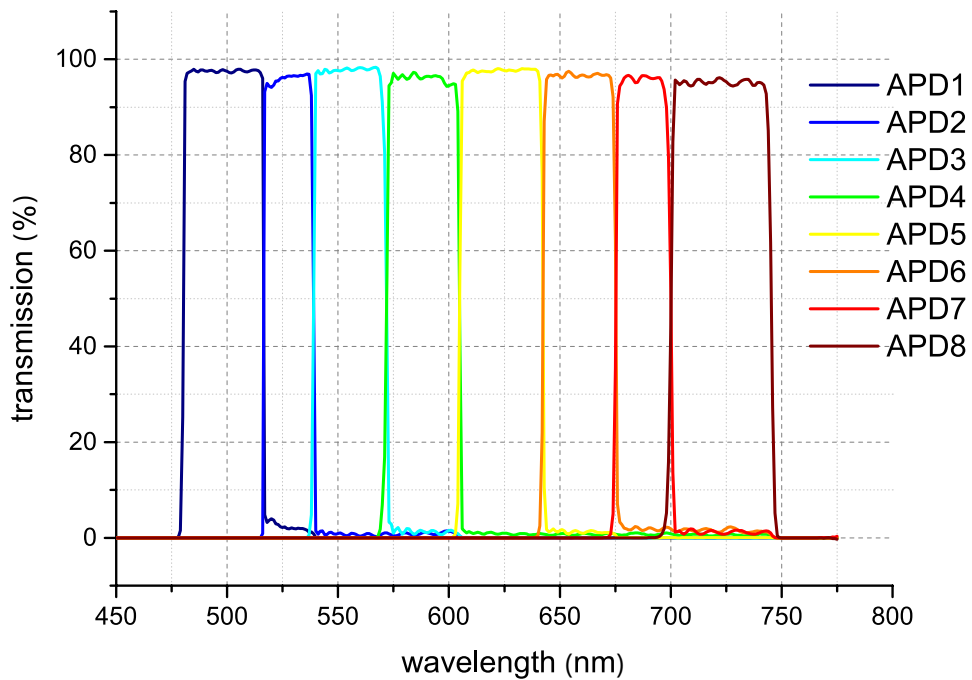


**Figure 3.5:** Spectral ranges of the 8 detection channels. From these 8 channels only APDs 3–8 were mounted.

Spectral separation of the fluorescence light was achieved by using longpass filters (LP) as beam splitters and collecting the transmitted as well as the reflected light. To do so the filters were mounted at an angle of  $10^\circ$  from the normal (see fig.

3.6). This ensured minimal separation of the s- and p-polarized components along with a negligible shift of the edge of the filter and a minimal drop in the transmission efficiency [82]. Note that depending on the exact excitation wavelength, an additional filter might need to be put into the beam path to suppress the excitation wavelength properly.

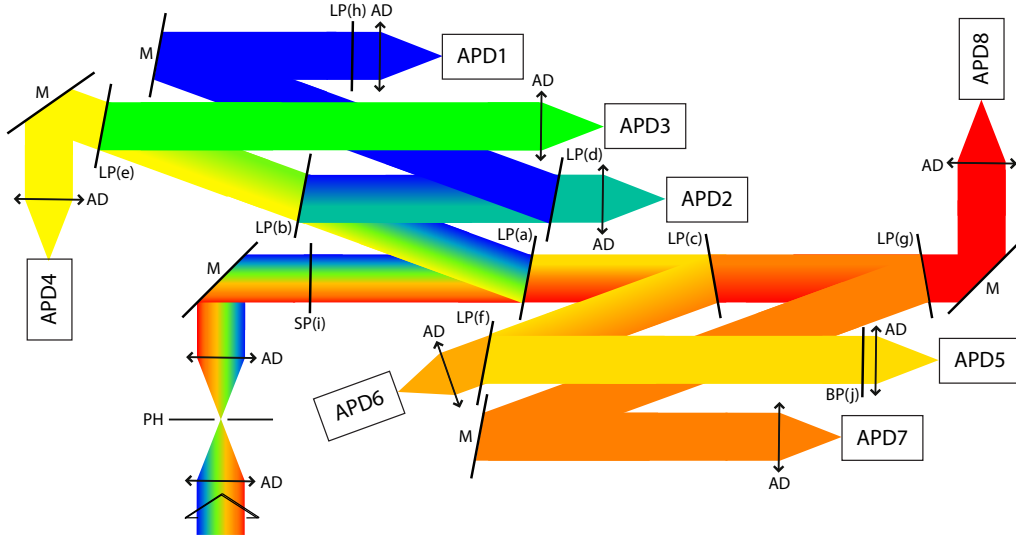


**Figure 3.6:** Beam paths in the detection unit. Separation of fluorescence in the different spectral channels was done by longpass filters (LP) at an angle of incidence of  $10^\circ$ . A bandpass (BP) was needed to suppress the excitation wavelength and a shortpass (SP) for the STED beam. The filter positions are denoted with small letter (a-j). A detailed list can be found in table 3.1. PH: pinhole, AD: achromatic doublet, APD: avalanche photo diode.

In figure 3.6 the positions of the individual filters are marked by small letters (a-j). A detailed list of the used filters and their corresponding position can be found in table 3.1. Furthermore figure 3.6 shows the use of a confocal pinhole (PH) of  $100\ \mu\text{m}$  diameter. This corresponded to 0.6 airy discs of fluorescence light with a wavelength of  $650\ \text{nm}$ .

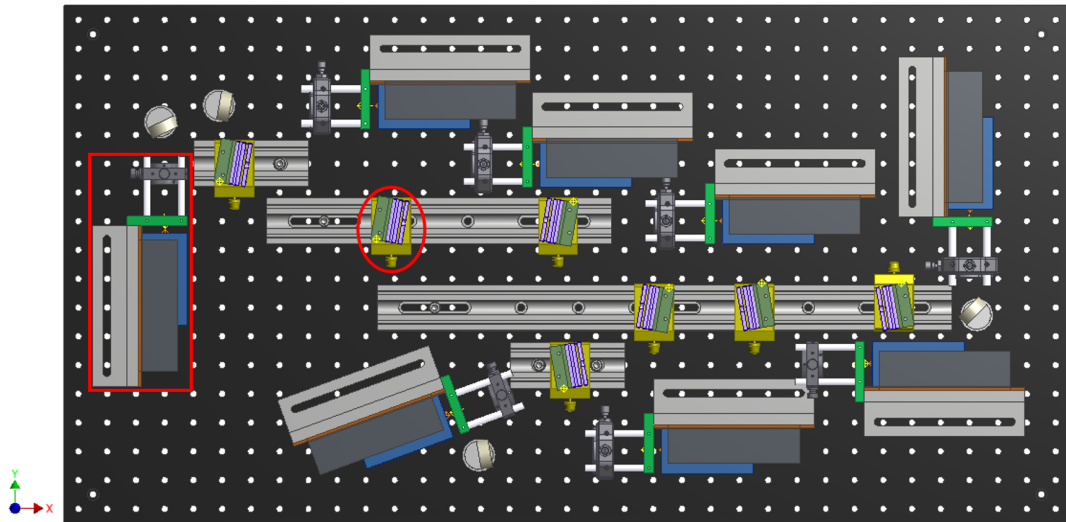
Since stability was one of the main goals, several mechanical components were custom made. A top view of the assembly is depicted in AutoCAD in figure 3.7.

The detection unit shown in figure 3.7 was made up of two main subunits. One was the detector assembly and the other one the filter mounting assembly. Both are shown in figure 3.9 and 3.8 respectively. All components were mounted on a custom made breadboard of dimension  $900 \times 450 \times 10\ \text{mm}$ .

In figure 3.8 the LP filters were all placed in flexure mounts (model MFM-100,

**Table 3.1:** Correspondence of position in the set-up to the used filter

position	company	filter
a	Semrock	BLP01-594R-25
b	Semrock	BLP01-532R-25
c	Semrock	BLP01-664R-25
d	Semrock	LP02-514RU-25
e	Semrock	BLP01-561R-25
f	Semrock	BLP01-633R-25
g	Semrock	FF01-692/LP-25
h	Semrock	BLP01-473R-25
i	Thorlabs	SP750
j	Semrock	FF01-650/60-25

**Figure 3.7:** Top view of the components of the detection unit. It was mounted on a  $900 \times 450 \times 10$  mm breadboard and consisted of two main subunits: detector assemblies (red square), total of 8 and filter mounting assemblies (red oval), total of 7.

Newport, Irvine, US) (purple) which were screwed to a custom made holder (green) giving them the desired inclination of  $10^\circ$ . These holders were then fixed to sliders (model FLR 40-34, Qioptiq, Göttingen, DE) (yellow) that were placed on rails FLS 40 (Qioptiq, Göttingen, DE). The two designs in figure 3.8 differed only by the orientation of the threaded holes in the custom made holder (green). The desired deflection of  $20^\circ$  to the left or right of the optical axis was achieved by the appropriate distances of the threaded holes to the centre axis.

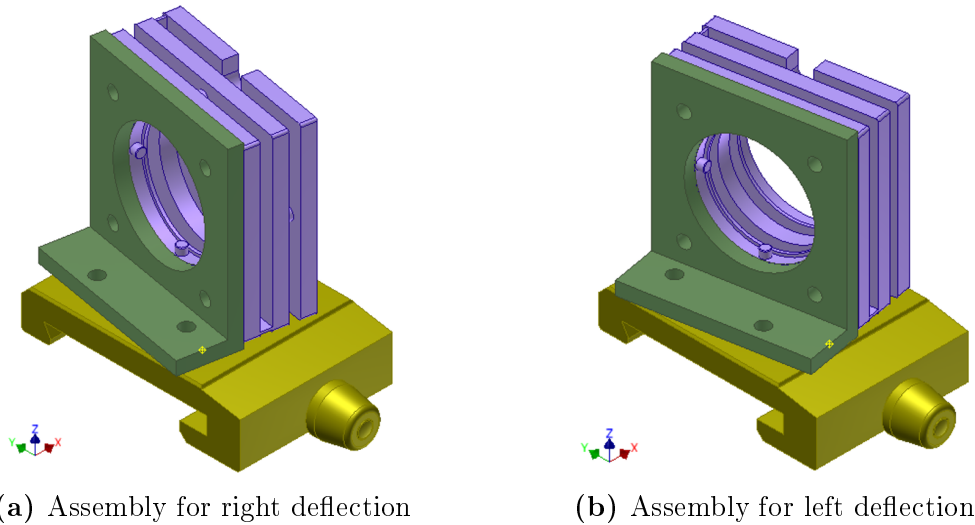


**Figure 3.8:** AutoCAD isometric view of the filter mounting assembly, each housing one filter. Two separate designs existed, one for deflection to the right (3.8a) and one to the left (3.8b) of the optical axis. The two assemblies differed by the orientation of the threaded holes in the green part. green: custom made holder, purple: Newport flexure mount, yellow: Qioptiq slider.

Figure 3.9 shows the individual components of the detector assembly. The detectors were either single photon counting modules (model SPCM-ARQH-13, Excelitas Technologies Corp., Waltham, US) (black) or single photon avalanche diodes (model PDM-R-100-C0B, Micro Photon Devices (MPD), Bolzani, IT) (blue). In the case of the MPD detector an additional adapter was needed to ensure the same position of the active area. The single photon counting modules from Excelitas had an active area of  $180\ \mu\text{m}$  and a quantum detection efficiency of 65% at 700 nm. The detectors were mounted vertically on custom made holders (light grey) to occupy less space. These holders enabled compatibility to the common 30 mm cage system from Thorlabs which was necessary to mount the lenses in front of all the detectors. The achromatic doublets had a focal length  $f = 40\ \text{mm}$  (model G063127000, Qioptiq, Göttingen) and were mounted in XY translation mounts (grey) (model CXY1, Thorlabs, Newton, US). This permitted individual fine alignment of the detectors. The expected focal spot size of this configuration was  $40\ \mu\text{m}$  which allowed for some drift on the  $180\ \mu\text{m}$  detection area once the detectors had been properly aligned. Furthermore, the lenses focusing and parallelizing the beam before and after the pinhole had a focal length  $f = 140\ \text{mm}$  and  $f = 200\ \text{mm}$  respectively (model G063146000 and model G063148000, Qioptiq, Göttingen, DE).

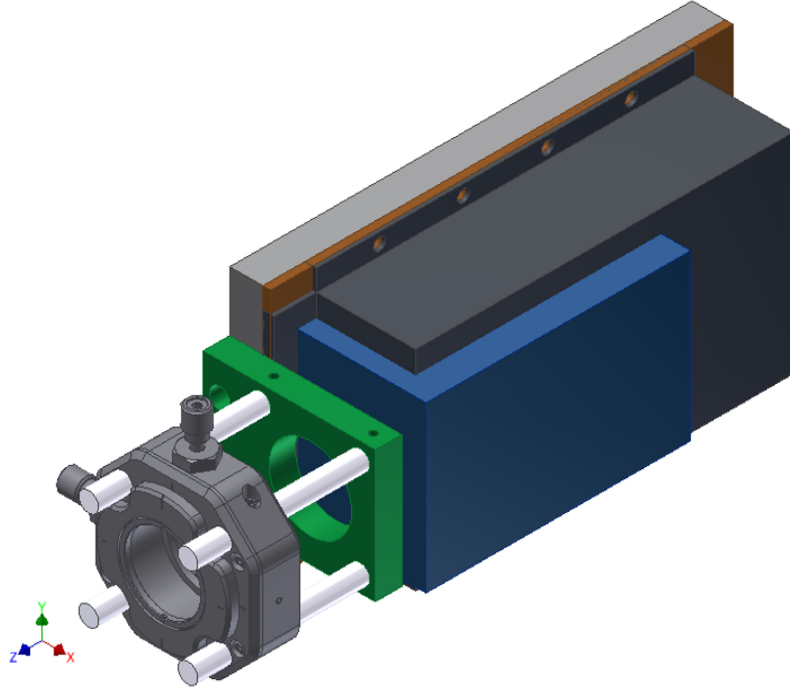


**Figure 3.9:** AutoCAD isometric view of the detector assembly. It could accommodate either of two different detectors while keeping their active areas at the same position. light grey: custom made holder, black: Excelitas detector, blue: Micro Photon Devices (MPD) detector, brown: adapter for MPD detector, green: custom made connector to 30 mm cage rod system, white: cage rods, grey: xy Thorlabs translation mount.

### 3.5 Experimental control and electronic pathways

A general flow chart of the electronic pathways is depicted in figure 3.10.

Most of the hardware control was done by an FPGA (field programmable gate array) (model PCIe-7852R, National Instruments, Austin, US). The voltages applied to the galvanometer driven mirrors X1, X2, Y1 and Y2 of the QS were set by the FPGA. The applied voltages defined the scan area. Moreover, the FPGA was responsible for the detector read out. Each detector had its own input channel and could internally be time gated to eliminate the early fluorescence [93]. In order to do so accurately, the FPGA needed to be provided with an external trigger. The latter came from the supercontinuum source which was also synchronized with the STED laser via an external delay. The FPGA also controlled the z piezo and provided the trigger signals to the breakout boxes of AOTF1 and AOTF3 which enabled fast switching via frequency shift keying (FSK) between preset wavelengths. These wavelengths were set by a custom made program via a USB interface [59].

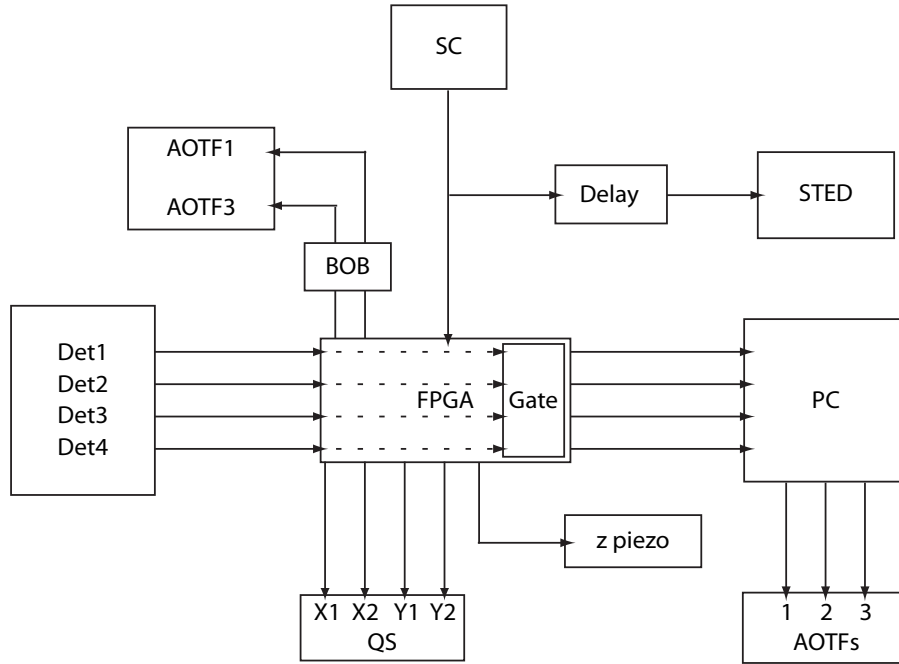


**Figure 3.10:** Flow chart of the electronic pathways. BOB: breakout box, Det: detector, FPGA: field-programmable gate array, QS: quadscanner, SC: supercontinuum, AOTF: acousto-optical tunable filter

## 3.6 Set-up characterization

In order to determine the capabilities of the set-up, several measures were investigated and optimized. In a first step the choice of the excitation wavelength was examined and calibrated (see section 3.6.1). Then the shapes of the PSFs of the excitation and STED beams were optimized and overlapped in  $xy$ ,  $xz$  and  $yz$  directions. Additionally it was investigated whether switching the excitation wavelength led to a change of position (see section 3.6.2). Further, the timing between the excitation and the STED beams was optimized (see section 3.6.3). In a final step, the settings for the time gates were determined (see section 3.6.4) and the maximum available STED power measured (see section 3.6.5).

### 3.6.1 Choosing the excitation wavelength

The final excitation wavelength was selected by AOTF1 and AOTF3 (see fig. 3.1). For any excitation light to reach the sample, the same RFs had to be applied to both AOTFs.

Figure 3.11 shows the relationship between the applied RF to AOTF1 and the resulting selected wavelength. To the data points a 3<sup>rd</sup> order polynomial was fit via a Levenberg-Marquardt method [66] for interpolation purposes. All wavelengths were

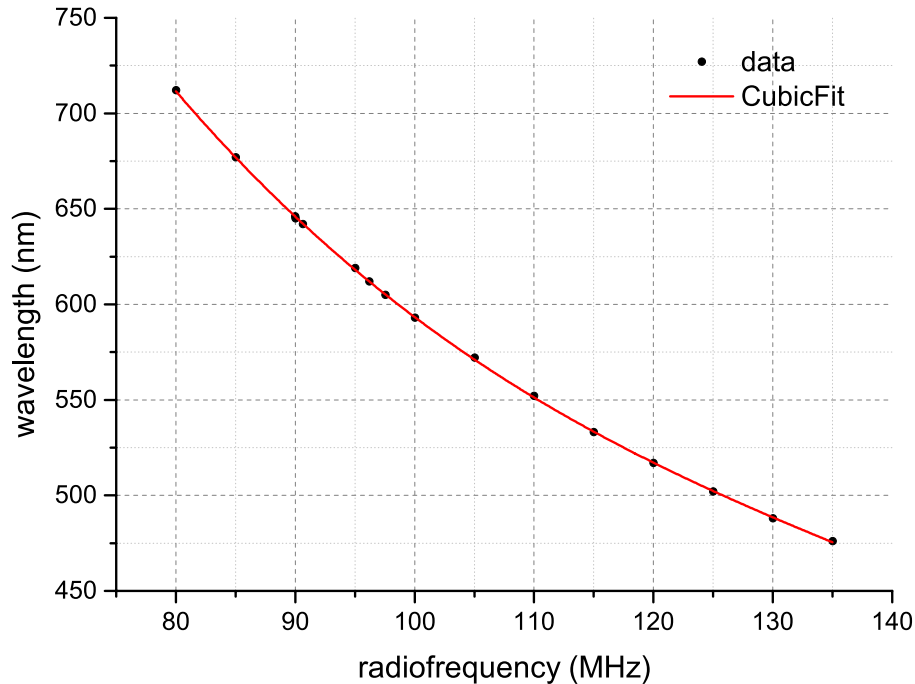


**Figure 3.11:** Relationship between applied radio frequency and wavelength for AOTF1. Black circles represent data points whereas the red solid line corresponds to a cubic polynomial fit.

chosen according to figure 3.11 and the corresponding RFs were applied to AOTF1 and AOTF3.

Since linewise switching between the chosen wavelengths was desired, both AOTFs were equipped with a fast switching mechanism; the frequency shift keying (FSK). This is a method where one had to predefine the wavelengths and the wanted power via a USB interface. Thereby each selected wavelength had its individual off wavelength to ensure a good switching contrast. This implied that great care had to be taken not to use the same off wavelength twice. Once set, one could switch between these preset wavelengths in the range of microseconds.

Switching between the wavelengths was done by applying an appropriate combination of TTL signals to the different pins of the individual breakout boxes of AOTF1 and AOTF3. For example, a single breakout box consisted of 8 FSK pins, 8 modulation pins, one of each for every channel, and one blanking pin. Additionally each of the 8 channels of the AOTF has four profiles. Now, to specifically select a certain profile, one had to take the combination of TTL signals on the FSK and blanking pin. Table 3.2 states the profile selection in FSK mode for one channel. 1 corresponds to a TTL high and 0 to a TTL low signal (see [59] for details). The modulation pin was an analog input which could further tune the power of the selected wavelength. Voltages between 0–5 V were applied to all modulation pins.

**Table 3.2:** Profile selection on one channel of one AOTF in FSK mode via combination of TTL signals on the FSK and blanking pins. 0 corresponds to a TTL low and 1 to a TTL high signal.

FSK	blanking	profile
1	1	3
0	1	2
1	0	1
0	0	0

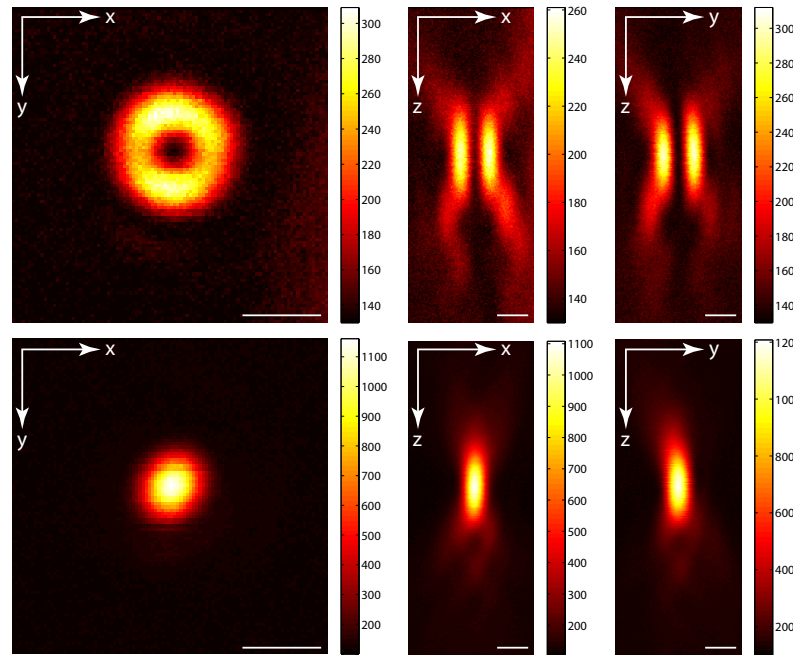
If the power of each chosen wavelength needed to be independently adjustable, the selected wavelengths had to correspond to different FSK pins. This limited the maximum number of selectable wavelengths to 8 since the breakout boxes were equipped with 8 modulation pins. If more than 8 excitation wavelengths were required, one single FSK pin could be used for two excitation wavelengths. However, in this case, their power would be coupled and finding good imaging parameters would be tedious.

### 3.6.2 PSF measurements and beam alignment

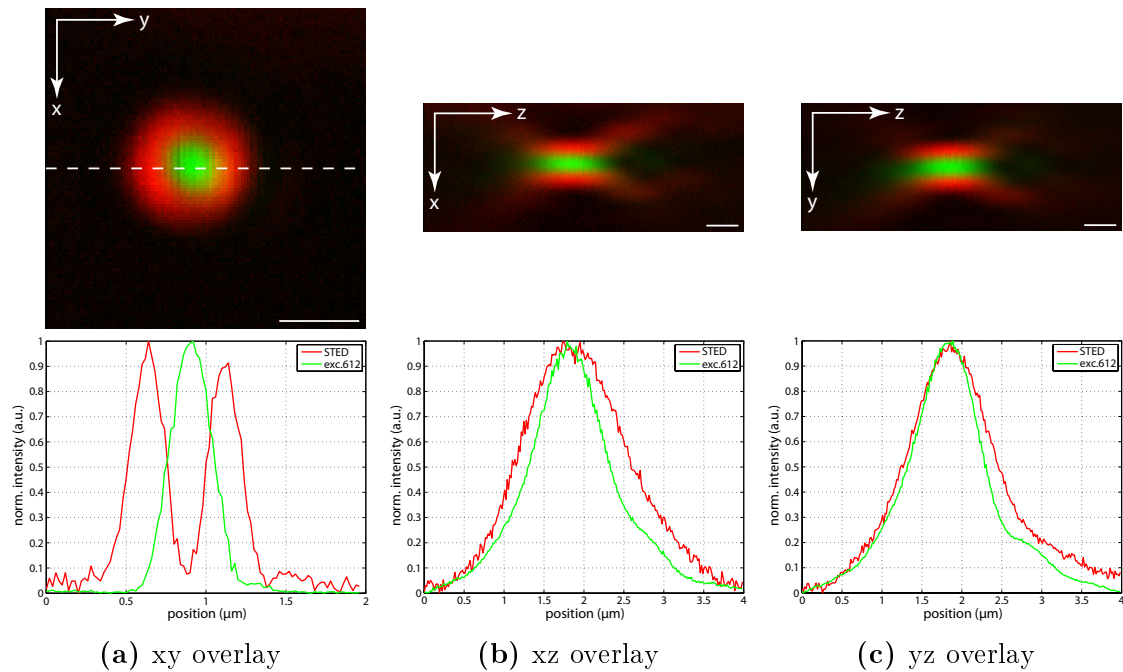
To ensure good image quality, not only the overlap of the excitation and STED beams was crucial but also their respective shapes in xy, xz and yz directions. Shape optimization was done by observing the reflected light from 150 nm gold beads on a photo multiplier tube (PMT). Figure 3.12 displays the PSFs for STED (top row) and excitation (bottom row). The columns show the respective PSFs in xy (left), xz (middle) and yz (right) views.

Figure 3.12 shows that the intensity distribution for the STED beam was good but not entirely homogeneous. Further the PSFs in z-direction were upright and the maxima of the intensity distribution were in the same position although not fully symmetric. The same holds for the PSFs of the excitation beam of 612 nm. Figure 3.12 confirms that the PSFs of the excitation and STED beams were good and could be used for STED imaging. Scanned areas were  $2\mu\text{m}\times 2\mu\text{m}$  for the xy-scan and  $2\mu\text{m}\times 4\mu\text{m}$  for xz- and yz-scans.

Figure 3.13 shows an excellent alignment. Not only did the STED doughnut exhibit a very good zero but also the centre z positions of the excitation and STED beams demonstrated an almost perfect overlap. Note that before any measurement was taken, the xy overlap was optimized whereas the z overlap did not require further optimization once it had been properly aligned.

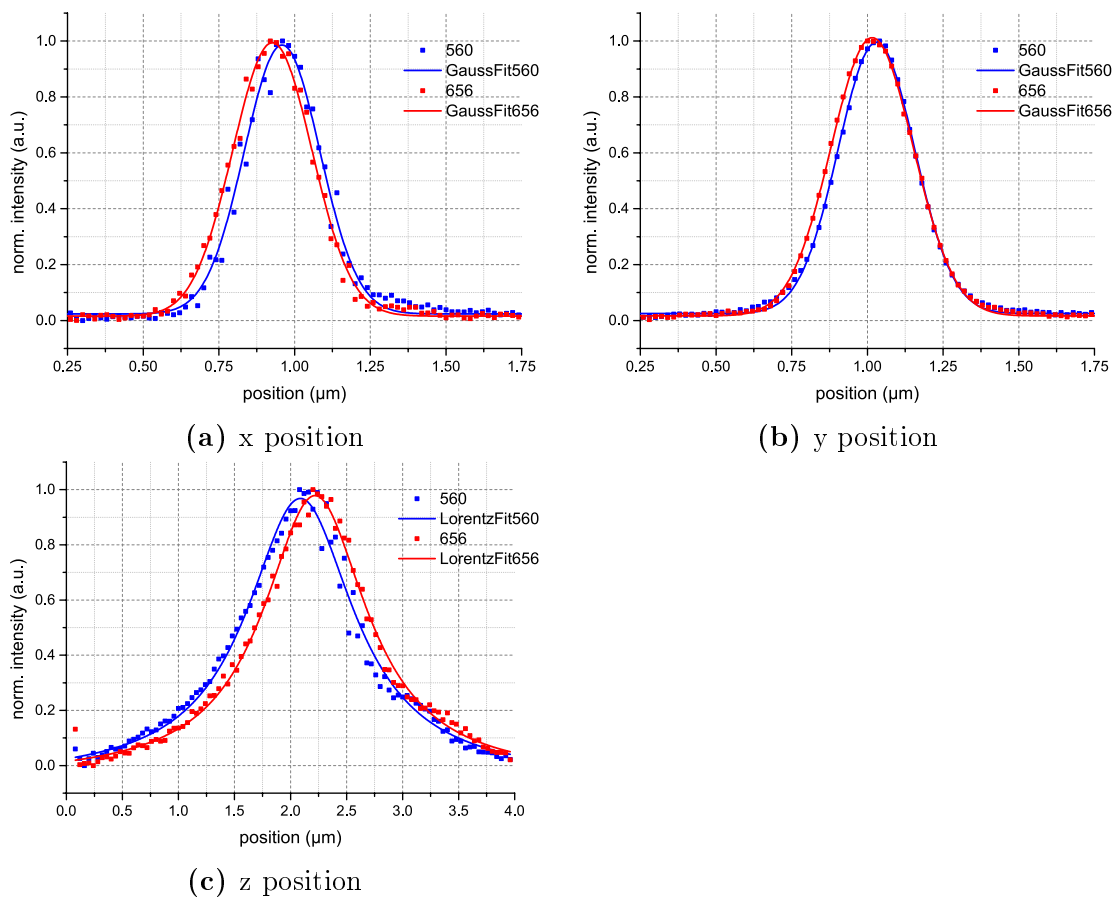


**Figure 3.12:** PSF measurements on 150 nm gold beads of the STED beam (top row) and the excitation beam of 612 nm (bottom row). Columns represent the xy (left), xz (middle) and yz (right) views. Scale bars are 500 nm.



**Figure 3.13:** Overlay of the PSF measurements for the STED (red) and the excitation beam (green) from fig. 3.12. Below each overlay the normalized sum along x or y direction is shown for the xz and yz measurements. For the xy measurement the green and red traces represent the normalized intensity profile along the white dashed line. Scale bars are 500 nm.

Since the here presented set-up allowed an arbitrary choice of up to 8 different excitation wavelengths between 480 and 690 nm, it was briefly studied how the alignment properties behaved when the excitation wavelength was changed. Therefore wavelengths of 560 nm and 656 nm were chosen and the PSFs were measured in two line steps. The first one corresponded to 656 nm and the second to 560 nm. This was done for xy and xz directions. Afterwards, for the xy measurement, the sum over x and y was calculated and a Gaussian intensity distribution was fit to the data points. Consequently, for the xz measurement, the sum over x was calculated and a Lorentzian intensity distribution was fit to the data points. Fitting was achieved via a Levenberg-Marquardt method [66]. The results are depicted in figure 3.14.



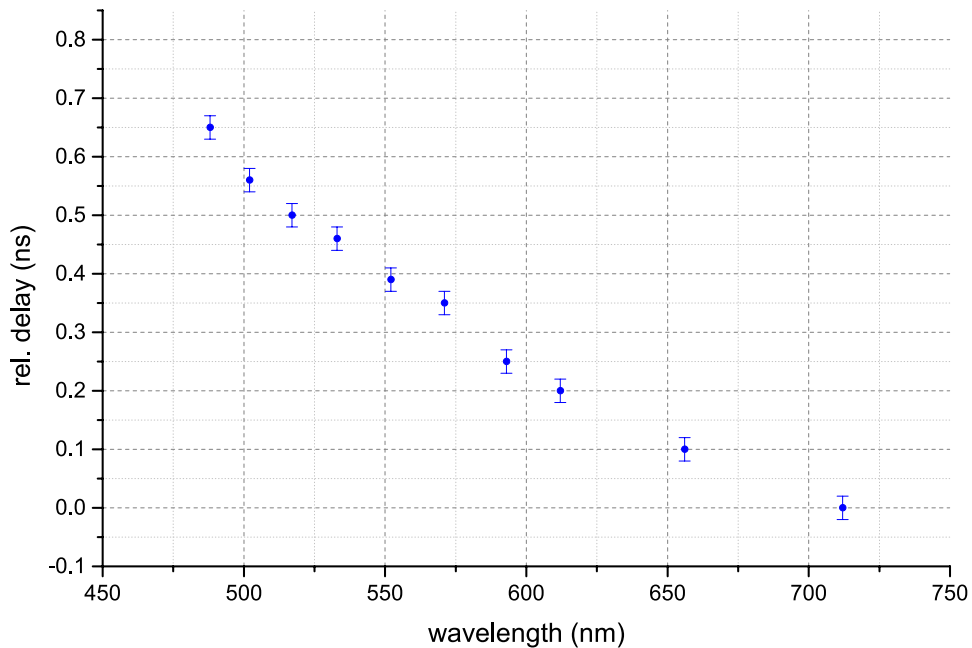
**Figure 3.14:** Position mismatch for 560 nm (blue) and 656 nm (red) excitation wavelength in x (top left), y (top right) and z directions (bottom left). Shapes represent the data points and the solid lines a Gaussian or Lorentzian fit.

Figure 3.14 clearly shows a small mismatch between 560 nm and 656 nm excitation wavelength in all three dimensions. Comparing the centre positions from the fits to each other, a mismatch in x of 30 nm, in y of 10 nm and in z of 130 nm was

obtained. These position differences were negligible because the diffraction unlimited spot was defined by the STED beam. And as long as a decent fluorescence signal was generated a small deviation from the perfect overlap neither jeopardized the STED efficiency nor the image quality.

### 3.6.3 Run time and timing issues of excitation and STED

The set-up built in this thesis operated at a repetition rate of 38.956 MHz. This required an optimization of the timing between the excitation and the STED beams. To obtain the best STED efficiency it was found that the STED beam should arrive ca. 880 ps after the excitation beam. Since the light generated by the supercontinuum source was fibre coupled, this led to a delay between the different wavelengths due to dispersion. The precise delay values can be extracted from figure 3.15. Run time differences were measured relative to a trigger signal. The obtained difference for the reddest wavelength was set to zero. All other run time differences were then shifted accordingly.



**Figure 3.15:** Relative run time differences between different excitation wavelengths coming from the supercontinuum source. The reddest wavelength was defined to have zero delay. All other delays were relative to that.

Figure 3.15 shows a significant difference of run times for different wavelengths. The redder the wavelength, the shorter its run time. For example, the difference between 517 nm and 656 nm was as large as 400 ps. This entailed that for each excitation wavelength the timing had to be individually optimized. This also posed

some limitations when two wavelengths should be used in a multiplexing measurement. For most wavelength pairs a single delay value could be found that resulted in a reasonable SNR and good resolution. Nevertheless, this was not ideal. Therefore a new electronic card was designed which will enable linewise switching between predefined delay values. This will be implemented soon in the set-up.

### 3.6.4 Setting the time gating parameters

The settings of the time gates consisted of two parameters: the gate delay and the gate width. The first one determined the starting point of the fluorescence recording with respect to an external trigger (here the supercontinuum source) and the second marked the temporal width in which the data was acquired. Usually the gate delay discards roughly the first nanosecond of the fluorescence decay in time gating measurements [93].

For each of the four detection channels the gate delay had to be calibrated independently in order to take signal run time variations due to optical path lengths or cable lengths differences into account. Here, no run time differences were found for APD5, 6 and 8. The signal of APD7 arrived ca. 600 ps later, meaning that to the gate delay of APD7, 0.6 ns were added in comparison to APD5, 6 and 8.

### 3.6.5 Available STED power and resolution

The maximum STED power available in the back aperture of the objective was around 400 mW. This power was controlled via a half wave plate and a polarizing beam splitter before the fibre coupling (see fig. 3.1).

A STED power of ca. 400 mW was equivalent to a pulse energy of approximately 10 nJ per pulse at 38.956 MHz or a peak intensity of roughly 112 MW/cm<sup>2</sup> which should be large enough to achieve resolutions below 35 nm. Note that the resolution strongly depended of the employed dye and the STED power. A detailed study of the resolution dependence on the dye will be conducted in section 5.2.

# Chapter 4

## Simulations

In this chapter the performances of three unmixing methods for hyperspectral images are examined and compared: linear unmixing (LinUnmix) [96], non-negative matrix factorization (NNMF) with a fixed or a simultaneously optimized transfer matrix [70] and the PoissonNMF plugin for ImageJ (ImageJ) [69]. Each method allowed several parameters to be chosen and kept constant or adapted during the analysis. The simulated objects were non-overlapping bead distributions (see section 4.1). The performance of the methods was evaluated by calculating the residual crosstalk after unmixing. Therefore a new measure was introduced (see section 4.2). In the case of NNMF, the optimum number of iteration was determined (see section 4.3). The effects of changes in the signal-to-noise ratio on the respective method were studied. This was done for two, three and four different dyes with one excitation wavelength (see section 4.4). The impact of adding a second excitation wavelength or lifetime as another means of discrimination was also simulated (see sections 4.5, 4.6). A short conclusion will be given in section 4.7.

### 4.1 Input parameters

An artificial data set was created as per equation (2.10) for the APDs 5–8 with an experimentally measured transfer matrix on single stained samples ( $\mathbf{A}_{\text{exp}}$ ). The exact values of  $\mathbf{A}_{\text{exp}}$  will be given in the section together with the dyes used. Noise was added according to a Poissonian noise distribution. As artificial data, four bead distributions were chosen, each of which consisted of a total number of 25 beads and always five beads exhibited the same brightness. The brightness levels were chosen to have 100, 200, 300, 400 and 500 counts (see fig. 4.1). Additionally, the distributions in figure 4.1 were also divided by a factor of 10 to simulate the low light regime. Analysis of this data was performed analogously to the data with brighter structures.

Figure 4.1 shows the chosen dye distributions without noise and PSF consideration. As can be seen, the structures were non-overlapping and each bead was

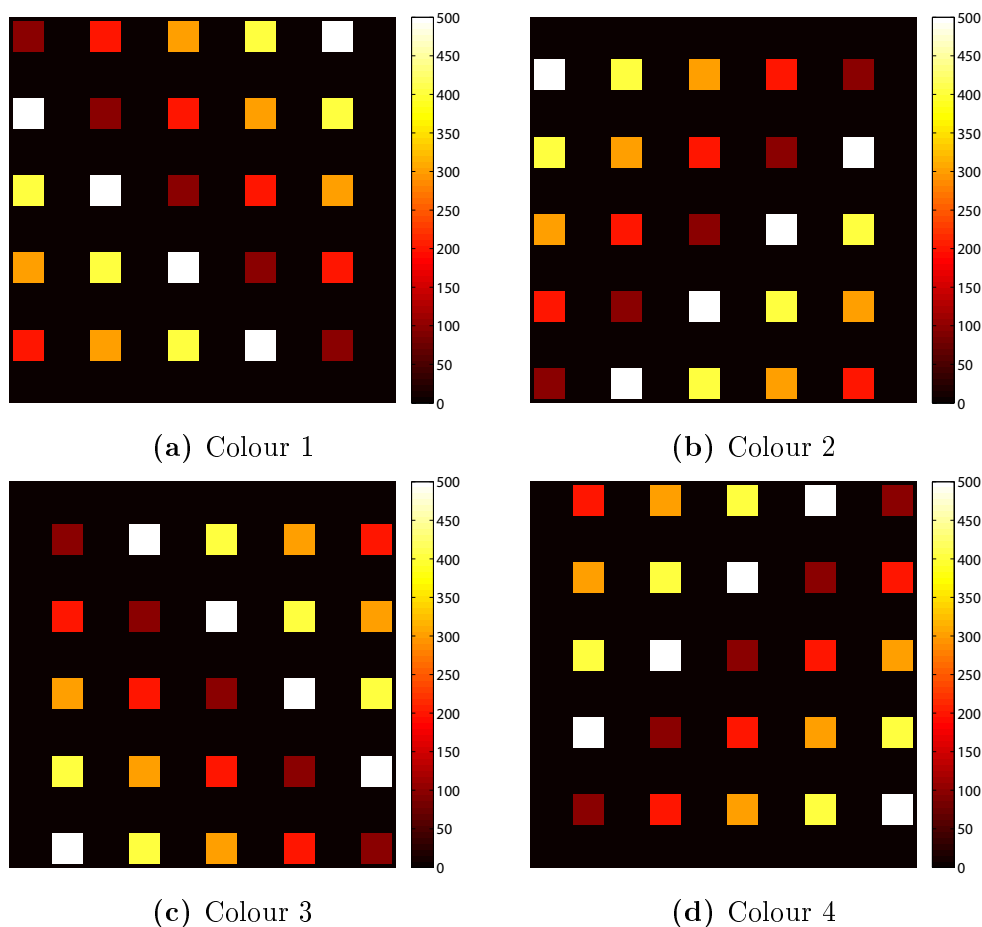


**Figure 4.1:** Original dye distributions without noise for generation of an artificial data set. The beads cover an area of  $8 \times 8$  pixels with a 1 pixel margin in each direction. Within one distribution the distance between the beads amounts to 20 pixels. They have different brightness levels of 100, 200, 300, 400 and 500 counts. Always 5 beads of each brightness level exist. The beads are non-overlapping.

allocated to a region of  $10 \times 10$  pixels. The bead itself was thereby  $8 \times 8$  pixels wide with a one pixel margin in each direction. The inter bead spacing was 20 pixels within one bead distribution. This made it very easy to calculate the crosstalk after the analysis, not only for the whole image, but also for each brightness level. The values stated later on will always represent the mean of either a single brightness level or the whole image. Error bars will represent the standard error of the mean. Note that in the case for two dyes, only the top row of figure 4.1 was used, whereas for three dyes, the top row plus the bottom left distribution was employed. For the case of four dyes, all four distributions were used.

The so generated data set was analyzed with the three aforementioned methods and various input parameters. Table 4.1 summarizes the input parameters, their meaning and their applicability to the individual methods.

**Table 4.1:** Input parameters into the different analysis methods and their meaning. Parameters are defined to be the elements of the transfer matrix  $\mathbf{A}$  (see section 2.4). ROI: region of interest.

parameter	applicable to	meaning
$\mathbf{A}_{\text{Gauss}}$	ImageJ	transfer matrix initialized with Gaussian distribution; adapted during analysis
$\mathbf{A}_{\text{ROI}}$	ImageJ	manually initialized transfer matrix by ROI selection for each dye in ImageJ; adapted during analysis
$\mathbf{A}_{\text{opt}}$	NNMF	transfer matrix initialized with $\mathbf{A}_{\text{exp}}$ ; adapted during analysis
$\mathbf{A}_{\text{exp}}$	NNMF LinUnmix	experimentally measured transfer matrix on single stained samples; kept fixed during analysis
$\mathbf{A}_{\text{mac}}$	NNMF LinUnmix	transfer matrix obtained by probability algorithm according to [63]; kept fixed during analysis
$\mathbf{A}_{\text{me2}}$	NNMF LinUnmix	manually optimized transfer matrix to yield the best separation in LinUnmix; kept fixed during analysis
$\mathbf{A}_{\text{me}}$	NNMF LinUnmix ImageJ	manually optimized transfer matrix to yield the best separation in NNMF; kept fixed during analysis

From table 4.1 it can be seen that five cases were examined for NNMF, four for LinUnmix and three for ImageJ. In all cases, the term input parameter referred to the elements of the transfer matrix  $\mathbf{A}$ . Manual tuning of the transfer matrix meant manual adjustment of the matrix elements such that the final unmixing result had minimal crosstalk. This was done by checking the residual crosstalk between the dyes and then adjusting the appropriate matrix element accordingly. Note that  $\mathbf{A}_{\text{exp}}$  was the same matrix that was used to create the artificial data set.

Optimizing the transfer matrix manually was tedious and time consuming. Moreover, even if the result looked good, there was no possibility of telling whether it actually was the best that one could do since it was subjective and depended on the patience, luck and experience of the user. Thus, an algorithm that correctly estimates the transfer matrix was needed. Originally, this was claimed in [70] to be accomplished by NNMF using the updating rule for  $\mathbf{A}$ . However, as will be shown later on, it did not yield the expected result. Hence, another algorithm was used that led to  $\mathbf{A}_{\text{mac}}$  [63] (see section 2.4.4).

## 4.2 Introduction of the measure $\xi$

To objectively evaluate the performance of the studied methods, the measure  $\xi$  was introduced. It is the square root of the sum of the squared differences between the ideal and the residual crosstalk after unmixing.  $\xi$  is similar to the standard deviation.

$$\xi = \sqrt{\sum_{ij} (e_{ij} - ct_{ij})^2} \quad (4.1)$$

where  $e_{ij}$  and  $ct_{ij}$  are the respective entries of the identity and the crosstalk matrix.

The crosstalk matrix gives the residual crosstalk after unmixing. It is a quadratic matrix and its length reflects the number of dyes. Each row  $i$  corresponds to one dye and the columns state how much the dye of row  $i$  is still present in the unmixed channel of dye  $j$ .

$$ct_{ij} = \frac{\text{counts}_{ij}}{\max_j (\text{counts}_{ij})}, \quad \text{usually : } \max_j (\text{counts}_{ij}) = \text{counts}_{ii}, \quad (4.2)$$

where  $\text{counts}_{ij}$  stands for the sum of all counts containing dye  $i$  in channel  $j$ .  $\max_j (\text{counts}_{ij})$  is the maximum number of counts of dye  $i$  in all the channels  $j$ .

In simulations  $CT$  is well defined and easily accessible making it suitable for the definition of the measure  $\xi$ .

For each set of input parameters in each method,  $\xi$  was calculated and used as a measure for the performance. The closer  $\xi$  is to zero, the better the separation, because in the ideal case of perfect separation for each dye, the crosstalk matrix is the identity matrix and  $\xi$  becomes zero.

## 4.3 Number of iterations needed for NNMF

This section deals with the question of how many iteration were needed in NNMF analysis with a fixed transfer matrix  $\mathbf{A}_{\text{me}}$  or with an adapted transfer matrix  $\mathbf{A}_{\text{opt}}$  and one excitation wavelength with four detection channels in order to yield good separation. Therefore, the two-dye combination Atto594/Atto647N was chosen. It was analyzed via NNMF with  $\mathbf{A}_{\text{me}}$  and  $\mathbf{A}_{\text{opt}}$  for brightness levels of 100 to 500 counts.  $\xi$  was calculated by taking the mean over all brightness levels after 10, 50, 100, 300, 500 and 1000 iterations. The result is shown in figure 4.2.

Figure 4.2 shows that for NNMF analysis with a fixed transfer matrix  $\mathbf{A}_{\text{me}}$  (blue bars),  $\xi$  dropped significantly until 300 iterations. After that the improvement became negligible indicating that 300 iterations were the optimum. In the case for NNMF analysis with an optimized transfer matrix  $\mathbf{A}_{\text{opt}}$  (cyan bars),  $\xi$  decreased until 100 iterations and then started to slowly rise again. This could be due to

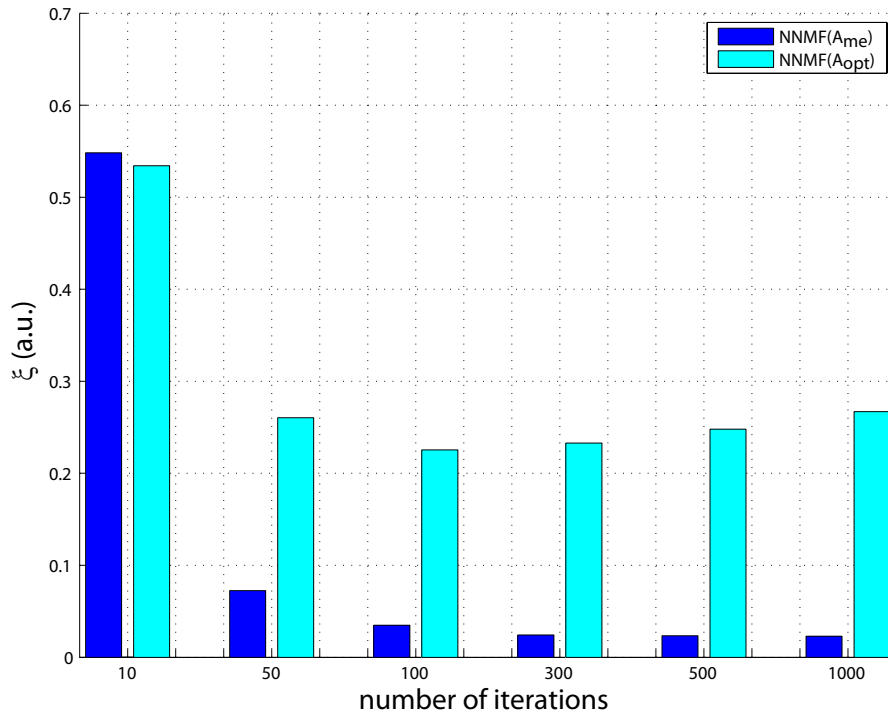


**Figure 4.2:** Bar chart of the measure  $\xi$  depending on the number of iterations performed in NNMF analysis with input parameters  $\mathbf{A}_{me}$  (blue) and  $\mathbf{A}_{opt}$  (cyan) for the two-dye combination of Atto594 and Atto647N.

an over-fitting issue [11] and indicated that the best number of iterations for  $\mathbf{A}_{opt}$  lay between 100 and 300. Moreover, the values for  $\xi$  were mostly larger in the case of NNMF with  $\mathbf{A}_{opt}$  indicating that the transfer matrix should be manually optimized and kept fixed during the analysis. A more detailed study on the best input parameters will be conducted in section 4.4.

In conclusion, the optimum number of iterations in NNMF analysis for one excitation wavelength and a two-dye sample seemed to be around 300. Hence, in all further NNMF analysis, 300 iterations were performed.

## 4.4 Excitation with one wavelength

In this section the separation and residual crosstalk between several dyes with one excitation wavelength was examined. In a first step, results were obtained for two dyes (4.4.1). The investigation was then extended to three dyes (4.4.2) and four dyes (4.4.3). A brief summary will be given in section 4.4.4.

### 4.4.1 Separation and crosstalk of two dyes

To examine the separation and residual crosstalk between two dyes with one excitation wavelength, Atto594 and Atto647N were chosen. Their respective absorption and emission spectra are depicted in figure 4.3.

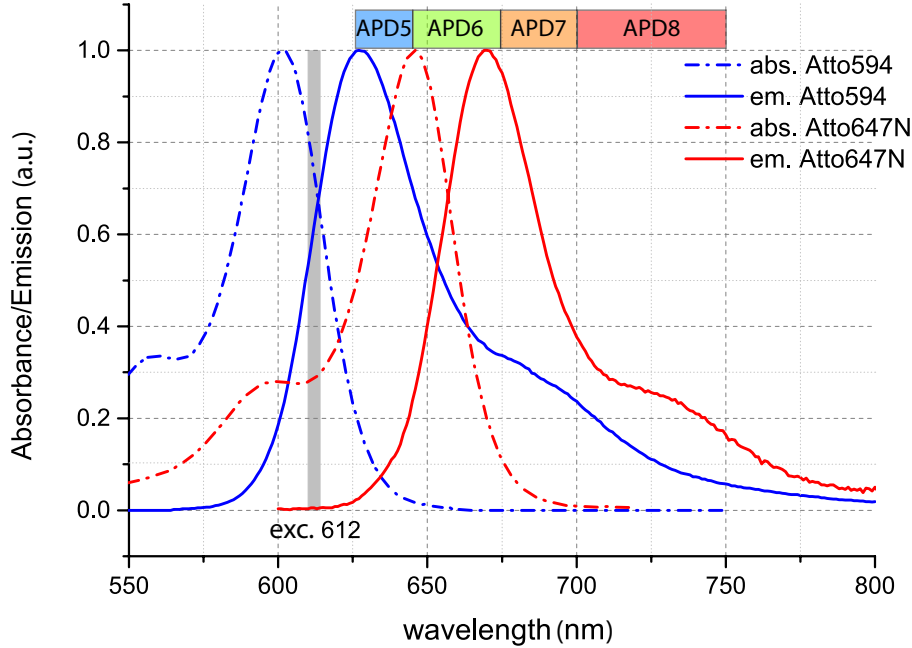


**Figure 4.3:** Absorption and emission spectra of Atto594 (blue) and Atto647N (red) as specified by the supplier. dashed lines: normalized absorbance, solid lines: normalized emission. Bars at the top represent the four detection windows. blue: APD5, green: APD6, orange: APD7 and red: APD8.

Figure 4.3 shows that the emission maxima of Atto594 (blue solid line) and Atto647N (red solid line) are ca. 40 nm apart. With this difference, discrimination based on their emission spectra should be possible. The width and position of the four detection windows are represented by the coloured bar above the absorption and emission spectra. The width of APD5 is shown in blue, APD6 in green, APD7 in orange and APD8 in red.

From the simulations conducted with the different input parameters and methods stated in table 4.1, one could draw several conclusions. For example, the crosstalk dropped with increasing brightness of the structure (see fig. 4.4).

Figure 4.4 shows a strong dependence of the crosstalk on the brightness. For beads with a brightness level of 10 counts, the remaining crosstalk amounted to 60 % whereas a brightness level of 500 counts, it was less than 0.5 % for the  $CT_{12}$

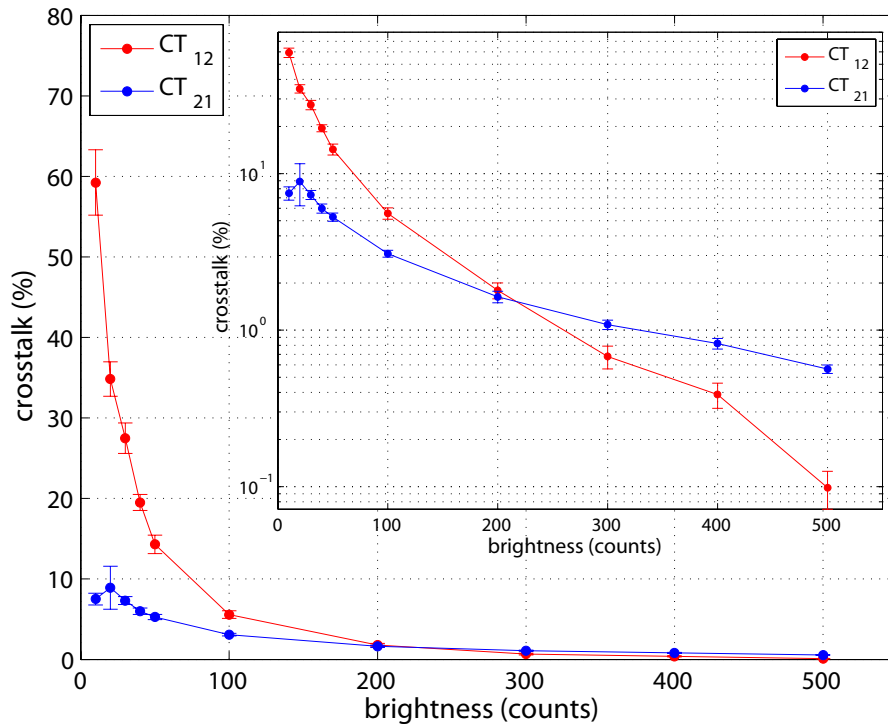


**Figure 4.4:** Dependence of the residual crosstalk on the brightness for the elements  $CT_{12}$  (red) and  $CT_{21}$  (blue). Values shown are the result of analysis with NNMF and  $\mathbf{A}_{me}$  as input parameters for Atto594 and Atto647N. The outer graph displays the values at a linear scale and the inset at a logarithmic scale.

element (red). In case of the  $CT_{21}$  element (blue), the crosstalk value amounted to 8% for a brightness level of 10 counts and decreased to a value of less than 1% at a brightness level of 500 counts.

From the inset of figure 4.4, one can see that the crosstalk dependence on the brightness of the two elements was different. For  $CT_{12}$  (red) an 8 fold improvement of the residual crosstalk is obtained by increasing the brightness by a factor of 2.5, i.e. from 40 counts to 100 counts. In the case of  $CT_{21}$  (blue), the improvement is less pronounced. For the same brightness change (from 40 counts to 100 counts), only a two fold improvement of the residual crosstalk was gained. A mathematical model that described the total dependency of the crosstalk on the brightness was not found. But for brightness levels above 40 counts, a power law seemed to describe the data. In any case, one could conclude that the brightness of a structure should be of 50 counts or higher for a good separation. Whereas it might be difficult to get to brightness levels of 500 counts, the levels of 100 to 300 counts should be achievable.

Without noise, the crosstalk stayed constantly zero for all brightness levels. The values shown in figure 4.4 were with noise and the result of analysis with NNMF and  $\mathbf{A}_{me}$  as input parameter. Note that for all other methods and input parameter

combinations, a similar behaviour was observed.

In a next step,  $\xi$  was calculated for the different methods and input parameter combinations for brightness levels of 100 to 500 counts. For the calculation of  $\xi$ , the mean over all brightness levels was used. The result is shown in figure 4.5.

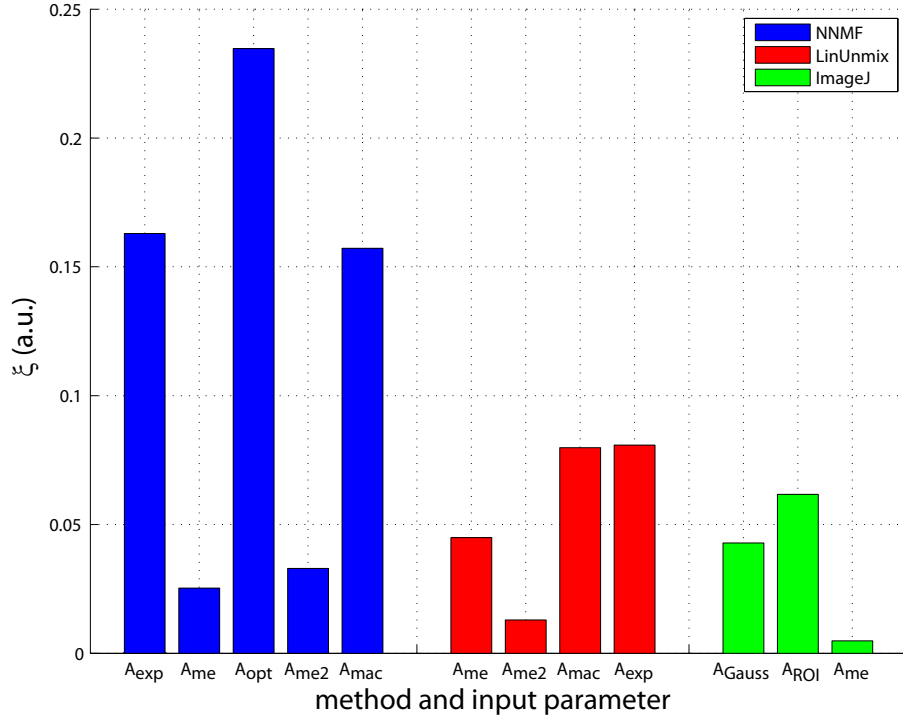


**Figure 4.5:** Bar chart of the measure  $\xi$  for the different methods and input parameter combinations for two dyes: Atto594 and Atto647N. blue: NNMF, red: Linear Unmixing, green: ImageJ.

Figure 4.5 shows a strong variance between the input parameters and the different methods. For example,  $\xi$  was the smallest (0.005) for  $\mathbf{A}_{me}$  with ImageJ as compared to 0.025 with NNMF and 0.045 with LinUnmix. Moreover, one can see that optimizing the transfer matrix never yielded the best separation. The values of  $\xi$  for  $\mathbf{A}_{opt}$ ,  $\mathbf{A}_{Gauss}$  and  $\mathbf{A}_{ROI}$  were all larger than the ones for a fixed and manually optimized transfer matrix ( $\mathbf{A}_{me}$ ,  $\mathbf{A}_{me2}$ ). Also, the algorithm according to [63] and leading to  $\mathbf{A}_{mac}$  was very close to the result for  $\mathbf{A}_{exp}$ . Thus,  $\mathbf{A}_{mac}$  did not lead to any improvement in the remaining crosstalk. But most striking was the fact that even though the correct transfer matrix was known, i.e.  $\mathbf{A}_{exp}$  with which the data was generated, this matrix did not yield the best unmixing result in the simulations. One had to push the transfer matrix to redder channels and to a stronger overlap of the dyes. This can be seen from the entries of  $\mathbf{A}_{exp}$  and  $\mathbf{A}_{me}$  given below where the first column contains the values for Atto594 and the second column those for Atto647N. The rows correspond to the detection channels from blue to red.

$$\mathbf{A}_{\text{exp}} = \begin{pmatrix} 0.33 & 0.07 \\ 0.45 & 0.61 \\ 0.13 & 0.20 \\ 0.09 & 0.12 \end{pmatrix}, \quad \mathbf{A}_{\text{me}} = \begin{pmatrix} 0.27 & 0.10 \\ 0.48 & 0.52 \\ 0.15 & 0.23 \\ 0.10 & 0.15 \end{pmatrix}$$

Note that in the case for two dyes with one excitation wavelength and four spectrally different detection channels, good results could be obtained with every method. For example, the largest element in the residual crosstalk matrix for NNMF with input parameters  $\mathbf{A}_{\text{me}}$  and noise was for Atto594 in the Atto647N channel ( $CT_{12}$ ) and amounted to 1.7 %.

#### 4.4.2 Separation and crosstalk of three dyes

To examine the separation and residual crosstalk between three dyes with one excitation wavelength, Atto594, Atto647N and CF680R were chosen. Their respective absorption and emission spectra can be seen in figure 4.6.

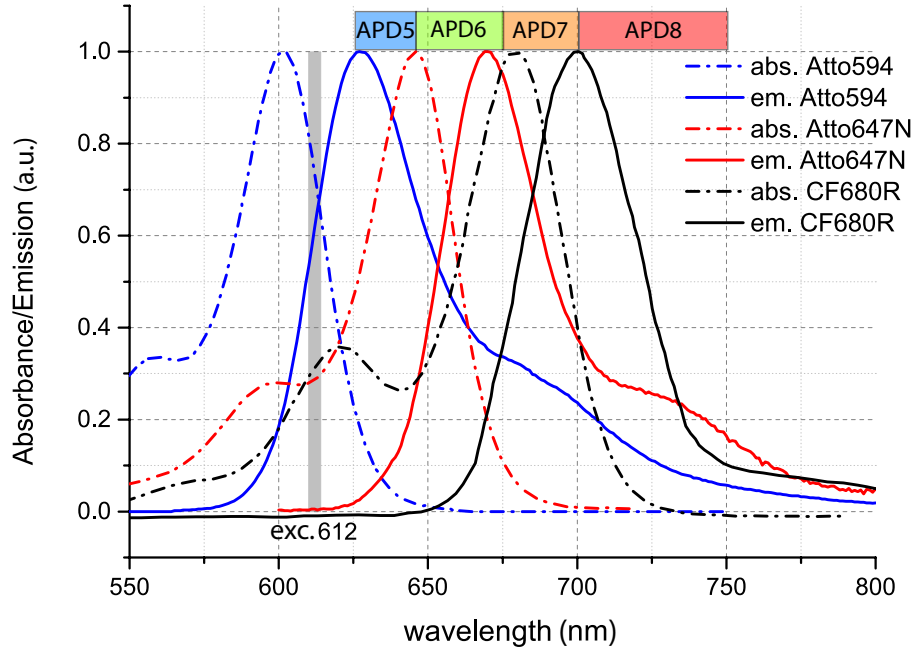


**Figure 4.6:** Absorption and emission spectra of Atto594 (blue), Atto647N (red) and CF680R (black) as specified by the suppliers. dashed lines: normalized absorbance, solid lines: normalized emission. Bars at the top represent the four detection windows. blue: APD5, green: APD6, orange: APD7 and red: APD8.

Figure 4.6 shows that the emission maxima of Atto594 (blue solid line), Atto647N (red solid line) and CF680R (black solid line) are ca. 40 nm apart for Atto594 and

Atto647N and ca. 30 nm apart for Atto647N and CF680R. With these differences, discrimination based on their emission spectra should be possible. The width and position of the four detection windows are represented by the coloured bar above the absorption and emission spectra. The width of APD5 is shown in blue, APD6 in green, APD7 in orange and APD8 in red.

From the simulations conducted with the different input parameters and methods stated in table 4.1, one could draw similar conclusions as in the case for two dyes (see section 4.4.1). For example, the crosstalk dropped with increasing brightness of the structure (see fig. 4.7).

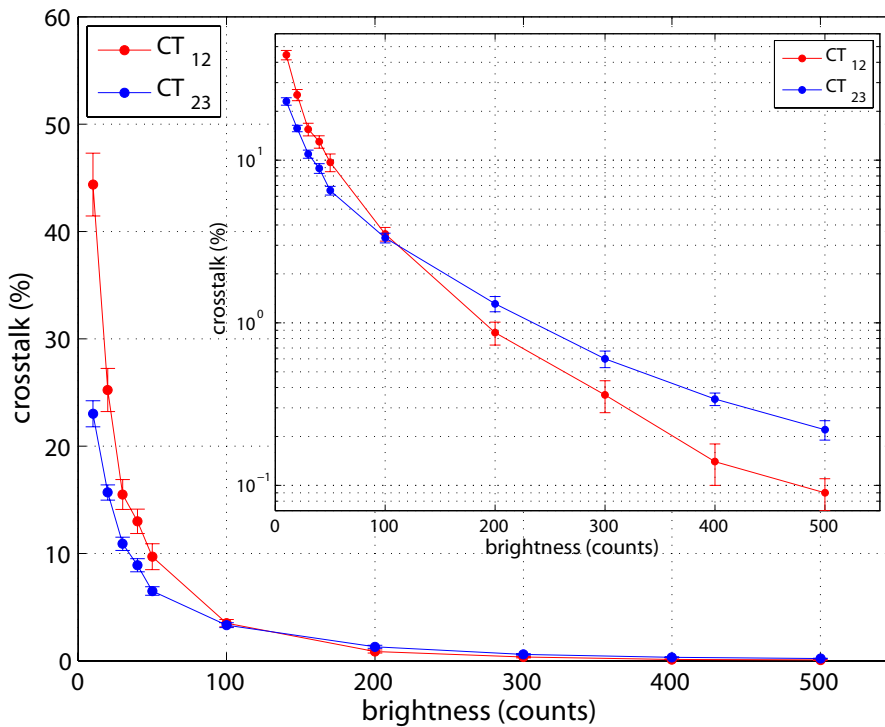


**Figure 4.7:** Dependence of the residual crosstalk on the brightness for the elements  $CT_{12}$  (red) and  $CT_{23}$  (blue). Values shown are the result of analysis with NNMF and  $\mathbf{A}_{me}$  as input parameters for Atto594, Atto647N and CF680R. The outer graph displays the values at a linear scale and the inset at a logarithmic scale.

Figure 4.7 shows the residual crosstalk elements with the strongest dependence of the crosstalk on the brightness. For beads with a brightness level of 10 counts, the remaining crosstalk amounted to 44% whereas for a brightness level of 500 counts, it was less than 0.1% for the  $CT_{12}$  element (red). In case of the  $CT_{23}$  element (blue), the crosstalk value amounted to 23% for a brightness level of 10 counts and decreased to a value of 0.2% at a brightness level of 500 counts.

From the inset of figure 4.4, one can see that the crosstalk dependence on the

brightness of the two elements was different. For brightness levels below 50 counts the curves seemed to be parallel before they reached a crossing point at around 100 counts. Below 100 counts the residual crosstalk for  $CT_{23}$  (blue) was lower and above 100 counts the situation was reversed. A mathematical model that described the total dependency of the crosstalk on the brightness was not found. But for brightness levels above 40 counts, a power law seemed to describe the data. In any case, one could conclude that the brightness of a structure should be of 50 counts or higher for a good separation. Whereas it might be difficult to get to brightness levels of 500 counts, the levels of 100 to 300 counts should be achievable.

Without noise, the crosstalk stayed constantly zero for all brightness levels. The values shown in figure 4.7 were with noise and the result of analysis with NNMF and  $\mathbf{A}_{me}$  as input parameter. Note that for all other methods and input parameter combinations, a similar behaviour was observed.

In a next step,  $\xi$  was calculated for the different methods and input parameter combinations for brightness levels of 100 to 500 counts. For the calculation of  $\xi$ , the mean over all brightness levels was used. The result is depicted in figure 4.8.

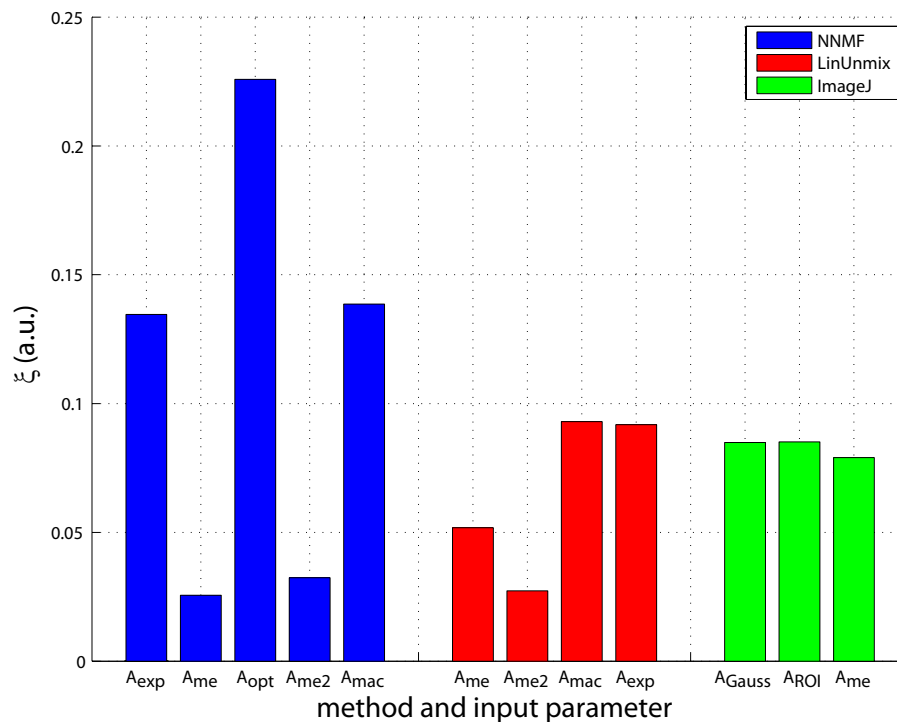


**Figure 4.8:** Bar chart of the measure  $\xi$  for the different methods and input parameter combinations for three dyes: Atto594, Atto647N and CF680R. blue: NNMF, red: Linear Unmixing, green: ImageJ.

Figure 4.8 shows the same variance between the input parameters and the differ-

ent methods as in the case for the separation of two dyes (see fig. 4.4). For example,  $\xi$  was the smallest (0.026) for  $\mathbf{A}_{\text{me}}$  with NNMF as compared to 0.027 with LinUnmix for  $\mathbf{A}_{\text{me2}}$  and 0.079 with ImageJ for  $\mathbf{A}_{\text{me}}$ . Moreover, one can see that optimizing the transfer matrix by the algorithm always led to a higher residual crosstalk. The values of  $\xi$  for  $\mathbf{A}_{\text{opt}}$ ,  $\mathbf{A}_{\text{Gauss}}$  and  $\mathbf{A}_{\text{ROI}}$  were all larger than the ones for a fixed and manually optimized transfer matrix ( $\mathbf{A}_{\text{me}}$ ,  $\mathbf{A}_{\text{me2}}$ ). Also, the algorithm according to [63] and giving  $\mathbf{A}_{\text{mac}}$  was very close to the result for  $\mathbf{A}_{\text{exp}}$ . Thus,  $\mathbf{A}_{\text{mac}}$  did not lead to any improvement in the remaining crosstalk. But most striking was the fact that even though the correct transfer matrix was known, i.e.  $\mathbf{A}_{\text{exp}}$  with which the data was generated, this matrix did not yield the best unmixing result. As in the case for two dyes (see section 4.4.1), one has to push the transfer matrix to a stronger overlap and further to the red. This can be seen in the differences for  $\mathbf{A}_{\text{exp}}$  and  $\mathbf{A}_{\text{me}}$  given below. The first column corresponds to Atto594, the second to Atto647N and the third to CF680R. The rows represent the four detection channels from blue to red.

$$\mathbf{A}_{\text{exp}} = \begin{pmatrix} 0.33 & 0.07 & 0.01 \\ 0.45 & 0.61 & 0.12 \\ 0.13 & 0.20 & 0.36 \\ 0.09 & 0.12 & 0.51 \end{pmatrix}, \quad \mathbf{A}_{\text{me}} = \begin{pmatrix} 0.27 & 0.10 & 0.02 \\ 0.48 & 0.52 & 0.13 \\ 0.15 & 0.23 & 0.38 \\ 0.10 & 0.15 & 0.47 \end{pmatrix}$$

Note that in the case for three dyes with one excitation wavelength and four spectrally different detection channels, good results could be obtained with NNMF and LinUnmix. Separation by ImageJ always led to higher residual crosstalk (see fig. 4.8). In the case for NNMF with input parameters  $\mathbf{A}_{\text{me}}$  and noise, the largest element in the residual crosstalk matrix was for Atto647N in the Atto594 channel ( $CT_{21}$ ) and amounted to 1.5%.

### 4.4.3 Separation and crosstalk of four dyes

To examine the separation and residual crosstalk between four dyes with one excitation wavelength, Atto594, Star635P, KK1441 and CF680R were chosen. Their respective absorption and emission spectra are shown in figure 4.9.

Figure 4.9 shows that the emission maxima of Atto594 (blue solid line), Star635P (red solid line), KK1441 (black solid line) and CF680R (green solid line) are ca. 26 nm apart for Atto594 and Star635P, ca. 22 nm apart for Star635P and KK1441 and ca. 25 nm apart for KK1441 and CF680R. With these differences, discrimination based on their emission spectra should be possible. The width and position of the four detection windows are represented by the coloured bar above the absorption and emission spectra. The width of APD5 is shown in blue, APD6 in green, APD7 in orange and APD8 in red.

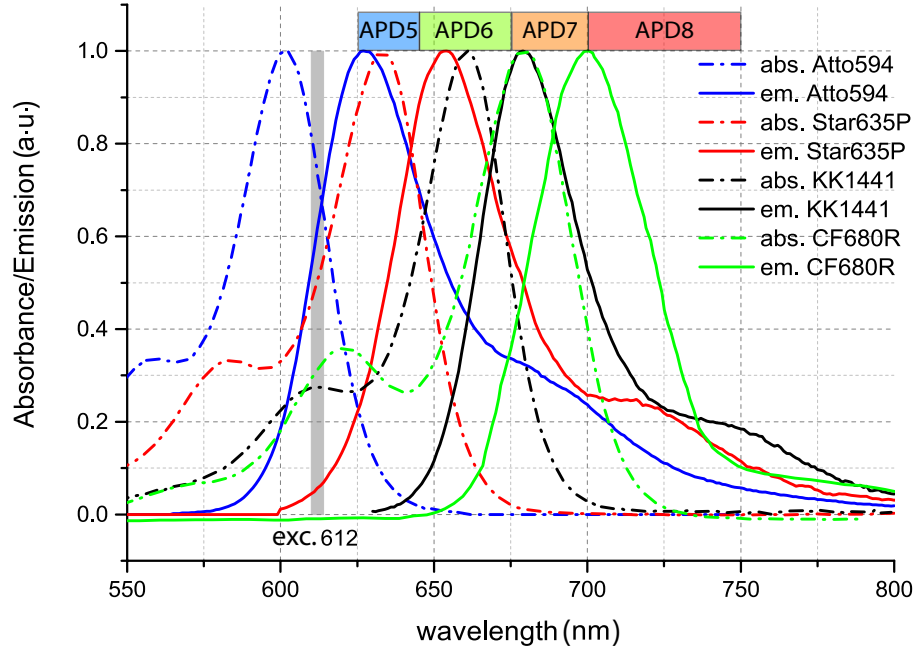


**Figure 4.9:** Absorption and emission spectra of Atto594 (blue), Star635P (red), KK1441 (black) and CF680R (green) as specified by the supplier. dashed lines: normalized absorbance, solid lines: normalized emission. Bars at the top represent the four detection windows. blue: APD5, green: APD6, orange: APD7 and red: APD8.

From the simulations conducted with different input parameters and methods stated in table 4.1, one could draw similar conclusions as in the case for two and three dyes (see sections 4.4.1 and 4.4.2). For example, the crosstalk dropped with increasing brightness of the structure (see fig. 4.10).

Figure 4.10 shows two out of the 12 residual crosstalk elements;  $CT_{23}$  (red) exhibited the strongest dependence of the residual crosstalk on the brightness and  $CT_{32}$  (blue) had a low dependence of the residual crosstalk on the brightness but converged to a value other than zero. For beads with a brightness level of 10 counts the remaining crosstalk of  $CT_{23}$  (red) amounted to 63% and dropped to less than 0.5% at brightness levels of 500 counts. In case of  $CT_{32}$  (blue), the remaining crosstalk amounted to 18% for beads with a brightness level of 10 counts whereas for a brightness level of 200 counts or more, it amounted to 5%.

From the inset of figure 4.10, one can see that the crosstalk dependence on the brightness of the two elements was different. In case of  $CT_{23}$  (red), a 2.5 fold improvement of the residual crosstalk was observed when increasing the brightness level from 50 to 100 counts. Moreover, there was a small kink in the curve between brightness levels of 40 and 50 counts whose origin is unclear and requires further simulations. The two curves had a crossing point around a brightness level of 100

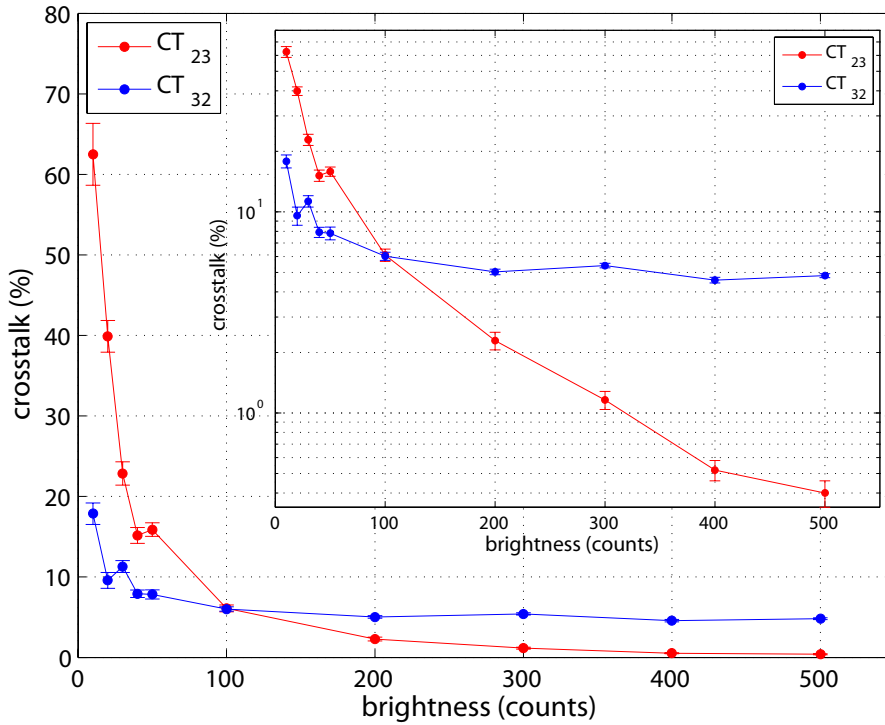


**Figure 4.10:** Dependence of the residual crosstalk on the brightness for the elements  $CT_{23}$  (red) and  $CT_{32}$  (blue). Values shown are the result of analysis with NNMF and  $\mathbf{A}_{me}$  as input parameters for Atto594, Star635P, KK1441 and CF680R. The outer graph displays the values at a linear scale and the inset at a logarithmic scale.

counts. Below 100 counts the residual crosstalk of  $CT_{32}$  (blue) was lower and above 100 counts the situation was reversed. A mathematical model that described the total dependency of the residual crosstalk on the brightness was not found. But for brightness levels above 50 counts, a power law seemed to describe the data. One could conclude that the brightness of a structure should be of 100 counts or higher for a good separation.

Without noise, the crosstalk stayed constant and was close to zero for all brightness levels for  $CT_{23}$ . In contrast were the values for  $CT_{32}$ . They amounted to 5% and stayed constantly at this level for all brightness levels. This indicated that either the spectra of Star635P and KK1441 were too close together to yield a better separation than 5% or that the transfer matrix  $\mathbf{A}_{me}$  was not yet fully optimized. In any case, no better separation than without noise could be obtained. Values shown in figure 4.10 were with noise and the result of the analysis with NNMF and  $\mathbf{A}_{me}$  as input parameter. Note that for all other methods and input parameter combinations, a similar behaviour was observed. Further, note that  $CT_{32}$  was the only matrix element with a significant difference from zero in the no noise case.

In a next step,  $\xi$  was calculated for the different methods and input parameter

combinations for brightness levels of 100 to 500 counts. For the calculation of  $\xi$ , the mean over all brightness levels was used. The result is depicted in figure 4.11.

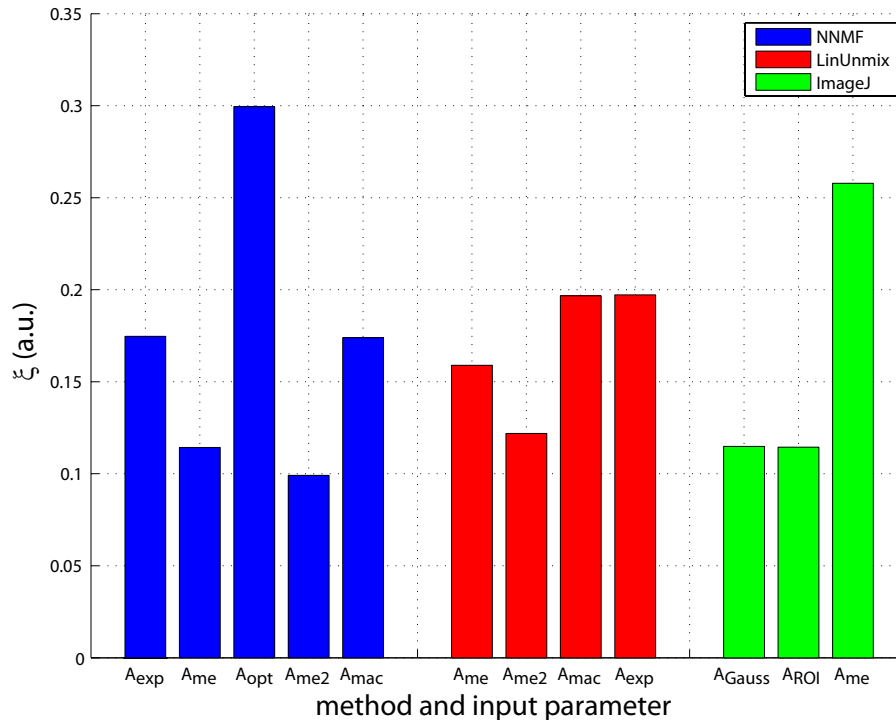


**Figure 4.11:** Bar chart of the measure  $\xi$  for the different methods and input parameter combinations for 4 dyes: Atto594, Star635P, KK1441 and CF680R. blue: NNMF, red: Linear Unmixing, green: ImageJ.

Figure 4.11 shows a less strong variance between the input parameters and the different methods as in the case for separation of two and three dyes (see fig. 4.4 and 4.7) and an overall larger value for  $\xi$ . This was expected since more off-diagonal matrix elements existed that contributed to  $\xi$ .  $\xi$  was the smallest (0.10) for  $\mathbf{A}_{\text{me2}}$  with NNMF as compared to 0.12 with LinUnmix and 0.11 with ImageJ for  $\mathbf{A}_{\text{ROI}}$ . Moreover, one can see that optimizing the transfer matrix by the algorithm only helped in the case of ImageJ. For NNMF, the separation deteriorated with optimization of the transfer matrix. The value of  $\xi$  for  $\mathbf{A}_{\text{opt}}$  was larger than the ones for a fixed and manually optimized transfer matrix ( $\mathbf{A}_{\text{me}}$ ,  $\mathbf{A}_{\text{me2}}$ ). Also, the algorithm according to [63] and leading to  $\mathbf{A}_{\text{mac}}$  was very close to the result for  $\mathbf{A}_{\text{exp}}$ . Thus,  $\mathbf{A}_{\text{mac}}$  did not lead to any improvement in the remaining crosstalk. But most striking was the fact that even though the correct transfer matrix was known, i.e.  $\mathbf{A}_{\text{exp}}$  with which the data was generated, this matrix did not yield the best unmixing result. As in the case for two and three dyes (see section 4.4.1 and 4.4.2), one had to push the transfer matrix to a stronger overlap of the dyes and further to the red. This can be seen in the differences for  $\mathbf{A}_{\text{exp}}$  and  $\mathbf{A}_{\text{me}}$  given below. The first column gives the

values for Atto594, the second for Star635P, the third for KK1441 and the fourth for CF680R. The rows correspond to the different detection channels from blue to red.

$$\mathbf{A}_{\text{exp}} = \begin{pmatrix} 0.33 & 0.11 & 0.02 & 0.01 \\ 0.45 & 0.63 & 0.34 & 0.12 \\ 0.13 & 0.16 & 0.43 & 0.36 \\ 0.09 & 0.10 & 0.21 & 0.51 \end{pmatrix}, \quad \mathbf{A}_{\text{me}} = \begin{pmatrix} 0.27 & 0.16 & 0.01 & 0.02 \\ 0.48 & 0.50 & 0.34 & 0.13 \\ 0.15 & 0.20 & 0.34 & 0.38 \\ 0.10 & 0.14 & 0.31 & 0.47 \end{pmatrix}$$

Note that in the case for four dyes with one excitation wavelength and four spectrally different detection channels, good results could be obtained with NNMF, LinUnmix and ImageJ where the result with NNMF was slightly better. In the case for NNMF with input parameter  $\mathbf{A}_{\text{me}}$  and noise, the largest element in the residual crosstalk matrix was for CF680R in the KK1441 channel ( $CT_{43}$ ) and amounted to 6 %.

#### 4.4.4 Summary of the simulations with one wavelength

From the results of the simulations with only one excitation wavelength of 612 nm, several conclusions could be drawn. First, it is important to note that in all cases (two, three or four dyes) it was best to keep the transfer matrix fixed during the analysis. The analyzing method itself – NNMF, LinUnmix or ImageJ – played a minor role. Especially for NNMF and LinUnmix transfer matrices could always be found that yielded a good unmixing result. For ImageJ this could only be achieved in the case for two dyes. For this reason, NNMF with a fixed and manually optimized transfer matrix was chosen as the unmixing method throughout this thesis.

However, keeping the transfer matrix fixed means that its values had to be known beforehand. Additionally, its entries did not correspond to the single stained samples. The transfer matrix elements always had to be pushed to a stronger spectral overlap of the individual dyes and further to the red. Introducing a new algorithm for estimating the transfer matrix ( $\mathbf{A}_{\text{mac}}$ ) and optimizing it during the analysis ( $\mathbf{A}_{\text{opt}}$ ) did not result in any improvement.

A reason for the worse result of  $\mathbf{A}_{\text{opt}}$  could be over-fitting. The NNMF algorithm might not have enough information to estimate every unknown value correctly in the presence of noise. A more detailed explanation of over-fitting can be found in [11]. To circumvent this problem, some input parameters had to be manually optimized and kept fixed throughout the analysis, i.e. the transfer matrix, leading then to  $\mathbf{A}_{\text{me}}$ .

A comparison of the largest crosstalk elements averaged over brightness levels of 100 to 500 counts for NNMF and the input parameter  $\mathbf{A}_{\text{me}}$  showed a good separation in all cases. For two dyes, the crosstalk value in the simulations amounted to 1.7 %, for three dyes to 1.5 % and for four dyes to 6 %.

Furthermore, it was shown that the noise level deteriorated the unmixing result. Nevertheless, adding noise is important since it is closer to reality. Therefore only simulations including noise and NNMF will be considered in the following sections.

## 4.5 Excitation with two wavelengths

In this section the effect of adding a second excitation wavelength in the analysis with NNMF was explored. Therefore, 593 nm and 656 nm were chosen as excitation wavelengths since they give a good excitation contrast. Note that the excitation wavelengths were not used simultaneously but in a multiplexed manner, meaning that with each excitation wavelength four detection windows were simulated leading to a total number of 8 detection channels.

As mentioned in 4.4.4, only simulations with added noise were performed and compared for two, three and four dyes. The brightness levels ranged from 100 to 500 counts. The values of  $\xi$  shown in figure 4.12 were the result of using the mean over all brightness levels for the calculation of  $\xi$ .

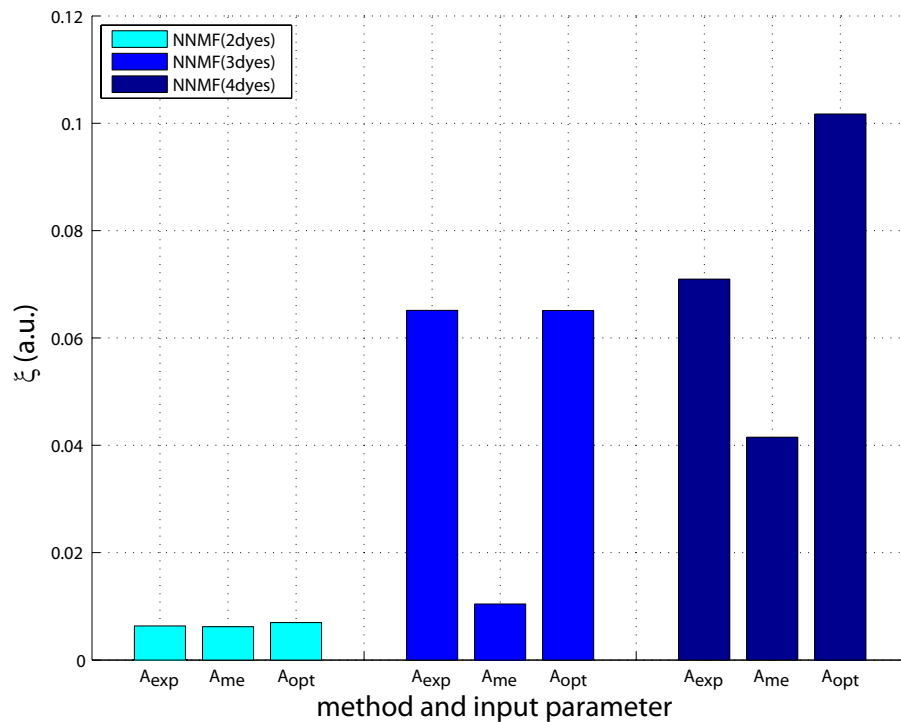


**Figure 4.12:** Bar chart of the measure  $\xi$  for NNMF with different input parameters and dye combinations for excitation with 593 nm and 656 nm. two dyes: Atto594, Atto647N (cyan), three dyes: Atto594, Atto647N, CF680R (blue) and four dyes: Atto594, Star635P, KK1441 and CF680R (dark blue).

In comparison with figures 4.5, 4.8 and 4.11, figure 4.12 highlights two properties. One is that the values for the measure  $\xi$  were smaller by at least a factor of two, indicating a better separation of the dyes. This manifested itself also in the largest crosstalk elements which were now 0.6 % for two dyes, 0.7 % for three dyes and 2.8 % for four dyes when excited with 593 nm and 656 nm as opposed to 1.7 %, 1.5 % and 6 % respectively when excited with one excitation wavelength at 612 nm.

The second observation is that in the case for two dyes, the choice of input parameters was irrelevant. Regardless of the chosen transfer matrix, the NNMF algorithm converged to a good unmixing result. Here, no a priori information was needed. For three and four dyes this was not true, meaning that for these cases a fixed and manually tuned transfer matrix was the better choice. This also indicated that the NNMF algorithm seemed to need many more detection channels than the number of dyes to fully exploit its advantage of not needing any a priori information.

## 4.6 Lifetime and one excitation wavelength

In this section the effects on separation and crosstalk were simulated by taking a single excitation wavelength and the lifetime into account. It has been demonstrated that including the lifetime in the unmixing analysis led to good separation if the lifetimes differed by more than 0.5 ns. Thereby two approaches can be taken: either the whole lifetime trace is recorded as in [4, 15, 90] or the lifetime is recorded in different time gates as in [29]. Here, the second approach was investigated since experimental implementation in the set-up described in chapter 3 could be done without further hardware requirement.

Section 4.6.1 will explain the mathematical background for the different time gates approach and section 4.6.2 will give the simulated results on the remaining crosstalk for several dye combinations.

### 4.6.1 Lifetime separation via two time gates

The algorithm for the analysis including the lifetime information in two time gates was essentially the same as in sections 4.4 and 4.5 except that the matrix  $\mathbf{Q}$  was replaced by the matrix  $\mathbf{T}$  (see also section 2.4.2). The latter had dimensions  $N_k \times N_m$ , where  $k$  is the index for the number of dyes  $N_k$  and  $m$  is the index for the number of time gates  $N_m$ . Note that the normalization was chosen such that the sum over each row was 1. Furthermore, the transfer matrices  $\mathbf{A}$  and  $\mathbf{T}$  were kept fixed during the analysis. This yielded the best results and is consistent with the observations in section 4.4.

The entries of  $\mathbf{T}$  were calculated according to the following equations. First, a single exponential decay of the fluorescence with the time constant being the characteristic

lifetime of the dye was assumed.

$$I(t) = a_0 \cdot e^{-t/\tau}, \quad (4.3)$$

where  $a_0$  is the amplitude and  $\tau$  the lifetime. Then the integral of the time gates in question was calculated.

$$\Delta t_m = \int_{t_0(m)}^{t_m} I(t) dt, \quad (4.4)$$

where  $t_0(m)$  is the starting point that can vary for every  $\Delta t_m$  and  $t_m$  is the end point of the integral. The matrix elements  $t_{km}$  of  $\mathbf{T}$  were obtained by normalizing the  $\Delta t_m$  to their sum.

$$t_{km} = \frac{\Delta t_m}{\sum_m \Delta t_m}. \quad (4.5)$$

Here, two time gates were simulated. The first one started 0.5 ns after the excitation pulse and was 1 ns wide, meaning that  $t_0(m = 1) = 0.5$  and  $t_1 = 1.5$ . The second time gate started, when the first one ended, i.e. 1.6 ns after the excitation, and was 10 ns wide, meaning that  $t_0(m = 2) = 1.6$  and  $t_2 = 11.6$ . These limits remained constant for all dyes  $k$  investigated.

The lifetimes of the different dyes inserted into the model of equation (4.3) are given in table 4.2.

**Table 4.2:** Estimated lifetimes  $\tau$  in ns, absorption (Abs) and emission (Em) maxima in nm and reference of the dyes used in the simulations sorted by absorption wavelength.

dye	supplier	Abs (nm)	Em (nm)	$\tau$ (ns)	reference
Atto594	ATTO-TEC	601	627	3.2	[24]
Star600	Abberior	604	627	1.2	this work
DyLight633	lietechnologies	623	649	1.7	this work
Star635P	Abberior	633	654	3.0	[24]
Atto647N	ATTO-TEC	644	669	2.0	[24]
KK1441	[52]	661	679	2.4	[52]
CF680R	Biotium	680	701	1.8	[24]

### 4.6.2 Separation and Crosstalk of two, three and four dyes

First, three different two-dye combinations were investigated: Atto594/Star600, DyLight633/Star635P and Atto594/Atto647N. The first two have almost identi-

cal emission spectra such that spectral separation with this set-up was not possible whereas Atto594 and Atto647N could be very well distinguished spectrally (see tab. 4.2). This pair was chosen to see whether the addition of lifetime gating resulted in better discrimination. Brightness levels of 100 to 500 counts were simulated and for the calculation of  $\xi$  the mean over all brightness levels was used. The results are shown in figure 4.13.

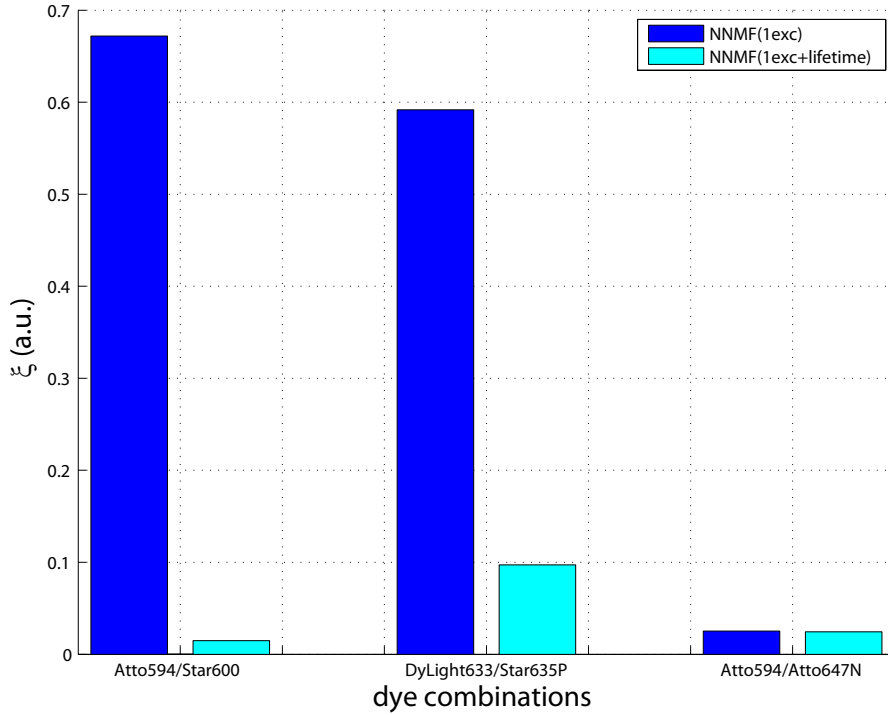


**Figure 4.13:** Bar chart of the measure  $\xi$  for the dye combinations Atto594/Star600 ( $\Delta\lambda_{em} = 0$  nm,  $\Delta\tau = 2$  ns), DyLight633/Star635P ( $\Delta\lambda_{em} = 5$  nm,  $\Delta\tau = 1.3$  ns) and Atto594/Atto647N ( $\Delta\lambda_{em} = 42$  nm,  $\Delta\tau = 1.2$  ns).  $\xi$  is calculated for analysis via NNMF with either one excitation wavelength alone (blue) or one excitation wavelength and lifetime information in two time gates (cyan). Input parameters are  $\mathbf{A}_{exp}$  for Atto594/Star600 and DyL633/Star635P and  $\mathbf{A}_{me}$  for Atto594/Atto647N.

Figure 4.13 clearly shows that better discrimination was achieved for dyes that have almost identical emission spectra when their lifetimes differed and were taken into account. In the case for Atto594 and Star600, the lifetimes differed by 2 ns and making use of that, the remaining crosstalk was reduced to 1% leading to almost perfect discrimination. When only the spectral information was considered, the crosstalk amounted to 52%. The case of DyL633 and Star635P also clearly showed a discrimination improvement when the lifetime information was included. However, since the lifetimes only differed by 1.3 ns, the remaining crosstalk was higher than it was the case for Atto594/Star600. Nevertheless, the largest residual crosstalk element after analysis amounted to 7% when the lifetime was included in the analysis whereas it was 53% when ignored.

The situation in the case of Atto594 and Atto647N was different. Here, good separation could already be achieved via their emission spectra and only little was gained when taking the lifetime into account, even though their lifetimes differed by 1.2 ns. In this case, different gate settings might lead to a larger improvement but the rise in complexity (more input parameters needed to be known) of the analysis outweighed the benefit.

Further, the dye combinations Atto594/Atto647N, Atto594/Atto647N/CF680R and Atto594/Star635P/KK1441/CF680R were investigated and the impact of including the lifetime information was compared to exciting with one or two excitation wavelengths. For all combinations and detection configurations brightness levels of 100 to 500 counts were simulated, the value of  $\xi$  was calculated by using the mean over all brightness levels. The results are shown in figure 4.14, where  $\xi$  for NNMF analysis with one excitation wavelength alone is displayed in blue, for NNMF analysis with one excitation wavelength and lifetime information in two time gates in cyan and for NNMF analysis with two excitation wavelengths in dark blue.

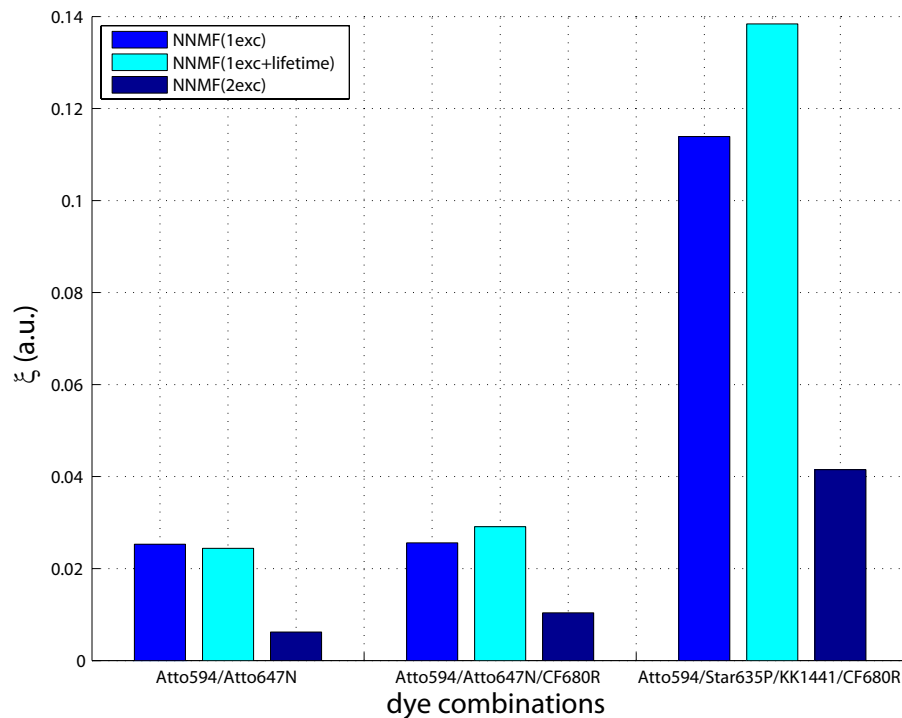


**Figure 4.14:** Bar chart of the measure  $\xi$  for the dye combinations Atto594/Atto647N, Atto594/Atto647N/CF680R and Atto594/Star635P/KK1441/CF680R.  $\xi$  is calculated for analysis via NNMF with either one excitation wavelength alone (blue), one excitation wavelength and lifetime information in two time gates (cyan) or two excitation wavelengths (dark blue).

Figure 4.14 shows that when the dyes could already be distinguished via their

emission spectra, adding the lifetime information did not necessarily lead to a better discrimination. In the cases for three and four different dyes, the increase in input parameters that had to be manually optimized even deteriorated the separation in this simulation.

Moreover, figure 4.14 reflects that when the dyes were spectrally distinct, it was more advantageous to add a second excitation wavelength as another means of discrimination than lifetime to improve their separation.

## 4.7 Conclusion of the simulations

Three different analysis algorithms for hyperspectral images were presented: a self-implemented non-negative matrix factorization algorithm (NNMF) [70], a Poisson-NMF plugin for ImageJ (ImageJ) [69] and self-implemented linear unmixing (Lin-Unmix) [96]. A new measure  $\xi$  was introduced to assess the residual crosstalk after analysis (see section 4.2) for different input parameters in the various methods (see section 4.1).

It was found that 300 iterations of NNMF with a fixed transfer matrix  $\mathbf{A}$  yielded the best separation for excitation with one wavelength (see sections 4.3 and 4.4). Therefore, all further simulations were conducted under these conditions.

Automatic adaption of the transfer matrix  $\mathbf{A}$  in NNMF always led to higher residual crosstalk after the analysis. This could be a result of over-fitting [11]. The algorithm might not have enough information to estimate every unknown parameter correctly in the presence of noise.

Further, the impact on the separation was investigated when either a second wavelength or lifetime was included in the analysis. It was found that for spectrally distinct dyes, the addition of a second excitation wavelength yielded better results than the inclusion of lifetime information (see section 4.5 and 4.6). However, when the dyes could not be distinguished spectrally, the lifetime provided a means of discrimination that allowed to decrease the remaining crosstalk below 10 % when the lifetimes differed by ca. 1 ns.

Note that the simulation performed here did neither take the bleaching of the dyes nor the influence of the PSF into account. Also, the impact of background noise on the unmixing result was not considered.

# Chapter 5

## Experimental results

This chapter presents the experimental results of multicolour STED nanoscopy with hyperspectral detection (HyperSTED). Throughout this chapter, the powers of the different laser beams will be stated as powers measured in the back focal plane of the objective ( $P_{\text{back}}$ ). In order to keep comparability to other set-ups and publications, table 5.1 gives the corresponding values also as a peak intensity  $P_{\text{peak}}$  and an energy per pulse  $E_{\text{pulse}}$ .

**Table 5.1:** Correspondence of the laser power in the back focal plane of the objective  $P_{\text{back}}$  to the peak intensity in the focus  $P_{\text{peak}}$  and the energy per pulse  $E_{\text{pulse}}$  for the different excitation and STED wavelengths. The repetition rate used for calculations was 40 MHz.

$\lambda$		$P_{\text{back}}$		$P_{\text{peak}}$		$E_{\text{pulse}}$	
560	nm	5	$\mu\text{W}$	2.67	$\text{kW}/\text{cm}^2$	125	fJ
612	nm	5	$\mu\text{W}$	2.24	$\text{kW}/\text{cm}^2$	125	fJ
656	nm	5	$\mu\text{W}$	1.95	$\text{kW}/\text{cm}^2$	125	fJ
775	nm	90	mW	25.1	$\text{MW}/\text{cm}^2$	2.25	nJ
775	nm	120	mW	33.5	$\text{MW}/\text{cm}^2$	3.00	nJ
775	nm	240	mW	67.0	$\text{MW}/\text{cm}^2$	6.00	nJ
775	nm	400	mW	112.0	$\text{MW}/\text{cm}^2$	10.00	nJ

In a first step, the set-up's performance was tested with fluorescent beads of different colours. They were used to characterize the achievable resolution and to get a first estimate of separability and crosstalk after data analysis (see section 5.1). Secondly, the dependence of the achievable resolution on the chromophore was examined (see section 5.2). A range of organic dyes from various companies was investigated to assess their STED performance (see section 5.3). Then, a set of several dye combinations was determined with minimal crosstalk. This was performed

with one excitation wavelength (see section 5.4) as well as with two excitation wavelengths (see section 5.5) and a single STED beam of 775 nm. A spectral shift of the emission spectra of some organic dyes to the blue was observed. Its appearance and mechanism will be further described in section 5.6. A short conclusion will be given in section 5.7.

## 5.1 Fluorescent beads

As a first sample, commercially available fluorescent beads were chosen (lifetechnologies now part of Thermo Fisher Scientific, Waltham, US). Note that some sizes of the beads are no longer available (see appendix B for used beads and sample preparation).

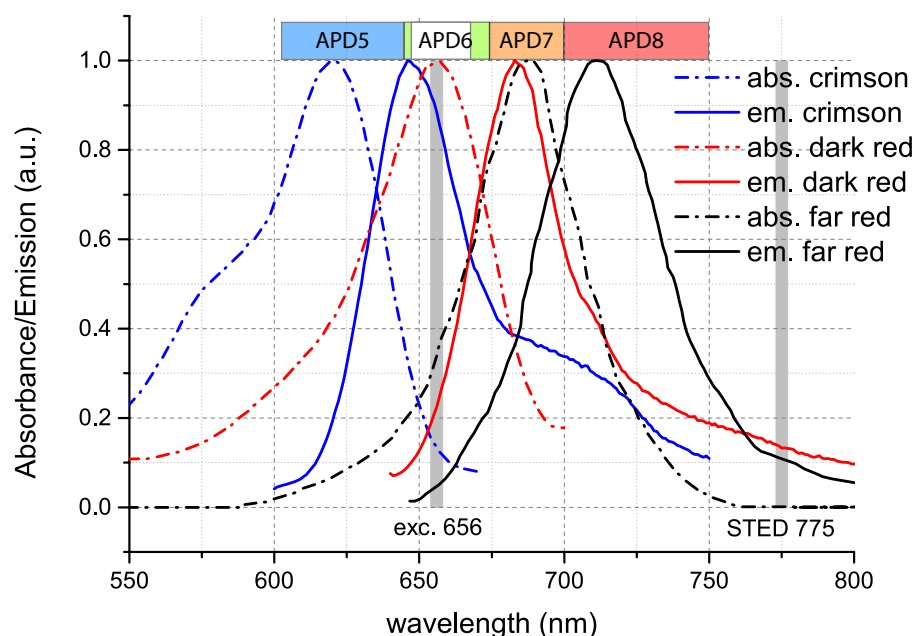


**Figure 5.1:** Normalized absorption and emission spectra of crimson (blue), dark red (red) and far red (black) fluorescent beads. Absorption spectra are represented by the dash-dotted lines whereas emission spectra correspond to the solid lines. Bars at the top represent the four detection windows. blue: APD5, green: APD6, orange: APD7 and red: APD8.

Figure 5.1 shows the normalized absorption and emission spectra of the crimson (blue), dark red (red) and far red (black) beads. The dash-dotted lines represent the absorption and the solid lines the emission spectra. The width and position of the four detection windows correspond to the coloured bar at the top. APD5 is shown in blue, APD6 in green, APD7 in orange and APD8 in red.

Figure 5.1 shows that the beads can be excited with a wide range of wavelengths.

When all three of them had to be excited simultaneously, 656 nm was chosen as excitation wavelength. When only one species was investigated, the excitation wavelength was adapted to the absorption spectrum, i.e. 612 nm for crimson beads.

### 5.1.1 Optical resolution on 24 nm crimson beads

To estimate the resolution that can be achieved with this set-up, 24 nm crimson beads were investigated (labelled 20 nm). They were imaged with an excitation wavelength of 612 nm at 5  $\mu$ W, a STED power of 420 mW in the back focal plane of the objective and time gating. The first nanosecond of the fluorescence was discarded and the gate width was 5 ns for each channel. A more detailed study on the resolution and its dependence on the organic dye and the STED power will be conducted in section 5.2.

From the raw data of the crimson beads, the 23 smallest and brightest beads were selected for analysis. To those beads a Gaussian profile was fit in x and y directions. Fitting occurred via a least squares method. The mean and standard deviation for the 23 beads were calculated. A value of  $43.6 \pm 5.6$  nm and  $36.9 \pm 3.3$  nm was obtained for x and y directions respectively meaning that resolutions below 50 nm were possible with dyes whose spectra were similar to those of the crimson beads.

The resolution could be improved by applying either a higher STED power and/or shifting the STED wavelength to the blue (e.g. 750 nm). The same would be true if another bead species were chosen as sample with an emission spectrum further to the red. Unfortunately, 20 nm far red beads were not available and 20 nm dark red beads were too dim to yield a good fitting result.

### 5.1.2 Data analysis and crosstalk of three bead species

Crimson, dark red and far red fluorescent beads (lifetechnologies, now part of Thermo Fisher Scientific, Waltham, US) were chosen as a first sample for evaluating the data analysis algorithm and testing the separation capability of the set-up. In order to have a good SNR, the size of the crimson, dark red and far red beads were specified to 100 nm, 200 nm and 100 nm respectively. They were mixed prior to adhesion to the coverglass. The excitation wavelength was 656 nm at 5  $\mu$ W, the STED power was 200 mW in the back focal plane and the time gating settings discarded the first nanosecond of the fluorescence with a gate width of 5 ns for each detection channel. Data acquisition was done in two line steps. In the first one, both, the excitation and the STED beams, were switched on (top row in fig. 5.2). The second line step recorded the reexcitation generated by the STED beam alone (bottom row in fig. 5.2).

As can be seen in figure 5.2 the dark red and far red beads predominantly visible in APD7 and APD8 (right and second right column of fig. 5.2), exhibited quite a

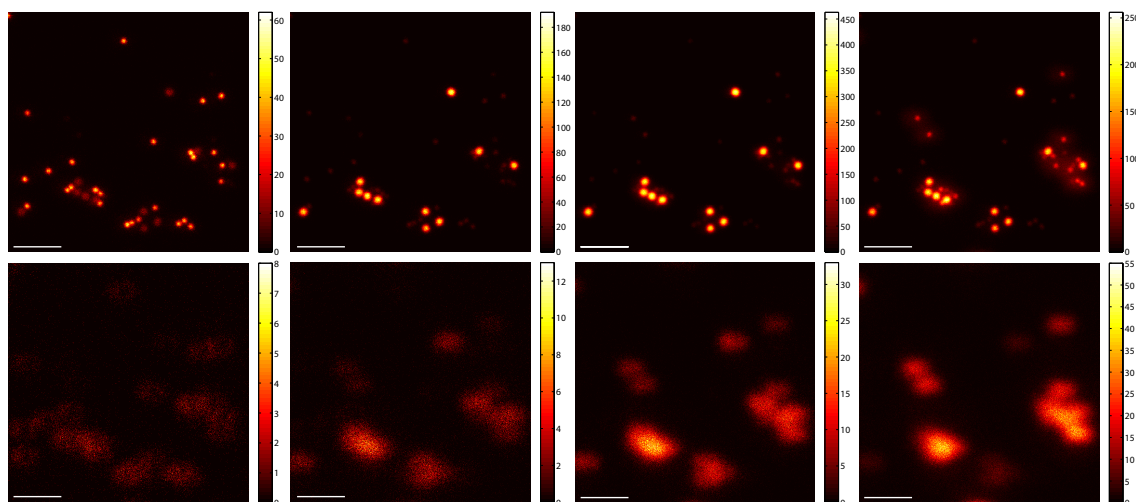


**Figure 5.2:** Raw STED data of a mixture of 100 nm crimson, 200 nm dark red and 100 nm far red beads. The upper row shows the data of the first line step (exc+STED). The bottom row shows the signal of the second line step (STED only). The columns correspond to the time gated data acquired by APD5, 6, 7 and 8 respectively. Imaged area is  $5\ \mu\text{m} \times 5\ \mu\text{m}$ . Scale bars are  $1\ \mu\text{m}$ .

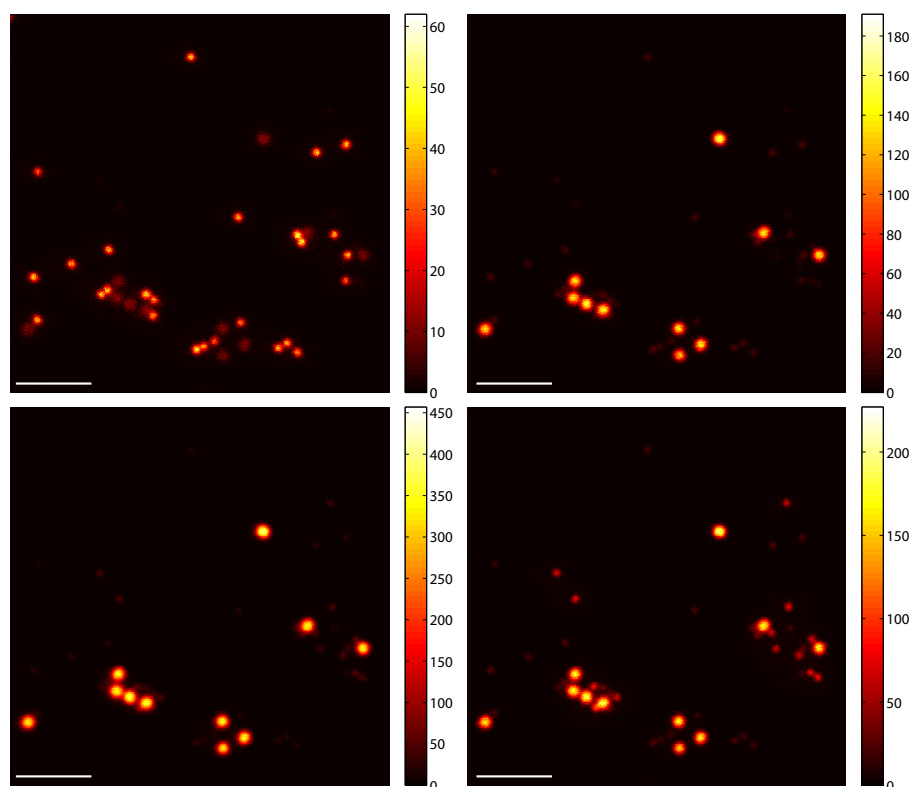


**Figure 5.3:** Resulting data when the reexcitation by the STED beam (bottom row of fig. 5.2) is subtracted from the raw data (top row of fig. 5.2). top left: APD5, top right: APD6, bottom left: APD7, bottom right: APD8. Scale bars are  $1\ \mu\text{m}$ .

strong excitation from the STED beam which resulted in a halo around the beads (see top right image in fig. 5.2). To alleviate this effect, the reexcitation data of the second line step (bottom row of fig. 5.2) was subtracted from the data in the first line step (top row of fig. 5.2). Any negative counts generated by this method were set to zero. This was not ideal but simple and effective. Including the reexcitation data in the unmixing algorithm would be complicated since in this case, the different shapes of the respective PSFs would also have to be taken into account. The result of the subtraction is displayed in figure 5.3. It can be seen that the noisy regions around the dark red and far red beads are less pronounced.

Subsequently, the data depicted in figure 5.3 was analyzed and unmixed with the non-negative matrix factorization (NNMF) algorithm with a manually optimized and fixed transfer matrix  $\mathbf{A}_{me}$ . The results are shown in figure 5.4.

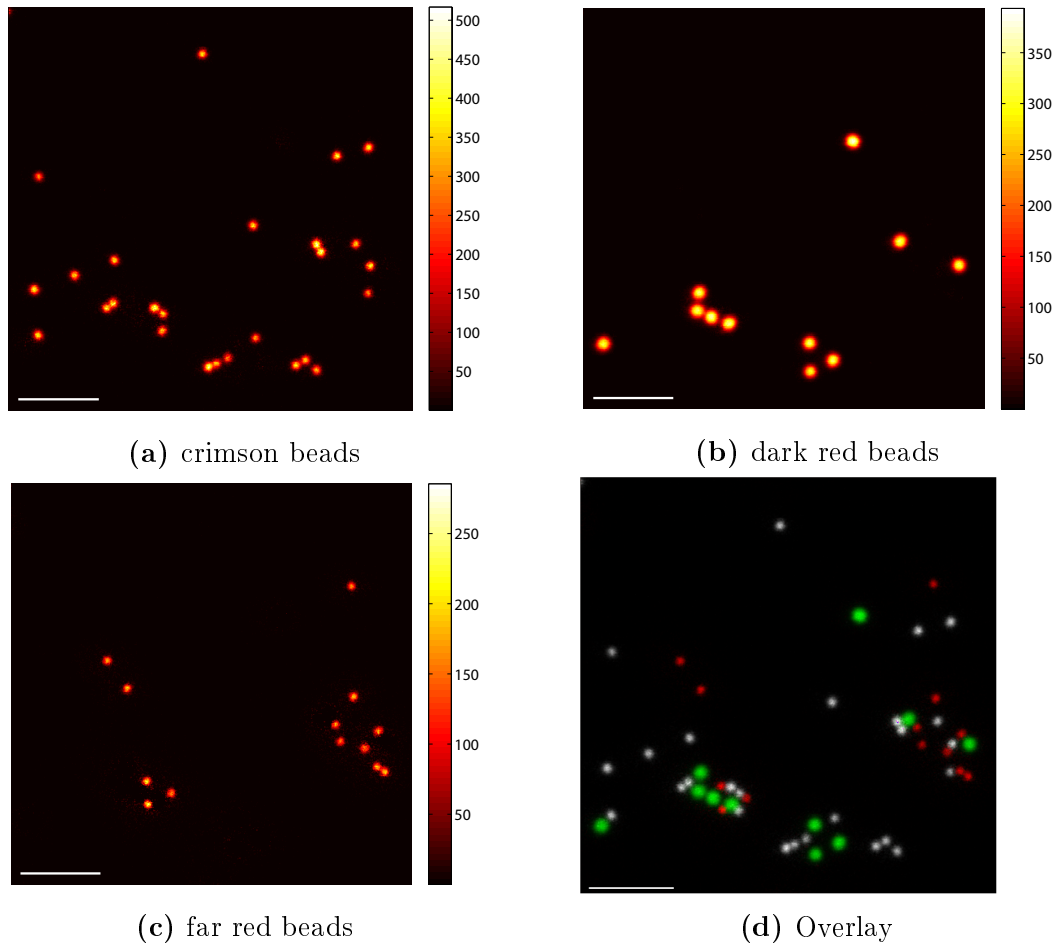


**Figure 5.4:** Unmixed data by NNMF with  $\mathbf{A}_{me}$  of figure 5.3. The sample contained 100 nm crimson beads (top left), 200 nm dark red beads (top right) and 100 nm far red beads (bottom left). The overlay is shown in 5.4d (bottom right). grey: crimson beads, green: dark red beads, red: far red beads. Scale bars are 1  $\mu\text{m}$ .

Figure 5.4 shows excellent separation of the crimson, dark red and far red beads. This becomes even more obvious when the overlay (see fig. 5.4d) is considered. In figure 5.4d the crimson beads are depicted in grey, the dark red beads in green and the far red beads in red.

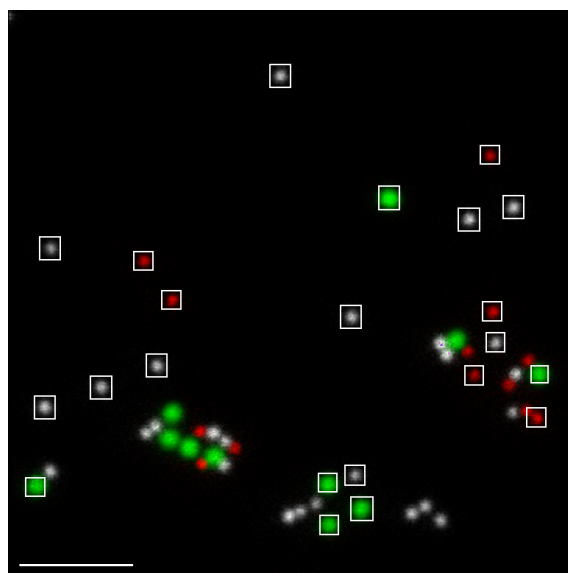


**Figure 5.5:** Overlay of the unmixed data from fig. 5.4. White boxes mark the areas which were used to determine the crosstalk (see fig. 5.6). grey: crimson beads, green: dark red beads, red: far red beads. Scale bar 1  $\mu\text{m}$ .

Furthermore, the overlay was employed to determine the residual crosstalk after analysis. For this the white squares in figure 5.5 were used. They mark the areas used in the calculation of the crosstalk matrix  $CT$  (see eq. (4.2)). The mean over all the squares of one bead species was calculated to give the final crosstalk values. For the dark red and far red beads, 6 beads were used for the averaging whereas 10 beads were averaged for the crimson beads. The final result of the residual crosstalk is shown in figure 5.6.

Figure 5.6 clearly shows the excellent separation of the three bead species. The remaining crosstalk was less than 3 % in every channel. The biggest contribution of 2.5 % came from the far red beads in the dark red channel. This may result from the reexcitation background which might not be fully removed by simple subtraction in the data analysis. Another indication for this was evidenced in the matrix element for the crosstalk of dark red fluorescence in the far red channel. Its value of 0.1 % was much lower than the 2.5 % for far red fluorescence in the dark red channel supporting the hypothesis of residual reexcitation in the data.

Now, the data of the crimson, dark red and far red beads was ideal to verify the

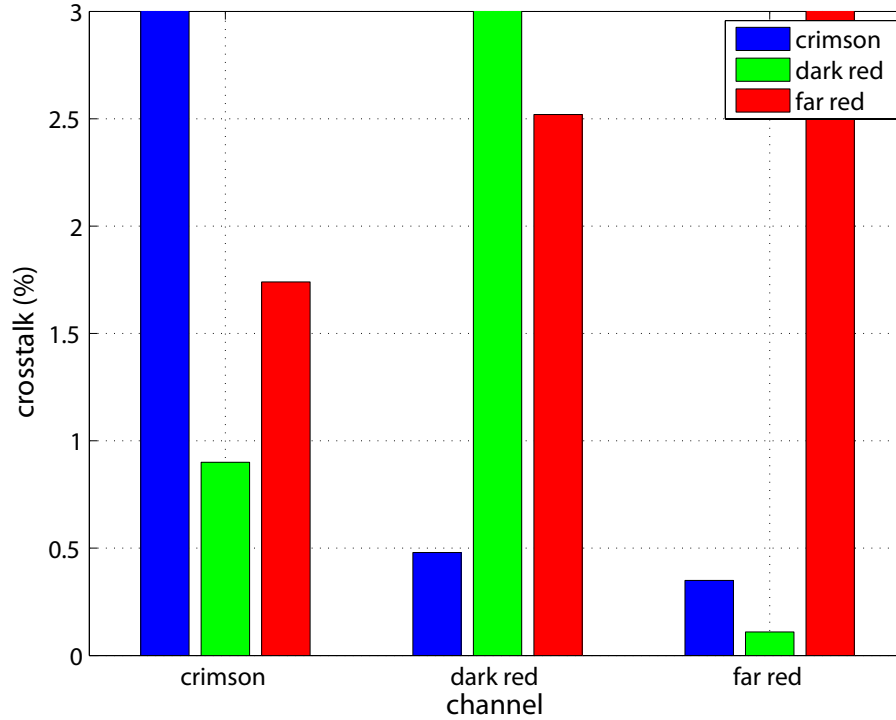


**Figure 5.6:** Residual crosstalk by NNMF with  $\mathbf{A}_{me}$  between crimson (blue), dark red (green) and far red (red) beads calculated in the areas pointed out by figure 5.5. y axis is limited to 3% for better visibility of the small values. Tallest bars amount to 100%.

results from chapter 4. To do so, the data displayed in figure 5.3 was also analyzed by ImageJ with input parameter  $\mathbf{A}_{Gauss}$  and LinUnmix with input parameter  $\mathbf{A}_{me2}$  (see tab. 4.1). The residual crosstalk after unmixing was calculated for each method in the areas pointed out by figure 5.5. Then the measure  $\xi$  was determined for each unmixing result (see section 4.2). The values of  $\xi$  for the different unmixing methods are shown in table 5.2.

**Table 5.2:** Measure  $\xi$  for analysis via NNMF with  $\mathbf{A}_{me}$ , LinUnmix with  $\mathbf{A}_{me2}$  and ImageJ with  $\mathbf{A}_{Gauss}$ . Input parameter  $\mathbf{A}_{me}$  is optimized for NNMF,  $\mathbf{A}_{me2}$  for LinUnmix.  $\mathbf{A}_{Gauss}$  refers to Gaussian initial spectra for ImageJ (see tab. 4.1 for details).

method	input	$\xi$ (a.u.)
NNMF	$\mathbf{A}_{me}$	0.0325
LinUnmix	$\mathbf{A}_{me2}$	0.1016
ImageJ	$\mathbf{A}_{Gauss}$	0.0783

Table 5.2 clearly shows that the best unmixing result was obtained by NNMF

with a fixed and manually optimized transfer matrix  $\mathbf{A}_{\text{me}}$  thereby confirming the results from chapter 4. The entries of the matrices  $\mathbf{A}_{\text{me}}$  and  $\mathbf{A}_{\text{me}2}$  are given below. The first column corresponds to the crimson, the second to the dark red and the third to the far red beads. The rows represent the four detection channels from blue to red.

$$\mathbf{A}_{\text{me}} = \begin{pmatrix} 0.36 & 0.02 & 0.03 \\ 0.16 & 0.21 & 0.09 \\ 0.22 & 0.48 & 0.32 \\ 0.26 & 0.29 & 0.56 \end{pmatrix}, \quad \mathbf{A}_{\text{me}2} = \begin{pmatrix} 0.35 & 0.02 & 0.03 \\ 0.16 & 0.21 & 0.09 \\ 0.23 & 0.48 & 0.39 \\ 0.26 & 0.29 & 0.50 \end{pmatrix}$$

## 5.2 Dependence of the resolution on the dye

With different dyes, different resolutions are obtained at the same STED power since they exhibit different depletion efficiencies. In the case where only one excitation wavelength and a single STED wavelength are used, the only parameter that is still dependent on the dye is the saturation intensity in equation (2.3). Here, the saturation intensities ( $P_{\text{sat}}$ ) of Atto590 (ATTO-TEC GmbH, Siegen, DE), Star635P (Abberior GmbH, Göttingen, DE), Atto655 (ATTO-TEC GmbH, Siegen, DE) and CF680R (Biotium, Inc., Hayward, US) were determined. They were obtained via pump probe measurements (see section 5.2.1) and via STED FCS measurements (see section 5.2.2). The results of the two different methods will be compared and discussed.

In order to assess the values of the saturation intensities, one first needed to ensure that the excitation power used was in the linear regime. This was done by gradually increasing the power of the 612 nm excitation light. It was found that an excitation power of 5  $\mu\text{W}$  was suitable and lay well in the linear regime of all dyes.

### 5.2.1 Estimating $P_{\text{sat}}$ via pump probe measurements

To determine the saturation intensity  $P_{\text{sat}}$ , a pump probe experiment with increasing STED power was performed where the excitation was off centre from the STED doughnut (see fig. 5.7).

In these pump probe measurements, the ratio  $R$  was calculated according to equation (5.1):

$$R = \frac{S_{\text{exc+STED}} - S_{\text{STED}}}{S_{\text{conf}}}, \quad (5.1)$$

where  $S_{\text{exc+STED}}$ ,  $S_{\text{STED}}$ ,  $S_{\text{conf}}$  stand for the sum of the fluorescence signal generated by the excitation and STED beams, the STED beam alone and the excitation beam

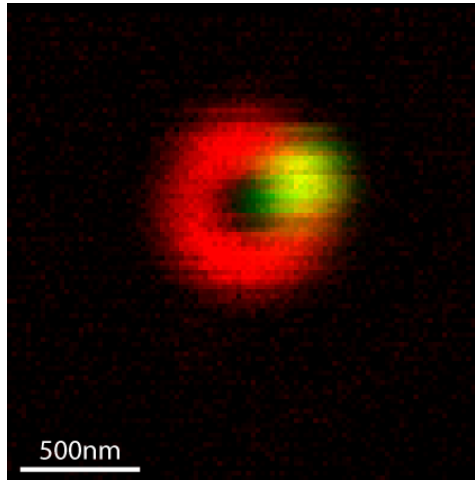


**Figure 5.7:** Intentional misalignment of the excitation (green) and the STED (red) beams for the measurements of saturation intensity estimation via pump probe measurements.

alone, respectively.

All results shown here followed the same measuring scheme. In a dye solution consisting of thiodiethylen glycol (TDE) and concentrations of  $1\ \mu\text{M}$  for Atto590, Star635P and Atto655 and  $5\ \mu\text{M}$  for CF680R an area of  $5\ \mu\text{m} \times 5\ \mu\text{m}$  with  $50\ \text{nm}$  pixel size and  $100\ \mu\text{s}$  dwelltime per pixel was scanned (see appendix B for sample preparation). Each line was recorded three times. In the first run, only the excitation was switched on, in the second run both, excitation and STED, were switched on simultaneously and in the third run only the STED beam was switched on. The pixels in each line steps were summed up. Then, the ratio  $R$  was calculated according to equation (5.1) and plotted against the STED intensity (see fig. 5.8).

Since always four detection channels (APDs 5–8) were recorded, one obtained four decay curves for each dye. To gain a more robust value for the decay constant, the mean of APDs 5–8 were taken for Atto590 and Star635P and the mean of APDs 6–8 for Atto655 and CF680R.

Figure 5.8 shows the decay curves for Atto590 (black), Star635P (blue), Atto655 (green) and CF680R (red) where the fluorescence intensity decreased with the STED power. To the data points (filled shapes), a double exponential decay was fit (solid line) for all dyes except Atto655. For the latter a single exponential decay described the data. Fitting was achieved via a Levenberg-Marquardt method [66]. A double exponential decay ( $y = y_0 + A_1 \exp(-x/t_1) + A_2 \exp(-x/t_2)$ ) was chosen as model because the STED doughnut did not cover the excitation PSF completely (see fig. 5.7). This entailed the superposition of two exponential decays in the data, one slow confocal decay coming from regions where the STED beam did not fully deplete the fluorescence due to the lack of overlap and a second fast decay for the depletion. The decay constant of this fast exponential decay was the saturation intensity of

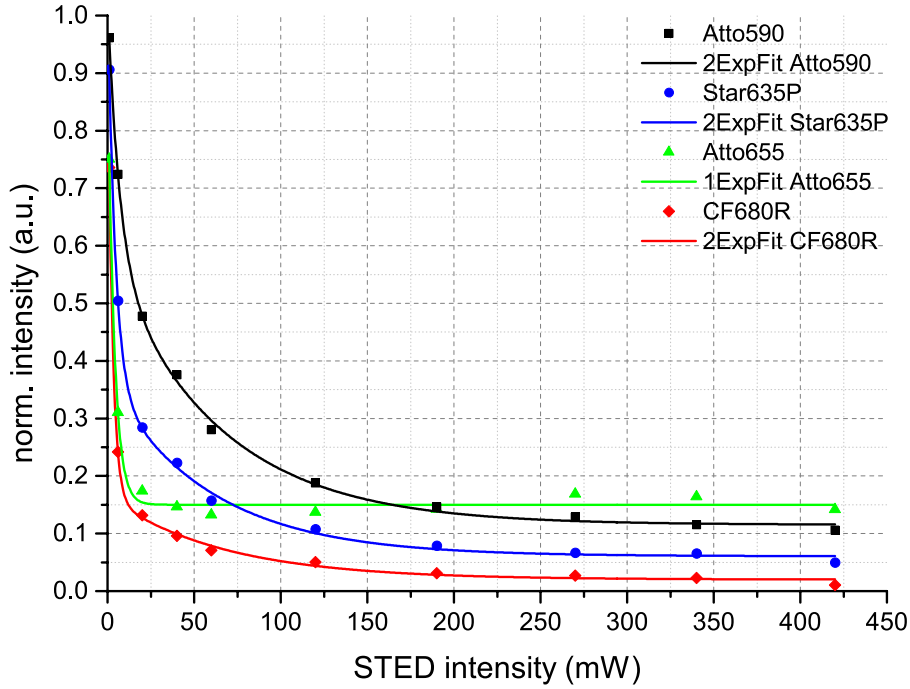


**Figure 5.8:** Data points (shapes) and double exponential fit (lines) of the fluorescence decrease with the STED power for Atto590 (black squares and line), Star635P (blue circles and line), Atto655 (green triangles and line) and CF680R (red diamonds and line).

the dye. The saturation intensities can be found in table 5.3.

**Table 5.3:** Saturation intensities for Atto590, Star635P, Atto655, CF680R by intentional misalignment in pump probe experiments.

dye	$P_{\text{sat}}$ (mW)
Atto590	$6.8 \pm 1.0$
Star635P	$4.3 \pm 0.3$
Atto655	$3.8 \pm 0.3$
CF680R	$2.7 \pm 0.2$

## 5.2.2 Estimating $P_{\text{sat}}$ via FCS measurements

To confirm the estimations of the saturation intensities in table 5.3, STED FCS (fluorescence correlation spectroscopy) measurements were performed. From these measurements, the diffusion time through the focus  $\tau_D$ , which is directly proportional

to the spot size, was calculated and plotted against the STED power (see fig. 5.9). For each STED power at least three measurements were taken and the diffusion time was extracted individually according to [57]. Then, all the diffusion times of the same STED power were averaged and the standard deviation was calculated. In a next step, the diffusion times were divided by the confocal diffusion time and errors were calculated according to the error propagation laws. Note that for Atto655 and CF680R at STED powers greater than 40 mW, excitation by the STED beam itself became non-negligible and disturbed the FCS measurements. Thus, for these dyes, all diffusion times that were greater than or close to the confocal diffusion time and those above 40 mW STED power were discarded. To the averaged data points in a double logarithmic display, a rational function ( $1/(1 + P_{\text{sat}}/P_{\text{STED}})$ ) was fit via a Levenberg-Marquardt method [66]. The results are depicted in figure 5.9 and the according saturation intensities are given in table 5.4.

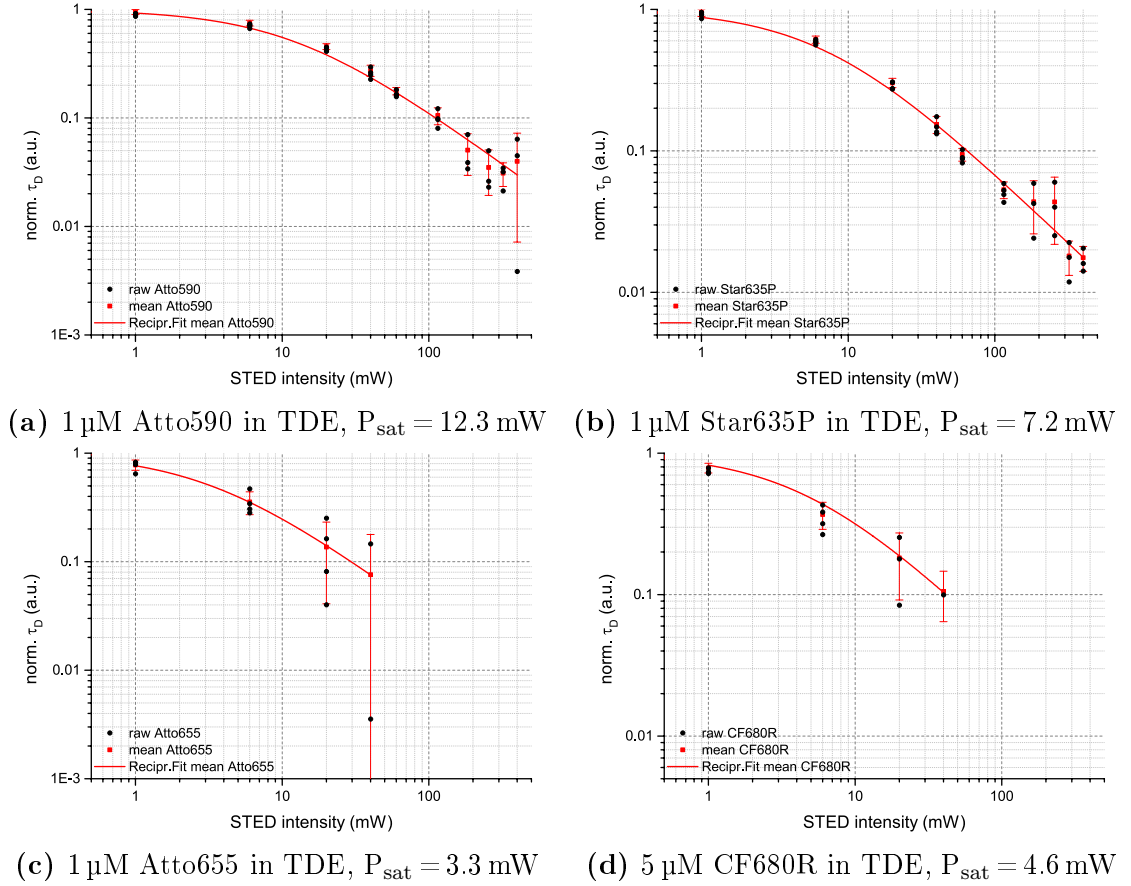


**Figure 5.9:** Normalized diffusion time  $\tau_D$  versus STED intensity in STED FCS measurements for Atto590, Star635P, Atto655 and CF680R. black circles: normalized diffusion times for each measurement, red squares: average of the black circles, error bars represent the standard deviation, red line:  $1/(1 + P_{\text{sat}}/P_{\text{STED}})$  fit.

**Table 5.4:** Saturation intensities for Atto590, Star635P, Atto655, CF680R by FCS measurements.

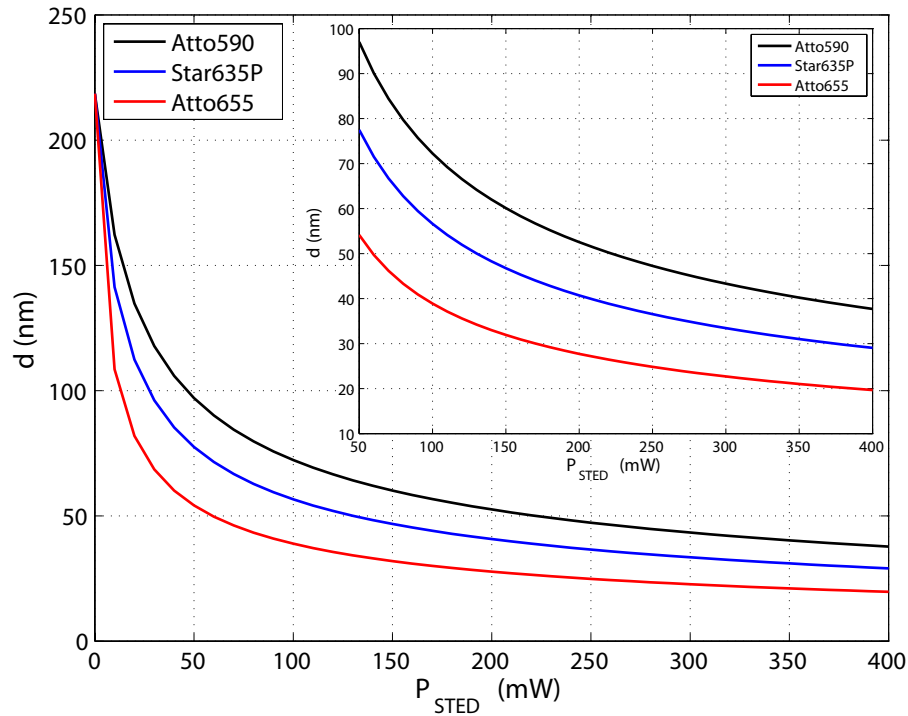
dye	$P_{\text{sat}}$ (mW)
Atto590	$12.27 \pm 0.0151$
Star635P	$7.19 \pm 0.0004$
Atto655	$3.27 \pm 0.0021$
CF680R	$4.63 \pm 0.0214$

Figure 5.9 shows that for Atto590 and Star635P (fig. 5.9a and 5.9b), the variation of individual measurements was quite small, excitation by the STED beam played a minor role and the model  $1/(1 + P_{\text{sat}}/P_{\text{STED}})$  was valid. For Atto655 and CF680R (fig. 5.9c and 5.9d), the spread of individual measurements was quite large even at low STED powers. The inclusion of only four data points in the fit made the obtained value for the saturation intensity only a rough estimate. Furthermore, the saturation intensity for Atto655 was lower than the one for CF680R, which should not be the case since the emission spectrum of CF680R is redder than the one of Atto655 giving a better STED efficiency. This indicated that for CF680R, the influence by the STED beam started to impact FCS measurements at powers as low as 40 mW.

Since only a rough estimate of the saturation intensity was required here to get a notion on the different expected resolution of the various dyes, further measurements were not necessary. However, one should keep in mind that the achievable resolution for CF680R was better than that for Atto655 although it was not reflected in the FCS measurements.

Figure 5.10 is the result of inserting the saturation intensities of table 5.4 in equation (2.3) together with an excitation wavelength of 612 nm and a NA of 1.4. Figure 5.10 shows the achievable resolution depending on the dye. One can see that a STED power of 100 mW would result in a minimal feature size of ca. 75 nm for Atto590, of ca. 55 nm for Star635P and of ca. 40 nm for Atto655. The resolution for CF680R should be smaller than the one for Atto655. In any case, figure 5.10 confirms that for all dyes a resolution well below the diffraction limit could be achieved at rather low STED intensities.

Now, comparing the results from table 5.3 and table 5.4, one notices that the two methods led to different saturation intensities and thus to different predicted resolutions. The saturation intensities obtained by STED FCS measurements were generally higher than the values obtained by pump probe measurements with intentional misalignment of the beams. This was a consequence of the two different beam



**Figure 5.10:** Achievable size  $d$  of objects in dependence of the STED power for Atto590 (black), Star635P (blue) and Atto655 (red) as determined by FCS measurements. The inset is a zoom to STED powers ranging from 50 to 400 mW.

overlap configurations. In the case where the beams were intentionally misaligned, one conducted pump probe measurements, meaning that the most depletion took place where there was also the most excitation. This led to an underestimation of the saturation intensity. In the case of FCS measurements, where there was perfect overlap between the excitation and the STED beams, depletion only took place in the periphery of the Gaussian excitation beam. This led to larger values for the saturation intensity because higher STED powers were needed to reach small focal volumes. Since this situation represents typical STED imaging conditions, the values for the saturation intensity gained by FCS measurements (see tab. 5.4) were more accurate and should be used as upper bounds for the dependence of the resolution on the dye.

### 5.3 Organic dyes feasible for HyperSTED

There exists a large number of organic dyes from various companies that are used in immunofluorescence labeling and imaging. In this work, dyes from Abberior GmbH (Göttingen, DE), ATTO-TEC GmbH (Siegen, DE), Biotium Inc. (Hayward, US) and lifetechnologies (now part of Thermo Fisher Scientific, Waltham, US) were examined. The focus was on organic dyes that could be depleted with a STED

wavelength of 775 nm. This entailed an emission maximum between 600 and 710 nm. In order to assess the feasibility for HyperSTED, single stained fixed-cell samples were investigated with regard to resolution enhancement, maximal applicable STED power and fluorescence distribution in the four spectral channels. Table 5.5 states the names of the tested dyes, their suppliers, their absorption and emission maxima as well as the maximal applicable STED power and a rating. Thereby, + means that the dye worked well, - means that the dye was not feasible for HyperSTED.

Further organic dyes that might be suitable for HyperSTED are given in appendix D (tab. D.1).

**Table 5.5:** Organic dyes feasible for HyperSTED. Abs: absorption maximum (nm), Em: emission maximum (nm), STED: maximum applicable STED power (mW), rating: +: the dye performed well, -: the dye was not feasible.

dye	supplier	Abs (nm)	Em (nm)	P <sub>STED</sub> (mW)	rating
Star580	Abberior	583	604	400	+
Alexa594	lifetechnologies	590	617	400	+
Atto590	ATTO-TEC	594	621	400	+
Atto594	ATTO-TEC	601	627	400	+
Star600	Abberior	604	627	400	+
Atto610	ATTO-TEC	615	634	400	+
Atto620	ATTO-TEC	619	643	400	+
DyLight633	lifetechnologies	623	649	400	+
Atto633	ATTO-TEC	629	657	400	+
Alexa633	lifetechnologies	632	647	200	+
Star635P	Abberior	633	654	400	+
KK114L	[52]	637	660	400	+
Atto647N	ATTO-TEC	644	669	400	+
DyLight650	lifetechnologies	652	672	120	+
Atto655	ATTO-TEC	660	684	200	+
KK1441	[52]	661	679	120	+
Alexa660	lifetechnologies	663	690		-
Alexa680	lifetechnologies	679	702		-
Atto680	ATTO-TEC	680	700		-
CF680R	Biotium	680	701	120	+
Atto700	ATTO-TEC	700	719		-
Alexa700	lifetechnologies	702	723		-

## 5.4 STED imaging with one excitation wavelength

If one wants to excite multiple dyes with only one excitation wavelength, their choice becomes crucial. The absorption cross section need to be high enough that a decent signal-to-noise ratio (SNR) is generated for all dyes at the same intensity of the excitation wavelength. Here, excitation wavelengths of 593 nm, 612 nm or 656 nm at 5  $\mu$ W were found to have the desired effects. All measurements shown here were recorded with either of these wavelength and power. Furthermore, the maximal STED power still yielding a good SNR differed from dye to dye. Depending on the number of dyes and their respective emission spectra, the STED power had to be adjusted at the expense of the resolution enhancement. Especially for the far red dyes, reexcitation by the STED beam played an important role and limited the maximal applicable STED power (see tab. 5.5).

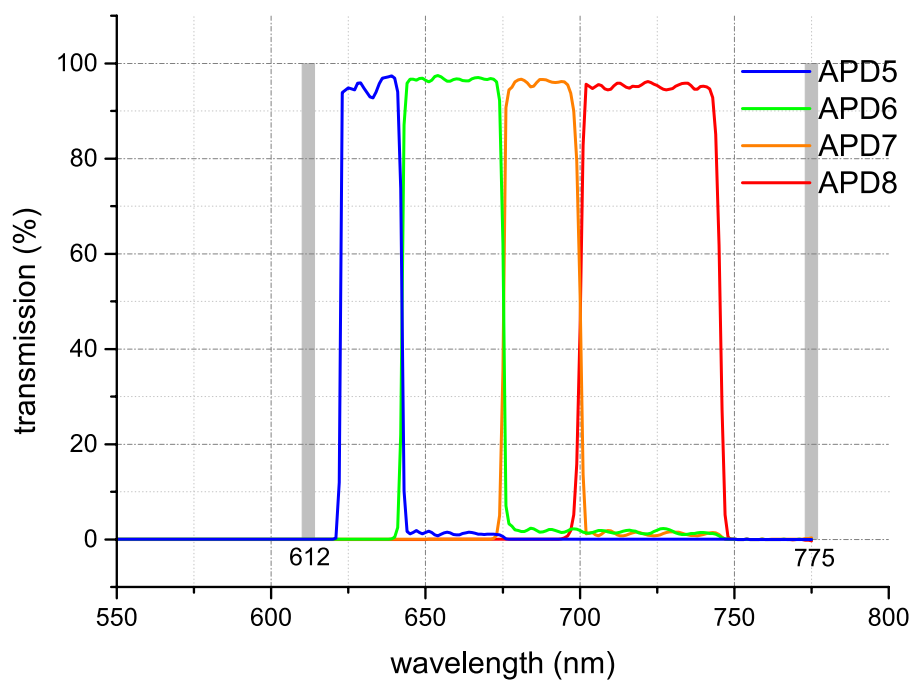
### 5.4.1 Minimal distance of emission maxima

To determine the minimal distance of the emission maxima of two-dye combinations by excitation with a single wavelength, several dyes were chosen from table 5.5 that covered the whole range of the detection windows. Two scenarios were investigated without time gating. One involved the excitation at 612 nm and an additional band pass filter in the detection path. The other consisted of an excitation at 656 nm or 593 nm with an additional notch filter in the detection path to block the excitation light. The latter were chosen as potential excitation wavelength pair for multiplexing experiments. The respective detection configurations are shown in figure 5.11.

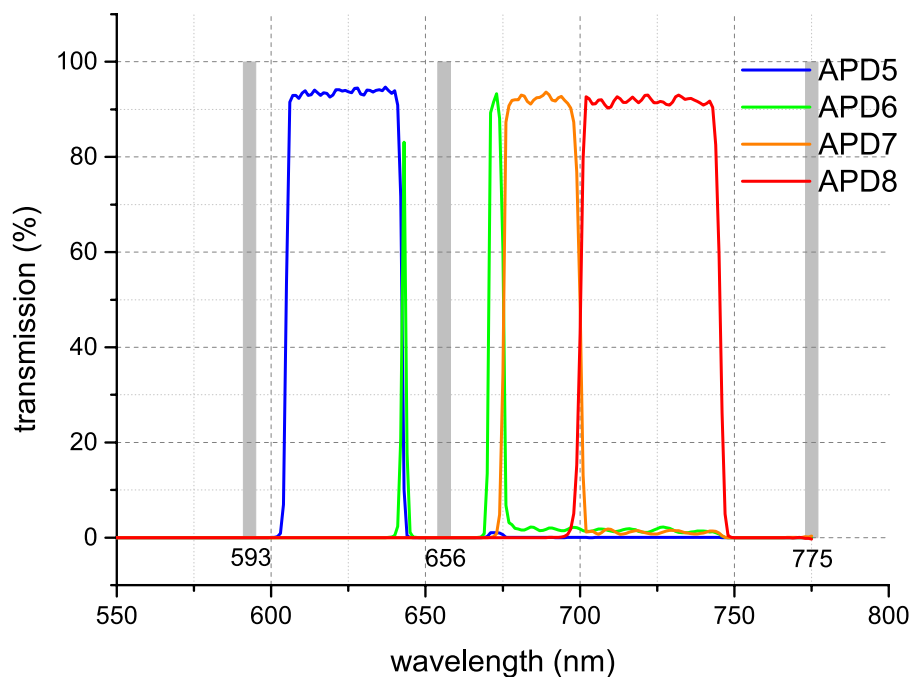
With the detection configurations of figure 5.11, various dye combinations were investigated with regard to their separability. The result is displayed in table 5.6 for excitation with 612 nm or table 5.7 for excitation with either 656 nm or 593 nm.

Table 5.6 and table 5.7 follow the same layout. The diagonal elements state the position of the emission maximum. The numbers inside each cell give the difference of the emission maxima of the two dyes. The colour of the cell indicates the goodness of separation: green means good separation (residual crosstalk < 20 %), red means no distinction was possible (residual crosstalk > 30 %) and orange means the dyes could be separated but with significant residual crosstalk (> 20 %). Anything to the right of a green cell can be considered green even though no measurement was taken.

Examining tables 5.6 and 5.7, one notices that exciting with 612 nm improved the separability in the far red regime compared to excitation at 656 nm. This was due to the notch filter that introduced a relatively broad gap in the detection (see fig. 5.11b). In general, if the emission maxima differed by ca. 22 nm the dyes could be separated when exciting with 612 nm in the blue regime or with 593 nm, 656 nm in the whole range. In case of far red dyes for excitation with 612 nm this number decreased to ca. 15 nm.



(a) detection windows for excitation with 612 nm



(b) detection windows for excitation with 656 nm or 593 nm

**Figure 5.11:** Detection windows for measurements with an excitation wavelength of 612 nm (5.11a) with an additional band pass filter BP650/60 or 656 nm, 593 nm (5.11b) with an additional notch filter NF658 in the detection path. blue: APD5, green: APD6, orange: APD7, red: APD8.



### 5.4.2 Four-colour separation in a fixed-cell sample

To demonstrate the discrimination of four different dyes purely based on distinguishing their emission spectra by splitting the fluorescence signal in four spectral channels, the following dyes were chosen: Atto594, STAR635P, KK1441 and CF680R. Their normalized absorption and emission spectra are shown in figure 5.12. The width and position of the four detection windows are represented by the coloured bar above the absorption and emission spectra. The width of APD5 is shown in blue, APD6 in green, APD7 in orange and APD8 in red.

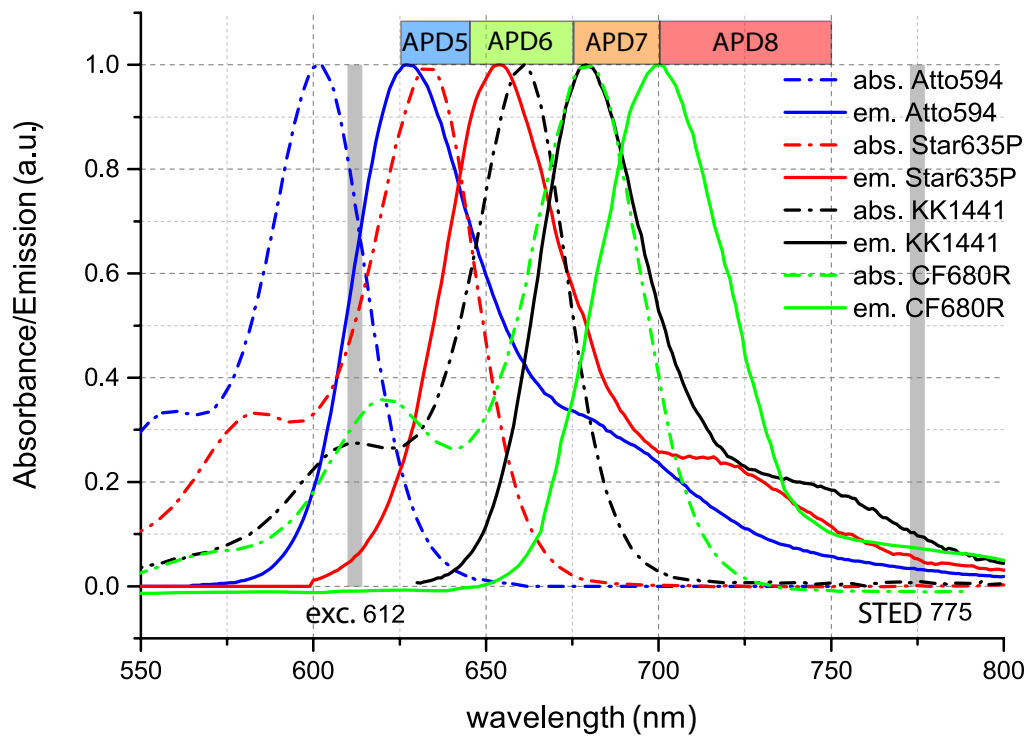


**Figure 5.12:** Absorption and emission spectra as specified by the suppliers for Atto594 (blue), Star635P (red), KK1441 (black) and CF680R (green). Dotted lines represent the absorption spectra and solid lines the emission spectra. Bars at the top correspond to the four detection windows: blue: APD5, green: APD6, orange: APD7 and red: APD8.

Figure 5.12 clearly shows that all dyes exhibited a reasonable absorption cross section for the chosen excitation wavelength of 612 nm. Also, they could be depleted via stimulated emission at a wavelength of 775 nm. All dyes had a decent saturation intensity resulting in a resolution improvement around 80 nm for Atto594, around 60 nm for Star635P and around 40 nm for KK1441 and CF680R (see section 5.2). The CF680R dye limits the applicable STED power to ca. 100 mW in the back aperture of the objective due to its high reexcitation (see fig. 5.13 bottom line).

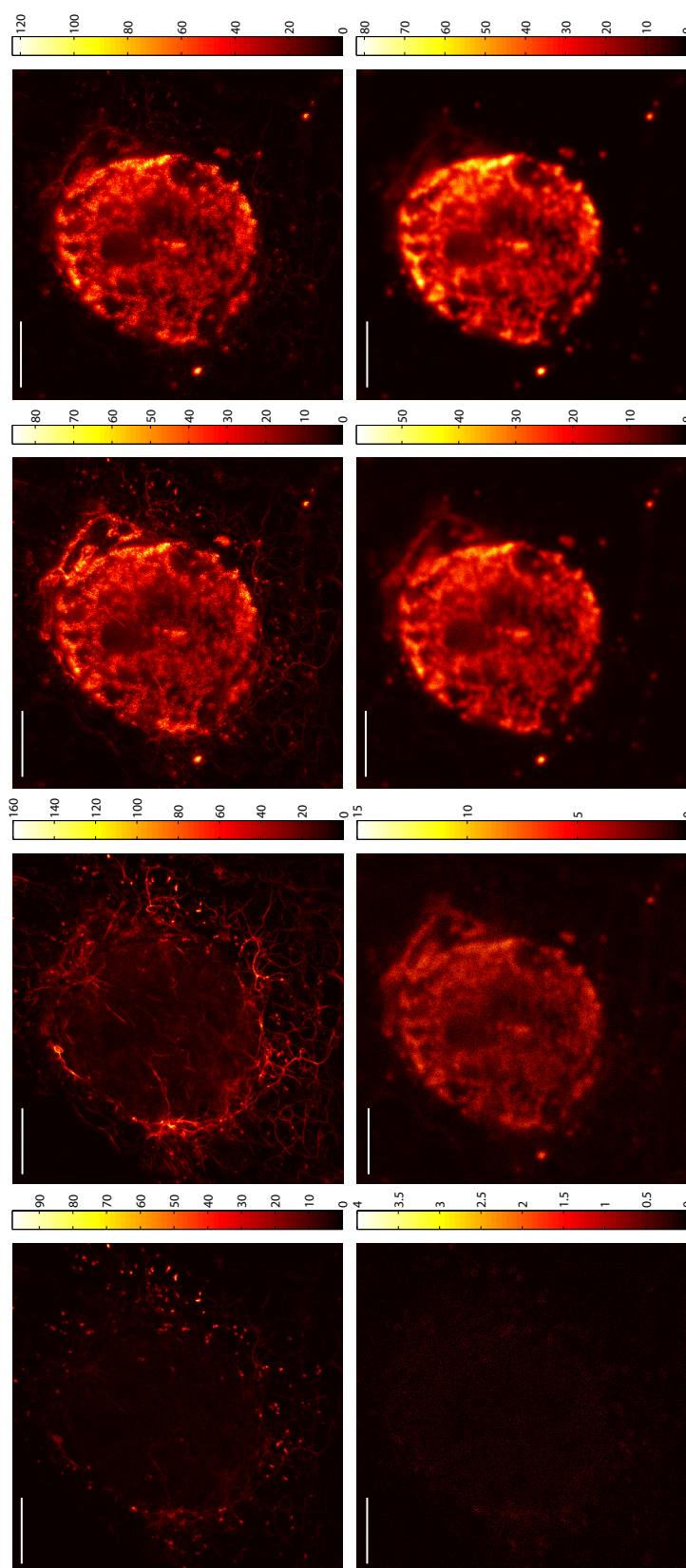


**Figure 5.13:** Raw STED data of a fixed Vero cell where peroxisomes were stained with Atto594, vimentin with Star635P, giantin with KK1441 and nuclear pores with CF680R. The upper row shows the data acquired in a first line step where both the excitation (656 nm, 5 μW) and the STED beam (775 nm, 90 mW) were switched on. The bottom row shows the signal generated by the STED beam alone in a second line step. Both line steps were time gated. The columns correspond to the data acquired by APD5, 6, 7 and 8 respectively. Imaged area is 25 μm × 25 μm. Scale bars are 5 μm.

Figure 5.13 shows the raw data of a quadruple stained fixed Vero cell. Peroxisomes were stained with Atto594, vimentin with Star635P, giantin with KK1441 and nuclear pores with CF680R. The used antibodies are given in appendix A and the staining protocol can be found in appendix B. Data was acquired in two line steps using time gating where the first nanosecond of the fluorescence was discarded and the gate width was 5 ns for each channel and line step. The top row displays the data from the first line step where the excitation of 612 nm at 5  $\mu$ W and the STED beam of 775 nm at 90 mW were switched on. The bottom row shows the data from the second line step where only the STED beam illuminated the sample. This data nicely demonstrated the reexcitation generated by the STED beam.

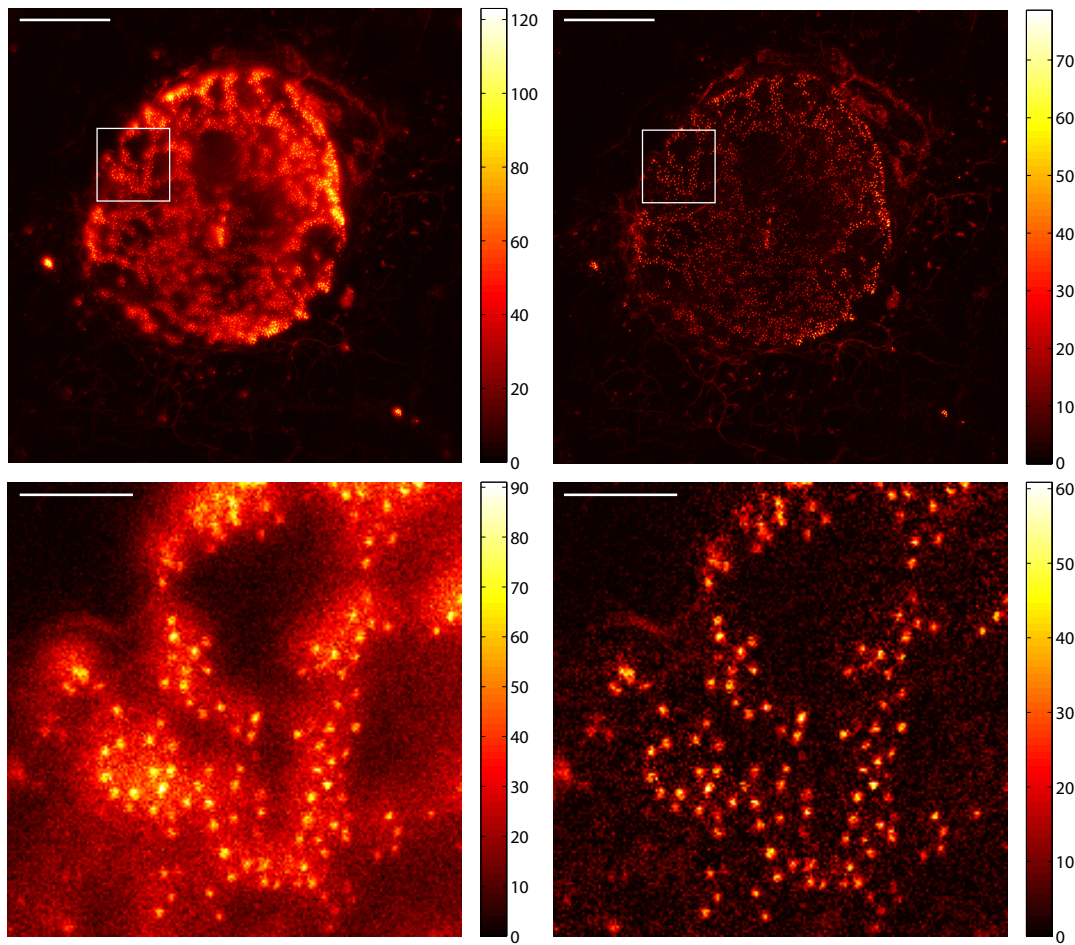
As can be seen from figure 5.13, all four structures were already distinguishable due to their different distribution in the four spectral channels. Atto594 was mainly present in APD5 and 6 (first and second column of fig. 5.13), Star635P mainly resided in APD6 (second column of fig. 5.13), KK1441 mainly fluoresced in APD7 (third column of fig. 5.13) and CF680R mainly appeared in APD7 and 8 (third and fourth column of fig. 5.13).

Before the data was further analyzed, the reexcitation data (bottom row of fig. 5.13), was smoothed with a Gaussian filter of a FWHM of three pixels and subtracted from the actual data (top row of fig. 5.13). Afterwards, all negative counts generated by the subtraction were set to zero. In random areas it was verified that no features disappeared. Furthermore, the maximum negative count amounted to 1 % of the maximum positive count for Atto594, to 2 % for Star635P, to 17 % for KK1441 and to 22 % for CF680R. The result of the subtraction is shown for APD8 in figure 5.14.

From figure 5.14, it can be seen that the data became less noisy, meaning that the features got clearer by subtracting the reexcitation from the STED beam. Albeit this method was straightforward and yielded quite good results it was not perfect. It would be better to not record the reexcitation at all. This could be done with a lock-in amplifier as it was demonstrated in [78]. Or, the reexcitation could be included in the analysis. To do so, the different PSFs would have to be known and taken into account in the NNMF algorithm rendering it much more complicated.

The data with subtracted reexcitation was then analyzed by NNMF explained in section 2.4.2 with a fixed and manually optimized transfer matrix  $\mathbf{A}_{\text{me}}$  (see chapter 4). The entries of the transfer matrix are given below, where the first column corresponds to Atto594, the second to Star635P, the third to KK1441 and the fourth to CF680R. Rows represent the different detection channels from blue to red.

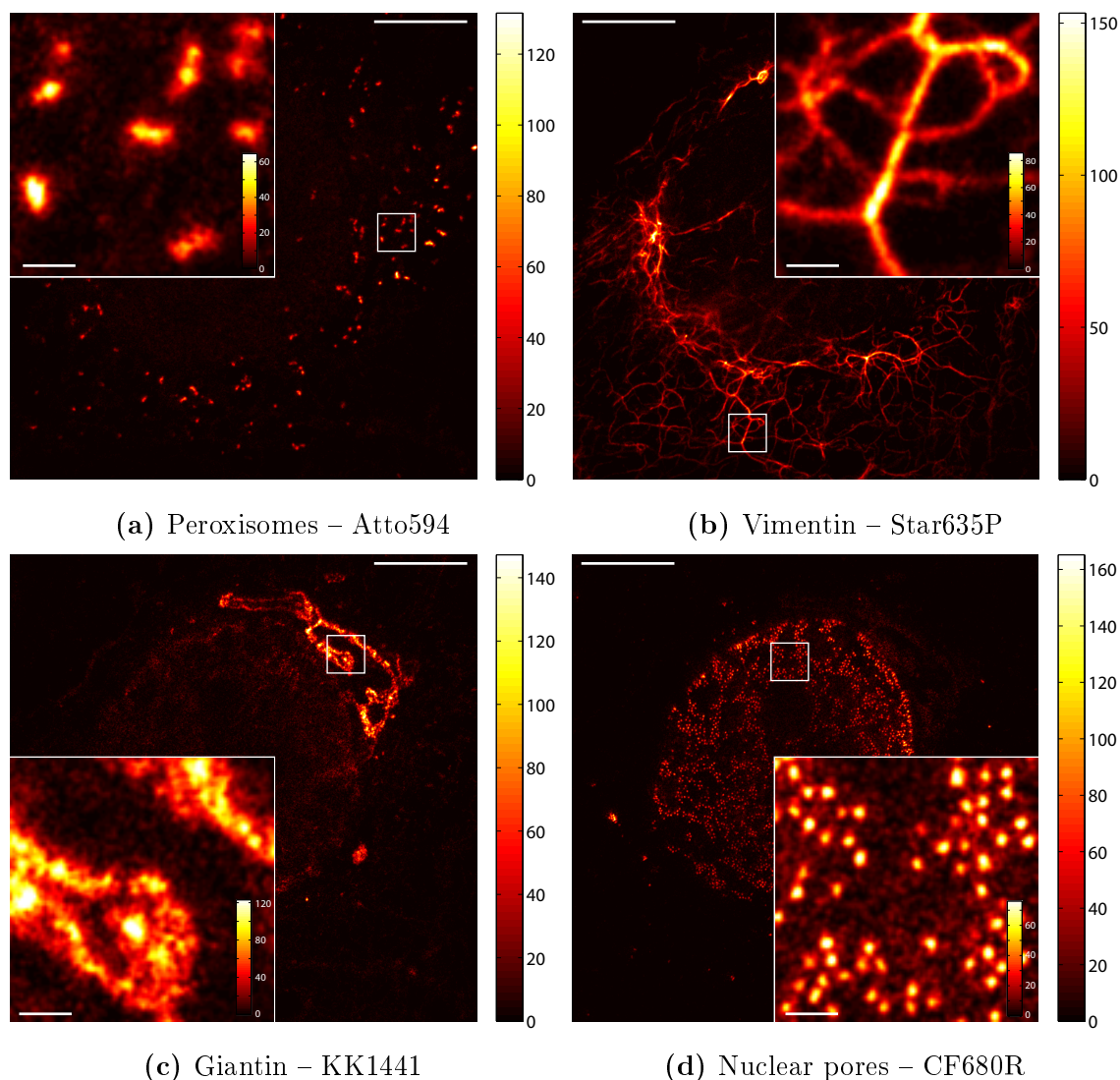
$$\mathbf{A}_{\text{me}} = \begin{pmatrix} 0.33 & 0.14 & 0.01 & 0.01 \\ 0.45 & 0.55 & 0.34 & 0.12 \\ 0.13 & 0.19 & 0.40 & 0.40 \\ 0.09 & 0.12 & 0.25 & 0.47 \end{pmatrix}$$



**Figure 5.14:** Data of APD8 showing the effect of subtracting the reexcitation by the STED beam (bottom right of fig. 5.13) from the raw data (top right of fig. 5.13). top left: raw data, top right: raw data minus the reexcitation, bottom left: zoom to white square of top left, bottom right: zoom to white square of top right. Scale bars are 5  $\mu\text{m}$  for the whole image and 1  $\mu\text{m}$  for the zoom.

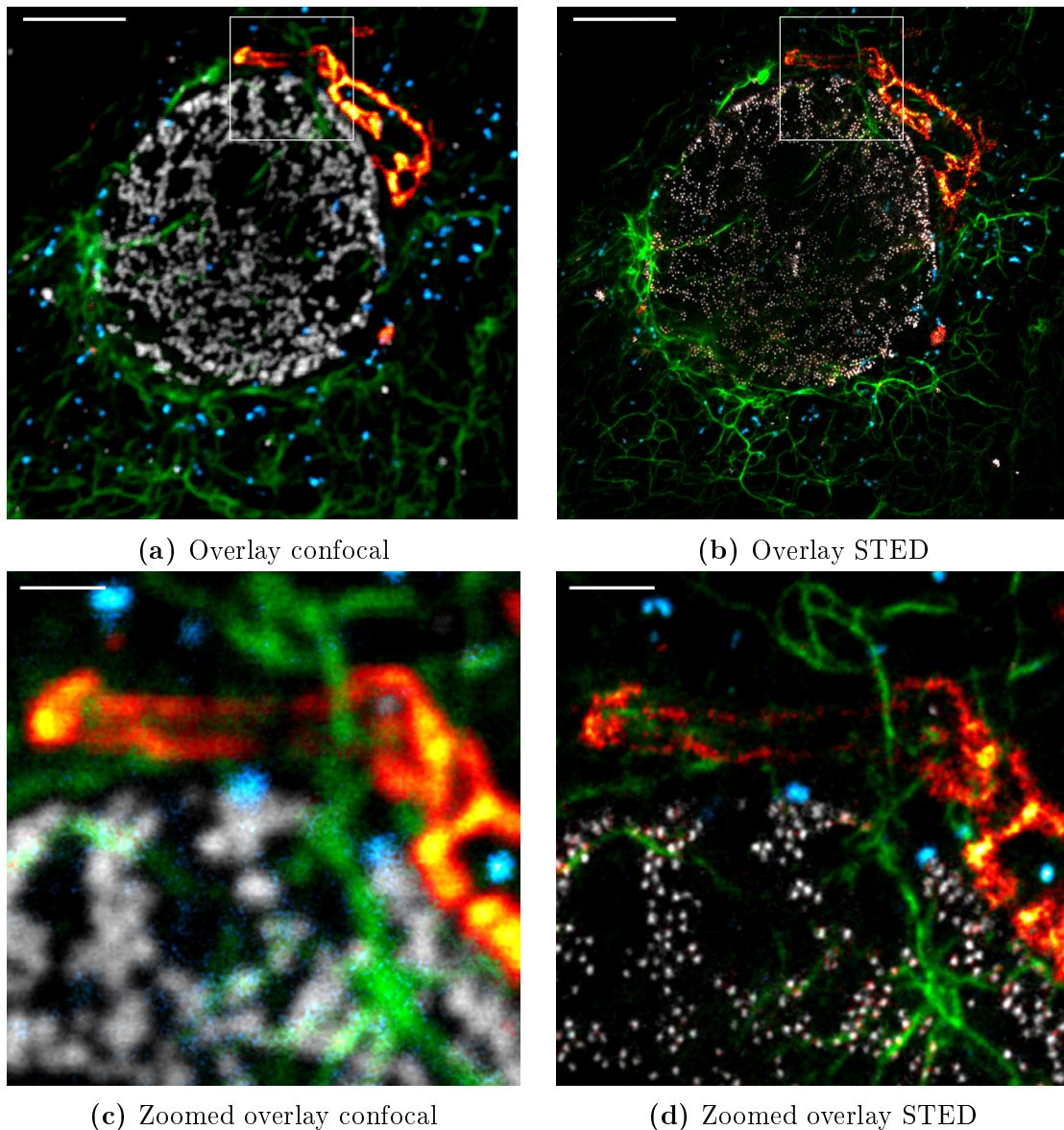
Unmixed data was additionally smoothed with a Gaussian filter of a FWHM of two pixels. The result is shown in figure 5.15.

Figure 5.15 clearly demonstrates a good separation of Atto594, Star635P, KK1441 and CF680R. However, two things attract attention. One is the apparent background from the staining as can be seen in figure 5.15a. The whole region of the nucleus was covered by a uniform haze. The same holds for figure 5.15c which must not be mistaken as crosstalk from the nuclear pores. On top of that, figure 5.15c shows additional background from vimentin and some minor crosstalk from the nuclear pores. Furthermore, figure 5.15d displays some haze throughout the nucleus region and the area where the golgi was situated. Here, it was not clear whether this was actual residual crosstalk or remaining reexcitation from the STED beam that had not been fully removed by subtraction.



**Figure 5.15:** Unmixed and smoothed data of figure 5.14. top left: peroxisomes – Atto594, top right: vimentin – Star635P, bottom left: giantin – KK1441, bottom right: nuclear pores – CF680R. Scale bars are 5  $\mu\text{m}$  for the whole image and 200 nm for the inset.

In any case, the background had to be taken into account. Therefore the colourmaps were adjusted. For each unmixed channel only those pixels were considered that lay above a certain starting value. The latter was determined manually such that most dim structures were still visible and never amounted to more than 10% of the maximum number of counts. For example, in the overlay of figure 5.16 the colourmaps were modified such that the minima and maxima were 4.5 and 165 for Atto594, 1 and 86 for Star635P, 1.4 and 160 for KK1441 and 6.5 and 89 for CF680R in the STED case. All other values of the minima and maxima are given in table 5.8.



**Figure 5.16:** Confocal and STED overlay of the data shown in figure 5.15 with the adjusted colourmaps of table 5.8. top left: confocal overlay, top right: STED overlay, bottom left: zoom to marked region, confocal overlay, bottom right: zoom to marked region, STED overlay. blue: peroxisomes – Atto594, green: vimentin – Star635P, red: giantin – KK1441, grey: nuclear pores – CF680R. Scale bars are  $5\ \mu\text{m}$  for the whole image and  $1\ \mu\text{m}$  for the zoom.

Figure 5.16 represents the final result. It clearly emphasizes the resolution enhancement by STED especially when figure 5.16c and 5.16d are compared. Only in the STED image became the individual nuclear pores (grey) visible. Also the vimentin filaments (green) were revealed in much finer detail in the STED image than in its confocal counterpart. If one takes the results from section 5.2 into account, the resolution for Atto594 should be ca. 80 nm, for Star635P ca. 60 nm, for KK1441 and CF680R ca. 40 nm. Further figure 5.16 demonstrates a good separation of the four

**Table 5.8:** Minima and Maxima of the adjusted colourmaps for fig. 5.16

dye	STED		confocal		STED zoom		confocal zoom	
	min	max	min	max	min	max	min	max
Atto594	4.5	165	5.5	69	5	53	3.3	32
Star635P	1	86	8	121	3	65	4	64
KK1441	1.4	160	25	285	5.5	176	15	366
CF680R	6.5	89	18	193	10	102	11	187

dyes. Note that the individual unmixed images of the zoomed area can be found in appendix E.

Although it was difficult to assess the remaining crosstalk after analysis in a sample with high colocalization of the individual structures, an attempt was made. First, a threshold  $\text{bg}(k)$  for each unmixed image was set in such a way that only the bright pixels  $\tilde{x}_{kj}$  of every colour  $x_{kj}$  remain. The values of  $\text{bg}(k)$  are 10, 10, 18 and 20 for Atto594, Star635P, KK1441 and CF680R respectively. Then those pixels  $m$  were determined where only one of the four dyes was present. The counts in these pixels were then summed up and divided by the sum of the counts of those pixels for the investigated dye giving the crosstalk matrix elements  $ct_{ki}$  (see eq. (5.4)).

$$\tilde{x}_{kj} = x_{kj} \geq \text{bg}(k), \quad \text{bg}(k) = [10, 10, 18, 20], \quad (5.2)$$

$$m = \tilde{x}_{kj} \wedge \neg(\tilde{x}_{rj} \vee \tilde{x}_{sj} \vee \tilde{x}_{tj}), \quad k \neq r \neq s \neq t, \quad (5.3)$$

$$ct_{ki} = \frac{\sum_j x_{ij}(m)}{\sum_j x_{kj}(m)}, \quad (5.4)$$

where  $k$  is the index for the dye,  $j$  for the pixel and  $i$  for the channel.

The values of  $CT$  can be learned from figure 5.17. The latter states a good separation although its values were generally higher than those obtained for the unmixing of fluorescent beads (see fig. 5.6) or the ones obtained by simulations (see section 4.4.3). Therefore the values in figure 5.17 represent an upper limit. Where the residual crosstalk was coming from, whether it was actual crosstalk, crosstalk due to the staining protocol, a background issue or due to the brightness differences of the different structures could not be determined.

Additional unmixed images of three colours in a fixed-cell sample can be found in appendix E.

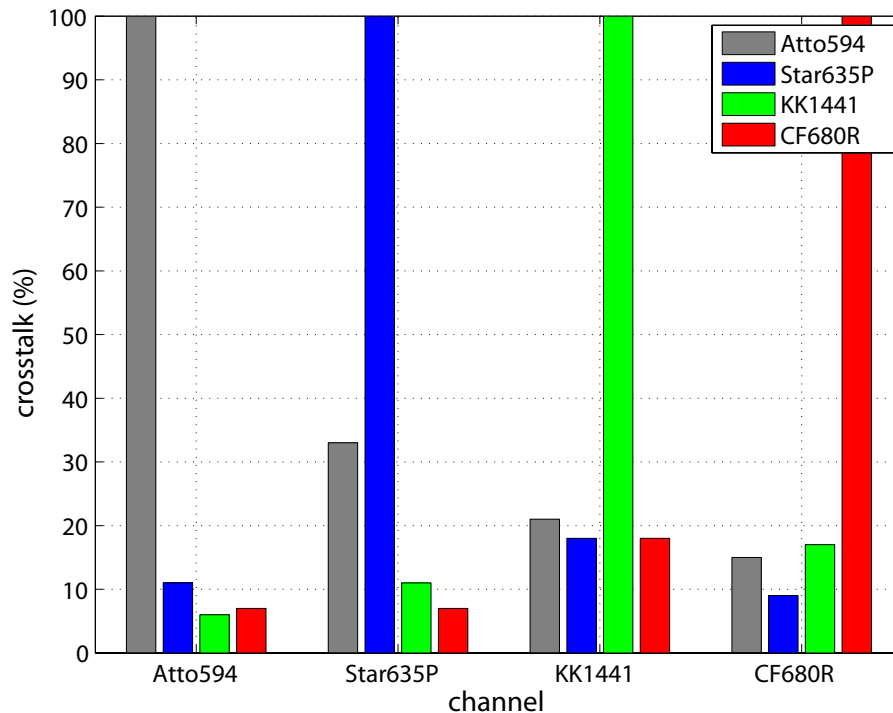


**Figure 5.17:** Remaining crosstalk in the STED image after unmixing for Atto594 (grey), Star635P (blue), KK1441 (green) and CF680R (red) in the fixed-cell sample of figure 5.16.

## 5.5 STED imaging with two excitation wavelengths

As described in chapter 4, adding a second excitation wavelength should decrease the residual crosstalk after analysis. To verify the simulations with experimental data, a double stained fixed-cell sample with Atto590 and KK114L was investigated. This was not the same dye combination as simulated in chapter 4 (Atto594/Atto647N), but the emission spectra are similar and also the difference of the emission maxima is comparable (see tab. 5.5). The reason for the change of dyes was purely practical, the sample was available.

### 5.5.1 Multiplexing a two-colour sample

A double stained fixed-cell sample with Atto590/KK114L was imaged with an excitation of 656 nm at 5  $\mu$ W in a first line step and with an excitation of 593 nm at 5  $\mu$ W in a second line step. The STED power was 90 mW in the back focal plane of the objective, the pixel dwell time 10  $\mu$ s, the pixel size 20 nm and the scanned area 10  $\mu$ m  $\times$  10  $\mu$ m. Every line was scanned 6 times with each wavelength and the counts were added up. No time gating was used. The raw data is shown in figure 5.18.

Figure 5.18 already shows good separation of Atto590 and KK114L, especially if

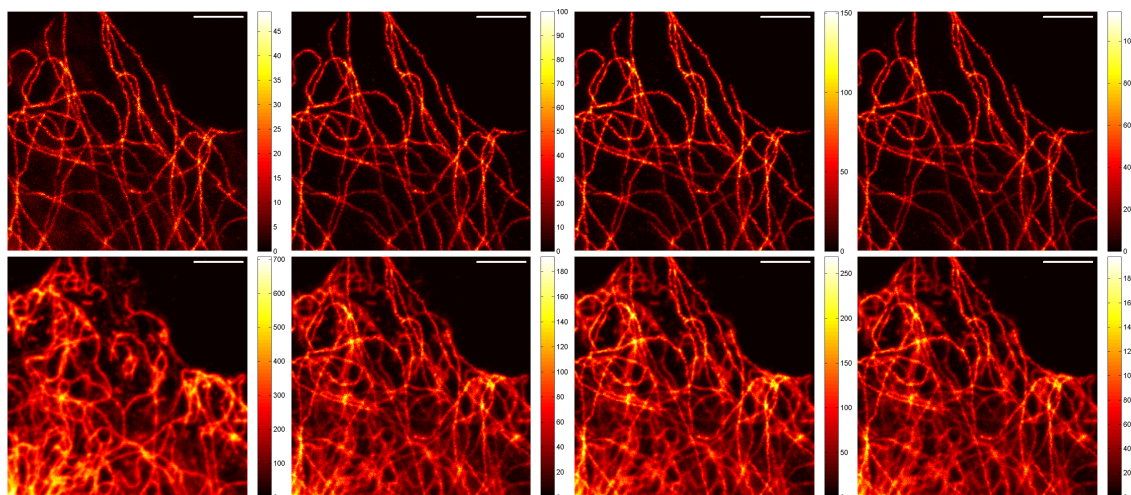


**Figure 5.18:** Raw STED data of a fixed Vero cell stained with Atto590 (vimentin) and KK114L (tubulin). The top row is the first line step excited with 656 nm at  $5 \mu\text{W}$  and the bottom row is the second line step excited with 593 nm at  $5 \mu\text{W}$ . STED power was 90 mW. Columns correspond to the four detection channels. Left: APD5, second left: APD6, second right: APD7 and right: APD8. Scanned area is  $10 \mu\text{m} \times 10 \mu\text{m}$ . Scale bars are  $2 \mu\text{m}$ .

one considers APD7 for 656 nm (second right of top row) and APD5 for 593 nm (left of bottom row). Moreover, one can see that Atto590 did not get excited by 656 nm and when excited with 593 nm, KK114L dominated the signal in APD6–8.

Next, the data was analyzed via NNMF and according to section 4.5 no a priori information should be needed for a good separation. Figure 5.19 shows the unmixing result after analysis with NNMF and  $\mathbf{A}_{\text{opt}}$  as input parameters and smoothing with a Gaussian filter of a FWHM of two pixels. Note that  $\mathbf{A}_{\text{opt}}$  was adapted during analysis and that it was initialized with the values obtained from single stained samples ( $\mathbf{A}_{\text{exp}}$ ). Clearly, there was almost perfect separation between Atto590 and KK114L in figure 5.19.

Figure 5.19 proves the simulations of section 4.5 right. Particularly, figure 5.19c that shows the line profile along the white dotted line of figures 5.19a and 5.19b demonstrates that the profiles of Atto590 (red) and KK114L (green) were very well distinct. Hence, an almost perfect separation result was obtained without the need of manually adjusting any input parameter.

In a next step, the resolution enhancement was examined. Therefore, the same sample was imaged with a higher STED power of 240 mW in the back focal plane of the objective. All other imaging parameters were kept constant. The raw data for these imaging conditions is shown in figure 5.20.

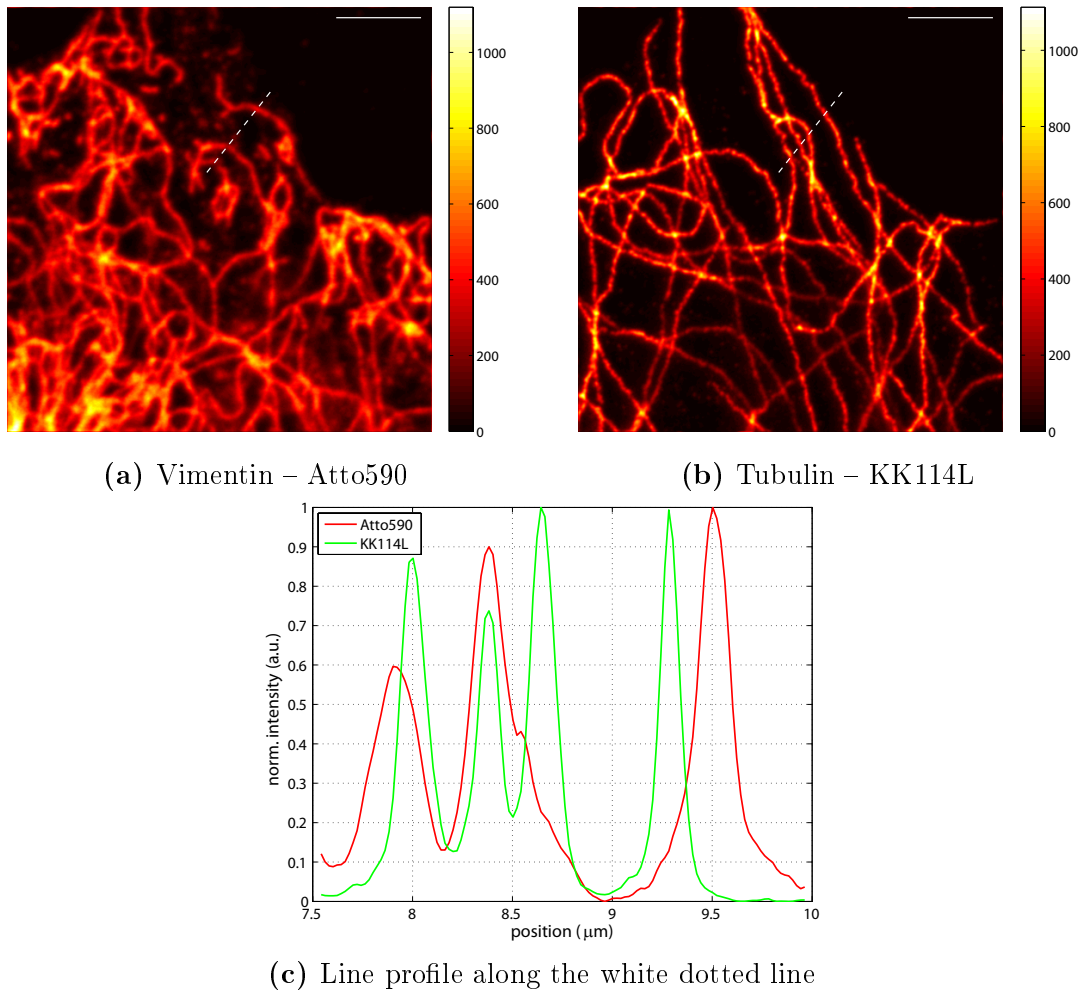
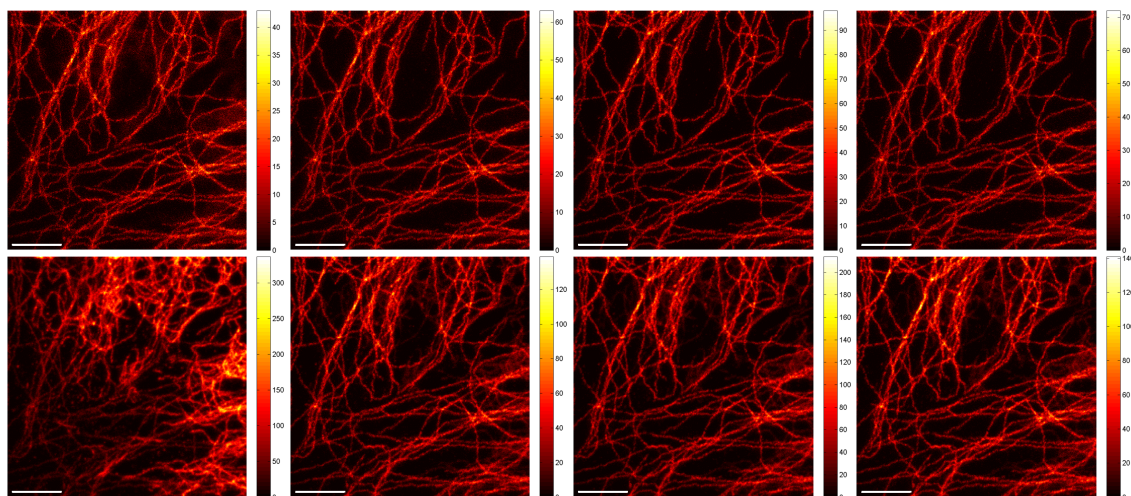


**Figure 5.19:** Unmixed data of vimentin stained with Atto590 (top left) and tubulin stained with KK114L (top right) of a fixed Vero cell (raw data in fig. 5.18, 90 mW STED power). Analysis was done with NNMF and  $\mathbf{A}_{\text{opt}}$ . Figure 5.19c shows the line profile along the white dotted line of Atto590 (fig. 5.19a) (red) and KK114L (fig. 5.19b) (green). Field of view is  $10\ \mu\text{m} \times 10\ \mu\text{m}$ . Scale bars are  $2\ \mu\text{m}$ .

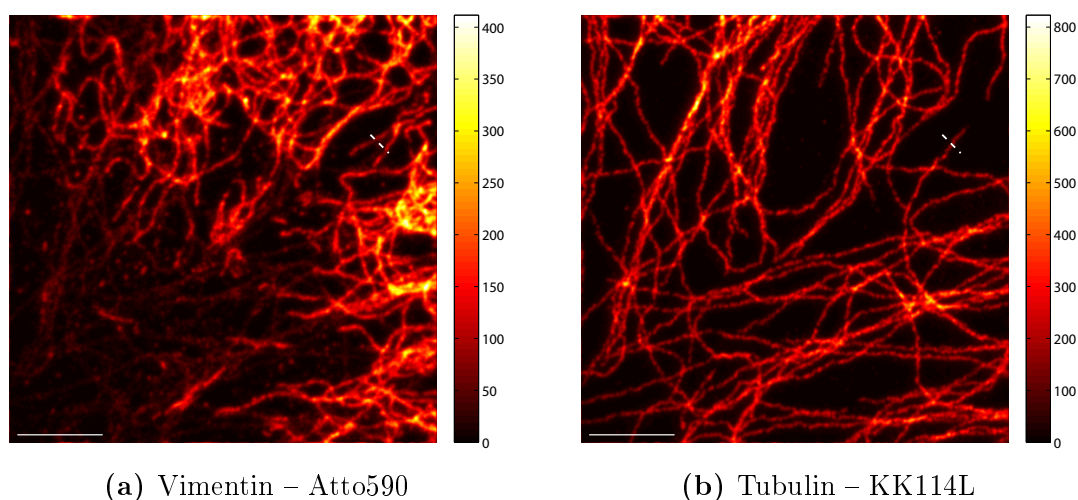
The data of figure 5.20 was then analyzed with NNMF and input parameter  $\mathbf{A}_{\text{opt}}$ . The unmixing result was smoothed with a Gaussian filter of a FWHM of two pixels and is shown in figure 5.21.

The result of figure 5.21 was unexpected since there was no perfect separation of Atto590 and KK114L. One can clearly see that there was some residual crosstalk from KK114L in the Atto590 channel (see fig. 5.21a) whereas the unmixed channel of KK114L did not have a contribution from Atto590. This was in dire contrast to figure 5.19 where the two dyes were almost perfectly separated.

Deviations between high and low STED powers could also be found in the raw data.

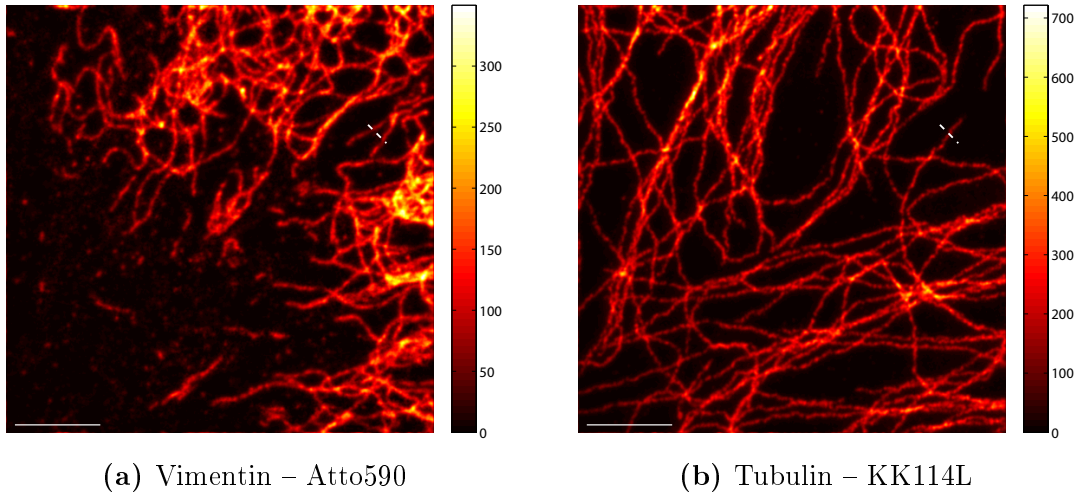


**Figure 5.20:** Raw STED data of a fixed Vero cell stained with Atto590 (vimentin) and KK114L (tubulin). The top row is the first line step excited with 656 nm at  $5 \mu\text{W}$  and the bottom row is the second line step with 593 nm at  $5 \mu\text{W}$ . STED power was 240 mW. Columns correspond to the four detection channels. Left: APD5, second left: APD6, second right: APD7 and right: APD8. Scanned area is  $10 \mu\text{m} \times 10 \mu\text{m}$ . Scale bars are  $2 \mu\text{m}$ .



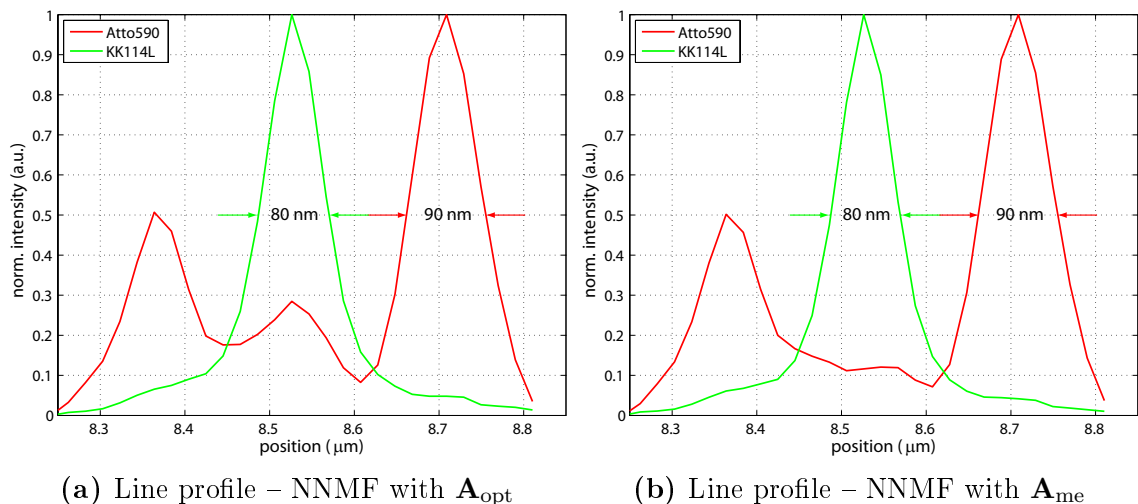
**Figure 5.21:** Unmixed data of vimentin stained with Atto590 (left) and tubulin stained with KK114L (right) of a fixed Vero cell (raw data in fig. 5.20, 240 mW STED power). Analysis was done with NNMF and  $\mathbf{A}_{\text{opt}}$ . Field of view is  $10 \mu\text{m} \times 10 \mu\text{m}$ . Scale bars are  $2 \mu\text{m}$ .

Figure 5.20 is similar to figure 5.18. Atto590 did not get excited at 656 nm (top row) and the details were finer. But the data with the 593 nm excitation wavelength was different. In figure 5.20 there was a stronger contribution from KK114L in APD5 (left of bottom row) as opposed to figure 5.18 where KK114L was negligible in APD5 when excited with 593 nm (left of bottom row). This seemed to give rise to the residual crosstalk after unmixing that is noticeable in figure 5.21.



**Figure 5.22:** Unmixed data of vimentin stained with Atto590 (left) and tubulin stained with KK114L (right) of a fixed Vero cell (raw data in fig. 5.20, 240 mW STED power). Analysis was done with NNMF and  $\mathbf{A}_{me}$ . Field of view is  $10\ \mu\text{m} \times 10\ \mu\text{m}$ . Scale bars are  $2\ \mu\text{m}$ .

But if the data of figure 5.20 was analyzed with NNMF and input parameter  $\mathbf{A}_{me}$ , one could still obtain a good unmixing result (see fig. 5.22 and fig. 5.23b).  $\mathbf{A}_{me}$  was thereby manually tuned by pushing it to a stronger overlap of the dyes for KK114L and kept fixed during the analysis.



**Figure 5.23:** Line profiles along the white dotted lines in figure 5.21 for analysis with NNMF and  $\mathbf{A}_{opt}$  (left) and figure 5.22 for analysis with NNMF and  $\mathbf{A}_{me}$  (right) for Atto590 (red) and KK114L (green). The respective FWHMs are given by the black numbers between the red arrows for Atto590 and the green arrows for KK114L.

Comparing figures 5.23a and 5.23b which show the line profiles along the white dotted lines in figures 5.21 and 5.22, clearly reveals that the undesired crosstalk from KK114L (green) in the Atto590 (red) channel could be removed by manually adjusting the transfer matrix. However, when doing so, the advantage of giving the algorithm no a priori information was lost. In this case, exciting with one excitation wavelength was already sufficient to yield good separation (see chapter 4 and section 5.4).

Note that the given FWHMs in figure 5.23 were the result of a convolution of the object with the resulting PSF of the excitation and STED beams and the smoothing PSF. Therefore they appear rather large and should not be confused with the resolution capability of the microscope. The latter was determined in dependence of the dye and the applied STED power in section 5.2 and should be around 50 nm for Atto590 and 40 nm for KK114L.

The entries of the matrices  $\mathbf{A}_{\text{exp}}$ ,  $\mathbf{A}_{\text{opt}}^{90}$ ,  $\mathbf{A}_{\text{opt}}^{240}$  and  $\mathbf{A}_{\text{me}}$  are given below. The first column corresponds to Atto590 and the second to KK114L. The rows represent the four detection channels from blue to red.

$$\mathbf{A}_{\text{exp}} = \begin{pmatrix} 0.67 & 0.16 \\ 0.10 & 0.22 \\ 0.14 & 0.35 \\ 0.09 & 0.27 \end{pmatrix}, \quad \mathbf{A}_{\text{opt}}^{90} = \begin{pmatrix} 0.65 & 0.11 \\ 0.10 & 0.24 \\ 0.15 & 0.39 \\ 0.10 & 0.26 \end{pmatrix},$$

$$\mathbf{A}_{\text{opt}}^{240} = \begin{pmatrix} 0.72 & 0.15 \\ 0.08 & 0.23 \\ 0.12 & 0.35 \\ 0.08 & 0.27 \end{pmatrix}, \quad \mathbf{A}_{\text{me}} = \begin{pmatrix} 0.67 & 0.27 \\ 0.10 & 0.20 \\ 0.14 & 0.32 \\ 0.09 & 0.21 \end{pmatrix},$$

### 5.5.2 Different emission spectra when multiplexing

As described in section 5.5.1 the applied STED power impacted the unmixing result by NNMF. This could be attributed to spectral changes of KK114L during STED imaging. To make these changes visible, a dye solution and a single stained fixed-cell sample of KK114L were investigated. They were multiplexed with 656 nm and 593 nm at 5  $\mu\text{W}$  without time gating. The scanned area was 10  $\mu\text{m} \times 10 \mu\text{m}$  for the fixed-cell sample or 5  $\mu\text{m} \times 5 \mu\text{m}$  for the dye solution. The pixel dwell time was 10  $\mu\text{s}$  and the pixel size 20 nm. For each mode (confocal, 90 mW STED power or 240 mW STED power), always 15 frames of the same area were taken. For each frame, the percentage distribution of the dye in the different detection channels was calculated. This was done by summing all the counts of all pixels in one channel and dividing it by the sum of all counts of all pixels in all channels.

$$r_i = \frac{\sum_j \text{counts}_{ij}}{\sum_{ij} \text{counts}_{ij}}, \quad (5.5)$$

where  $i$  is the index for the channel,  $j$  for the pixels and  $r_i$  the percentage distribution in channel  $i$ .

In the following figures the  $r_i$  will be displayed as solid lines (black: APD5, blue: APD6, green: APD7, red: APD8) together with an overall bleaching curve. The latter represents the sum of all counts in all detection channels normalized to the brightest frame and will be displayed as black dashed line.

### KK114L dye solution

As expected, the percentage distributions  $r_i$  per frame stayed constant such that the mean and standard deviation over all frames were taken as a more robust value of the percentage distribution in a specific channel. Both, the mean and the standard deviation, are given in table 5.9 for each APD and for each imaging mode (confocal, low STED power of 90 mW, high STED power of 240 mW).

**Table 5.9:** Value and standard deviation in % of the percentage distribution  $r_i$  in the different detection channels (APD5–8) for multiplexing with 656 nm and 593 nm for confocal imaging (confocal) and STED imaging at low STED power (STED 90 mW) and high STED power (STED 240 mW).

mode	$\lambda_{exc}$ (nm)	APD5 (%)	APD6 (%)	APD7 (%)	APD8 (%)
confocal	593	7.29±0.01	24.69±0.02	45.14±0.02	22.88±0.02
	656	5.59±0.01	24.91±0.01	46.32±0.02	23.18±0.01
STED 90 mW	593	8.24±0.03	24.31±0.05	44.90±0.05	22.55±0.04
	656	5.83±0.03	24.58±0.04	46.79±0.04	22.79±0.05
STED 240 mW	593	8.39±0.05	24.04±0.05	44.62±0.07	22.95±0.07
	656	5.89±0.02	24.40±0.04	46.59±0.08	23.12±0.07

Table 5.9 shows significant differences for the distribution of KK114L in the four detection channels not only when the imaging mode (confocal, STED 90 mW, STED 240 mW) was varied but also for the two excitation wavelengths of 593 nm and 656 nm within one imaging mode. For example, already in the confocal mode, APD5 recorded 7.29 % of KK114L when excited with 593 nm whereas this value dropped to 5.59 % in the case for excitation with 656 nm. This was a difference of almost 2%. For APDs 6–8 the differences were not as pronounced but still significant. It seemed that the emission spectrum depended on the excitation wavelength.

When comparing the different imaging modes, one notices that the differences between 593 nm and 656 nm excitation became larger during STED imaging. For a STED power of 240 mW the difference on APD5 amounted to 2.5 % whereas it was 2.4 % for 90 mW STED power and 1.7 % in the confocal mode. The changes on APDs 6–8 were smaller but lay still outside one sigma (see tab. 5.9). The deviation between high and low STED power was not very pronounced. This could be a sample issue, any changes induced by the power of the STED beam quickly reached an equilibrium state via diffusion.

### **KK114L fixed-cell sample**

In a fixed-cell sample of KK114L an area of  $10\ \mu\text{m} \times 10\ \mu\text{m}$  was imaged without time gating in confocal, low STED (90 mW) and high STED (240 mW) mode with 656 nm and 593 nm as excitation wavelengths. Always 15 frames were taken and for each frame the  $r_i$  were calculated. The result is shown in figure 5.24.

Not only does figure 5.24 confirm the results from the dye solution measurements, it also shows some kinetics of the process. For example, the percentage increase of APD5 was the fastest for the high STED power of 240 mW (see fig. 5.24c). Here, the crossing of the ratios of APD5 and APD8 took place in frame 6–7 whereas in the low STED and confocal imaging case (see fig. 5.24b and 5.24a), no crossing of these ratios was observed. Further, one notices that the percentage distributions for an excitation of 593 nm changed quicker and more dramatically as it was the case for an excitation of 656 nm and that their values generally differed. Moreover, the percentage increase of APD5 was coupled to a percentage loss of APD7, the ratios of APD6 and APD8 experienced only a minor decrease.

In summary, KK114L seemed to exhibit a spectral blue shift that became stronger with increasing STED power and was mainly noticeable when exciting with a rather blue wavelength (in this case 593 nm) left of the absorbance maximum. It was not only observed in a fixed-cell sample but also in a dye solution (see fig. 5.24 and tab. 5.9). Moreover, the fact that spectral differences were already detected in the confocal imaging mode indicated that differences were already present in the initial conditions. This led to the hypothesis that the dye existed in two different populations; a blue and a red/original population. If this were the case, then illumination with excitation or STED light would convert the red to the blue population leading to a percentual change in spectral distribution along the way. Also, it seemed that this conversion got stronger the more light intensity was used as can be seen from the crossing of the percentage distributions in APD5 and APD8 in figure 5.24. In a fixed-cell sample, the percentage changes were clearly a function of the STED power whereas for a dye solution, such a conclusion could not be drawn.

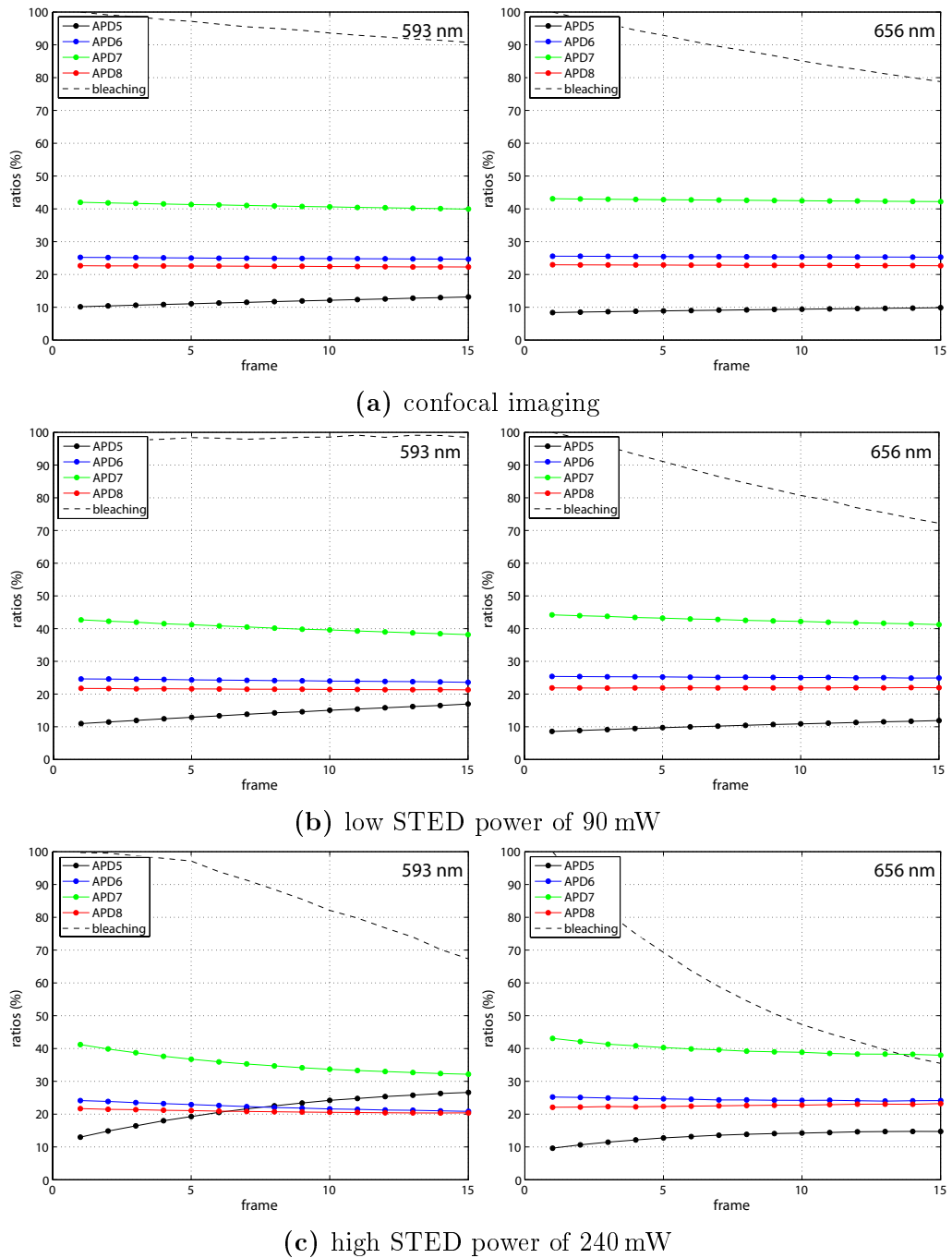


**Figure 5.24:** Ratios  $r_i$  in APDs 5–8 for a single stained fixed-cell sample of KK114L over 15 frames. The left column shows the ratios for 593 nm excitation and the right column for 656 nm. The top row corresponds to the confocal imaging mode, the middle row to low STED imaging with 90 mW and the bottom row to high STED imaging with 240 mW. solid black: ratios of APD5, solid blue: ratios of APD6, solid green: ratios of APD7, solid red: ratios of APD8. dashed black: overall bleaching curve (counts of all APDs combined normalized to the brightest frame).

Furthermore, it seemed that the NNMF algorithm allowed some variability in the unmixing parameters. Otherwise, the unmixing result of figure 5.19 should not be as perfect. But as can be seen from figure 5.21, the NNMF algorithm became unstable when the changes in the percentage distribution were more pronounced. In this case, fixing and manually optimizing the transfer matrix was an option for obtaining a good unmixing result (see fig. 5.22) at the expense of needing a priori knowledge.

## 5.6 Spectral blueing during STED imaging

As pointed out in section 5.5, a spectral blue shift of KK114L occurred during multiplexing experiments. This blueing affected the unmixing algorithm and thus the image quality in the unmixed channels leading to undesired crosstalk. Moreover, it might also increase the bleaching and deteriorate the achievable optical resolution. Here, the blueing was investigated for two sets of dyes; five dyes that have their emission maxima between 650 nm and 660 nm and two dyes whose emission maxima lie at 627 nm. For the two sets, different excitation wavelengths and detection configurations were chosen (see section 5.6.1). The measuring scheme, the different blueing conditions and the analysis will be described in more detail in section 5.6.2. The results for the two sets of dyes will be shown in section 5.6.3. A preliminary hypothesis of the origins of the spectral blueing will be given in section 5.6.4.

Note that results of this section were obtained in collaboration with Maria Loidolt. Further results regarding the blueing will be presented in her PhD thesis (Georg-August-Universität Göttinge, to be published end of 2017).

### 5.6.1 Examined dyes and detection configurations

To the first set of dyes belong: Atto633 (ATTO-TEC GmbH, Siegen, DE), DyLight633 (DyL633) (lifetechnologies now part of Thermo Fisher Scientific, Waltham, US), Alexa633 (lifetechnologies now part of Thermo Fisher Scientific, Waltham, US), Star635P (Abberior GmbH, Göttingen, DE) and KK114L [52]. They were multiplexed with 656 nm and 560 nm and detected with APDs 4–7. Their respective absorption (dash-dotted lines) and emission spectra (solid lines) together with the detection configuration (coloured bar at the top) are shown in figure 5.25. A detailed listing of the names, suppliers, absorption and emission maxima as well as the absorption at the employed wavelengths of the used dyes is given in table 5.10.

To the second set of dyes belong: Atto594 (ATTO-TEC GmbH, Siegen, DE) and Star600 (Abberior GmbH, Göttingen, DE). They were multiplexed with 612 nm and 517 nm and detected with APDs 3–6. Their respective absorption (dash-dotted lines) and emission spectra (solid lines) together with the detection configuration (coloured bar at the top) are shown in figure 5.26. A detailed listing of the names,

suppliers, absorption and emission maxima as well as the absorption at the employed wavelengths of the used dyes is given in table 5.11.

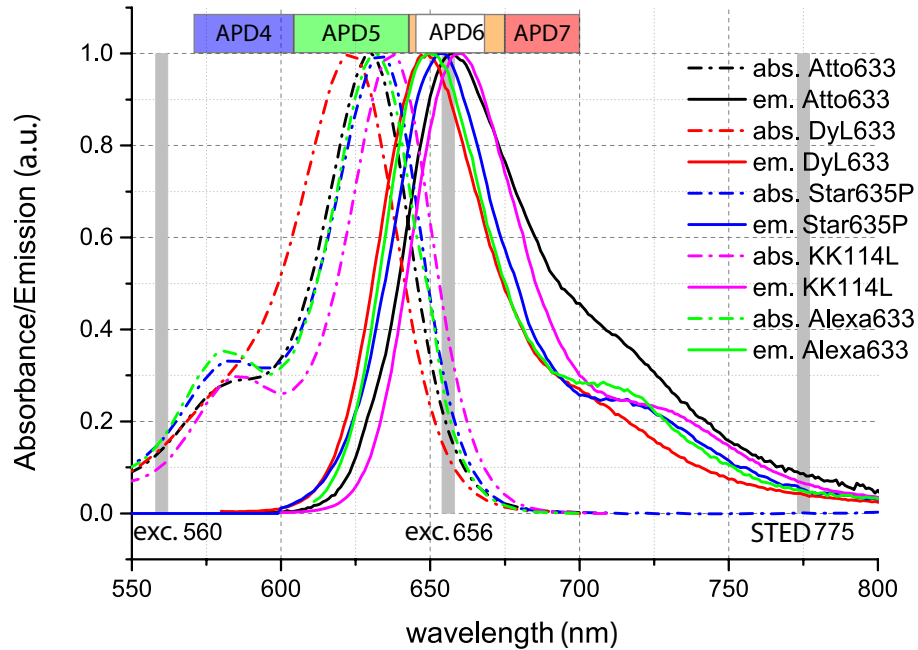


**Figure 5.25:** Absorption and emission spectra of Atto633 (black), DyLight633 (DyL633) (red), Star635P (blue), KK114L (pink) and Alexa633 (green). Solid lines: emission curves, dashed-dotted lines: absorption curves. Bars at the top represent the four detection windows. blue: APD4, green: APD5, orange: APD6 and red: APD7.

**Table 5.10:** Absorption (Abs(max)) and emission (Em(max)) maxima in nm as well as the absorption for 656 nm (Abs(656)) and 560 nm (Abs(560)) in % for the first set of investigated dyes.

dye	supplier	Abs(max) (nm)	Em(max) (nm)	Abs(656) (%)	Abs(560) (%)
DyLight633	lifetechnologies	623	649	12.3	14.3
Atto633	ATTO-TEC	629	657	18.1	13.8
Alexa633	lifetechnologies	632	647	21.8	16.0
Star635P	Abberior	633	654	25.5	15.9
KK114L	[52]	637	660	38.5	10.4

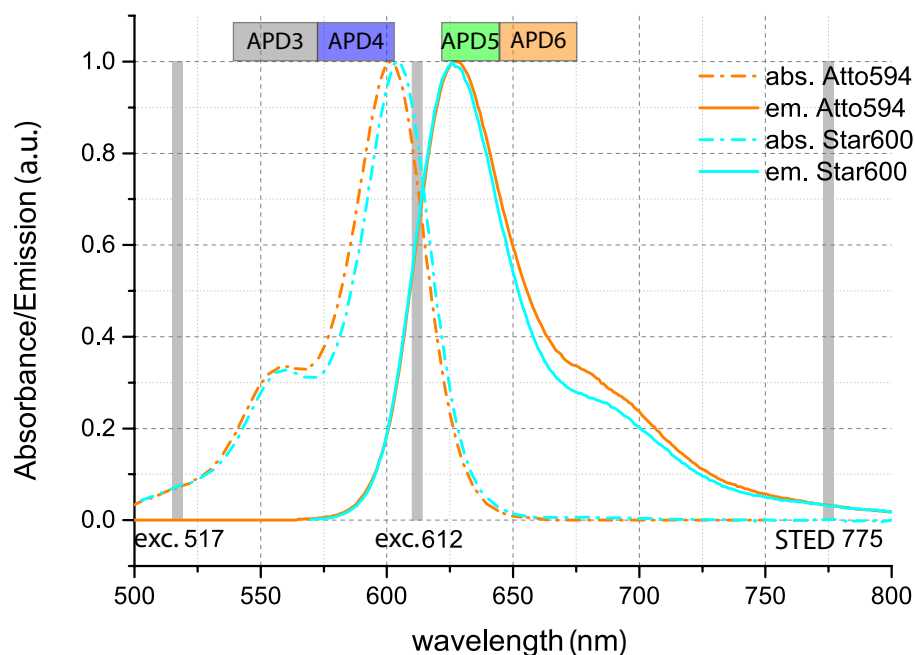


**Figure 5.26:** Absorption and emission spectra of Atto594 (orange) and Star600 (cyan). Solid lines: emission curves, dashed-dotted lines: absorption curves. Bars at the top represent the four detection windows. grey: APD3, blue: APD4, green: APD5 and orange: APD6.

**Table 5.11:** Absorption (Abs(max)) and emission (Em(max)) maxima in nm as well as the absorption for 612 nm (Abs(612)) and 517 nm (Abs(517)) in % for the second set of investigated dyes.

dye	supplier	Abs(max) (nm)	Em(max) (nm)	Abs(612) (%)	Abs(517) (%)
Atto594	ATTO-TEC	601	627	73.6	0.72
Star600	Abberior	604	627	83.3	0.74

## 5.6.2 Measuring scheme, blueing conditions and analysis

### Measuring scheme and samples

The examined samples were all single stained fixed Vero cells in which the Nup153 complex was marked via a mouse primary and a sheep anti-mouse secondary antibody coupled to the dyes in tables 5.10 and 5.11.

The measuring scheme involved two line steps; one for each excitation wavelength, where the redder wavelength occupied the first line step. For one cell and a chosen area of  $10\ \mu\text{m} \times 10\ \mu\text{m}$ , three data sets were acquired. The first data set was a confocal image of  $10\ \mu\text{s}$  dwell time per  $20\ \text{nm}$  pixel and served as reference for the

initial conditions. It will be referred to as c1. The second data set contained the blueing condition, meaning that the sample was illuminated with a combination of excitation and STED beam that supposedly induced the spectral blue shift. Here, the dwell time was also 10  $\mu$ s per 20 nm pixel but 10 consecutive frames were taken. From this second data set, conclusion about the kinetics of the process could be drawn since the changes were tracked over 10 frames. The third data set was another confocal image of 10  $\mu$ s dwell time per 20 nm pixel and served as reference for the end conditions. It will be referred to as c2. This sequence was repeated three times for three different cells for each blueing condition.

### Blueing conditions

The so called blueing conditions were different combinations of switched on excitation and STED beams as a function of the STED power and timing between the excitation and STED pulses. Here, two STED powers were investigated, 110 mW and 240 mW. For these two STED powers four different blueing configurations were examined; optimum timing between the red excitation wavelength and the STED beam (opt. timing), the STED beam alone (STEDonly), slightly order reversed pulse sequence of the excitation wavelengths and the STED beam (pulse rev.I) and much reversed pulse sequence of the excitation and STED beam (pulse rev.II). The exact pulse timing differences between the excitation wavelengths and the STED beam are given in table 5.12.

**Table 5.12:** Timing differences between the different excitation wavelengths and the STED beam for the various blueing conditions. +: the STED beam arrived after the excitation, -: the STED beam arrived before the excitation.

$\lambda_{exc}$	opt. timing 612	opt. timing 656	pulse rev. I	pulse rev. II
517 nm	+520 ps	+420 ps	-1000 ps	-2260 ps
560 nm	+640 ps	+540 ps	-880 ps	-2140 ps
612 nm	+840 ps	+740 ps	-680 ps	-1940 ps
656 nm	+980 ps	+880 ps	-540 ps	-1800 ps

The timing differences were a result of the run time differences explained in section 3.6.3. Further, note that opt. timing 656 was employed for the first set of dyes (see tab. 5.10) and that opt. timing 612 was employed for the second set of dyes (see tab. 5.11).

The pulse durations were ca. 100 ps for the excitation pulses and ca. 800 ps for the STED pulses. Hence, there was a small timing overlap for the excitation wavelength

of 656 nm in the pulse rev.I configuration whereas in the pulse rev.II configuration there was no timing overlap.

### Analysis with the measure $\delta$

For each blueing condition and timing configuration there were three data sets taken (c1, blueing condition, c2). Each contained a total number of 8 recorded detection channels, four for the red excitation wavelength (612 nm or 656 nm) and four for the blue excitation wavelength (517 nm or 560 nm). The spectral composition of the detection channels was the same for the two excitation wavelengths but varied with the set of investigated dyes (see fig. 5.25 and 5.26).

The red and the blue excitation wavelengths were treated separately, leading to a total number of 6 different conditions (two wavelengths and three data sets). For each of the 6 conditions the percentage distribution  $r_i$  in the four detection channels was calculated according to equation (5.5). For the data sets of the blueing condition, the  $r_i$  were then plotted against the number of frames to observe and detect the kinetic of the blueing process. For the data sets of the confocal images (c1, c2), a further analysis step was performed. Additionally to the ratios  $r_i$ , their difference  $\delta$  was taken.

$$\delta_i = r_i(c2) - r_i(c1), \quad (5.6)$$

where  $i$  is the index of the channel.

If  $\delta_i = 0$ , then there is no percentage change in channel  $i$  from c1 to c2. If  $\delta_i > 0$ , then there is a percentage increase in channel  $i$  from c1 to c2. If  $\delta_i < 0$ , then there is a percentage decrease in channel  $i$  from c1 to c2. The sum over  $i$  of the differences  $\delta_i$  intrinsically amounts to zero.

The more the  $\delta_i$  differ from zero and have positive values for the bluer detection channels, the more pronounced is the spectral shift to the blue. Thus, the position of the positive  $\delta_i$  indicates the direction of the shift and the value of the  $\delta_i$  gives an indication of the magnitude of the conversion. That is, the higher the value, the more the initial red population is converted into the blue population.

### 5.6.3 Results for the two sets of dyes

The following figures display the measure  $\delta$  for each detection channel, blueing condition, and excitation wavelength. Results for the blue excitation wavelength are depicted on the left, whereas the results for the red excitation wavelength are on the right. The blueing conditions are colour coded and grouped in the detection channels. The optimum timing is presented in grey, STEDonly in blue, pulse rev.I in red and pulse rev.II in green.

The values of  $\delta$  will be compared between the different blueing conditions and STED

powers for each excitation wavelength separately but also between the excitation wavelengths themselves for each dye. Then, the various dyes will be compared to each other.

### **Atto633, Star635P, KK114L, DyLight633 and Alexa633**

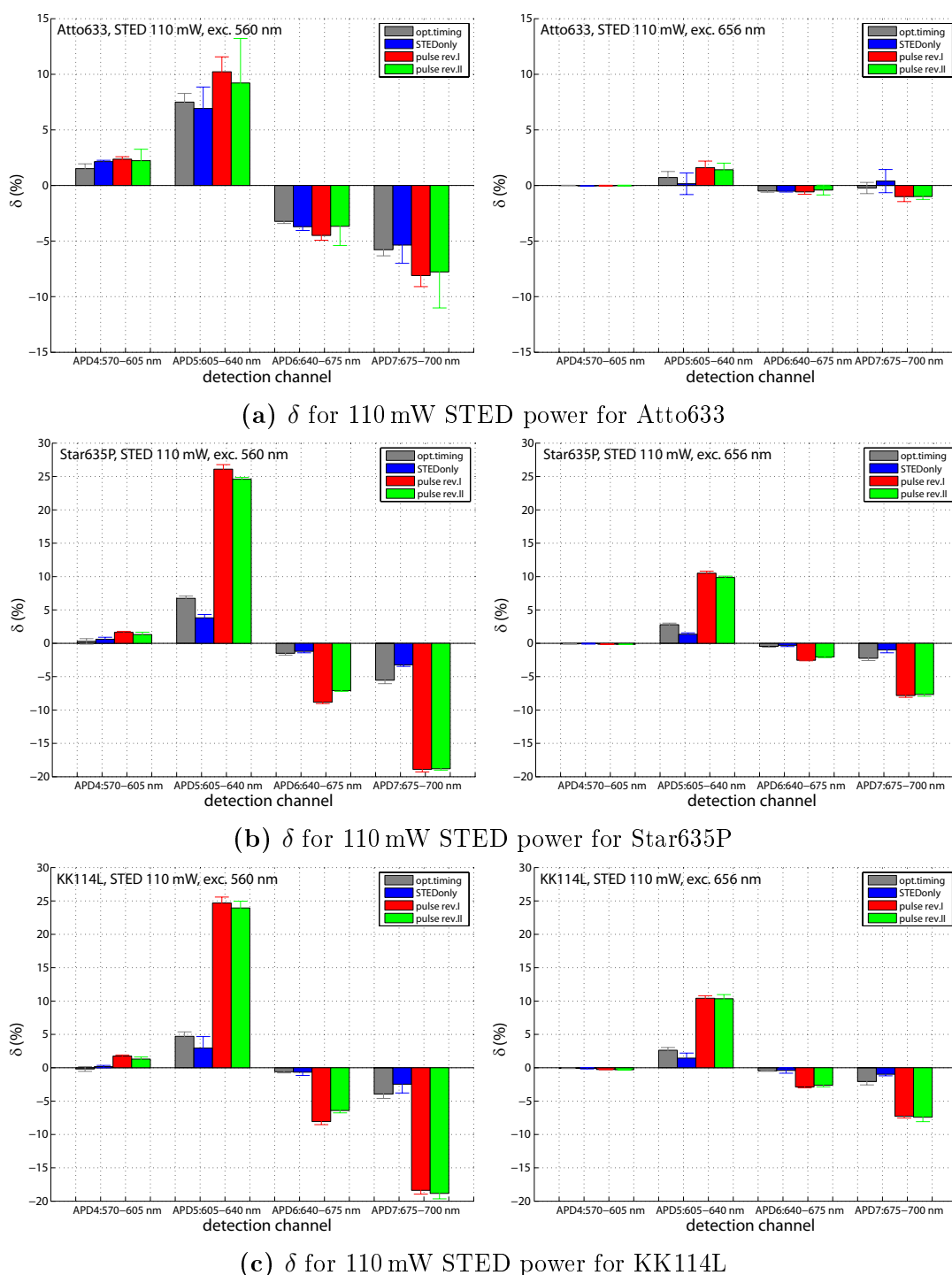
The first set of dyes was divided into two groups depending on the bleaching behaviour of the individual dyes. For Atto633, Star635P and KK114L measurements were taken for two different STED powers (110 mW and 240 mW). For DyLight633 and Alexa633, the STED beam bleached the dye very quickly such that reliable measurements could not be obtained with a STED power of 240 mW. Therefore, for DyLight633 and Alexa633 only results with 110 mW STED power will be presented.

Figure 5.27 shows the values of  $\delta$  for Atto633 (top), Star635P (middle) and KK114L (bottom) for a STED power of 110 mW. Looking at figure 5.27 reveals strong differences between the dyes. Atto633 (see fig. 5.27a) had its maximum positive change of the percentage distribution in APD5 with a small contribution in APD4. Further, figure 5.27a shows a minor contribution from the presumed blue population in the detection channels when excited with 656 nm (values of  $\delta$  were close to zero for 656 nm). Moreover, the blueing condition itself had a small influence (values of  $\delta$  varied little with the blueing condition).

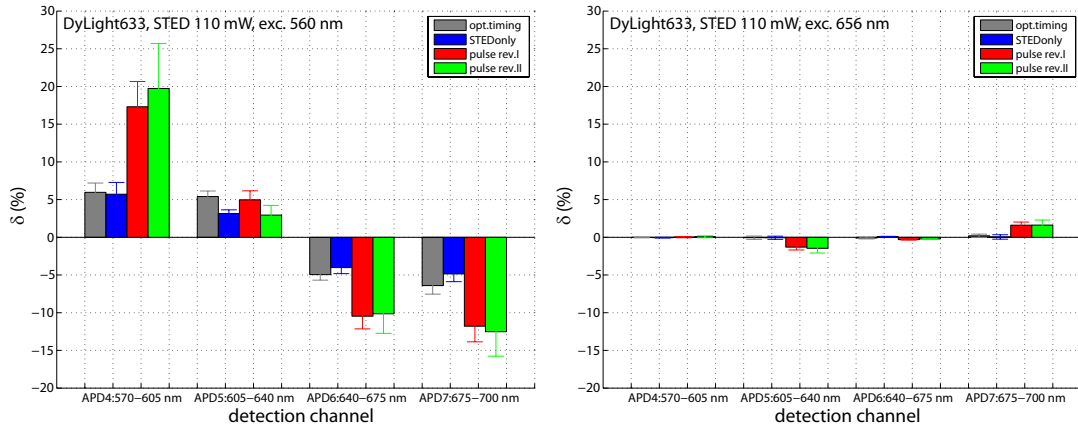
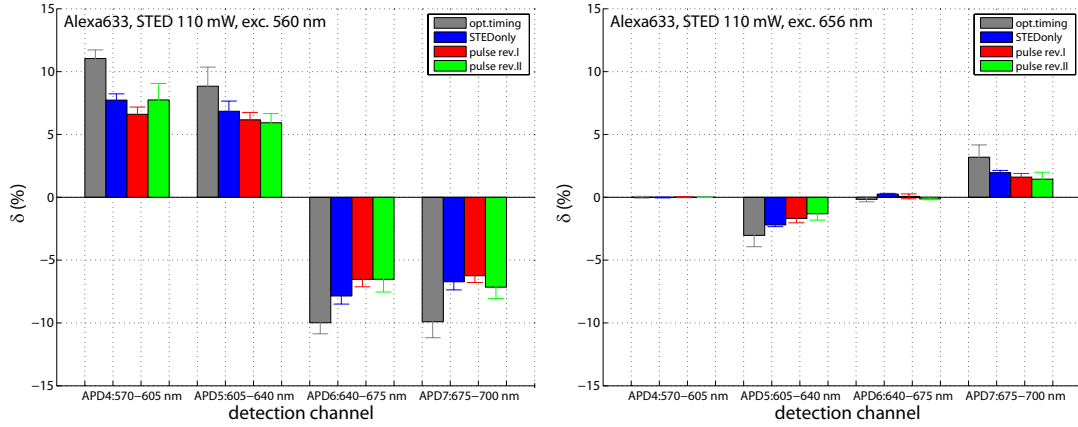
Star635P and KK114L behaved in the same way as can be seen from figures 5.27b and 5.27c. Both had their maximum positive change in the percentage distribution in APD5 and also showed a noticeable contribution from the presumed blue population in the detection channels when excited with 656 nm (values of  $\delta$  had the same shape for 560 nm and 656 nm excitation). Further, they exhibited a strong dependence on the blueing condition. In the pulse rev. modes I and II the values for  $\delta$  were comparable and much larger than the ones for optimum timing and STEDonly.

From the position of the positive values of  $\delta$  when exciting with 560 nm and the values of  $\delta$  when exciting with 656 nm, one could deduce the magnitude of the spectral shift to the blue. The data in figure 5.27 indicates that the spectral blue shift of Atto633 was larger than the one of Star635P and KK114L. Considering that their emission maxima specified by their respective suppliers differ by as little as 6 nm (see tab. 5.10), indicated that the structure of the dye might play an important role.

When the STED power was increased to 240 mW (see fig. E.4) the distribution of the positive and negative values for  $\delta$  was similar to 110 mW but the values of  $\delta$  were mainly larger. This indicated that the conversion of the red to the blue population increased with rising STED power. Moreover, Atto633 seemed to show a small red shift when excited with 656 nm. So far, there was no explanation for this behaviour. Whether this was actually the case and not a measuring or analyzing artefact and why it only appeared at high STED powers would require further investigation.



**Figure 5.27:** Bar chart of  $\delta$  for Atto633 (top), Star635P (middle) and KK114L (bottom) for 110 mW STED power and 560 nm excitation (left) or 656 nm excitation (right). The four different blueing conditions are colour coded. grey: optimum timing, blue: STEDonly, red: pulse rev.I, green: pulse rev.II.

(a)  $\delta$  for 110 mW STED power for DyLight633(b)  $\delta$  for 110 mW STED power for Alexa633

**Figure 5.28:** Bar chart of  $\delta$  for DyLight633 (top) and Alexa633 (bottom) for 110 mW STED power and 560 nm excitation (left) or 656 nm excitation (right). The four different blueing conditions are colour coded. grey: optimum timing, blue: STEDonly, red: pulse rev.I, green: pulse rev.II.

Figure 5.28 shows the values of  $\delta$  for DyLight633 (top) and Alexa633 (bottom) for a STED power of 110 mW. DyLight633 (see fig. 5.28a) had its maximum positive change in the percentage distribution in APD4 with a small contribution in APD5. Further, figure 5.28a shows almost no contribution from the presumed blue population in the detection channels when excited with 656 nm (values of  $\delta$  were almost always zero for 656 nm). Moreover, the blueing condition influenced the forming of the blue population (values of  $\delta$  strongly depended on the blueing condition). The values of  $\delta$  for pulse rev.I and II were comparable and much larger than the ones for optimum timing and STEDonly.

Alexa633 (see fig. 5.28b) exhibited the strongest positive change in  $\delta$  in APD4 and APD5. Further, figure 5.28b shows only a minor dependence of  $\delta$  on the blueing condition. Its values were comparable for STEDonly, pulse rev.I and pulse rev.II and generally smaller than the ones for optimum timing. Moreover, Alexa633 seemed to

have a small red shift when excited with 656 nm which was comparable to Atto633 at a STED power of 240 mW (see fig. E.4a). As it is the case for Atto633, this red shift of Alexa633 would require further investigation since its appearance could not be explained so far and may be due to a measuring or analyzing artefact.

As for Atto633, Star635P and KK114L, one could deduce the magnitude of the blue shift by looking at the position of the positive values of  $\delta$  when exciting with 560 nm and the values of  $\delta$  when exciting with 656 nm. A ranking of the different dyes according to the magnitude of their blue shift as well as their absorption and emission maxima as specified by the suppliers is given in table 5.13.

**Table 5.13:** Ranking of the five investigated dyes having an emission maximum between 650 and 660 nm according to the magnitude of their spectral blue shift. The absorption (Abs.) and emission (Em.) maxima as specified by their respective suppliers are given as a reference.

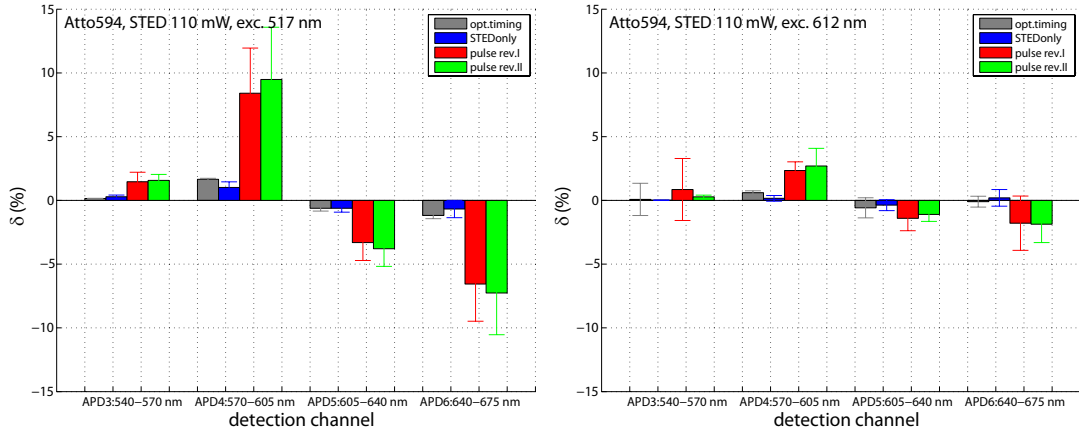
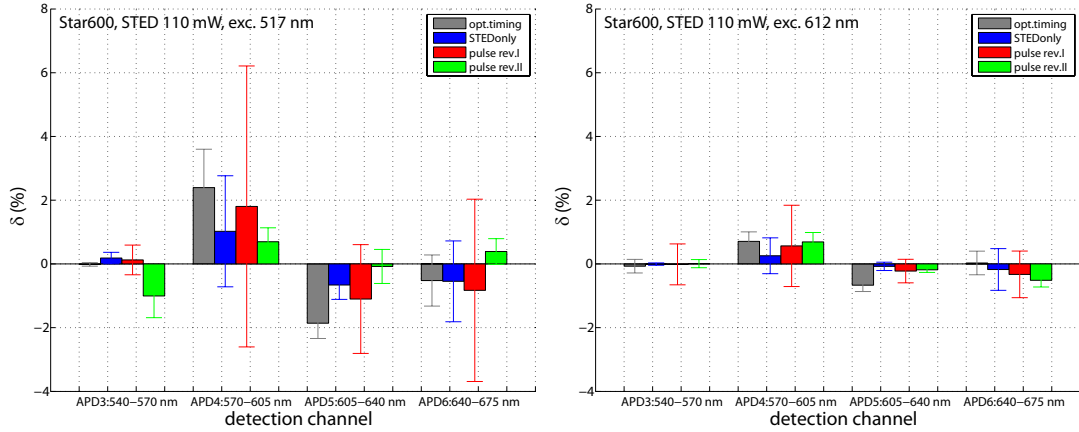
order of shift	dye	supplier	Abs. (nm)	Em. (nm)
much	DyLight633	lifetechnologies	623	649
	Alexa633	lifetechnologies	632	647
	Atto633	ATTO-TEC	629	657
	Star635P	Abberior	633	654
not much	KK114L	[52]	637	660

The fact that the different dyes exhibited a large variation with regard to the magnitude and the pulse order inducing the spectral blue shift, indicated that its origins should be found in the chemical structure, the embedding environment and the imaging parameters. One could think that in cases where the pulse rev. modes led to the strongest blueing (Star635P, KK114L, DyLight633), the blue shift might happen through a triplet state. In these cases the optimum timing condition between the excitation and STED pulses might lead to some sort of protective effect due to the active deexcitation by the STED beam. In cases in which the optimum timing condition led to the strongest blueing (Alexa633), one could think that the interplay of the excitation and STED beam might be responsible for the blueing.

The graphs displaying the behaviour of the  $r_i$  over the 10 consecutive frames can be found in appendix E.

### Atto594 and Star600

For the second set of dyes consisting of Atto594 and Star600, there were also measurements with two different STED powers (110 mW and 240 mW) taken.

(a)  $\delta$  for 110 mW STED power for Atto594(b)  $\delta$  for 110 mW STED power for Star600

**Figure 5.29:** Bar chart of  $\delta$  for Atto594 (top) and Star600 (bottom) for 110 mW STED power and 517 nm excitation (left) or 612 nm excitation (right). The four different blueing conditions are colour coded. grey: optimum timing, blue: STEDOnly, red: pulse rev.I, green: pulse rev.II.

Figure 5.29 shows the values of  $\delta$  for Atto594 (top) and Star600 (bottom) for a STED power of 110 mW. Atto594 (see fig. 5.29a) had its maximum positive change in the percentage distribution in APD4. Further, figure 5.29a shows a minor contribution from the presumed blue population in the detection channels when excited with 612 nm (values of  $\delta$  were close to zero for 612 nm). Moreover, Atto594 exhibited a strong dependence of  $\delta$  on the blueing condition. The values of  $\delta$  for the pulse rev. modes I and II were comparable and much larger than the ones for optimum timing and STEDOnly where there was only a minor change.

The measurements of Star600 (see fig. 5.29b) had a strong variance leading to large error bars for 110 mW STED. For measurements of 240 mW STED (see fig. 5.30b), the error bars were smaller indicating that for 110 mW STED, they were due to a measuring artefact. Nevertheless, similar conclusions as for the other dyes could be drawn. The maximum positive change in the percentage distribution occurred in

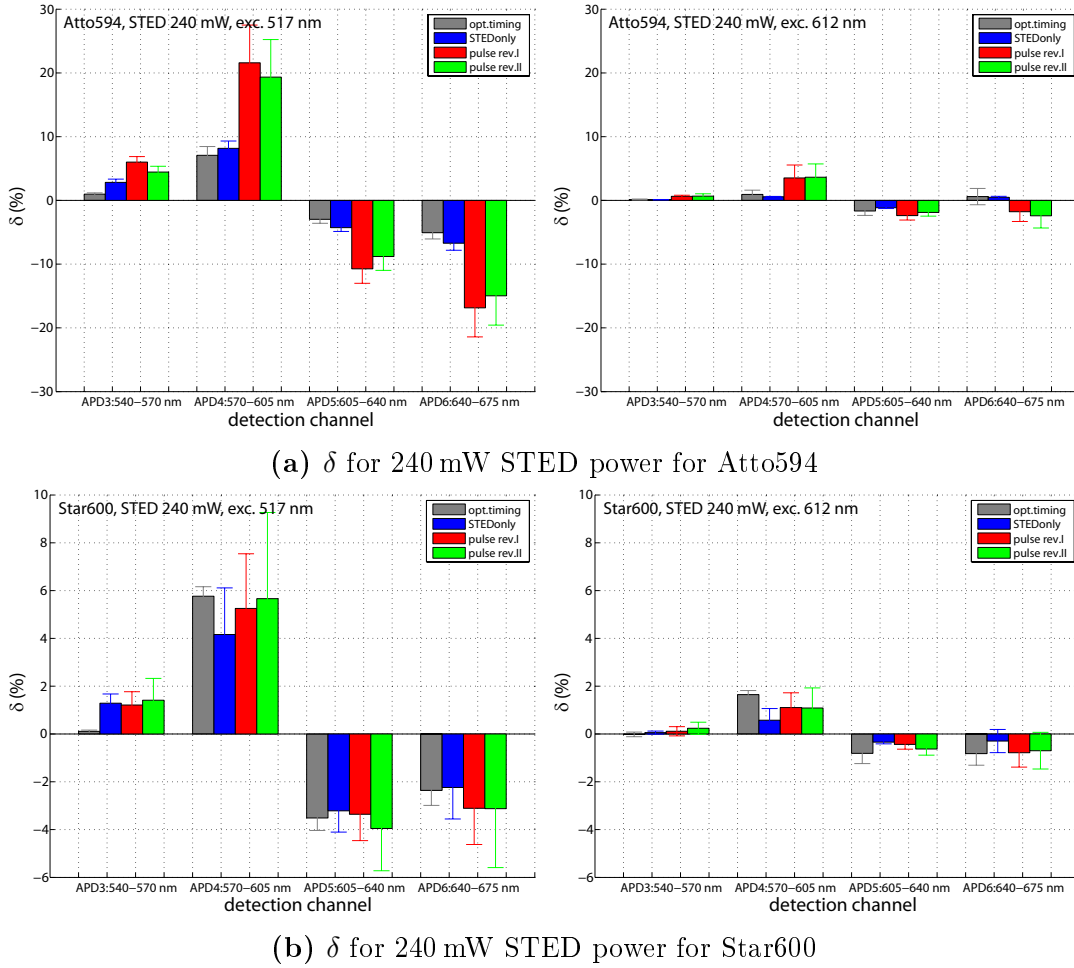


**Figure 5.30:** Bar chart of  $\delta$  for Atto594 (top) and Star600 (bottom) for 240 mW STED power and 517 nm excitation (left) or 612 nm excitation (right). The four different blueing conditions are colour coded. grey: optimum timing, blue: STEDOnly, red: pulse rev.I, green: pulse rev.II.

APD4 and there was almost no contribution from the blue population in the detection channels when exciting with 612 nm (values of  $\delta$  were almost always zero). Moreover, Star600 only exhibited a significant positive value of  $\delta$  in the case for optimum timing.

From the position of the positive values of  $\delta$  when exciting with 517 nm and its values when exciting with 612 nm, the magnitude of the spectral blue shift could be deduced. The data in figure 5.29 indicates that the spectral blue shift of Atto594 was larger and that the blue population was quicker produced than the one of Star600 considering that their emission maxima as specified by their respective suppliers are the same (see tab. 5.11).

Figure 5.30 shows the values of  $\delta$  for Atto594 (top) and Star600 (bottom) for

a STED power of 240 mW. It confirms the results and the drawn conclusions from figure 5.29. Atto594 (see fig. 5.30a) showed a stronger and quicker blue shift than Star600 (see fig. 5.30b) since the values of  $\delta$  were larger for Atto594. Moreover, the blue shift of Atto594 was the strongest in the pulse rev. modes I and II whereas for Star600 all blueing conditions were comparable.

Comparing figure 5.29 and figure 5.30 shows that the conversion of the red to the blue population increased with rising STED power (values of  $\delta$  were generally larger for the higher STED power).

The graphs displaying the behaviour of the  $r_i$  over the 10 consecutive frames can be found in appendix E.

### 5.6.4 Hypothesis of the origin of the blue population

Section 5.6.3 showed that during STED imaging a blue population of the red dyes arose that changed the spectral distribution of the dye in the four detection channels. Since there were already variations in the spectral distribution of the first confocal image between the blue and the red excitation wavelength, it seemed that right from the beginning the dye existed in two different populations. This led to a percentage distribution in the different spectral channels that was dependent on the excitation wavelength.

The mechanism behind the conversion from the red to the blue population might be explained by the breaking of two double bonds. When these double bonds break, they shorten the pi-electron system which leads to a spectral blue shift. Figure 5.31 displays the structural formula of Star600 (left) [65] and Star635P, KK114L (right) [52]. These were the only structural formulas that could be obtained. All other suppliers did not communicate the exact formulas.

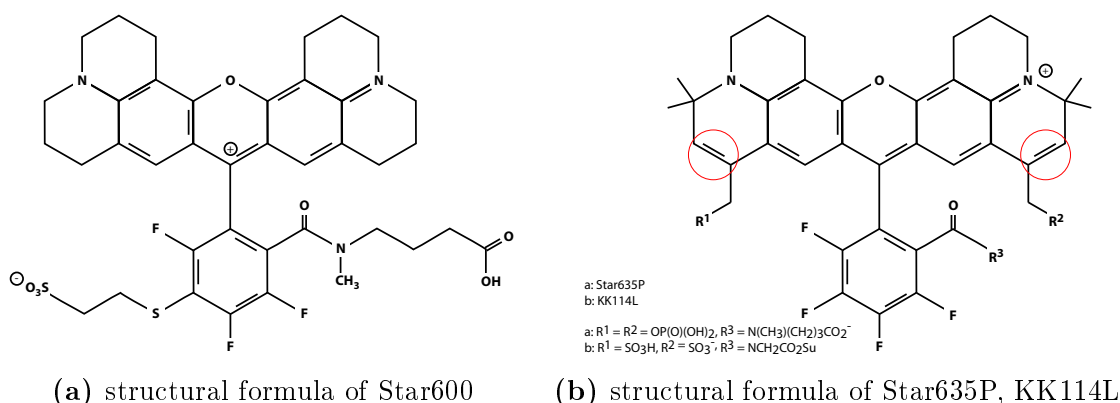


**Figure 5.31:** Structural formula of Star600 (left) [65] and Star635P, KK114L (right) [52]. The blue population might arise from breaking two double bonds (red circles).

As can be seen from figure 5.31a, Star600 does not have the double bonds that are prone to breaking. Nevertheless, a less pronounced spectral shift to the blue was detected especially for high STED power (see fig. 5.30b). This indicated that there was something else contributing to the blue shift. In order to understand in more detail the spectral blue shift further experiments would be necessary that would also be sensitive to lifetime changes and have a better spectral resolution. Moreover, the embedding medium and the fixation protocol might influence the spectral blueing. Additionally, it would be great to isolate the two populations and determine their chemical structure. This could probably be done by mass spectrometry.

## 5.7 Conclusion of the results

This chapter presented the results of multicolour STED nanoscopy with hyperspectral detection. In section 5.1 it was demonstrated that the spatial resolution on 24 nm fluorescent crimson beads was around  $43.6 \pm 5.6$  nm and  $36.9 \pm 3.3$  nm for x and y directions respectively. This was comparable to other state of the art STED systems, e.g. [29, 32, 37]. Further, separation of three different bead species was achieved by NNMF. The residual crosstalk of the crimson, dark red and far red fluorescent beads was less than 3% in every channel.

Section 5.2 investigated the dye dependent spatial resolution in the STED mode for the same STED power. This was done by FCS measurements that determined the dye specific saturation intensity  $P_{\text{sat}}$ . It was found that for a STED wavelength of 775 nm and a power of 100 mW, the achievable resolution for dyes having an emission spectrum similar to Atto590 was around 75 nm, for emission spectra similar to Star635P 55 nm and for emission spectra similar to Atto655 and CF680R 40 nm.

In section 5.3, a list of organic dyes from various suppliers was given that were tested with regard to their applicability in multicolour experiments with a STED beam of 775 nm.

Moreover, it was shown in section 5.4 that the minimal distance between different emission spectra for successful separation with minor crosstalk depended on the exact configuration of the detection windows. For an excitation wavelength of 593 nm or 656 nm, the minimal distance amounted to 22 nm. When an excitation wavelength of 612 nm was employed this value decreased for far red dyes to 15 nm and remained at 22 nm for dyes in the blue regime. Further, good separation of four colours with one excitation wavelength and one STED beam was demonstrated in a fixed-cell sample in which vimentin, giantin, peroxisomes and the nuclear pores were stained with Atto594, Star635P, KK1441 and CF680R respectively.

Section 5.5 described a spectral blue shift when multiplexing two excitation wavelengths (593 nm and 656 nm) that impeded the analysis by NNMF at high STED powers. For low STED powers, where the blue shift was small, the analysis was

robust.

The spectral blue shift, or blueing, was further studied in section 5.6. A total number of 7 dyes (Atto633, Star635P, KK114L, DyLight633, Alexa633, Atto594, Star600) and four different blueing conditions were investigated. It was found that all dyes exhibited a spectral blue shift. But the appearance and the magnitude of the shift strongly depended on the dye and the blueing condition. In cases where the STED pulse arrived before the excitation pulse and led to the strongest blue shift (Atto594, Star635P, KK114L, DyLight633), the blueing might happen via a triplet state. For these dyes, the STED beam in the optimum timing condition might exert some sort of protective effect due to its active deexcitation preventing strong blue shifts. The largest shift was detected for DyLight633 and the smallest for Star600. Also, the more STED power was used, the larger was the effect. A hypothesis of the origin was given by the breaking of two double bonds in the chemical structure. However, Star600 does not have these double bonds and still showed a blue shift, albeit smaller. This indicated that there was something else contributing to the spectral blue shift. Possible reasons could be the embedding environment and the fixation protocol. So far, the underlying mechanisms of the spectral blue shift are mostly unknown therefore further investigation would be needed that preferably include a better spectral resolution for more details on the magnitude of the blue shift, lifetime measurements for detecting possible variations in the lifetime and mass spectrometry for determining possible structural changes.

Another aspect that needs to be examined in more detail would be the impact of the spectral blue shift on the achievable resolution. When the emission spectra shift to the blue, the reachable optical resolution should decrease since the depletion efficiency at the STED wavelength becomes lower. The studies conducted here were not suitable to detect a change in optical resolution since it was not possible to track the size of one structure over several frames due to a short pixel dwell time. The photons emitted by the structure within one frame were not sufficient to obtain a good fitting result for the FWHM. In order to assess whether there might be changes in the optical resolution further measurements with a longer pixel dwell time should be conducted. Here, this was not investigated since the mechanism and kinetics of the spectral blue shift was of more interest.



# Chapter 6

## Discussion and outlook

Even though two-colour STED nanoscopy is not new [22] and has even become a routine method in biological applications [20, 32, 49, 71, 92], it was and still is a struggle in STED microscopy to label, image and distinguish multiple markers. In particular, the number of markers is limited to two if the observation should be simultaneous, below the diffraction limit and solely based on their emission properties. For the discrimination of multiple markers different methods have been developed, including excitation, emission, lifetime, photostability or any combination thereof. Typically, such multicolour set-ups require some form of unmixing as a post-processing step. Also, the sample itself, be it living or fixed, puts some constraints on the available markers.

In this thesis, a simple and versatile STED set-up with a hyperspectral detection of 8 channels was designed and built. Four of these detection channels were used together with a single STED beam at a wavelength of 775 nm. The other four channels may be used with a bluer STED wavelength in the future. Further, the set-up allowed the selection of up to 8 different excitation wavelengths provided by a single supercontinuum source. The choice of the excitation wavelengths was arbitrary as long as they were within the spectral range of the supercontinuum source. Moreover, the selected excitation wavelengths could either be used simultaneously or in sequence. Since only two beams, namely the supercontinuum source and the STED laser, had to be superimposed, the set-up was very stable without sacrificing the flexibility of having multiple excitation wavelengths.

Several spectral unmixing methods were compared, their performances objectively evaluated in simulations and then verified with experimental data. The best separation results were obtained using NNMF with a fixed and manually optimized transfer matrix  $\mathbf{A}_{\text{me}}$  as compared to  $\mathbf{A}_{\text{exp}}$ , the matrix consisting of the individual spectra of the different dyes. In comparison to  $\mathbf{A}_{\text{exp}}$ ,  $\mathbf{A}_{\text{me}}$  had to be pushed to a stronger overlap of the individual dyes to obtain the best discrimination. It was possible to reduce the residual crosstalk after analysis to less than 10% in simulations for brightness levels which could also be expected in experimental data. Furthermore,

the NNMF algorithm easily allowed the inclusion of multiple excitation wavelengths and/or lifetime separation by various time gates. In simulations it was shown that for spectrally distinct dyes, adding a second excitation wavelength was preferable to lifetime separation for reducing the residual crosstalk after analysis. In the case of similar emission spectra however, lifetime separation provided a means of discrimination, which could decrease the remaining crosstalk after unmixing below 10 % as long as the lifetimes differed by approximately 1 ns. Because good separation results were obtained with NNMF, there was no need to try other unmixing methods such as MCR or SPA.

Further, it was experimentally demonstrated that the number of simultaneously observable structures in STED imaging could be pushed to four in a fixed-cell sample using the NNMF algorithm as the analyzing method. For this, the acquisition of only one scan with one excitation wavelength and a single STED beam was sufficient for separation. This clearly outperformed the earlier work by Rönnlund [76] in which three scans were taken, and two excitation wavelengths, two STED beams and an additional bleaching step had to be applied for discrimination of four markers.

For sample preparation, a labeling protocol involving two nanobodies and two antibodies was established, which enabled staining of four cellular structures or proteins of choice. The achievable resolution of the different markers varied with each but was always well below the diffraction limit. The optical resolution was shown to be around 80 nm for the bluest and around 40 nm for the reddest dye at a STED power of 100 mW in the back focal plane.

The minimal distance required in order to discriminate two emission spectra was shown to be approximately 22 nm for a hyperspectral detection consisting of four channels. This number could be decreased by using more spectral channels. In this case the limiting factor would be the SNR for each detection channel. When using conventional APDs as detectors, a spectral width of 20 nm for each channel should be sufficient to yield a good SNR while providing a decent spectral resolution at the same time. In this work the spectral width of the detection channels varied for each channel and was around 35 nm.

The assessment of the remaining crosstalk after analysis in a quadruple stained fixed-cell sample was difficult due to highly overlapping structures. The estimation of an upper bound for the residual crosstalk showed it to be less than 30 %. Considering the results from the simulations where the residual crosstalk was shown to be less than 10 %, its value should also be in this range for biological samples. To better determine the actual remaining crosstalk values from experimental data, a technical sample with defined, non-overlapping structures labeled with the same organic dyes would be needed. This would not only allow a more detailed evaluation of the remaining crosstalk but also enable quantitative colocalization studies. The latter are typically limited by the residual crosstalk levels after analysis.

---

In comparison to four-colour stochastic super resolution reports in STORM [19, 95], GSDIM [91] and PAINT [47], the STED approach in this work has several advantages but also some drawbacks. Note that STORM [79, 80] and GSDIM [26] operate on the basis of randomly blinking single molecules and that PAINT [83] exploits the diffusion of fluorescent molecules and their binding/release to a target for blinking. In the stochastic approaches, several analyzing steps such as molecule localization and image reconstruction are required that could introduce undesired artefacts. Here, the only necessary post-processing step was the spectral unmixing. In the stochastic methods however, the localization precision of individual molecules can be quite good leading then to a better non-marker dependent resolution. For the same reason, the remaining crosstalk after analysis could be reduced to less than 2% in STORM [95] or even non-existent in PAINT [47]. But the reasons behind these benefits could also be seen as flaws. Localizing individual stochastically switching molecules requires long acquisition times. This is especially true for Exchange-PAINT [47] in which sequential imaging and washing steps are needed for multicolour images therefore significantly slowing down the data acquisition with the need of drift correction. In contrast is the more direct targeted read-out approach of STED used in this work. It allows rather quick data recording suitable to study dynamic processes involving multiple protagonists. Moreover, the use of only one excitation wavelength and a single STED beam, as presented here, made the optical set-up both stable and simple as compared to most other multicolour super resolution set-ups.

The use of a single STED beam is also advantageous in terms of phototoxicity to the cell, although it puts some constraints on the spectrum of the usable dyes. The redder the dye, the higher the reexcitation generated by the STED beam alone. It was crucial to find imaging parameters that were suitable for every dye, i.e. that each of them had a decent SNR above the reexcitation background. In this thesis, the reexcitation was recorded line-interleaved with the actual data and was implemented in the analysis by simple subtraction. Although easy and straightforward, this method was not ideal. A better way would be to model the reexcitation data perhaps as an additional wavelength within the NNMF algorithm. This would require knowledge and implementation of the excitation and STED PSFs and would be complicated. Another way would be to exclude the reexcitation data from the recordings. This could be done by modulating the excitation light with a certain frequency and passing the detected fluorescence signals through a lock-in amplifier, as it was done in [78].

During multiplexing experiments with two excitation wavelengths of 593 nm and 656 nm, a spectral blue shift of several organic dyes was observed which caused the NNMF algorithm to fail at high STED powers. It seemed that the organic dye existed in two populations; an red and a blue one. It was found that these two populations were already present in the initial conditions leading to different spectral distributions for different excitation wavelengths. Further, it was shown that a light

induced conversion from the initial red population to the blue population occurred. This conversion was influenced by the combination and pulse order of the excitation and the STED light. The kinetics and the magnitude of the spectral blue shift were strongly dependent on the dye. For some dyes, the strongest blue shift was observed when the STED pulse arrived before the excitation pulse whereas the blueshift was less strong when the timing between excitation and STED was optimized for good STED efficiency and the STED pulse came after the excitation pulse. In the cases where the STED pulse arrived first, the blueing might happen through a triplet state and the optimum timing condition between the excitation and STED pulses might prevent strong blue shifts. This could be interpreted as some sort of protective effect by the STED beam caused by its active depletion of the excited state. A possible reason for the origin of the blueing could be the breaking of two double bonds in the chemical structure. But even the one dye that did not have these double bonds exhibited a blue shift, albeit slower and smaller. This indicated that something else was also contributing to the blueing, possibly the fixation protocol, the embedding environment or further structural changes. To investigate the underlying mechanisms in more detail, additional studies would be required involving a better spectral resolution for a more precise determination of the magnitude of the spectral shift, lifetime measurements for observing possible lifetime changes and mass spectrometry for exactly determining structural alterations.

Note that the blueing might also affect conventional STED set-ups with two excitation wavelengths, two spectral detection channels and one STED beam. In this case, the blueing might lead to undesired crosstalk between the different detection channels. Also, if the bleaching behaviour were studied using only one or two detection channels, it could lead to a more complex situation. The dye might shift to the blue so that it could not be detected anymore. An effect that might be mistaken as bleaching would actually be blueing.

The aim of this thesis was focused on the development of a multicolour STED microscope for as many colours as possible. With the use of four detection channels, it was possible to successfully discriminate four colours purely based on their emission spectra. Adding lifetime information using two time gates as another means of discrimination would push the number of distinguishable markers even further. In the near future, it should be possible to separate 6 dyes with four spectral detection channels, lifetime information using two time gates, one excitation wavelength and a single STED beam. Therefore Atto594, Star600, DyLight633, Star635P, KK1441 and CF680R are suggested. Atto594 and Star600 as well as DyLight633 and Star635P should be discriminated by lifetime and all the others spectrally.

The use of various long Stokes' shift dyes or even caged dyes in combination with the appropriate excitation or switching wavelengths could also increase the number of distinguishable dyes. If this were done, the blueing would need to be kept in mind especially for long Stokes' shift dyes, since it could counteract the benefit by

changing the percentage distribution in the various detection channels for the different excitation wavelengths. Additionally, the use of Exchange-PAINT [47] could further increase the number of distinguishable markers, but at the expense of imaging speed.

The observation of more than four different markers requires further labeling protocols, as well. One could think of combining quantum dots [36], nanobodies [67], various (CLIP- [50], SNAP- [27], Halo- [60]) tags and conventional antibodies for fixed-cell stainings. For live-cell stainings, a combination of fluorescent proteins together with silicon rhodamines (SiR) [61, 62], various (CLIP-, SNAP-, Halo-) tags [74, 87] and CRISPR/Cas9 mediated endogenous tagging [75] could be a promising approach.

In conclusion, the current limitations to multicolour STED nanoscopy were extended. For the first time four colours were successfully discriminated using only one excitation wavelength and a single STED beam. In the near future, separation of 6 colours could be accomplished. The simplicity and the stability of the here presented set-up exceeded that of most other multicolour STED microscopes. Its versatility opens up a wide range of opportunities for biological applications, especially allowing mechanisms involving multiple protagonists to be observed and their interaction to be studied simultaneously on the nanometer scale. Thus, multicolour STED nanoscopy with hyperspectral detection is an important step forward for unraveling the complexities of biological multiprotein processes.



# Appendix A

## Antibodies

**Table A.1:** Primary antibodies and plasmids used in the staining protocols.

catalogue no.	supplier	species	structure
ab24700	Abcam	mouse	Nup153
T5168	Sigma	mouse	tubulin
V6389	Sigma	mouse	vimentin
ab3421	Abcam	rabbit	peroxisomes
ab24586	Abcam	rabbit	giantin
ab18251	Abcam	rabbit	tubulin
GP433	MPIbpc	mOrange	peroxisomes
GP230	MPIbpc	citrine	vimentin

**Table A.2:** Secondary antibodies and nanobodies used in the staining protocols.

catalogue no.	supplier	host species	reactivity	dye
M8890	Sigma	goat	anti-mouse	Star580
515-005-003	Dianova	sheep	anti-mouse	Atto590
515-005-003	Dianova	sheep	anti-mouse	Atto594
515-005-003	Dianova	sheep	anti-mouse	Atto620
515-005-003	Dianova	sheep	anti-mouse	DyL633
515-005-003	Dianova	sheep	anti-mouse	Star635P
515-005-003	Dianova	sheep	anti-mouse	Atto633
515-005-003	Dianova	sheep	anti-mouse	Atto647N
515-005-003	Dianova	sheep	anti-mouse	KK114L
515-005-003	Dianova	sheep	anti-mouse	Atto655
515-005-003	Dianova	sheep	anti-mouse	CF680R
R3128	Sigma	goat	anti-rabbit	Star580
111-005-045	Dianova	goat	anti-rabbit	Atto590
111-005-003	Dianova	goat	anti-rabbit	Atto594
111-005-003	Dianova	goat	anti-rabbit	DyL633
111-005-003	Dianova	goat	anti-rabbit	Star635P
111-005-003	Dianova	goat	anti-rabbit	Atto633
111-005-003	Dianova	goat	anti-rabbit	KK114L
40839	Sigma	goat	anti-rabbit	Atto647N
111-005-003	Dianova	goat	anti-rabbit	KK1441
111-005-045	Dianova	goat	anti-rabbit	Atto655
111-005-003	Dianova	goat	anti-rabbit	CF680R
gbaAS635p	Chromotek	nanobody	anti-GFP	Star635P
rba594	Chromotek	nanobody	anti-RFP	Atto594

# Appendix B

## Sample Preparation

### Dye solution sample

Dissolve the solid dye compound in 2  $\mu$ l dimethyl sulfoxide (DMSO) (Sigma-Aldrich, München, DE) and fill the eppendorf tube with thiodiethylene glycol (TDE) (model 88559, Sigma-Aldrich, München, DE). Vortex and sonificate the solution until homogenously mixed. Dilute the solution to the desired concentration with TDE. Put 100  $\mu$ l of the desired concentration on single concave microscope slide (GT vision Ltd., Stansfield, GB). Slide 24 mm $\times$ 24 mm coverglass (model 1014 from Glaswarenfabrik Karl Hecht GmbH & Co KG, Sondheim v. d. Rhön, DE) slowly over the microscope slide and wait until the coverglass is fully emerged in the solution. Remove the excess solution with a tissue. Then seal with nail polish.

### Fluorescent bead sample

**Table B.1:** Used fluorescent beads.

catalogue no.	supplier	name	size (nm)
F8782	lifetechnologies	crimson	20
	invitrogen	crimson	100
F8807	lifetechnologies	dark red	200
F8789	Molecular Probes	far red	100

Put 70  $\mu$ l of poly-L-lysine solution 0.1% (w/v) water (Sigma-Aldrich, München, DE) on a 24 mm $\times$ 24 mm coverglass (model 1014 from Glaswarenfabrik Karl Hecht GmbH & Co KG, Sondheim v. d. Rhön, DE). Wait for 2 min. Then rinse with deionized water and with distilled water. Dry with compressed air. Add 70  $\mu$ l of the bead

solution. Wait for 2 min. Then rinse with deionized water and with distilled water. Dry with compressed air. Put a drop of Mowiol with DABCO (25 % (w/v) Glycerin, 9 % (w/v) Mowiol 4-88, 0.1 M Tris/Cl, 0.1 % (w/v) 1,4-Diazabicyclo[2.2.2]octane, pH 8.5) on a microscope slide (model ECN 631-1551, VWR, Radnor, US) and put coverglass face down on the drop. Wait until the capillary effect emerged the coverglass completely. Then seal with nail polish.

## Four-colour fixed-cell sample

Fix double transfected Vero cells with GP230 and GP433 with 4 % paraformaldehyde (PFA) in phosphate buffered saline (PBS) (137 mM NaCl, 2.68 mM KCl, 10 mM Na<sub>2</sub>HPO<sub>4</sub>, pH 7.4) for 10 min at room temperature. Then add Triton X-100 (model T8787, Sigma-Aldrich, München, DE) in 0.1 % PBS (v/v) for 5 min at room temperature. Add primary antibodies Nup153 (1:100) and giantin (1:500) (see tab. A.1) and incubate for 1 h at room temperature. Wash three times 5 min in PBS with 2 % bovine serum albumin (BSA). Add secondary antibodies anti-mouse CF680R and anti-rabbit KK1441 (both 1:50) (see tab. A.2) and incubate for 1 h at room temperature. Wash three times 5 min in PBS with 2 % bovine serum albumin (BSA). Add nanobodies anti-GFP Star635P and anti-RFP Atto594 (both 1:50) (see tab. A.2) and incubate for 1 h at room temperature. Wash three times 5 min in PBS. Mount in Mowiol with DABCO (25 % (w/v) Glycerin, 9 % (w/v) Mowiol 4-88, 0.1 M Tris/Cl, 0.1 % (w/v) 1,4-Diazabicyclo[2.2.2]octane, pH 8.5).

It was important to apply the nanobodies as the very last staining step, otherwise a coupling of the primary mouse antibody to the anti-GFP nanobody was observed.

# Appendix C

## Algorithms

### NNMF

Listing C.1: Self-implemented NNMF algorithm

```
1 % This is the self-implemented NNMF-algorithm that take multiple excitation
2 % wavelengths into account. After Neher, Blind Source Separation,
3 % Biophysical Journal 2009
4
5 % input:      Y:          data of the form n_apd x n_pix x n_exc
6 %            n_dye:       number of dyes in which Y is factorized
7 %            max_iter:    number of performed iterations
8 %            A0:          Estimate or real distribution of the dyes in the
9 %                        different channels (transfer matrix), n_apd x n_dye
10 %            X0:          Estimate of the dye distribution per pixel, n_dye x
11 %                        n_pix
12 %            Q0:          Estimate of the excitation strength for each dye,
13 %                        n_dye x n_exc
14
15 % output:     A:          transfer matrix adapted by the algorithm, if kept
16 %                        fixed A = A0
17 %            X:          estimated dye distribution per pixel by the
18 %                        algorithm, n_dye x n_apd
19 %            Q:          adapted Q with starting values Q0, n_dye x n_exc
20
21 function [A, X, Q] = NMF_algo_n_exc_v6 (Y, n_dye, max_iter, A0, X0, Q0)
22
23 n_apd = size(Y,1);
24 n_pix = size(Y,2);
25 n_exc = size(Y,3);
26 counts_Y = sum(Y(:));
27
28 if A0 == 0
29     A = rand(n_apd, n_dye);
30     sum_A = repmat(sum(A), n_apd, 1);
31     A = A ./ sum_A;
32 else
33     A = A0;
34     sum_A = repmat(sum(A), n_apd, 1);
35     A = A ./ sum_A;
36 end
37
38 if X0 == 0;
39     X = rand(n_dye, n_pix);
40 else
```

```

41     X = X0;
42 end
43
44 if Q0 == 0
45     Q = rand(n_dye, n_exc);
46 else
47     Q = Q0;
48 end
49
50 fig = figure();
51 lim = 1e-10;
52 for z = 1:max_iter
53     % normalize A such that sum columns = 1
54     sum_A = repmat(sum(A), n_apd, 1);
55     A = A ./ sum_A;
56
57     A_iter = A;
58     X_iter = X;
59     Q_iter = Q;
60
61     temp = permute(A_iter, [1 4 3 2]);
62     A_4d = temp(:,ones(n_pix,1),ones(n_exc,1),:); % n_apd x n_dye x n_exc x n_pix
63
64     temp = permute(Q_iter, [3 4 2 1]);
65     Q_4d = temp(ones(n_apd,1),ones(n_pix,1),:,:);
66
67     temp = permute(X_iter, [3 2 4 1]);
68     X_4d = temp(ones(n_apd,1),:,ones(n_exc,1),:);
69
70     AXQ = sum(A_4d .* X_4d .* Q_4d, 4); % n_apd x n_pix x n_exc
71     YAXQ_4d = Y(:, :, :, ones(n_dye,1)) ./ AXQ(:, :, :, ones(n_dye,1));
72
73     %% update rule A
74     if mod(z, 3) == 0 && z > round(3*max_iter/4);
75         XQ_4d = X_4d .* Q_4d;
76         sum_XQ = squeeze(sum(sum(XQ_4d,2),3)); % n_apd x n_dye
77
78         YXQ = YAXQ_4d .* XQ_4d;
79         sum_YXQ = squeeze(sum(sum(YXQ,2),3)); % n_apd x n_dye
80
81         A = A_iter .* (sum_YXQ ./ sum_XQ);
82     end
83
84     %% update rule X
85     AQ_4d = A_4d .* Q_4d;
86     sum_AQ = squeeze(sum(sum(AQ_4d),3)); % n_dye x n_pix
87
88     YAQ = YAXQ_4d .* AQ_4d;
89     sum_YAQ = squeeze(sum(sum(YAQ),3)); % n_dye x n_pix
90
91     X = X_iter ./ sum_AQ .* sum_YAQ;
92     counts_X = sum(X(:));
93
94     % normalize the counts in X such that they equal the counts in Y. i.e.
95     % all counts in X = all counts in Y
96     X = (X / counts_X) * counts_Y;
97
98     %% update rule Q
99     if (mod(z, 3) == 1 || mod(z, 3) == 2) && z > round(2*max_iter/3)
100         if n_exc == 1
101             AX_4d = A_4d .* X_4d;
102             sum_AX = squeeze(sum(sum(AX_4d),2)); % n_dye x n_exc
103
104             YAX = YAXQ_4d .* AX_4d;
105             sum_YAX = squeeze(sum(sum(YAX),2)); % n_dye x n_exc

```

```

106         Q = Q_iter .* (sum_YAX ./ sum_AX);
107     else
108         AX_4d = A_4d .* X_4d;
109         sum_AX = squeeze(sum(sum(AX_4d),2))'; % n_dye x n_exc
110
111         YAX = YAXQ_4d .* AX_4d;
112         sum_YAX = squeeze(sum(sum(YAX),2))'; % n_dye x n_exc
113
114         Q = Q_iter .* (sum_YAX ./ sum_AX);
115     end
116 end
117
118 % make all matrices positive
119 A = max(A, lim);
120 X = max(X, lim);
121 Q = max(Q, lim);
122
123 % if desired the dye distribution X is displayed in each iteration
124 figure(fig);
125 imagesc(reshape(X(1, :), sqrt(n_pix), sqrt(n_pix)));
126 title(sprintf('it_%d', z)); % shows the number of iteration
127 end
128 end
129 end
130 end

```

As can be seen from listing C.1, the matrix  $\mathbf{X}$  was adapted in every iteration whereas the matrix  $\mathbf{A}$  was adapted only every third iteration in the last quarter of the iterations. The matrix  $\mathbf{Q}$  was adapted in those iterations when  $\mathbf{A}$  was not adapted and only in the last third of the iterations. Usually,  $\mathbf{A}$  was kept fixed during the analysis then the according section was commented in the code and  $\mathbf{X}$  and  $\mathbf{Q}$  were adapted. In case of adaption of  $\mathbf{A}$ , the sum over the columns of  $\mathbf{A}$  was normalized to one and the sum of all entries in  $\mathbf{X}$  was set to the sum of all entries of the data  $\mathbf{Y}$  in each iteration. The maximum number of iteration performed could freely be chosen but was usually set to 300 iterations (see chapter 4).

The alterations and restrictions to the update rules were made to improve the convergence of the algorithm. If wanted, one could only update one of the matrices by commenting all other update rules.

## LinUnmix

**Listing C.2:** Self-implemented linear unmixing algorithm

```

1 % This is the self-implemented LinUnmix algorithm. It calculates the
2 % individual contributions of the different dyes to one pixel after
3 % Zimmermann, Adv Biochem Engin/Biotechnol (2005) and Tsurui, J Histochem
4 % Cytochen(2000) whwere the pseudoinverse (Moore-Penrose-Inverse) is
5 % calculated
6
7 % input:      data:          n_apd x n_pix
8 %            verhaeltnisse: n_apd x n_dye, Spaltensumme = 1;
9 % output:    pure_dyes:     n_dye x n_pix
10
11 function [pure_dyes, exitflag] = lin_unmix_algo(data, verhaeltnisse)
12

```

```

13 n_dye = size(verhaeltnisse, 2);
14 % n_apd = size(verhaeltnisse, 1);
15 n_pix = size(data, 2);
16 if rank(verhaeltnisse) < n_dye
17     warning('caution: rank(verhaeltnisse) < n_dye');
18 end
19
20 % pseudoinverse = pinv(verhaeltnisse);
21 %
22 % pure_dyes = pseudoinverse * data;
23
24 pure_dyes = zeros(n_dye, n_pix);
25 exitflag = zeros(1, n_pix);
26 for ki = 1:n_pix
27     a = data(:, ki);
28     [pure_dyes(:, ki), ~, ~, exitflag(:,ki)] = lsqnonneg(verhaeltnisse, a);
29 end
30
31 if any(exitflag < 0)
32     warning('lsqnonneg did not always converge');
33 end
34
35 end

```

Listing C.2 shows the exact code for the linear unmixing algorithm as used within this thesis.

## ImageJ

In the input parameter dialog of the PoissonNMF plugin for ImageJ [69], one could specify the number of sources, iterations and subsamples. Further, the segregation bias, the saturation and the background threshold as well as the background spectrum had to be assigned. The initial spectra of the number of sources could be chosen either by a Gaussian distribution, region of interest (ROI) selection or manually by the user. The spectra could be kept fixed during the analysis. The mode of the input spectra was the only parameter varied. All other parameters were kept constant within this thesis and their values are given in table C.1.

**Table C.1:** Input parameters and their values for the PoissonNMF plugin for ImageJ.

input parameter	value
number of iterations	300
subsamples	3
segregation bias	1
saturation threshold	4000
background threshold	1
background spectrum	minimal values

# Appendix D

## Further organic dyes

**Table D.1:** Further organic dyes that might be usable for HyperSTED. Abs: absorption maximum (nm), Em: emission maximum (nm).

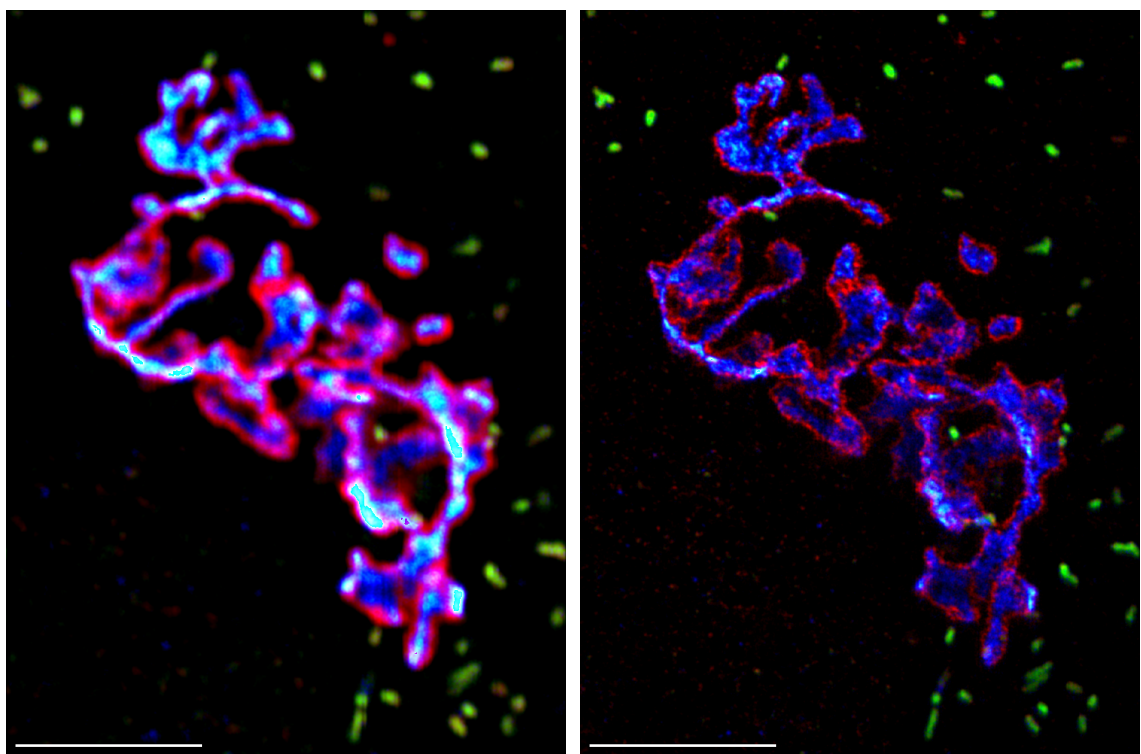
dye	supplier	Abs (nm)	Em (nm)
CF594	Biotium	593	614
DyL594	lifetechnologies	593	618
CF620R	Biotium	617	639
AttoRho14	ATTO-TEC	625	646
CF640R	Biotium	642	662
Aelxa647	lifetechnologies	650	665
CF660R	Biotium	663	682
AttoOxa12	ATTO-TEC	663	684
DyL680	lifetechnologies	682	715



# Appendix E

## Supplementary images

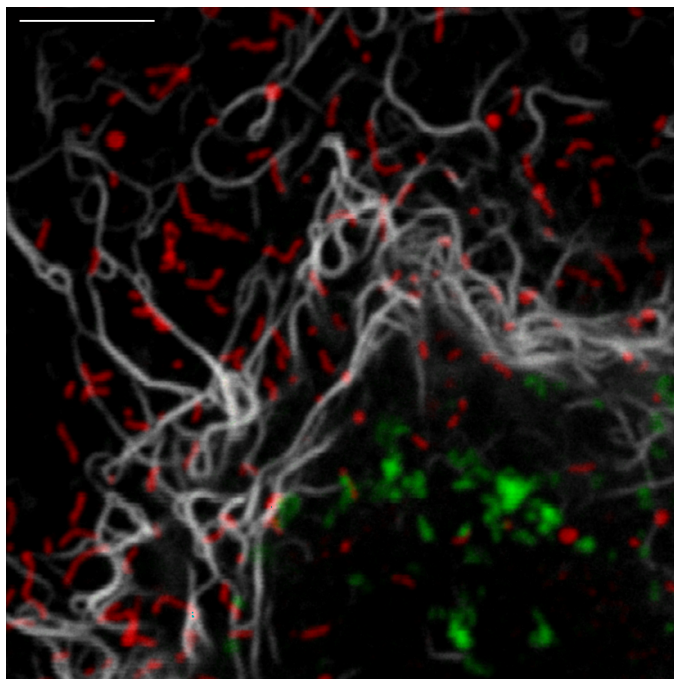
### Three colour



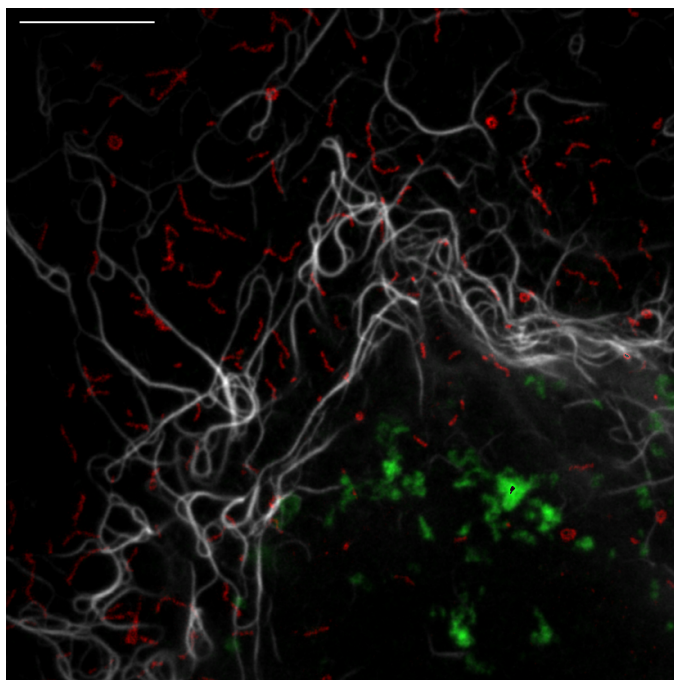
(a) Confocal overlay

(b) STED overlay

**Figure E.1:** Overlay of a fixed-cell sample where peroxisomes were stained with Atto594, GM130 with Atto647N and giantin with CF680R. top: confocal overlay, bottom: STED overlay. red: giantin – CF680R, green: peroxisomes – Atto594, blue: GM130 – Atto647N. Scale bars are 5  $\mu\text{m}$ .



(a) Confocal overlay



(b) STED overlay

**Figure E.2:** Overlay of a fixed-cell sample where GM130 was stained with Alexa594, vimentin with Atto647N and peroxisomes with CF680R. top: confocal overlay, bottom: STED overlay. red: peroxisomes – CF680R, green: GM130 – Alexa594, grey: vimentin – Atto647N. Scale bars are 5  $\mu\text{m}$ .

## Four colour

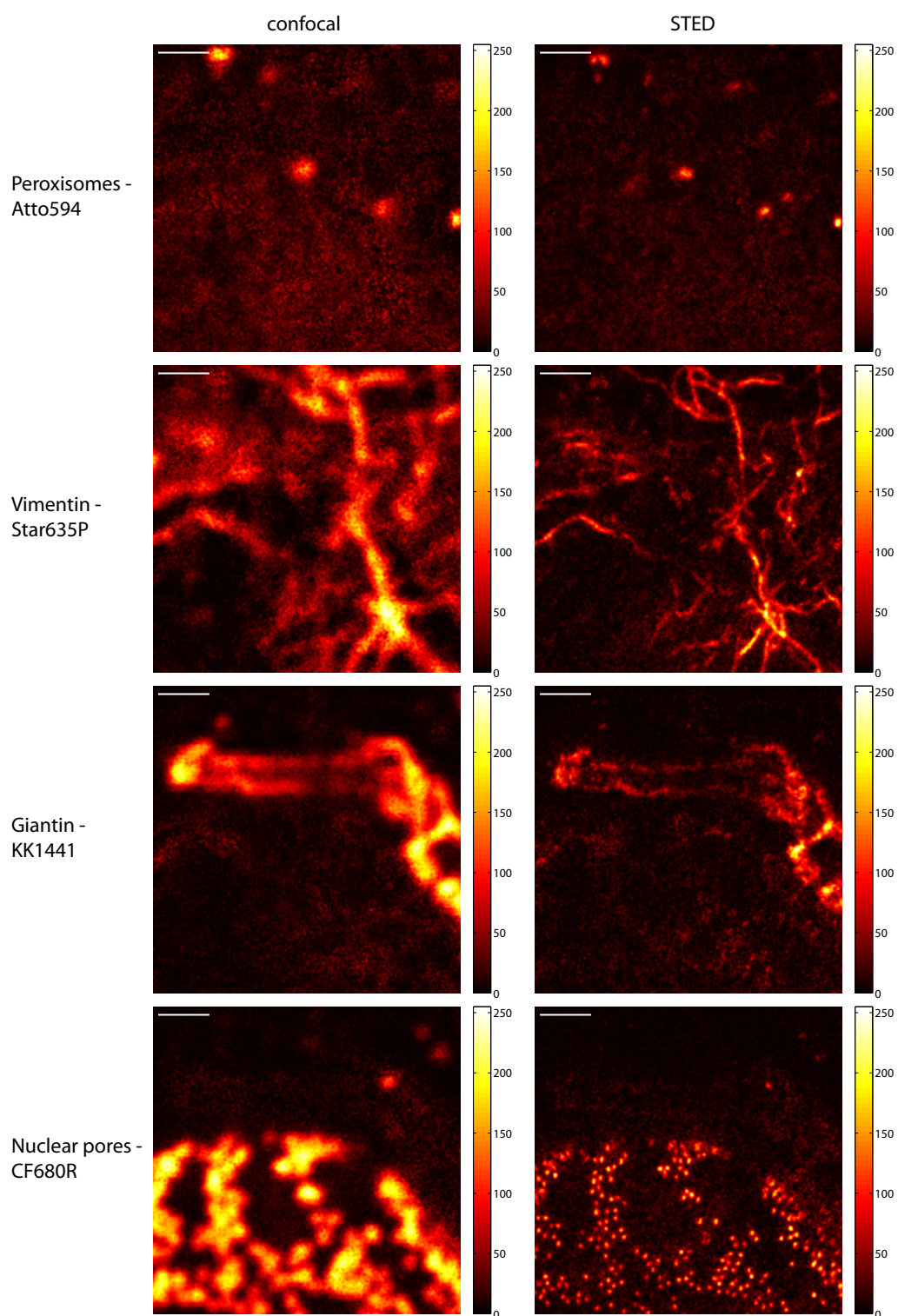


**Figure E.3:** Zoom of the unmixed conf (right) and STED data (left) when the reexcitation by the STED beam (bottom row of fig. 5.13) is subtracted from the raw data (top row of fig. 5.13) and unmixed via NNMF with  $\mathbf{A}_{me}$ . top: peroxisomes – Atto594, second top: vimentin – Star635P, second bottom: giantin – KK1441, bottom: nuclear pores – CF680R. Scale bars are 1  $\mu\text{m}$ .

## Blueing

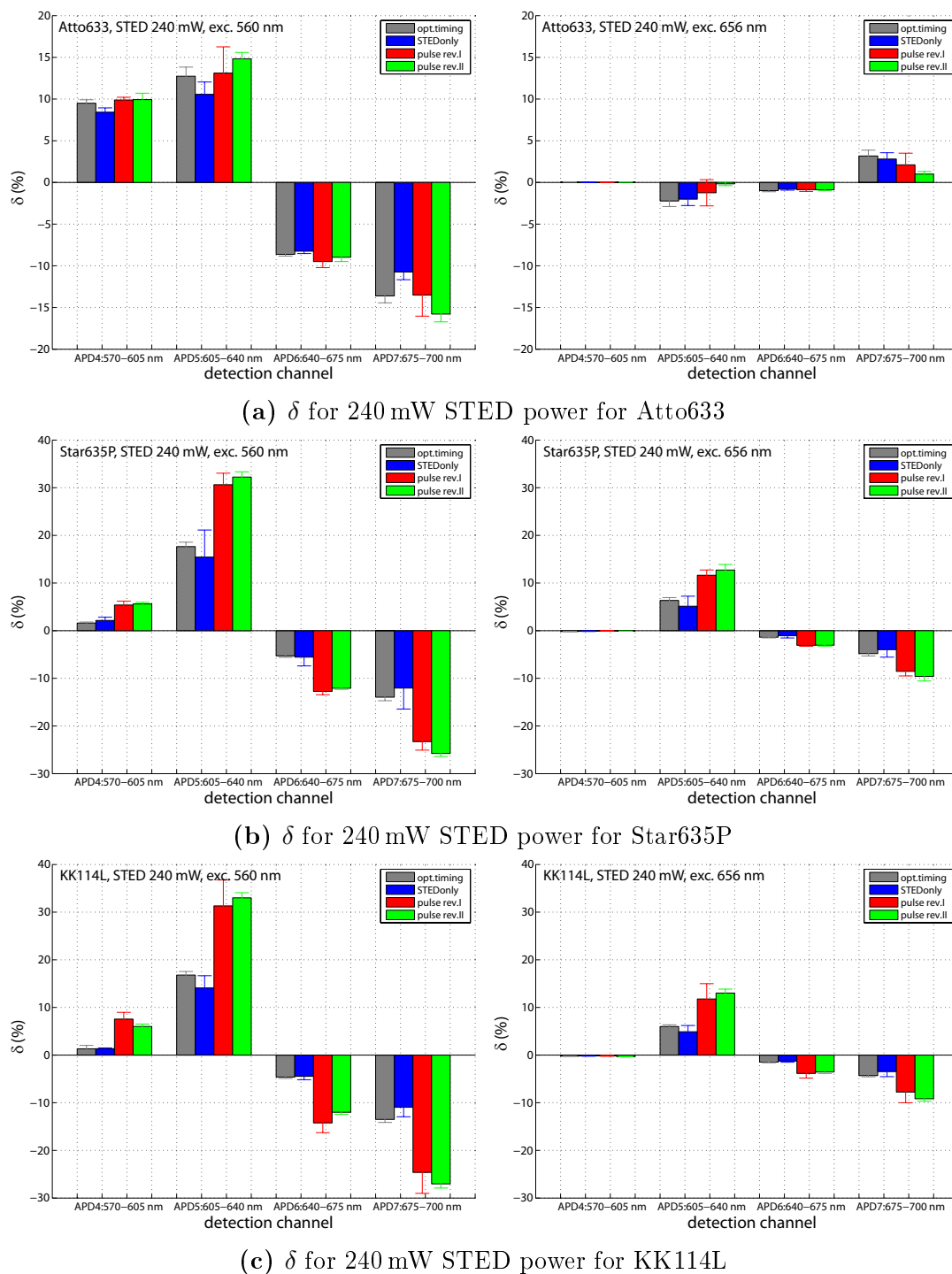


**Figure E.4:** Bar chart of  $\delta$  for Atto633 (top), Star635P (middle) and KK114L (bottom) for 240 mW STED power and 560 nm excitation (left) or 656 nm excitation (right). The four different blueing steps are colour coded. grey: optimum timing, blue: STEDonly, red: pulse rev.I, green: pulse rev.II.

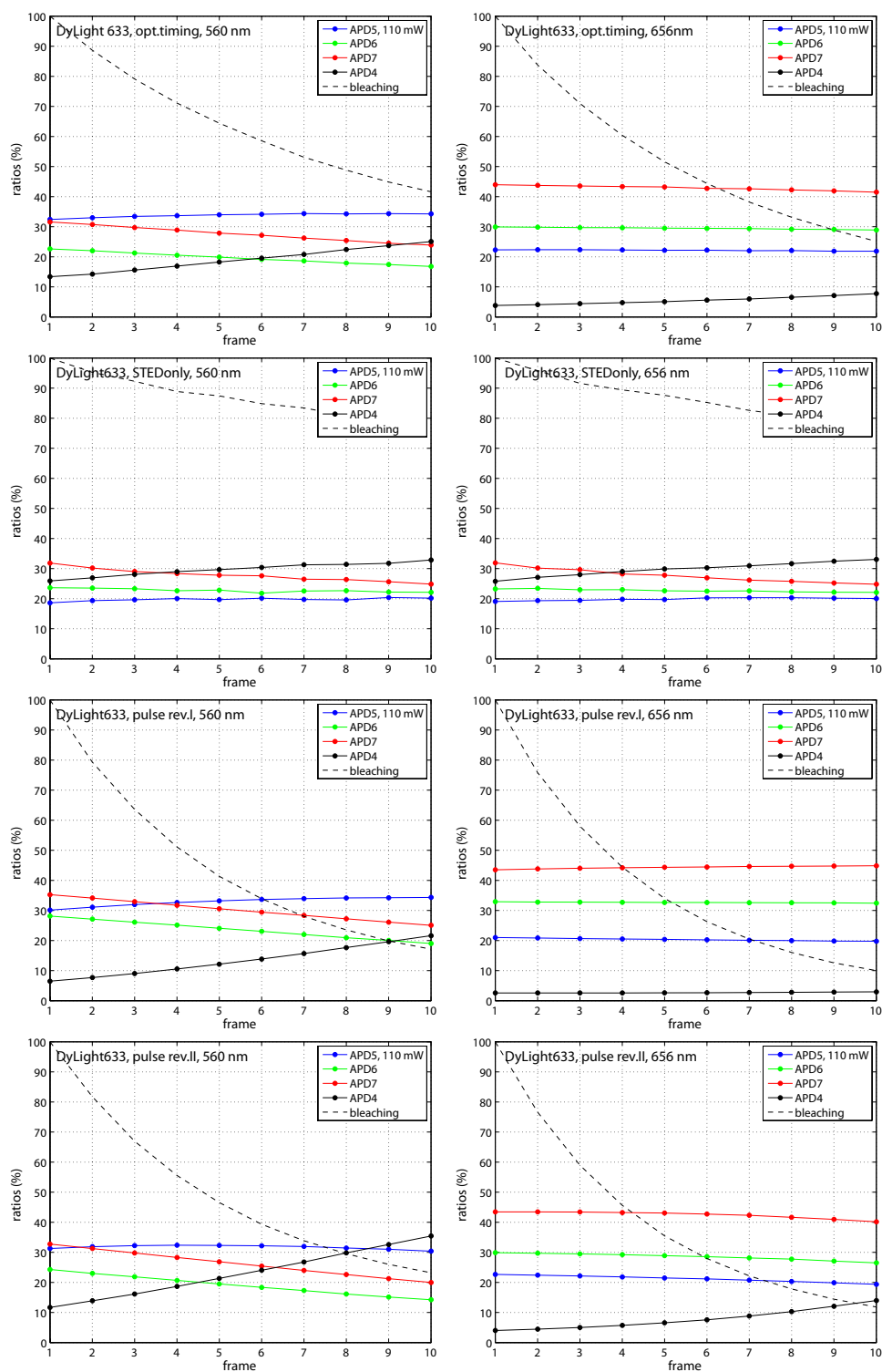


**Figure E.5:** Ratios  $r_i$  in APDs 4-7 for DyLight633 over 10 frames for a STED power of 110 mW. The column shows the ratios for 560 nm excitation (left) and 656 nm (right). The rows correspond to the different bleaching conditions. top: opt. timing, second top: STEDOnly, the second bottom: pulse rev.I and bottom: rev.II. solid black: ratios of APD4, solid blue: ratios of APD5, solid green: ratios of APD6, solid red: ratios of APD7. dashed black: overall bleaching curve (counts of all APDs combined normalized to the brightest frame).

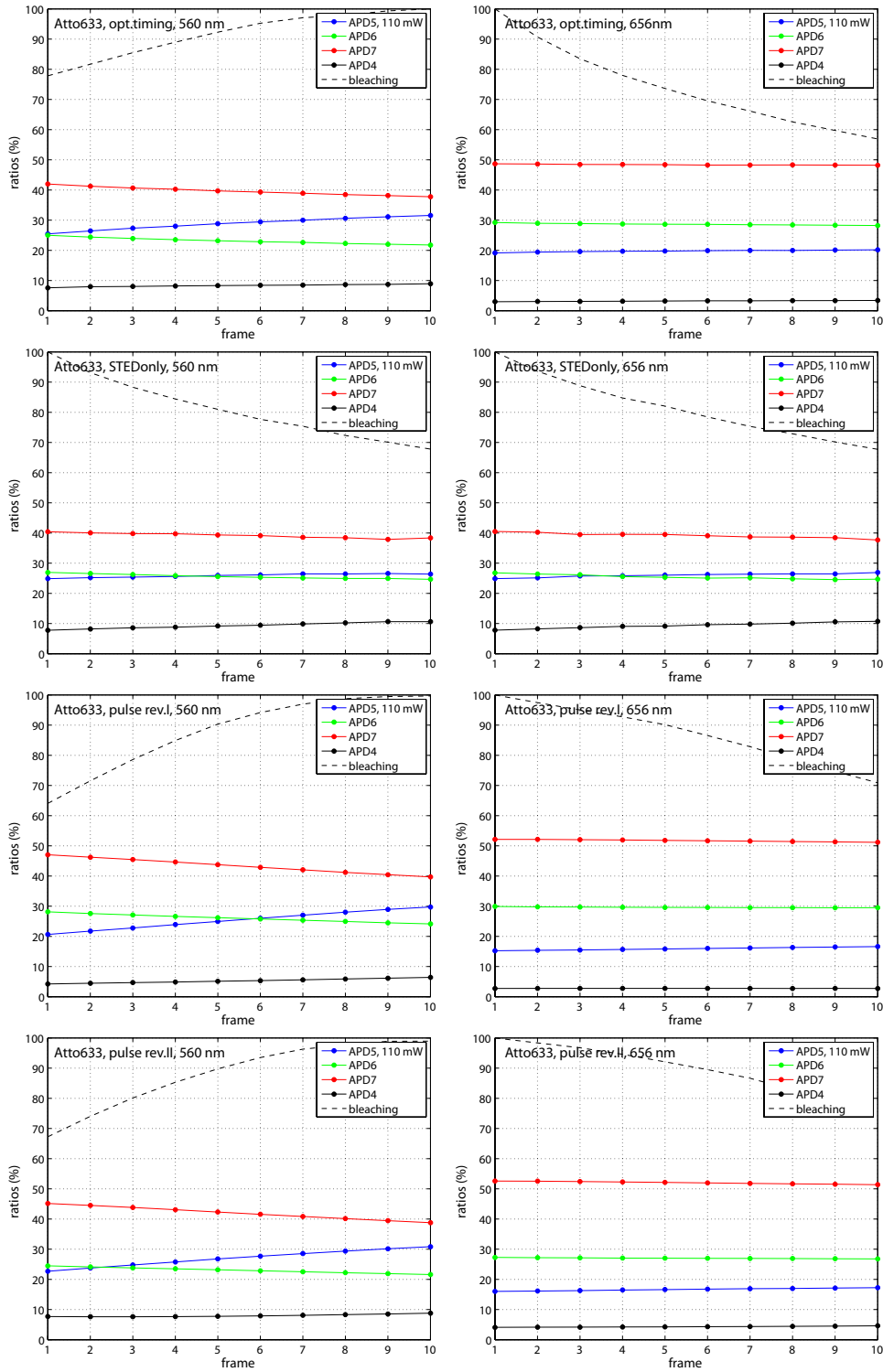


**Figure E.6:** Ratios  $r_i$  in APDs 4–7 for Atto633 over 10 frames for a STED power of 110 mW. The column shows the ratios for 560 nm excitation (left) and 656 nm (right). The rows correspond to the different bleaching conditions. top: opt. timing, second top: STEDonly, the second bottom: pulse rev.I and bottom: rev.II. solid black: ratios of APD4, solid blue: ratios of APD5, solid green: ratios of APD6, solid red: ratios of APD7. dashed black: overall bleaching curve (counts of all APDs combined normalized to the brightest frame).

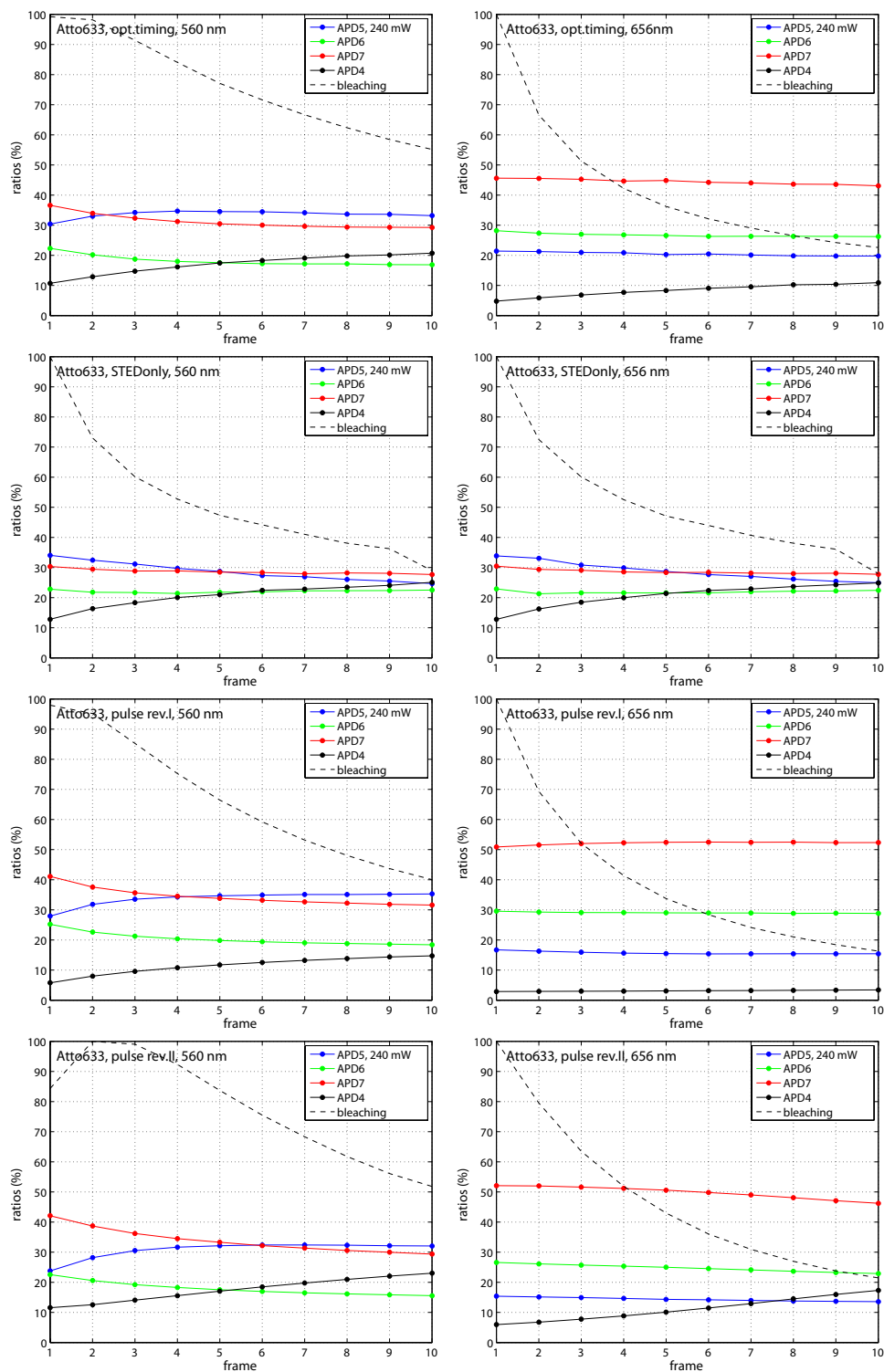


**Figure E.7:** Ratios  $r_i$  in APDs 4–7 for Atto633 over 10 frames for a STED power of 240 mW. The column shows the ratios for 560 nm excitation (left) and 656 nm (right). The rows correspond to the different bleaching conditions. top: opt. timing, second top: STEDonly, the second bottom: pulse rev.I and bottom: rev.II. solid black: ratios of APD4, solid blue: ratios of APD5, solid green: ratios of APD6, solid red: ratios of APD7. dashed black: overall bleaching curve (counts of all APDs combined normalized to the brightest frame).

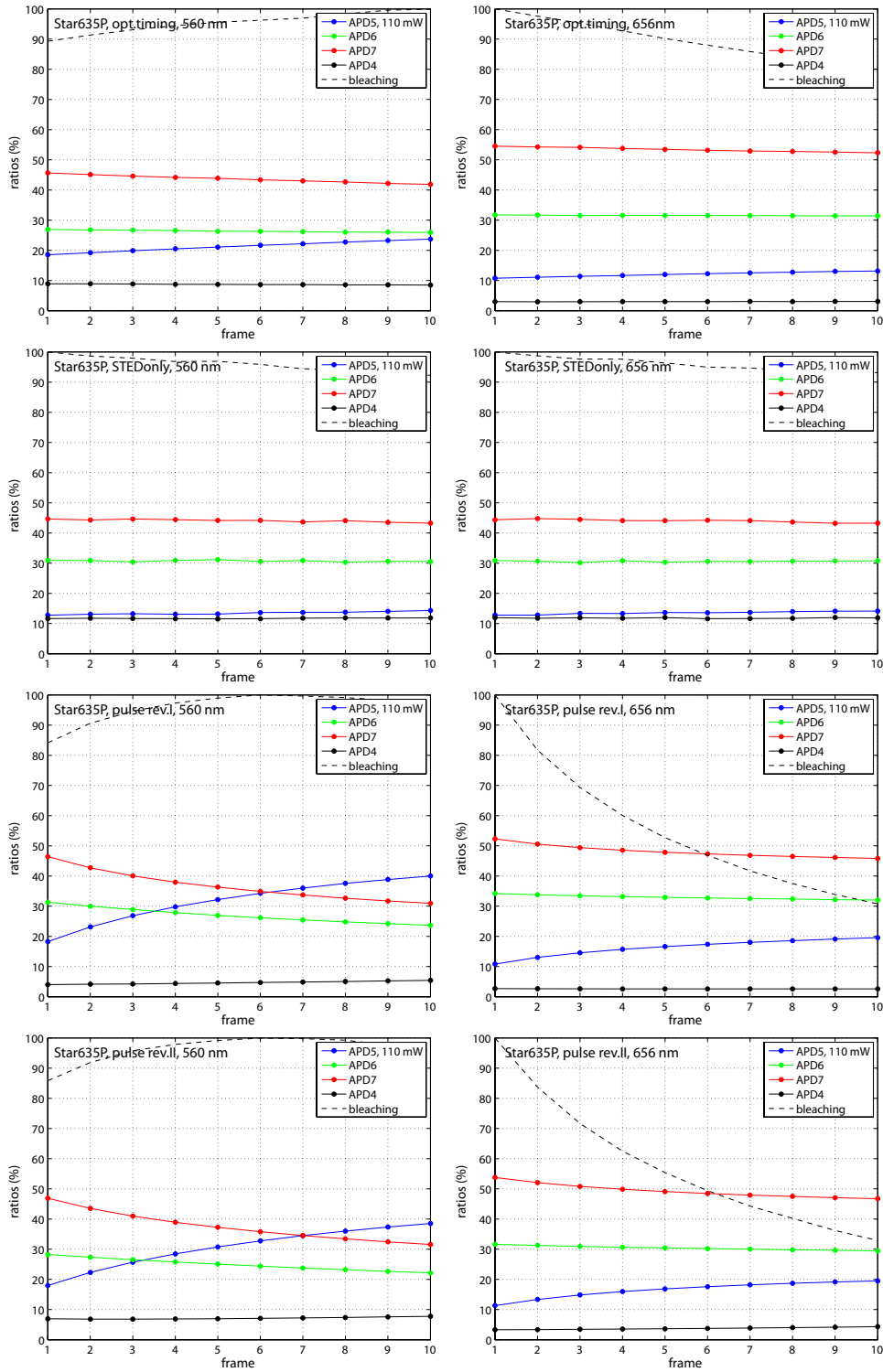


**Figure E.8:** Ratios  $r_i$  in APDs 4–7 for Star635P over 10 frames for a STED power of 110 mW. The column shows the ratios for 560 nm excitation (left) and 656 nm (right). The rows correspond to the different bleaching conditions. top: opt. timing, second top: STEDonly, the second bottom: pulse rev.I and bottom: rev.II. solid black: ratios of APD4, solid blue: ratios of APD5, solid green: ratios of APD6, solid red: ratios of APD7. dashed black: overall bleaching curve (counts of all APDs combined normalized to the brightest frame).

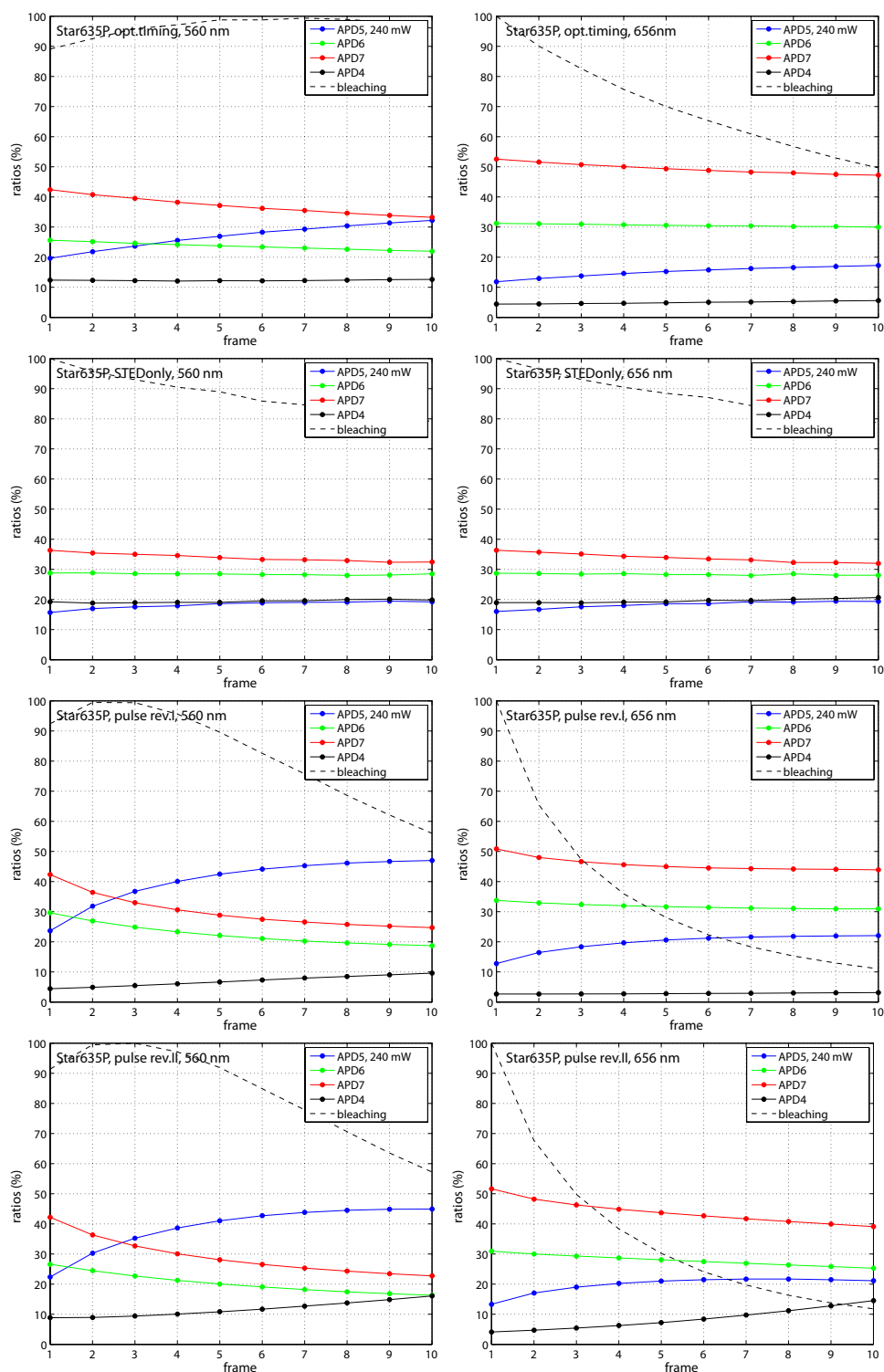


**Figure E.9:** Ratios  $r_i$  in APDs 4–7 for Star635P over 10 frames for a STED power of 240 mW. The column shows the ratios for 560 nm excitation (left) and 656 nm (right). The rows correspond to the different bleaching conditions. top: opt. timing, second top: STEDonly, the second bottom: pulse rev.I and bottom: rev.II. solid black: ratios of APD4, solid blue: ratios of APD5, solid green: ratios of APD6, solid red: ratios of APD7. dashed black: overall bleaching curve (counts of all APDs combined normalized to the brightest frame).

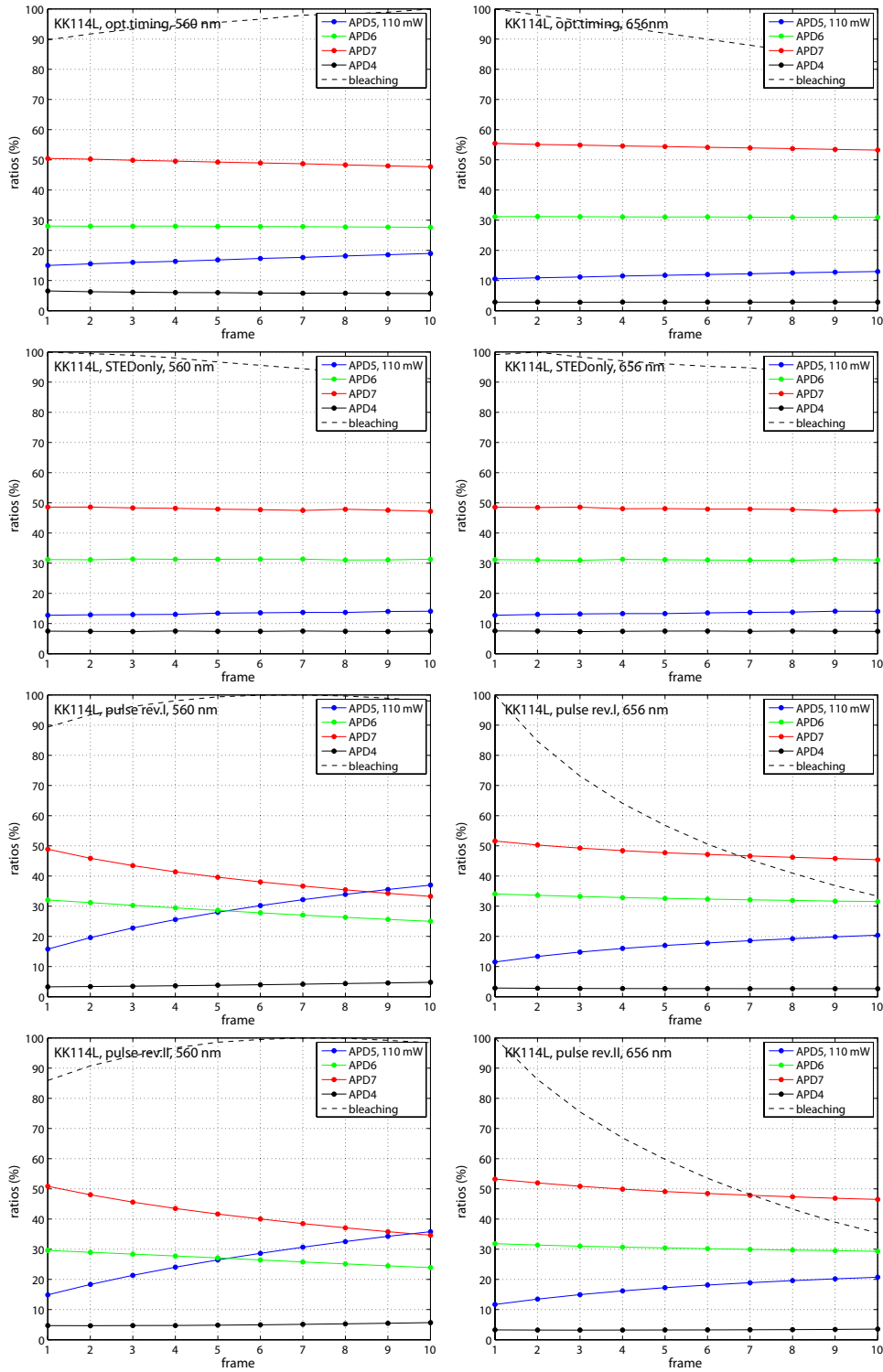


**Figure E.10:** Ratios  $r_i$  in APDs 4–7 for KK114L over 10 frames for a STED power of 110 mW. The column shows the ratios for 560 nm excitation (left) and 656 nm (right). The rows correspond to the different bleaching conditions. top: opt. timing, second top: STEDonly, the second bottom: pulse rev.I and bottom: rev.II. solid black: ratios of APD4, solid blue: ratios of APD5, solid green: ratios of APD6, solid red: ratios of APD7. dashed black: overall bleaching curve (counts of all APDs combined normalized to the brightest frame).

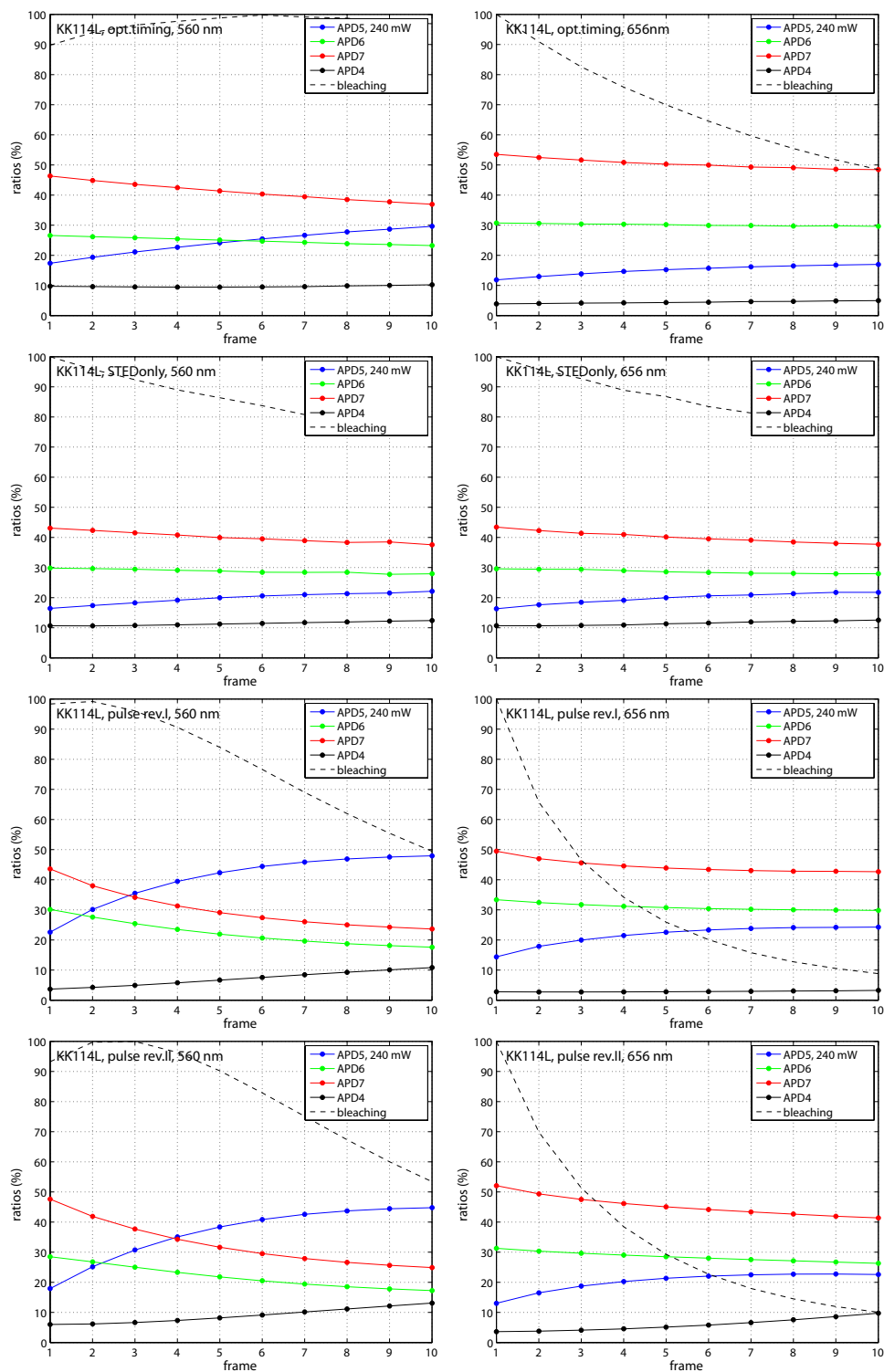


**Figure E.11:** Ratios  $r_i$  in APDs 4–7 for KK114L over 10 frames for a STED power of 240 mW. The column shows the ratios for 560 nm excitation (left) and 656 nm (right). The rows correspond to the different bleaching conditions. top: opt. timing, second top: STEDonly, the second bottom: pulse rev.I and bottom: rev.II. solid black: ratios of APD4, solid blue: ratios of APD5, solid green: ratios of APD6, solid red: ratios of APD7. dashed black: overall bleaching curve (counts of all APDs combined normalized to the brightest frame).

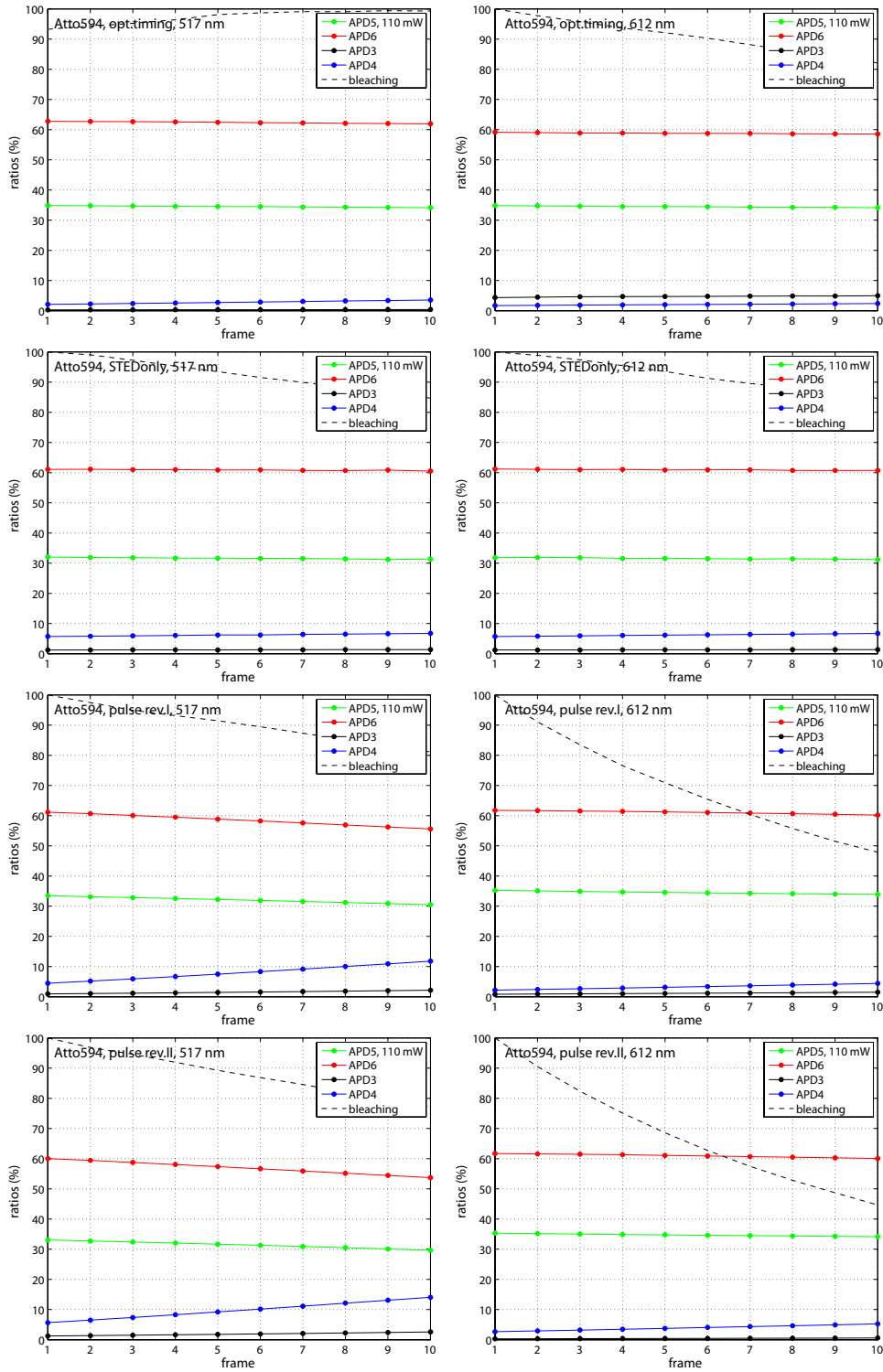


**Figure E.12:** Ratios  $r_i$  in APDs 3–6 for Atto594 over 10 frames for a STED power of 110 mW. The column shows the ratios for 517 nm excitation (left) and 612 nm (right). The rows correspond to the different bleaching conditions. top: opt. timing, second top: STEDonly, the second bottom: pulse rev.I and bottom: rev.II. solid black: ratios of APD3, solid blue: ratios of APD4, solid green: ratios of APD5, solid red: ratios of APD6. dashed black: overall bleaching curve (counts of all APDs combined normalized to the brightest frame).

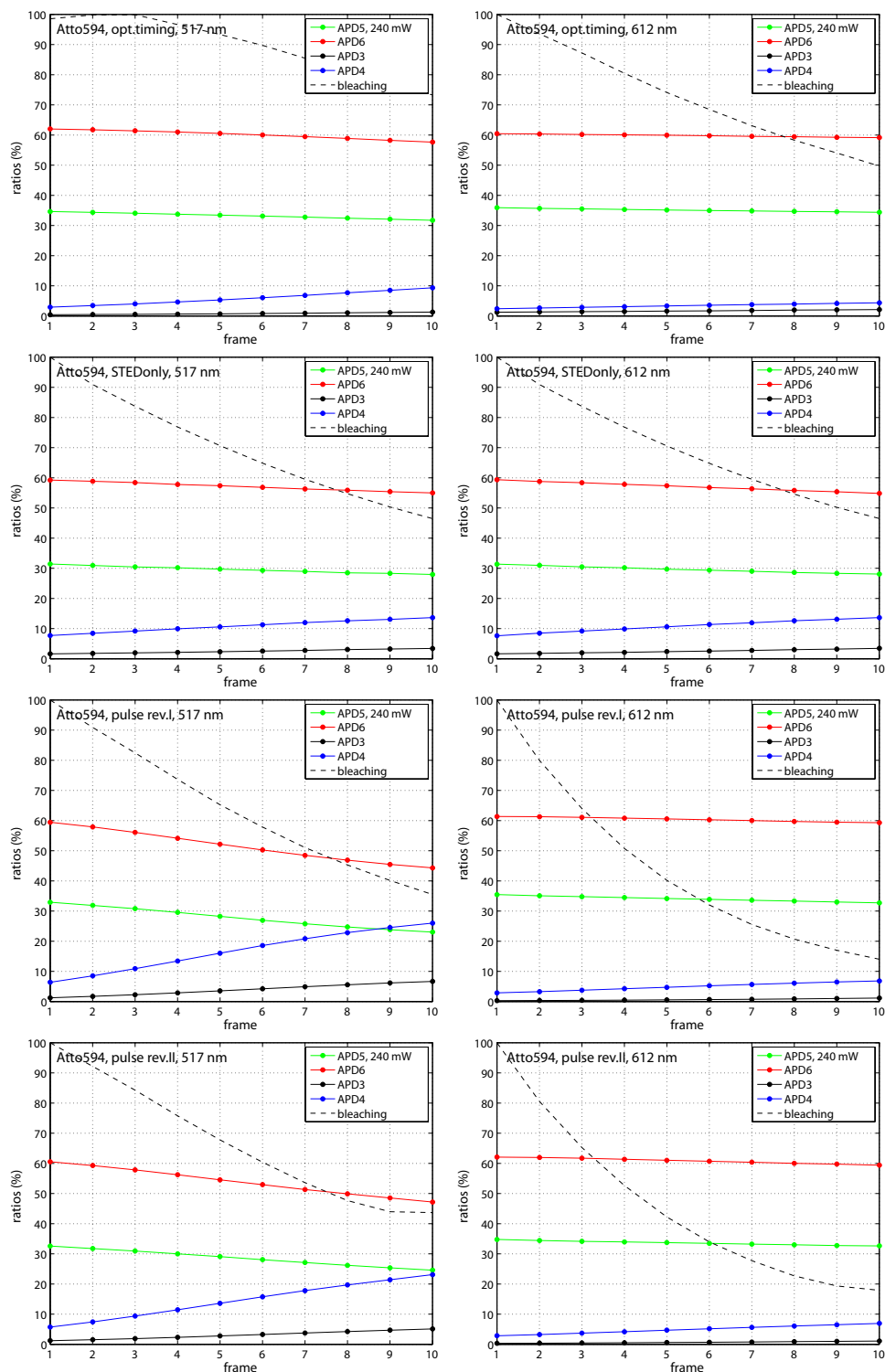


**Figure E.13:** Ratios  $r_i$  in APDs 3–6 for Atto594 over 10 frames for a STED power of 240 mW. The column shows the ratios for 517 nm excitation (left) and 612 nm (right). The rows correspond to the different bleaching conditions. top: opt. timing, second top: STEDonly, the second bottom: pulse rev.I and bottom: rev.II. solid black: ratios of APD3, solid blue: ratios of APD4, solid green: ratios of APD5, solid red: ratios of APD6. dashed black: overall bleaching curve (counts of all APDs combined normalized to the brightest frame).

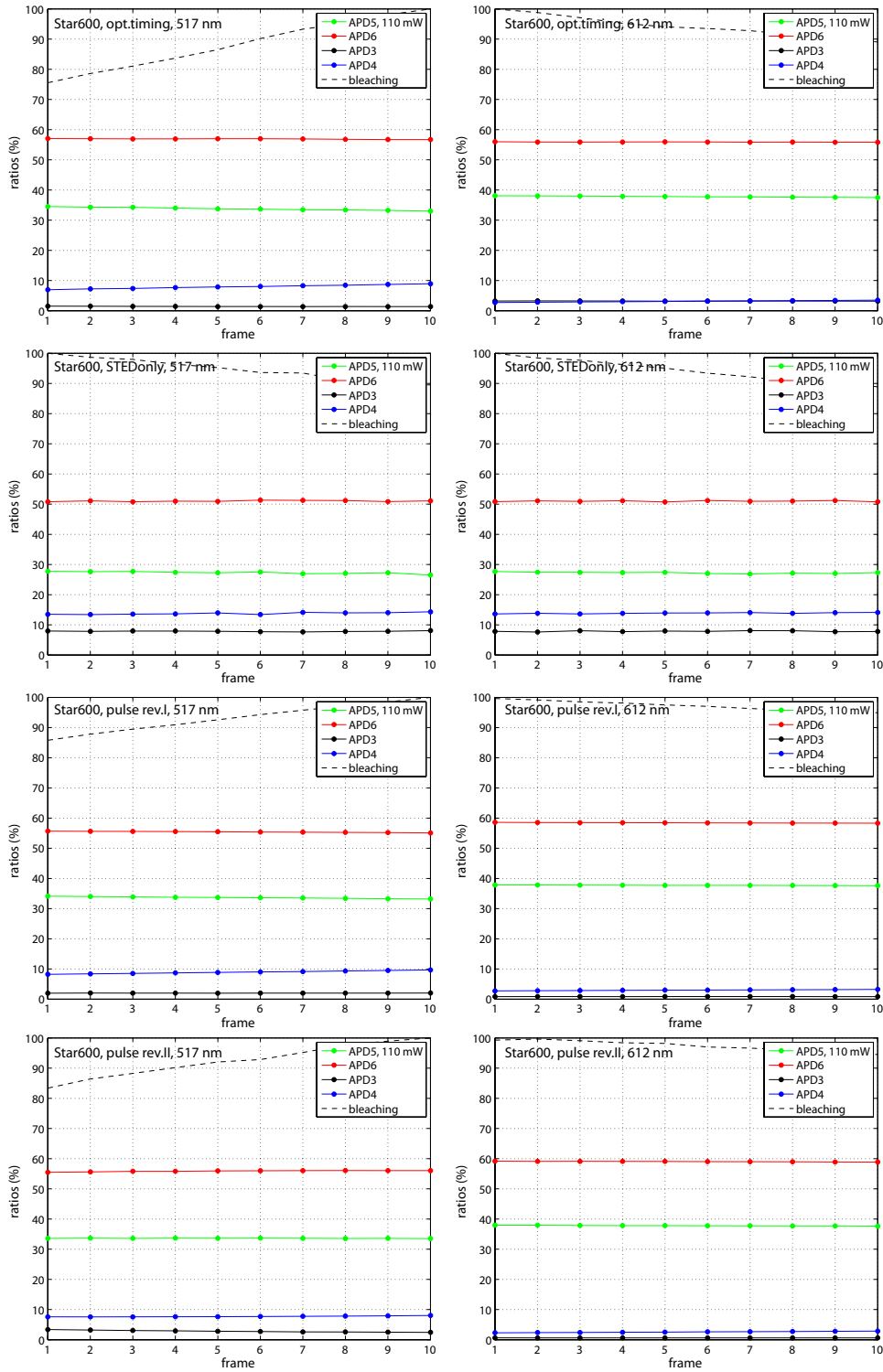


**Figure E.14:** Ratios  $r_i$  in APDs 3–6 for Star600 over 10 frames for a STED power of 110 mW. The column shows the ratios for 517 nm excitation (left) and 612 nm (right). The rows correspond to the different bleaching conditions. top: opt. timing, second top: STEDonly, the second bottom: pulse rev.I and bottom: rev.II. solid black: ratios of APD3, solid blue: ratios of APD4, solid green: ratios of APD5, solid red: ratios of APD6. dashed black: overall bleaching curve (counts of all APDs combined normalized to the brightest frame).

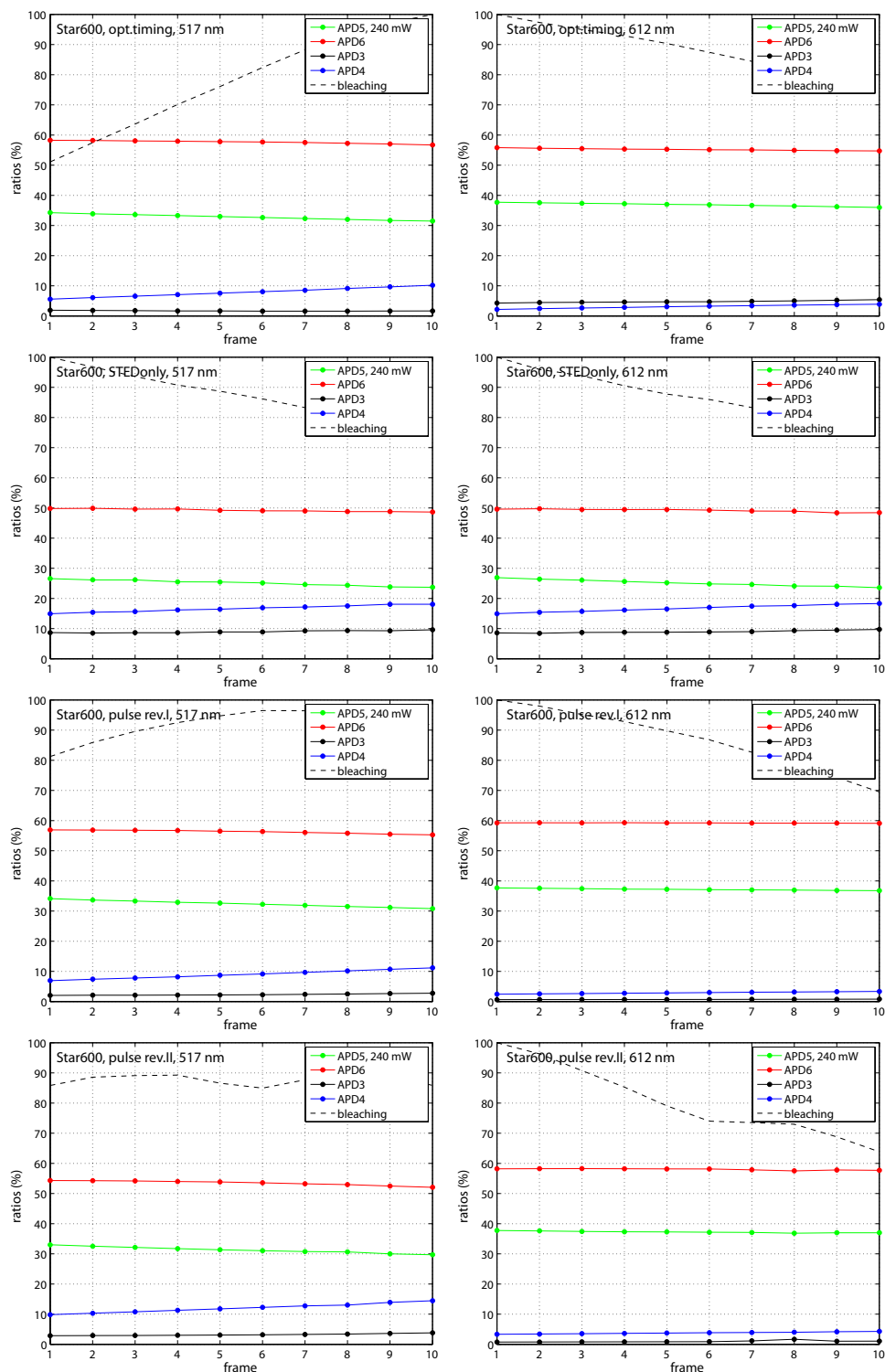


**Figure E.15:** Ratios  $r_i$  in APDs 3–6 for Star600 over 10 frames for a STED power of 240 mW. The column shows the ratios for 517 nm excitation (left) and 612 nm (right). The rows correspond to the different bleaching conditions. top: opt. timing, second top: STEDonly, the second bottom: pulse rev.I and bottom: rev.II. solid black: ratios of APD3, solid blue: ratios of APD4, solid green: ratios of APD5, solid red: ratios of APD6. dashed black: overall bleaching curve (counts of all APDs combined normalized to the brightest frame).

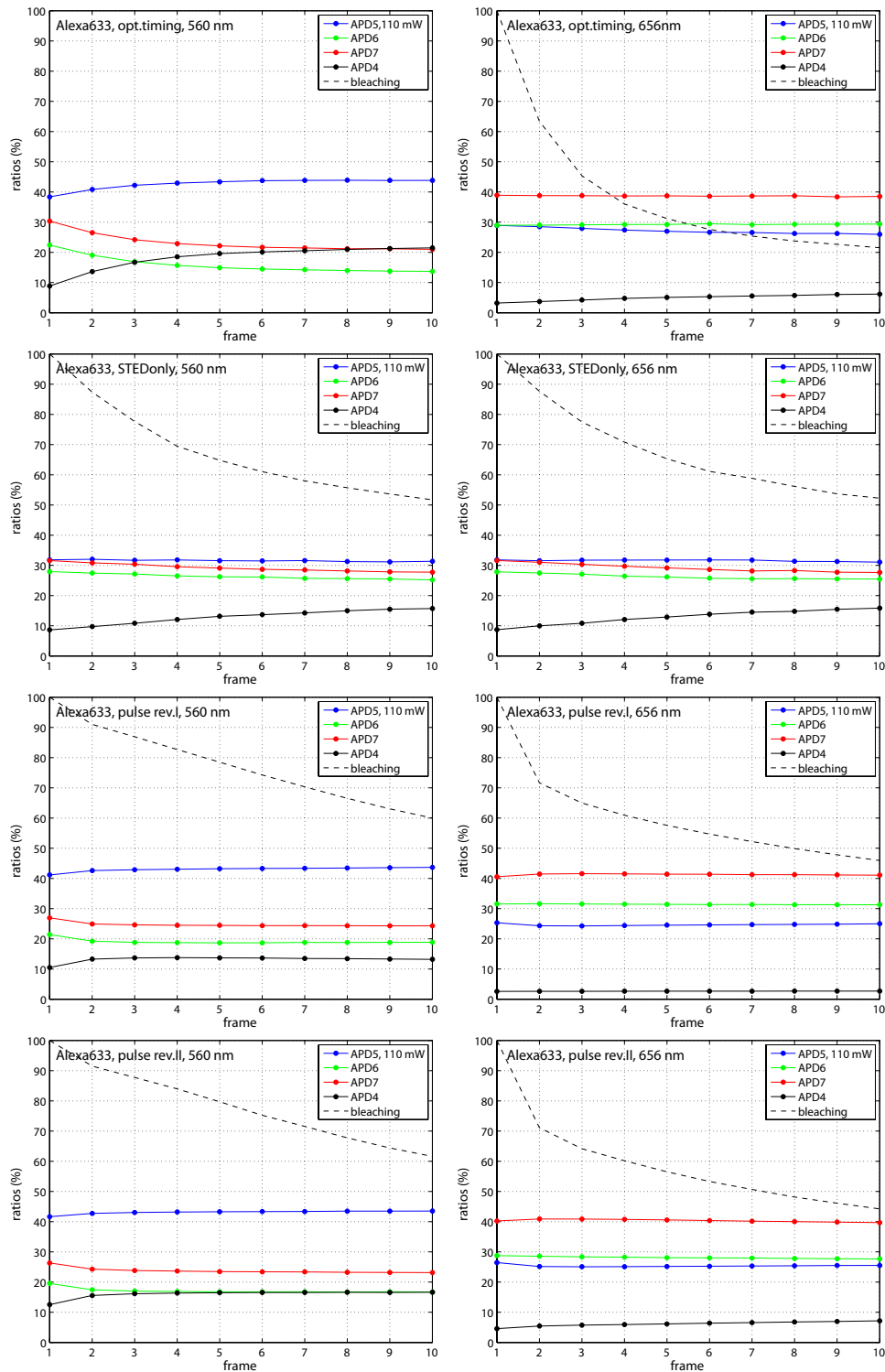


**Figure E.16:** Ratios  $r_i$  in APDs 4–7 for Alexa633 over 10 frames for a STED power of 110 mW. The column shows the ratios for 560 nm excitation (left) and 656 nm (right). The rows correspond to the different bleaching conditions. top: opt. timing, second top: STEDonly, the second bottom: pulse rev.I and bottom: rev.II. solid black: ratios of APD4, solid blue: ratios of APD5, solid green: ratios of APD6, solid red: ratios of APD7. dashed black: overall bleaching curve (counts of all APDs combined normalized to the brightest frame).

# Bibliography

- [1] *Geschichte der Mikroskopie - Meilensteine*. [http://www.zeiss.de/corporate/de\\_de/geschichte/technische-meilensteine/mikroskopie.html#{}meilensteine](http://www.zeiss.de/corporate/de_de/geschichte/technische-meilensteine/mikroskopie.html#{}meilensteine).
- [2] E. Abbe. *Beiträge zur Theorie des Mikroskops und der mikroskopischen Wahrnehmung*. Arch. Mikr. Anat., 1873.
- [3] D. Aquino, A. Schonle, C. Geisler, C. v. Middendorff, C. A. Wurm, Y. Okamura, T. Lang, S. W. Hell, and A. Egner. *Two-color nanoscopy of three-dimensional volumes by  $4\pi$  detection of stochastically switched fluorophores*. Nat Meth, 8(4):353–359, Apr. 2011.
- [4] E. Auksorius, B. R. Boruah, C. Dunsby, P. M. P. Lanigan, G. Kennedy, M. A. A. Neil, and P. M. W. French. *Stimulated emission depletion microscopy with a supercontinuum source and fluorescence lifetime imaging*. Opt. Lett., 33(2):113–115, Jan. 2008.
- [5] M. Bates, B. Huang, G. T. Dempsey, and X. Zhuang. *Multicolor Super-Resolution Imaging with Photo-Switchable Fluorescent Probes*. Science, 317(5845):1749–1753, Sept. 2007.
- [6] F. Bergermann, L. Alber, S. J. Sahl, J. Engelhardt, and S. W. Hell. *2000-fold parallelized dual-color STED fluorescence nanoscopy*. Opt. Express, 23(1):211–223, Jan 2015.
- [7] S. Berning, K. I. Willig, H. Steffens, P. Dibaj, and S. W. Hell. *Nanoscopy in a Living Mouse Brain*. Science, 335(6068):551–551, Feb. 2012.
- [8] E. Betzig, G. H. Patterson, R. Sougrat, O. W. Lindwasser, S. Olenych, J. S. Bonifacino, M. W. Davidson, J. Lippincott-Schwartz, and H. F. Hess. *Imaging Intracellular Fluorescent Proteins at Nanometer Resolution*. Science, 313(5793):1642–1645, Sept. 2006.
- [9] P. Bingen. *Parallelised STED nanoscopy*. PhD thesis, Ruperto-Carola University of Heidelberg, 2012.

- 
- [10] P. Bingen, M. Reuss, J. Engelhardt, and S. W. Hell. *Parallelized STED fluorescence nanoscopy*. *Opt. Express*, 19(24):23716–23726, Nov 2011.
- [11] C. M. Bishop. *Pattern Recognition and Machine Learning*. Springer, 2006.
- [12] H. Bock, C. Geisler, C. Wurm, C. von Middendorff, S. Jakobs, A. Schönle, A. Egner, S. Hell, and C. Eggeling. *Two-color far-field fluorescence nanoscopy based on photoswitchable emitters*. *Applied Physics B*, 88(2):161–165, 2007.
- [13] M. Bossi, J. Fölling, V. N. Belov, V. P. Boyarskiy, R. Medda, A. Egner, C. Eggeling, A. Schönle, and S. W. Hell. *Multicolor Far-Field Fluorescence Nanoscopy through Isolated Detection of Distinct Molecular Species*. *Nano Letters*, 8(8):2463–2468, 2008.
- [14] I. N. Bronstein, K. A. Semendjajew, and G. Musiol. *Taschenbuch der Mathematik*. Deutsch (Harri), Aug. 2005.
- [15] J. Bückers, D. Wildanger, G. Vicidomini, L. Kastrup, and S. W. Hell. *Simultaneous multi-lifetime multi-color STED imaging for colocalization analyses*. *Opt. Express*, 19(4):3130–3143, Feb. 2011.
- [16] I. C. Chang. *Tunable Acousto-Optic Filters: An Overview*. *Optical Engineering*, 16(5), 1977.
- [17] I. C. Chang. *Acousto-Optic Tunable Filters*. *Optical Engineering*, 20(6), 1981.
- [18] P. J. Cutler, M. D. Malik, S. Liu, J. M. Byars, D. S. Lidke, and K. A. Lidke. *Multi-Color Quantum Dot Tracking Using a High-Speed Hyperspectral Line-Scanning Microscope*. *PLoS ONE*, 8(5), May 2013.
- [19] G. T. Dempsey, J. C. Vaughan, K. H. Chen, M. Bates, and X. Zhuang. *Evaluation of fluorophores for optimal performance in localization-based super-resolution imaging*. *Nat Meth*, 8(12):1027–1036, Dec. 2011.
- [20] E. D’Este, D. Kamin, F. Göttfert, A. El-Hady, and S. Hell. *STED Nanoscopy Reveals the Ubiquity of Subcortical Cytoskeleton Periodicity in Living Neurons*. *Cell Reports*, 10(8):1246 – 1251, 2015.
- [21] G. Donnert, J. Keller, R. Medda, M. A. Andrei, S. O. Rizzoli, R. Lührmann, R. Jahn, C. Eggeling, and S. W. Hell. *Macromolecular-scale resolution in biological fluorescence microscopy*. *Proceedings of the National Academy of Sciences*, 103(31):11440–11445, Aug. 2006.
- [22] G. Donnert, J. Keller, C. A. Wurm, S. O. Rizzoli, V. Westphal, A. Schönle, R. Jahn, S. Jakobs, C. Eggeling, and S. W. Hell. *Two-Color Far-Field Fluorescence Nanoscopy*. *Biophysical Journal*, 92(8), 2007.

- [23] J. Engelhardt. *Verfahren und Vorrichtung zur dynamischen Verlagerung eines Lichtstrahls gegenüber einer den Lichtstrahl fokussierenden Optik*, June 2010.
- [24] H. J. Falk. *Multi-label combinations for long-wave STED Microscopy with a single depletion wavelength*. Master's thesis, Ruprecht-Karls-Universität Heidelberg, 2013.
- [25] F. Fereidouni, A. N. Bader, and H. C. Gerritsen. *Spectral phasor analysis allows rapid and reliable unmixing of fluorescence microscopy spectral images*. *Opt. Express*, 20(12):12729–12741, 2012.
- [26] J. Fölling, M. Bossi, H. Bock, R. Medda, C. A. Wurm, B. Hein, S. Jakobs, C. Eggeling, and S. W. Hell. *Fluorescence nanoscopy by ground-state depletion and single-molecule return*. *Nat Meth*, 5(11):943–945, Nov. 2008.
- [27] A. Gautier, A. Juillerat, C. Heinis, I. R. C. Jr., M. Kindermann, F. Beaufils, and K. Johnsson. *An Engineered Protein Tag for Multiprotein Labeling in Living Cells*. *Chemistry & Biology*, 15(2):128 – 136, 2008.
- [28] C. Geisler, A. Schönle, C. von Middendorff, H. Bock, C. Eggeling, A. Egner, and S. Hell. *Resolution of  $\lambda/10$  in fluorescence microscopy using fast single molecule photo-switching*. *Applied Physics A*, 88(2):223–226, 2007.
- [29] F. Goerlitz, P. Hoyer, H. Falk, L. Kastrop, J. Engelhardt, and S. W. Hell. *A STED microscope designed for routine biomedical applications*. *Progress in Electromagnetics Research*, 147:57–68, 2014.
- [30] J. Goldstein. *Scanning Electron Microscopy and X-ray Microanalysis: Third Edition*. Springer US, 2003.
- [31] F. Görlitz. *Aufbau eines mehrkanaligen STED Mikroskops für biomedizinische Anwendungen*. Master's thesis, Ruprecht-Karls-Universität Heidelberg, 2013.
- [32] F. Göttfert, C. Wurm, V. Mueller, S. Berning, V. Cordes, A. Honigmann, and S. Hell. *Coaligned Dual-Channel STED Nanoscopy and Molecular Diffusion Analysis at 20 nm Resolution*. *Biophysical Journal*, 105(1):L01–L03, May 2013.
- [33] L. Große. *Untersuchung der sub-mitochondrialen Proteinverteilung von MICOS mittels STED-Mikroskopie*. PhD thesis, Georg-August-Universität Göttingen, 2015.
- [34] D. M. Haaland, H. D. T. Jones, M. H. V. Benthem, M. B. Sinclair, D. K. Melgaard, C. L. Stork, M. C. Pedroso, P. Liu, A. R. Brasier, N. L. Andrews, and D. S. Lidke. *Hyperspectral Confocal Fluorescence Imaging: Exploring Alternative Multivariate Curve Resolution Approaches*. *Appl. Spectrosc.*, 63(3):271–279, Mar. 2009.

- [35] D. M. Haaland, J. A. Timlin, M. B. Sinclair, M. H. Van Benthem, M. J. Martinez, A. D. Aragon, and M. Werner-Washburne. *Multivariate curve resolution for hyperspectral image analysis: applications to microarray technology*. Proc. SPIE, 4959:55–66, 2003.
- [36] J. Hanne, H. J. Falk, F. Gorlitz, P. Hoyer, J. Engelhardt, S. J. Sahl, and S. W. Hell. *STED nanoscopy with fluorescent quantum dots*. Nat Commun, 6, May 2015.
- [37] B. Harke, J. Keller, C. K. Ullal, V. Westphal, A. Schönle, and S. W. Hell. *Resolution scaling in STED microscopy*. Opt. Express, 16(6):4154–4162, Mar. 2008.
- [38] E. Hecht. *Optics*. Addison-Wesley, 2002.
- [39] S. Hell and M. Kroug. *Ground-state-depletion fluorescence microscopy: A concept for breaking the diffraction resolution limit*. Applied Physics B, 60(5):495–497, 1995.
- [40] S. W. Hell. *Far-Field Optical Nanoscopy*. Science, 316(5828):1153–1158, 2007.
- [41] S. W. Hell. *Microscopy and its focal switch*. Nat Meth, 6(1):24–32, Jan. 2009.
- [42] S. W. Hell. *Nanoscopy with focused light*. Annalen der Physik, 2015.
- [43] S. W. Hell. *Nanoscopy with Focused Light (Nobel Lecture)*. Angewandte Chemie International Edition, 54(28):8054–8066, 2015.
- [44] S. W. Hell, M. Dyba, and S. Jakobs. *Concepts for nanoscale resolution in fluorescence microscopy*. Current Opinion in Neurobiology, 14(5):599 – 609, 2004.
- [45] S. W. Hell and J. Wichmann. *Breaking the diffraction resolution limit by stimulated emission: stimulated-emission-depletion fluorescence microscopy*. Opt. Lett., 19(11):780–782, June 1994.
- [46] S. W. Hell, K. Willig, and V. Westphal. *Fluoreszenzmikroskopie ohne Beugungsgrenze*. BIOSpektrum, 2006.
- [47] R. Jungmann, M. S. Avendano, J. B. Woehrstein, M. Dai, W. M. Shih, and P. Yin. *Multiplexed 3D cellular super-resolution imaging with DNA-PAINT and Exchange-PAINT*. Nat Meth, 11(3):313–318, Mar. 2014.
- [48] J. Keller. *Optimal de-excitation patterns for RESOLFT-Microscopy*. PhD thesis, Ruperto-Carola University of Heidelberg, 2006.

- [49] C. Kempf, T. Staudt, P. Bingen, H. Horstmann, J. Engelhardt, S. W. Hell, and T. Kuner. *Tissue Multicolor STED Nanoscopy of Presynaptic Proteins in the Calyx of Held*. PLoS ONE, 8(4), Apr. 2013.
- [50] A. Keppler, S. Gendreizig, T. Gronemeyer, H. Pick, H. Vogel, and K. Johnson. *A general method for the covalent labeling of fusion proteins with small molecules in vivo*. Nat Biotech, 21(1):86–89, Jan. 2003.
- [51] T. A. Klar, E. Engel, and S. W. Hell. *Breaking Abbe’s diffraction resolution limit in fluorescence microscopy with stimulated emission depletion beams of various shapes*. Phys. Rev. E, 64, Nov. 2001.
- [52] K. Kolmakov, E. Hebisch, T. Wolfram, L. A. Nordwig, C. A. Wurm, H. Ta, V. Westphal, V. N. Belov, and S. W. Hell. *Far-Red Emitting Fluorescent Dyes for Optical Nanoscopy: Fluorinated Silicon-Rhodamines (SiRF Dyes) and Phosphorylated Oxazines*. Chemistry A European Journal, 2015.
- [53] J. Lakowicz. *Principles of Fluorescence Spectroscopy*. Springer US, 2007.
- [54] F. Lavoie-Cardinal, N. A. Jensen, V. Westphal, A. C. Stiel, A. Chmyrov, J. Bierwagen, I. Testa, S. Jakobs, and S. W. Hell. *Two-Color RESOLFT Nanoscopy with Green and Red Fluorescent Photochromic Proteins*. ChemPhysChem, 15(4):655–663, 2014.
- [55] D. Lee and H. Seung. *Algorithms for non-negative matrix factorization*. Adv. Neural Info. Proc. Syst., 13:556–562, 2001.
- [56] P. Lemmer, M. Gunkel, D. Baddeley, R. Kaufmann, A. Urich, Y. Weiland, J. Reymann, P. Müller, M. Hausmann, and C. Cremer. *SPDM: light microscopy with single-molecule resolution at the nanoscale*. Applied Physics B, 93(1):1–12, 2008.
- [57] M. Leutenegger, C. Eggeling, and S. W. Hell. *Analytical description of STED microscopy performance*. Opt. Express, 18(25):26417–26429, Dec 2010.
- [58] D. S. Lidke, N. L. Andrews, J. R. Pfeiffer, H. D. Jones, M. B. Sinclair, D. M. Haaland, A. R. Burns, B. S. Wilson, J. M. Oliver, and K. A. Lidke. *Exploring membrane protein dynamics by multicolor single quantum dot imaging using wide field, TIRF, and hyperspectral microscopy*. Proc. of SPIE, 6448, 2007.
- [59] M. Loidolt. *Mehrfarben-STED-Mikroskopie*. Master’s thesis, Technische Universität Kaiserslautern, 2013.
- [60] G. V. Los, L. P. Encell, M. G. McDougall, D. D. Hartzell, N. Karassina, C. Zimprich, M. G. Wood, R. Learish, R. F. Ohana, M. Urh, D. Simpson, J. Mendez, K. Zimmerman, P. Otto, G. Vidugiris, J. Zhu, A. Darzins, D. H. Klaubert, R. F. Bulleit, and K. V. Wood. *HaloTag: A Novel Protein Labeling Technology*

- for Cell Imaging and Protein Analysis*. ACS Chemical Biology, 3(6):373–382, 2008.
- [61] G. Lukinavicius, L. Reymond, E. D’Este, A. Masharina, F. Gottfert, H. Ta, A. Guthier, M. Fournier, S. Rizzo, H. Waldmann, C. Blaukopf, C. Sommer, D. W. Gerlich, H.-D. Arndt, S. W. Hell, and K. Johnsson. *Fluorogenic probes for live-cell imaging of the cytoskeleton*. Nat Meth, 11(7):731–733, July 2014.
- [62] G. Lukinavičius, K. Umezawa, N. Olivier, A. Honigmann, G. Yang, T. Plass, V. Mueller, L. Reymond, I. R. Corrêa Jr, Z.-G. Luo, C. Schultz, E. A. Lemke, P. Heppenstall, C. Eggeling, S. Manley, and K. Johnsson. *A near-infrared fluorophore for live-cell super-resolution microscopy of cellular proteins*. Nat Chem, 5(2):132–139, Feb. 2013.
- [63] D. J. C. MacKay. *Information Theory, Inference & Learning Algorithms*. Cambridge University Press, New York, NY, USA, 2005.
- [64] L. Meyer, D. Wildanger, R. Medda, A. Punge, S. O. Rizzoli, G. Donnert, and S. W. Hell. *Dual-Color STED Microscopy at 30-nm Focal-Plane Resolution*. Small, 4(8):1095–1100, 2008.
- [65] G. Y. Mitronova, S. Polyakova, C. A. Wurm, K. Kolmakov, T. Wolfram, D. N. H. Meineke, V. N. Belov, M. John, and S. W. Hell. *Functionalization of the meso-Phenyl Ring of Rhodamine Dyes Through SNAr with Sulfur Nucleophiles: Synthesis, Biophysical Characterizations, and Comprehensive NMR Analysis*. European Journal of Organic Chemistry, 2015(2):337–349, 2015.
- [66] J. J. Moré. *The Levenberg-Marquardt algorithm: implementation and theory*. In *Numerical analysis*, pages 105–116. Springer, 1978.
- [67] S. Muyldermans. *Nanobodies: Natural Single-Domain Antibodies*. Annual Review of Biochemistry, 82(1):775–797, 2013.
- [68] R. Neher and E. Neher. *Optimizing imaging parameters for the separation of multiple labels in a fluorescence image*. Journal of Microscopy, 213(1):46–62, 2004.
- [69] R. A. Neher. *Documentation PoissonNMF*. <https://neherlab.wordpress.com/poissonnmf-documentation/>.
- [70] R. A. Neher, M. Mitkovski, F. Kirchhoff, E. Neher, F. J. Theis, and A. Zeug. *Blind Source Separation Techniques for the Decomposition of Multiply Labeled Fluorescence Images*. Biophysical Journal, 96(9):3791 – 3800, 2009.
- [71] D. Neumann, J. Buckers, L. Kastrup, S. Hell, and S. Jakobs. *Two-color STED microscopy reveals different degrees of colocalization between hexokinase-I and the three human VDAC isoforms*. PMC Biophysics, 3(1), 2010.

- [72] Nobelprize.org. *The Nobel Prize in Chemistry 2014 - Press Release*. [http://www.nobelprize.org/nobel\\_prizes/chemistry/laureates/2014/press.html](http://www.nobelprize.org/nobel_prizes/chemistry/laureates/2014/press.html), 2014.
- [73] J. Pawley. *Handbook of Biological Confocal Microscopy*. Springer US, 2006.
- [74] P. A. Pellett, X. Sun, T. J. Gould, J. E. Rothman, M.-Q. Xu, I. R. Corrêa, and J. Bewersdorf. *Two-color STED microscopy in living cells*. *Biomed. Opt. Express*, 2(8):2364–2371, Aug 2011.
- [75] M. Ratz, I. Testa, S. W. Hell, and S. Jakobs. *CRISPR/Cas9-mediated endogenous protein tagging for RESOLFT super-resolution microscopy of living human cells*. *Scientific Reports*, 5, Apr. 2015.
- [76] D. Rönnlund. *Super resolution optical imaging - image analysis, mulicolor development and biological applications*. PhD thesis, KTH Engineering Sciences, 2014.
- [77] D. Rönnlund, L. Xu, A. Perols, A. K. B. Gad, A. Eriksson Karlström, G. Auer, and J. Widengren. *Multicolor Fluorescence Nanoscopy by Photobleaching: Concept, Verification, and Its Application To Resolve Selective Storage of Proteins in Platelets*. *ACS Nano*, 8(5):4358–4365, 2014.
- [78] E. Ronzitti, B. Harke, and A. Diaspro. *Frequency dependent detection in a STED microscope using modulated excitation light*. *Opt. Express*, 21(1):210–219, Jan 2013.
- [79] M. J. Rust, M. Bates, and X. Zhuang. *Sub-diffraction-limit imaging by stochastic optical reconstruction microscopy (STORM)*. *Nat Meth*, 3(10):793–796, Oct. 2006.
- [80] M. Sauer. *Reversible molecular photoswitches: A key technology for nanoscience and fluorescence imaging*. *Proceedings of the National Academy of Sciences of the United States of America*, 102(27):9433–9434, July 2005.
- [81] R. Schmidt, C. A. Wurm, S. Jakobs, J. Engelhardt, A. Egner, and S. W. Hell. *Spherical nanosized focal spot unravels the interior of cells*. *Nat Meth*, 5(6):539–544, June 2008.
- [82] I. Semrock. *Filter Spectra at Non-normal Angles of Incidence*. <http://www.semrock.com/filter-spectra-at-non-normal-angles-of-incidence.aspx>.
- [83] A. Sharonov and R. M. Hochstrasser. *Wide-field subdiffraction imaging by accumulated binding of diffusing probes*. *Proceedings of the National Academy of Sciences*, 103(50):18911–18916, Dec. 2006.

- [84] H. Shroff, C. G. Galbraith, J. A. Galbraith, H. White, J. Gillette, S. Olenych, M. W. Davidson, and E. Betzig. *Dual-color superresolution imaging of genetically expressed probes within individual adhesion complexes*. Proceedings of the National Academy of Sciences, 104(51):20308–20313, Dec. 2007.
- [85] M. B. Sinclair, D. M. Haaland, J. A. Timlin, and H. D. T. Jones. *Hyperspectral confocal microscope*. Appl. Opt., 45(24):6283–6291, Aug 2006.
- [86] M. B. Sinclair, J. A. Timlin, D. M. Haaland, and M. Werner-Washburne. *Design, construction, characterization, and application of a hyperspectral microarray scanner*. Appl. Opt., 43(10):2079–2088, Apr 2004.
- [87] F. Stagge, G. Y. Mitronova, V. N. Belov, C. A. Wurm, and S. Jakobs. *Snap-, CLIP- and Halo-Tag Labelling of Budding Yeast Cells*. PLoS ONE, 8(10):e78745, Oct. 2013.
- [88] F. V. Subach, G. H. Patterson, S. Manley, J. M. Gillette, J. Lippincott-Schwartz, and V. V. Verkhusha. *Photoactivatable mCherry for high-resolution two-color fluorescence microscopy*. Nat Meth, 6(2):153–159, Feb. 2009.
- [89] A. Szymborska, A. de Marco, N. Daigle, V. C. Cordes, J. A. G. Briggs, and J. Ellenberg. *Nuclear Pore Scaffold Structure Analyzed by Super-Resolution Microscopy and Particle Averaging*. Science, 341(6146):655–658, Aug. 2013.
- [90] I. Testa, E. D’Este, N. T. Urban, F. Balzarotti, and S. W. Hell. *Dual Channel RESOLFT Nanoscopy by Using Fluorescent State Kinetics*. Nano Letters, 15(1):103–106, 2015.
- [91] I. Testa, C. A. Wurm, R. Medda, E. Rothermel, C. von Middendorf, J. Fölling, S. Jakobs, A. Schönle, S. W. Hell, and C. Eggeling. *Multicolor Fluorescence Nanoscopy in Fixed and Living Cells by Exciting Conventional Fluorophores with a Single Wavelength*. Biophysical Journal, 99(8):2686 – 2694, 2010.
- [92] J. Tønnesen, F. Nadrigny, K. Willig, R. Wedlich-Söldner, and U. Nägerl. *Two-Color STED Microscopy of Living Synapses Using A Single Laser-Beam Pair*. Biophysical Journal, 101(10):2545–2552, Oct. 2011.
- [93] G. Vicidomini, G. Moneron, K. Y. Han, V. Westphal, H. Ta, M. Reuss, J. Engelhardt, C. Eggeling, and S. W. Hell. *Sharper low-power STED nanoscopy by time gating*. Nat Meth, 8(7):571–573, July 2011.
- [94] V. Westphal, S. O. Rizzoli, M. A. Lauterbach, D. Kamin, R. Jahn, and S. W. Hell. *Video-Rate Far-Field Optical Nanoscopy Dissects Synaptic Vesicle Movement*. Science, 320(5873):246–249, Apr. 2008.

- 
- [95] Z. Zhang, S. J. Kenny, M. Hauser, W. Li, and K. Xu. *Ultrahigh-throughput single-molecule spectroscopy and spectrally resolved super-resolution microscopy*. *Nat Meth*, 12(10):935–938, Oct. 2015.
- [96] T. Zimmermann. *Spectral Imaging and Linear Unmixing in Light Microscopy*. In J. Rietdorf, editor, *Microscopy Techniques*, volume 95 of *Advances in Biochemical Engineering*, pages 245–265. Springer Berlin Heidelberg, 2005.



# Acknowledgements

Es gibt eine Menge Leute, ohne die die letzten fast fünf Jahre nicht möglich gewesen wären, die es vollbrachten sich mit mir über Erfolge zu freuen und mir halben Niederlagen mit Humor leichter wegzustecken. Es war eine Erfahrung und Bereicherung meines Lebens in einer derart exzellenten interdisziplinären Umgebung zu arbeiten, zu lernen, Wissenschaft zu betreiben und Freunde zu finden.

Zu allererst möchte ich mich bei Stefan W. Hell für die Möglichkeit bedanken meine Promotion in seiner Arbeitsgruppe durchführen zu dürfen. Seine Ideen, Ratschläge und Einsichten waren maßgeblich für den Erfolg dieses Projektes.

Zudem gilt mein besonderer Dank Volker Westphal und Lars Kastrup, die mir in allen konzeptionellen und technischen Fragen mit Rat und Tat zur Seite standen, nie um eine Diskussion verlegen waren, um das beste aus allem herauszuholen.

Ein weiteres großes Dankeschön gilt Ellen Rothermel und Tanja Gilat, die nicht nur alle Antikörper verwalten, aliquotieren, koppeln und katalogisieren sondern die auch mit ihrer großen Erfahrung wesentlich dazu beigetragen haben, das Färbeprotokoll zu optimieren und die schönste Färbung zu bewerkstelligen. In diesem Zuge möchte ich auch Marianne Pulst danken, die für mich viele neue Farbstoffe bestellt, aliquotiert und verstaut hat.

Jan Keller hat sich nicht nur die Mühe gemacht meine Arbeit zu lesen und zu korrigieren sondern war außerdem die beste Anlaufstelle in Sachen Datenauswertung und Matlabfragen, und das immer gut gelaunt. Ohne ihn, würde der Auswertalgorithmus sicherlich nicht so gut laufen. Danke. Auch darf man Lars Frahm nicht vergessen, der sich mehr als nur fünf Gedanken über meine Probleme gemacht hat und mich auf den Wahrscheinlichkeitsansatz hinwies und immer ein offenes Ohr für mathematische Ansätze hatte.

Des Weiteren gilt ein besonderer Dank Jaydev Jethwa, der nicht nur fast alle Teile meiner Arbeit auf Fehler durchsuchte sondern der auch mit seiner freundlichen und hilfsbereiten Arbeit mir immer dann aushelfen konnte, wenn ich mal gerade wieder unbedingt und jetzt sofort diesen oder jenen Adapter, Steckdose, Kabel oder was auch immer brauchte.

Ohne Johann Engelhardt und Andreas Schönle, die die ganze Programmierung

des FPGAs bewerkstelligt haben, wäre die Durchführung dieses Projektes nicht so schnell möglich gewesen. Danke euch, ihr wart eine große Hilfe. Gleiches gilt auch für Marco Roose, der wann immer mein Rechner nicht das tat, was er tun sollte, wusste, wie, wo, was, warum zu tun ist damit alles wieder läuft.

Außerdem möchte ich mich auch bei Vladimir Belov bedanken, der mit seinem großen Wissen bezüglich organischer Farbstoffe ein guter Ansprechpartner für das Verhalten eben jener unersetzlichen Bestandteile für die STED Mikroskopie ist.

Ein ganz besonders großes Dankeschön gilt Nicolai Urban, der mir nicht nur immer wieder seine Schulter zum ausweinen und abreagieren angeboten hat sondern auch immer gut war für eine hochrangige Diskussion, sei es wissenschaftlicher Natur oder eben auch Filme, Bier, Spiele oder einfach nur Quatsch. Gleiches gilt für Lena Große. Sie hat mir nicht nur mit unentbehrlicher, schokoladiger Nervennahrung sondern auch mit ihrem schon fast zwanghaften sonnigem Gemüt und ihrer Erfahrung in biologischem Blabla den Alltag erträglicher gemacht. Liebe Lena, lieber Nicolai, ohne euch wär das hier ganz anders ausgegangen.

Ein weiterer Dank geht an Elke Hebisch, Débora Machado Andrade Schubert und Maria Loidolt. Ladies, Ihr wart und seid das beste und einzige Mädchenbüro der ganzen Abteilung. Mit euch gab es eine Vielzahl an stimulierenden Diskussionen bezüglich aller möglichen Belange.

Zudem möchte ich mich bei Gaël M., Christian E., Christian W. und Dominik W. bedanken, die mir gerade in der Anfangszeit alles Nötige über Optik, Justage, Teile, Farbstoffe und Laser beibrachten, das ich im Nachhinein so gut gebrauchen konnte.

Ein weiterer Dank geht an Philipp A., Fabian G., Flavie L.-C., Doug R., Sebastian S., Martin A. und Marcel L., die sowohl persönlich als auch wissenschaftlich immer ein offenes Ohr hatten und den grauen Alltag etwas farbenfroher werden ließen.

Last but not least sind natürlich die Personen aus meinem engen, familiären Umfeld. Es gibt kaum genug Dankesworte für die vielfältige und unersättliche Unterstützung, die ich von euch bekommen habe. Mein größter Dank gilt meinem Mann René, der mir mit viel Verständnis, Zeit und der immer währenden Bereitschaft unseren Sohn Jonas zu betreuen alle notwendigen Arbeiten ermöglichte. Zudem gilt den beiden ein ganz besonderes Dankeschön dafür, dass sie mir jeden Tag auf Neue zeigen, wie lebenswert das Leben eigentlich ist und mir damit durch jede noch so schwere Zeit halfen. Auch ohne meine Mama und meinen Bruder wäre vieles ganz anders gekommen. Vielen, vielen Dank, was würde ich nur ohne euch machen?

Alle, die ich auf Grund meiner Dusseligkeit vergessen habe zu erwähnen, mögen es mir bitte verzeihen. Es war keine Absicht. Auch wenn ihr euch jetzt vielleicht so fühlt wie nach allen Credits von einem Marvel Film, nur um dann festzustellen, dass es keine zusätzliche Szene gibt... Es tut mir leid oder auch suck it and move on!

